Tunable multicolour emission from dysprosium-doped mixed rare-earths oxyorthosilicate nanophosphors for application in ultraviolet-pumped multicolour and white light emitting diodes

By

Ogugua Simon Nnalue

(B.Sc. Hons.)

This thesis is submitted in partial fulfilment of the requirements for the degree

Magister Nanoscientiae

in the

Faculty of Natural and Agricultural Science

Department of Physics

Bloemfontein

at the

University of the Free State

South Africa

Promoter: Prof. O.M. Ntwaeaborwa

Co-Promoter: Prof. H.C. Swart

February 2015

Quote

Proverbs 18:15: An intelligent heart acquires knowledge, and the ear of the wise seeks knowledge

Dedication

This thesis is dedicated to Almighty God for His love and mercy towards me and my family

Declaration

I Ogugua Simon Nnalue, 2010062897, affirm solemnly that the content of this thesis is mine and that it has not been submitted previously for any type of degree or qualification of any kind in this or any other University.

-Ogugua Simon Nnalue-

Sign………………………. at……………………………………………………….

On the ……………………. day of ……………………… 2015

Acknowledgments

I would like to express my sincere gratitude to some individual of which without this dissertation could have not been possible:

- ***Prof. Odireleng M. Ntwaeaborwa*** (promoter) for giving me the opportunity into the world of research and for addressing my shortcomings politely.
- ***Prof. Hendrik C. Swart*** (Co-promoter) for his invaluable advices and contributions to this work.
- ***Dr. Samy K.K. Shaat*** for his assistances and invaluable contributions to the success of this work.
- ***Mr. M.Y.A. Yagoub, Miss M.A. Tshabalala and Mr. R.L. Nyenge*** for their invaluable advices.
- ***Miss P.P. Mokoena*** for assisting with FE-SEM measurement, ***Dr. E. Coetsee-Hugo*** for assisting me with XPS measurement and ***Dr. M. Duvenhage*** for assisting with ToF-SIMS measurement.
- I am grateful to the entire staff and fellow student of physics department for their invaluable contributions.
- Thanks to the Department of Science and Technology South Africa who sponsored this thesis under the South African National Nanoscience Postgraduate Teaching and Training Platform.
- Above all, thanks to Almighty ***God*** who in His infinite mercy gave me the strength, knowledge and willpower to finish this work. I am also grateful to ***Dr. Alexander Ogugua*** for his encouragement and support, ***Miss Sandra Muomezie*** for her prayers and the entire ***Ogugua*** family for their prayers.

Abstract

Phosphors have many uses today in applications such as electronic information displays, solid state lighting, solar cells, advertising and theft prevention. By using urea-assisted solution combustion method, we prepared tunable multicolour and white light emitting dysprosium (Dy^{3+}) doped rare earth oxyorthosilicate (R_2SiO_5) (R = La, Y, Gd) powder phosphors. We prepared five sets of powder samples, namely $LaYSiO_5:Dy^{3+}$, $LaGdSiO_5:Dy^{3+}$, $GdYSiO_5:Dy^{3+}$, $La_{2-x}Gd_xSiO_5:Dy^{3+}$ (x = 0, 0.5, 1.0, 1.5 and 2.0) and $LaGdSiO_5:Dy^{3+}$ x mol% (x = 0.05, 0.1, 0.25, 0.75, 1.0, 1.5, 2.0, 3.0 and 5.0). The structure and the stretching modes of vibration of the phosphors were analyzed using X-ray diffractometer (XRD) and Fourier transform infrared (FT-IR) spectrometer respectively while the morphologies and the elemental composition of the phosphors were analyzed using, respectively, field emission scanning electron spectroscopy (FE-SEM) and energy dispersive X-ray spectroscopy (EDS). In addition, X-ray photoelectron spectroscopy (XPS) was also used to analyze the elemental composition, chemical and electronic states of the phosphors while the distribution of atomic and molecular ionic species on the surface region of the samples was studied using the time-of-flight secondary ion mass spectroscopy (TOF-SIMS). The elemental composition analysis indicated that there was a correlation among the EDS, XPS and TOF-SIMS data. The TOF-SIMS overlay images suggested that the dopant ions were evenly distributed and co-localized with major ionic species on the surface. The crystallite sizes calculated from the X-ray diffraction peaks using Williamson-Hall equation were in the range of 8.0 to 21.0 nm. The band gaps of the phosphors determined from the diffuse reflectance data using Tauc plot were found to vary from 5.0 to 4.45 eV. The photoluminescence spectra recorded when the samples were excited using the 325 nm He-Cd laser consisted of broad band and line emission peaks which we assigned respectively to self-trapped excitons (STE) in SiO_2 and $^4F_{9/2}\rightarrow{}^6H1_{5/2}$ and $^4F_{9/2}\rightarrow{}^6H_{13/2}$ transitions of Dy^{3+}. The peak intensities of the emission bands were shown to depend on the molar ratios of La to Gd, La to Y and Gd to Y on the mixed rare-earths oxyorthosilicate hosts. The colour purity of the bands estimated using CIE coordinates confirmed that our samples were emitting tunable multicolour and white light. These results suggest that our material can be used as single host phosphors in energy efficient UV-pumped multicolour and white light emitting diodes (LED). The structure, particle morphology, surface chemical composition and electronic states, photoluminescent properties and possible applications of these materials in UV-pumped LEDs were investigated.

Keywords

Combustion synthesis, Phosphors, X-ray Diffraction, Photoluminescence, Microscopy, Spectroscopy

List of Acronyms

Techniques

XRD: X-ray Diffraction

FE-SEM: Field Emission Scanning Electron Microscopy

EDS: Energy Dispersive X-ray Spectrometer

XPS: X-ray Photoelectron Spectroscopy

FTIR: Fourier Transform Infrared Spectroscopy

ToF-SIMS: Time of Flight Secondary Ion Mass Spectroscopy

UV-Vis: Ultraviolet-Visible Spectroscopy

PL: Photoluminescence

Chemical elements and compounds

Dy^{3+}: Dysprosium

La: Lanthanum

Gd: Gadolinium

Y: Yttrium

Si: Silicon

La_2SiO_5: Lanthanum oxyorthosilicate

Gd_2SiO_5: Gadolinium oxyorthosilicate

Y_2SiO_5: Yttrium oxyorthosilicate

$LaGdSiO_5$: Lanthanum gadolinium oxyorthosilicate

$LaYSiO_5$: Lanthanum yttrium oxyorthosilicate

$GdYSiO_5$: Gadolinium yttrium oxyorthosilicate

Table of Contents

CHAPTER ONE

Nanoscience and Nanotechnology

CHAPTER TWO

Literature Review

CHAPTER THREE

Combustion Synthesis

CHAPTER FOUR

Experimental Techniques

CHAPTER FIVE

Structure, Optical Properties and Elemental Analyses of Mixed Rare Earth Oxyorthosilicate (R_2SiO_5, R = La, Gd and Y) Doped Dy^{3+} Phosphors.

CHAPTER SIX

Structure, Scanning Electron Microscopy, and Spectroscopy of $La_{2-x}Gd_xSiO_5:Dy^{3+}$ Nanophosphors

CHAPTER SEVEN

The Influence of Dy^{3+} ions Concentration and Post-Annealing on the Properties of $LaGdSiO_5:Dy^{3+}$ x mol % Nanophosphors

CHAPTER EIGTH

Blue Light Excited $LaGdSiO_5:Dy^{3+}$ x mol % White Light-Emitting Nanophosphors for Solid State Lighting Applications

CHAPTER NINE

Summary, Conclusion and Future Work

CHAPTER ONE

Nanoscience and Nanotechnology

1.1. Historical Background of Nanotechnology: The historical application of nanotechnology can be traced back to the staining of church windows with gold and silver nanoparticles in the middle ages and the Lycurgus cup manufactured in Roman times – now at the British Museum, London (Fig. 1.1). Other early histories of nanotechnology are; the noble price award winning report in 1925 by Richard Adolf Zsigmondy in chemistry for making a detailed study of gold sols and other nanomaterials with particle sizes of 10 nm using ultramicroscope, noble price award winner in chemistry, Irving Langmuir in 1932, Katharine B. Blodgett who introduced the concept of a monolayer material of one molecule thick the same year and Derjaguin and Adrikosova who conducted the first measurement of surface forces in the early 1950s.

Fig. 1.1: Lycurgus cup, 4th century AD (currently at the British Museum, London). The colours are as a result of metal nanoparticles embedded in the glass. It appears red at a place where light is transmitted through the glass and green at a place where light is scattered near the surface.

However, in spite of all these earlier events, nanotechnology was introduced proper by Richard P. Feynman on 29th December 1959 in his talk entitled “There’s Plenty of Room at the Bottom” [1] at the annual meeting of the American Physical Society at the California Institute of technology. In his talk, Feynman envisioned the possibility of a great future in which we can arrange atoms one by one the way we want, which is more of bottom-up approach. The term "nanotechnology" was coined in 1974 by a Japanese scientist at the university of Tokyo named Norio Taniguchi who reported on the tunable material properties that nanotechnology can render [2, 3]. Moreover, the official concept of nanotechnology was invented by Drexler at Massachusetts Institute of Technology (MIT) in 1977.

In 1981, K.E. Drexler published the first technical paper on molecular engineering [4] which inspired Gerd Binnig and Heinrich Rohrer of international business machine (IBM) to build the 1986 physics nobel award winning Scanning Tunneling Microscopy (first machine constructed using atomic precision). Richard Smalley and Robert Curl both professor of chemistry at Rice University, Houston and Harold Kroto a chemistry professor at the University of Sussex in 1985 discovered the 1996 chemistry noble award winning fullerenes (also known as buckyballs). The controversial book (also the first book in nanotechnology) 'Engines of Creation' the coming era of nanotechnology [5] was published in 1986. Also in the same year Binning et al [6] invented the Atomic Force Microscope (AFM) and Japan formed the first nanoscience organization called the Humane Frontier Science program [7] aiming to develop the "sixth generation computer". In 1987, Hugues Bedouelle and Greg Winter [8] report the first paper on protein engineering and the first university symposium at MIT. The first university course on nanotechnology titled "Nanotechnology and Exploratory Engineering" held for ten weeks at Stanford University in 1988 was attended by 50 students and were taught by Drexler. In 1989, IBM Don Eigler and his team used 35 xenon atoms to spell their IBM logo. In the same year, the first national conference on nanotechnology chaired by Drexler was held at the Stanford University.

R.T. Bate in 1990 published the first nanotechnology journal [9] and Japan's Science and Technology Agency (STA) begins to fund nanotechnology projects. In 1991, Japan's Ministry of International Trade and Industry (MITI) launched bottom-up approach and committed $200 million into the project after it was endorsed by IBM. Later in the same year, a Japanese physicist Iijima Sumio discovered carbon nanotubes [10] at Nippon Electric Company (NEC). The first textbook [11] for students was published in 1992 and Drexler was invited later the same year by the U.S. senate committee on commerce, science and transportation's subcommittee on science, technology, and space to testify on molecular nanotechnology. In 1993, Charles Musgrave, a Ph.D. chemistry student at the California Institute of Technology won the first Feynman prize on nanotechnology following his work "Modelling a hydrogen abstraction tool useful in nanotechnology"[12]. Nanotechnology was covered for the first time in the white house office of science and technology policy entitled

“Science and Technology: report to the president” [13]. Rice University announced their plans to build nanotechnology research center and laboratory [14]. In 1994, Prof. Ari Requicha of the computer science and electrical engineering department of the University of the Southern California introduced the first nanotechnology university course based on the book “Nanosystems: Molecular Machinery, Manufacturing, and Computation”[15]. The U.S. White House Office of Science and Technology Policy, Dr. Jack Gibbons advocates nanotechnology [16]. In 1995, the first think tank report on nanotechnology [17] was presented by Max Nelson and Calvin Shipbaugh and supported by RAND (Research and Development) Corporation. Tom McKendree of Foresight Institute reported Hughes aircraft study on the industrial analysis of nanotechnology application in military for the first time [18]. The 1995 Feynman price in nanotechnology was awarded to Nadrian C. Seeman, a Ph.D. chemistry professor at New York University for pioneering the synthesis of 3-D DNA objects [19]. In 1996, Feynman prize of $250,000 announced by the foresight instituted for the first time for a person who can design nano-computer [20]. The first European nanotechnology conference was held in Copenhagen Denmark and European Nanotechnology Initiative was created [21]. National Aeronautic and Space Administration (NASA) showed interest in computational nanotechnology [22]. International Business Communication (IBC) organized the first nanobio conference on “Biological Approach and Novel Applications in Molecular Nanotechnology” held in San Diego California [23]. In 1997, the first nanotechnology Development Company was built by Zyvex in Richardson, Texas, with the aim of building the first molecular assembler [24]. Dr. K. Eric Drexler of IMM (Institute for Molecular Manufacturing) designed the first nanorobotic system [25]. For the first time Feynman prize was divided for experimental work and for theoretical work. The prize for the experimental work was won by the IBM research division Zurich research laboratory at CEMES-CNRS (France) for manipulating molecules using scanning probe microscopes. Meanwhile, the theoretical work prize went to NASA Ames research center for their work in computational nanotechnology [26]. In 1998, the first National Science Foundation (NSF) forum held in conjunction with the sixth foresight conference on molecular nanotechnology [27]. Dr. Nadrian C. Seeman of the New York University and his co-workers announced molecular nanotechnology that is based on DNA molecules [28]. Feynman nanotechnology prize for theoretical work was won by Ralph Merkle of Xerox Palo Alto Research Center and Stephen Walch of ELORET at NASA Ames Research Center for their work on computational modeling of molecular tools for atomically-prices chemical reactions, while, the prize for experimental work went to M. Reza Ghadiri of Scripps Research Institute

[29]. In 1999, Robert A. Freitas Jr. wrote the first nanomedicine book [30]. The first safety guidelines for responsible nanotechnology development were presented by Foresight Institute and IMM [31]. The U.S. House of Representatives committee on Science, subcommittee on basic research had a congressional hearing on the proposed national nanotechnology initiative [32]. In 2000, U.S.A government inaugurated the National Nanotechnology Initiative (NNI) and California was the first state to kick of the research initiative with $ 100 million [33].

1.2. What is nano?

The nano is from the Greek word "dwarf" or in Latin nanus and mathematically it means 10^{-9}, or one-billionth. Nano generally refers to one-billionth of a meter, or 1 nanometer (nm) and it is about 3-5 atoms lined up in a row. Nanometer is a very small measure. For instance, a sheet of paper is 100,000 nm thick and the human hair is about 80,000 nm in diameter. By and large, nanoscale ranges from 1-100 nm. Hence nanoscale science (or nanoscience) studies the properties, phenomena, behaviours of materials at atomic and molecular scales between the sizes ranging from 1-100 nm. The nanoscale lies midway between the atomic scale and quantum phenomenon, and microscale. In the nanoscale, the properties of materials are quite different from those of microscale [34]. For instance, gold is solid, yellow and inert at room temperature in microscale, but liquid, red and catalytic at the same temperature in nanoscale. Other instances are copper which is opaque substance in microscale but becomes transparent in nanoscale, silicon which is insulator becomes conductor, aluminum which is stable becomes combustible and platinum which is inert becomes catalytic.

1.3. What is so special about nano?

Nanoscale particles (nanoparticle) are neither new in nature nor in science. However, with the help of modern microscopes scientists have been able to understand phenomena that occur naturally at nanoscale. Basically, these phenomena are as a result of quantum size effect (the unusual behaviour of crystals when they become extremely small due to electrons confinement in small regions of space in one, two or three dimensions) and other simple physical effect such as increased surface area. As surface area per unit volume of a material increases, a greater number of atoms in the material will be exposed to the surface (Fig. 1.2). The quantum size effect improves the electrical, optical and magnetic properties of nanoparticles while the increased surface area of nanoparticles improves their chemical reactivity and the electrical properties.

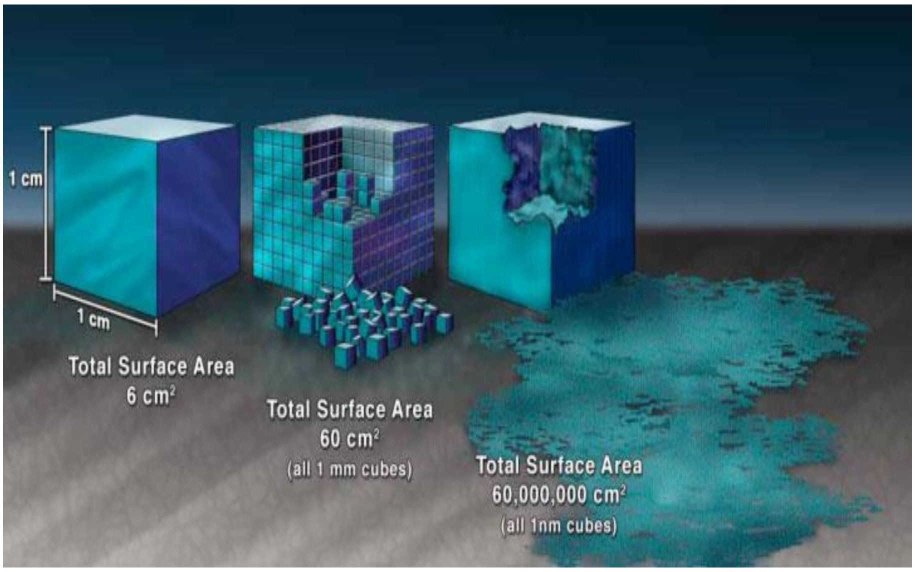

Fig. 1.2: Illustration demonstrating the effect of the increased surface area provided by nanostructured materials.

In Fig. 1.2, consider a cube of a material 1 cm on each sides; it has surface area of 6 square centimeters. If the same volume is filled with cubes of 1 mm on each side, there will be total of 1000 mm cubes (10 × 10 × 10) each having surface area of 6 square millimeters i.e. 60 square centimeter. When filled with 1 micrometer sized cubes, there will be total of 10^{12} cubes ($10^4 \times 10^4 \times 10^4$), with surface area of 6 square micrometers i.e. 60,000 square centimeters. However, when the same volume is filled with cubes of 1 nm on each side, it will amount to total of 10^{21} cubes ($10^7 \times 10^7 \times 10^7$), each having total surface area of 60,000,000 square centimeters. [35].

1.4. Applications of nanotechnology

Nanotechnologies are regarded today as the major technologies for innovations and technological advancement in most branches of economy. Nanotechnology deals with research, processing and production of items as well as structures that are smaller than 100 nm [36]. According to NNI, nanotechnology is the understanding and control of matter at dimension of roughly 100 nm, where unique phenomena enable novel applications [37]. There is no single field of nanotechnology rather it broadly refers to such fields like biology, chemistry, physics, any scientific field or a combination of any of these fields that deals with the deliberate and controlled manufacturing of nanostructures. As a multidisciplinary field, nanotechnology has found application in all sectors of the economy, ranging from electronics, information and communication technology, biotechnology, medicine, optics, energy production, environmental sciences, cosmetics, processed food pharmaceutics etc. A few of these applications are discussed below.

1.4.1. Electronics applications

Switching devices: As a result of its high electrical conductivity, carbon nanotubes (CNTs) can be used in the production of ultra-fine wires and channels that can be used in field-effect transistors. Nanotubes have the electrical properties that enable them to perform as molecule-sized diodes, wires and transistors. A team of scientists led by Cees Dekker has discovered that nanotubes with twists in their cylindrical bodies allow current to flow in single direction [38]. This characteristic of nanotubes has a promising application in future nano diode and can ultimately lead to the production of transistors and integrated circuits with areas comparable to the size of few atoms [39]. RIKEN laboratory in Japan have also developed electron spin based switching devices instead of electron charge. These so called “spintronic” devices may one day become a substitute for traditional silicon based semiconductors [40].

Flexible displays: There has been a dream of fold-up television and computer screens which can fit inside peoples pocket but this could not be achieved using silicon semiconductor because of its rigid nature. Although some organic semiconductors have been used in bendable displays, their performance is limited. However, this dream can be made a reality with the flexible CNTs. A group of researchers at Purdue and the University of Illinois-Urbana-Champaign have developed CNTs flexible display which in the future could be applied in electronic newspapers and roll-up handled devices [41].

Thinner Television Sets: In tube televisions, a beam of electrons is fired on a phosphor material which glows and produces the coloured light that displays the television picture. This requires relatively large electron gun and big tube. However, the advent of field emission displays (FED) in which tiny electron emitters positioned behind phosphor (light emitting material deposited on the TV screens) dots has miniaturized the whole process. CNTs are exceptional electron emitters, therefore using them to excite the phosphor dots in FED could create a brighter and higher resolution display that will be few millimeter thick and consume less energy compared to plasma and liquid crystal displays [41].

1.4.2. Computing applications

Memory devices: Ascribe newswire on February 29, 2000 reported that nanotubes can be applied in electronics and storage devices. Better memory devices can be created by sandwiching C_{60} atoms inside a nanotube and assigning binary “1s” and “0s” to ends of the tube. The buckyballs takes on the “0s” state as it moves to one side and the tube takes on the “1s” state as it moves to the opposite side [42].

Faster computing chips: The number of transistor in a computer chip determines its processing speed. The existing laptop processors use silicon transistors and it contains less than half a billion transistors. CNTs based computer chips will be far greater than that. With its tiny sizes (only a nanometer wide) it implies that billions of CNTs based transistors could be contained in a single processing chip hence building smaller and faster computers and electronics [41].

Quantum computing: Unlike the classical model of computing where the bit can only exist in either 0s or 1s energy states, in quantum computing, bit is referred to as ‘qubit’ and they exist in the usual classical state of 0s and 1s as well as in coherent superposition of both states. In coherent superposition state, the qubit is thought to exist in two universes, as 0 in one and 1 in the other universe. Therefore single operation in a qubit will act on both values simultaneously. In general, by performing single operation on a qubit, the operation has been performed on two different values. Similarly, two qubit systems would perform the operation on 4 values, three qubit on eight values and four qubit systems would perform on 16 values.

Quantum dot technology is one of the most promising ways of achieving this. The flow of electrons through quantum dot can be controlled by passing small voltage to the leads and at the same time take measurement of the spin and other properties. With several entangled dots, or qubits one can find a way of performing operation and quantum calculations might be possible [43-45].

1.4.3. Optical applications

Field emission devices (FED): Nanotubes can be made to eject electrons from their ends by applying just little voltage across them. Millions of nanotubes can be carefully arranged in a flat surface and the amount of electrons they emit can be controlled using electric field [46]. FED is the one of the most promising and immediate application of CNTs. Nanotube based FED light bulb which is more efficient, twice brighter, and more durable than the present day light bulbs has been reported by engineers at Isa electronic corporation in Japan and Stanford, Georgia Institution of Technology. Nanotube based FEDs are hoped to replace CRT and LCD screens one day [38]. With the advent of FEDs, there will be brighter and more colourful desktop monitors which could have the capability to support full-motion video having almost 180 degree viewing angle [47].

Light emitting diodes (LEDs): Because of their ability to emit in specific Gaussian distributions, quantum dots (QDs) can be applied in displays. Unlike LCD which uses single fluorescence lamp that is colour filtered to produce red, green and blue pixels, quantum dots produce monochromatic light making it more efficient, less power consuming and brighter. QDs based LED are designed by a process called alloying, which can be either overcoating the QD core with a material or by grading the QD core composition [48].

1.4.4. Energy production Applications

Solar cells: Because of their small size, billions of CNTs could be closely arranged onto solar cells and because of their high electrical conductivity; they can release more electricity per unit area than silicon. Group of researchers at Rensselaer Polytechnic Institute, Troy, New York have reported that CNTs total reflectance of 0.045% which is about three times lower than the lowest ever reported values of optical reflectance from any material, therefore CNTs can be said to be the darkest man-made material ever [49]. So since an ideal black material is known to be a perfect light absorber at all angles and over all wavelengths, CNTs are the best known light absorber.

Furthermore, group of researchers at Georgia Tech Research Institute have also reported CNTs based 3D solar cell which consists of tower structured photovoltaic cells (about 100 microns tall, 40 microns by 40 microns square and 10 microns apart) that traps light between the structures. The photovoltaic cells were built from arrays containing millions of vertically aligned CNTs. Unlike the conventional flat solar cells that reflect a significant portion of the light that arrive on their surface, in CNTs based solar cells, the tower structures traps and absorbs light emerging from different angles hence the solar cell remains efficient even when the sun is not overhead. Because of their ability to absorb virtually all the incident photons, the 3D cell coatings were made thin such that electron exits quickly therefore reducing any chance of recombination and hence increasing the quantum efficiency [50].

Energy storage: Unlike batteries which stores electricity chemically, by building charge on dielectric materials, capacitors can hold electricity physically. The amount of charge that can be stored by a capacitor varies with the surface area of the dielectric material. With their exceptional surface area, using CNTs as dielectric materials could increase the electricity storage capacity of capacitors [41].

1.4.5. Biomedical applications

Biomedical applications of nanotechnology can be generally grouped into three categories: drug delivery, diagnostic techniques and prostheses and implants [51]. Researchers at the moment are more interested in biomedical applications for use outside the body, such as sensors. On the other hand, much research is also going on for biomedical application inside the body such as anticancer drugs etc. Nonetheless, other researchers are also working on prostheses and implants using nano-structured materials.

Biosensors: A sensor can be defined as a device capable of recognizing a specific chemical species and ‘signaling’ the presence, activity or concentration of that species in solution through some chemical change. A transducer converts the chemical signal (for instance the catalytic activity of a particular biomolecule) into a quantifiable signal (such as change in intensity or colour) with a defined sensitivity. Sensors are called biosensors when sensing is based on biomolecular recognition. Biosensors can be enzyme based, nucleic acid based or antibody/antigen based. They can also be classified depending on the technique used in the signal transduction into electrochemical, optical, mass-sensitive and thermal biosensors [52, 53]. Nanomaterials such as CNTs [54], QDs [55], porous silicon [56], metallic nanoparticles [57], nanowires [58] and nanofibers [59] have been used as elements for biosensors. The nanomaterials are used as substrates on which biological molecules are attached to recognize the analytes (the target) of interest. Biosensor works as probes recognizing or differentiating between analytes of interest by change in mass, colour, intensity or other physical properties.

CNTs based field-effect transistor biosensors used for protein detection has been reported which relies on changing the electrical resistance of the nanotubes when it comes in contact with a specific protein [60]. In conjunction with the University of Illinois at Urban-Champaign, Rush Medical College in Chicago and the University of Arkansas, the Defense Advanced Research Projects Agency (DARPA) are trying to develop a biosensor which can identify bacteriological infections in biowarfare. It was also reported that the American army want to integrate a wearable biosensor in clothing [61]. A professor of mechanical engineering at Michigan State University, Peter Lillehoj received $ 400,000 award from the National Science Foundation (NSF) with the aim of developing wearable biosensors that can be incorporated into clothing to detect illness and monitor health [62].

Drug delivery: Ideally, for an effective treatment of cancer or tumor, the drugs should be able to reach the desired destination by penetrating the cell membrane without loss of reasonable quantity of their volume in the blood circulation. On reaching the target, the drug should be able to kill the tumor cells without harming the normal ones. These are the major factors that determine the probability of the survival of the patient. However, cells are always conscious of what is happening in their environment and are good at protecting their contents; as a result it's very hard to penetrate their membrane walls to deliver drugs, nutrients or biosensors without causing damages or even destroying the cell. Nevertheless, with the use of nanoparticles, drugs can be delivered to a specific cell without causing damages or destroying the cell. The aim of targeted drug delivery is to prolong the duration of the nanoparticles in the blood stream without being eliminated, localization of the drug such that the concentration is higher in some parts of the patient's body relative to others, have the ability to target the cell in question and to interact with only the diseased tissue. Scientists have by different mechanism used different nanomaterials to develop some nanobots that can target cancer cells [63].

Star-shaped-like nanobot termed "nanostars" has been developed using gold nanoparticles which can deliver drugs directly to the nuclei of cancer cells [64]. DNA-based nanobots have been created that can target cancer cells [65]. Researchers at Massachusetts Institute of Technology (MIT) have demonstrated the feasibility of self-assembling "nanofactories" which were capable to make protein compound on demand at target sites [66]. Jeffrey Zink and Fuyu Tamanoi reported what they called "light-activated drug delivery", where nanoparticles can carry chemotherapy drugs directly to tumor cells and when activated by a two-photon laser in the infrared region, they release the drugs [67].

Nanosurgery: Nanosurgery as it applied in biology uses narrow laser beams focused by microscopic objective lens to apply an adjustable force onto organelles and other subcellular structures. Through the manipulation of the beams, this technique can be made so precise that it can be used for destruction of a single cell without damaging the adjacent cells. Conventionally, nanosurgery involves the use of optical tweezers composed of laser light beams manipulate dielectric particles. The strong electric field gradient at the tip of the laser beam attracts these particles in a manner that they tend to move in the direction of the gradient with respect to the center of where the electric field is strongest. As a result of this attraction, the particle can be moved from one point to another without being touched. The process of the dielectric particles being attracted by the laser beam is known as “trapping” [68]. This process has been applied by many scientists in carrying out nanosurgery.

A group of researchers at Eric Mazur’s photonics laboratory at Harvard University have employed near-infrared femtosecond laser in ablate AFD sensory neurons in nematode worm [69]. Similarly, a femtosecond laser has also been used together with gold nanoparticles to perform nanometric-scale surgery [70]. The gold nanoparticles were deposited on the cells and when the laser light is shun on the cells, nanoparticles concentrates the laser’s energy on the cancer cells making it possible to perform nanometric-scale surgery in an excellent way. D.M. Gavin et al reported the use of polarization-shaped optical vortex traps which minimized photodamage to the trapped particles as a result of the polarization effect for carrying out single-cell nanosurgical procedures [71].

Optical biopsy: Optical biopsy is a general name given to different optical techniques applied in the diagnoses of diseases such as cancer and atherosclerosis without the remove of any tissue from the body [72]. The process involves the use of fluorescence spectroscopy to generate optical imaging for differentiating between healthy, malignant and premalignant tissues of different organs. This noninvasive, high-resolution imagine techniques employs optical components such as light emitting diodes, laser lights, CCD detectors, endoscopes, fibers .etc. in its operation. With the aid of optical biopsy, the need for surgical tissue removal can be eliminated and the often long wait for lad results can also be a thing of the past. Most importantly, it enhances the ability to detect, diagnose and monitor diseases.

Fluorescence-based optical biopsy relies in two approaches for the detection of diseases. The first approach relies on the differences in the compositions and morphology of the infected and normal tissue and their effect on the autofluorescence to differentiate between the tissues. However, the second approach relies on the presence of difference fluorescent material such as exogenous fluorophores, fluorescence markers and sensitizers for differentiation of the tissues [73]. The use of nanomaterials such as QDs in optical biopsy could lead to a better imaging.

Materials which can selectively bind to various biological molecules can be used to coat QDs. The coating material makes it possible to find the desired biostructure while the coated QDs show the trail of the movement when excited with ultraviolet light. Monitoring the movement of this dots helps in locating the tumors and by studying the light emitted by each tumor gives detailed information about the tumor at the molecular level. The common coatings used for tracking the movement of protein inside cancer cells include nucleic acids, peptides and antibodies [73].

1.4.6. Other Applications

Catalysis: The major aim of nanocatalysis is to control chemical reaction by changing material properties such as size, shape, morphology and the chemical composition. With its increased surface area to volume ratio, nanoparticles increased the exposed surface area of catalyst; a host of chemical reactions occur on the surface of the catalyst, and the larger the surface area, the more active the catalyst become. Other properties such as structure and shape of nanoparticles also effect on their catalytic activities. Nanomaterials such as Pt [74], Pd [75], Ag [76], Au [77], TiO_2 [78], Al_2O_3 [79], CNTs [80] etc. have been applied in nanocatalysis.

The Shenhua group, the largest coal company in China is embarking on a project in which they use gel-based nanocatalyst in the liquefaction of coal and turn it to gas. With this, coal can be converted into diesel fuel and gasoline [81].

Military: Seeman's lab at New York University has constructed a 10 nm long nanobot from DNA fragment which can walk on two legs [82]. This device may have future application in military. Group of researchers at Cambridge University reported on how to spin tiny CNTs together to produce fiber with the strength of Kevlar (a composite material for making bullet proof). With the rapid improvement in the technique for production of longer CNTs, spun fibers made of CNTs very soon may have higher strength than Kevlar and will also have lighter weight. Spun CNT fiber could be used to make stronger and lighter body amour [41]. U.S Department of Defense has shown the possibility of the use of nanometals such as nanoaluminum to build bombs more powerful than the present conventional bombs with high order of magnitude [83]. Nanoparticles of silica can be used to create shear thickening fluid body amour which act similar to water but stiffens upon impact [84]. Also durable and lightweight body armor has been produced using aluminium alloy combined with CNTs [83].

1.5. Brief Introduction to Phosphors

Invented in the early 17th century by Vincentinus Casciarolo an alchemist of Bologna, Italy, "phosphor" means "light bearer" in Greek. Casciarolo fired a glossy heavy crystalline stone he picked at the foot of a volcano in an oven charcoal with the aim of converting it to a noble metal. However, his end product was something he never expected; he discovered that after exposure to sunlight, the sintered stone emitted red light when placed in the dark. The stone named "Bolognian stone" is currently known as barite ($BaSO_4$), and the fired product BaS.

Subsequent to this finding, similar discovery were reported in other places in Europe, and afterwards they came up with the name "phosphor" for these light emitting stones. In a more general term, phosphor can be defined as chemical materials that emit light when excited by radiation, and are usually in the form of micro or nanocrystalline powders and thin-films designed to provide visible colour emission. Luminescence refers to a phenomenon in which a material absorbs energy of a certain wavelength and subsequently emits light at another wavelength.

In a broader sense, the definition of fluorescence and phosphorescence given above applies to inorganic materials. For organic materials, fluorescence is defined as light emission from a singlet excited state, while phosphorescence is defined as light emission from a triplet excited states. The definition of the word "phosphor" most of the times depends on the user. Precisely, it used to mean inorganic phosphors, which comprises those in powder form. While the single crystals such as thin-films and organic molecules that luminesce are seldom referred to as phosphors. By and large, phosphor is a term used to describe "solid luminescence materials" [85].

1.6. Basics for Phosphor Engineering

Phosphors materials, known for their ability to luminesce, are mainly solid inorganic materials comprising of host lattice which are normally doped with impurity known as dopants [86]. The host in a sense is regarded as the "home" of the dopant. In most cases, the host ions are replaced by the dopant ions substitutionally sitting at the host lattices. As a result, the distance between the dopant ions are determined by the properties of the host lattice. The environment of the host atom is influenced in many ways by the dopant atom; hence it is very crucial to consider some basic factors when engineering a phosphor. Factors such as the radius of the dopant cations, the valence state, the coordinate number as well as the spin state should be carefully considered when making choice of host matrix and the activator (dopant) [87]. These factors must be the same or similar for both the host material and the dopant ion in order to avoid formation of lattice stresses and/or crystal defects as a result of doping. Other factors that should be considered when selecting host materials are; (i) the magnitude of its phonon energy, since host materials with low phonon energy minimize non-radiative relaxation and hence increases metastable energy lifetime. (ii) A host material should be mechanically and chemically stable. Both absorption and emission of energy in phosphors can take place from the host matrices and the dopants. In some cases, when the activator ion shows weak emission, a second type of impurity ion (co-activator or co-dopant) called a sensitizer is added which absorbs the energy and subsequently transfer it to the activator to resulting in improved emission. Quite often, the emission colour can be varied by choosing the appropriate activator since each activator has a characteristic colour emission, but the host material may not be changed [86]. Host materials employed in LED and optical display applications are required to have wide band gap in order to allow visible light transmission. As a result, insulators are usually used as hosts in such applications. However, some wide band gap semiconductors such as ZnO and GaN with optically active ions can be used as host materials provided the excited state of their luminescence does not overlap with their conduction band since this may lead to luminescence quenching [88].

1.7. Luminescence Mechanisms

Luminescence basically refers to the emission from photons within the range of visible region of the electromagnetic spectrum under the influence of certain radiation with exclusion of heat. The word "luminescence" originated from the Latin word "lumen" meaning "light" was first used as "luminescenz" by a physicist Eihardt Wiedemann in 1888, to explain light phenomena that doesn't involve temperature rise. Unlike incandescence which involves light emission from hot body as a result of its temperature (above 600℃), luminescence involves cold temperature emission where excited valence electrons subsequently relaxes to its ground state and emits a photon [89]. Luminescence process can be classified based on their mode of excitation as shown in table. 1.1.

1.7.1. Photoluminescence (PL)

Photoluminescence is a term used to describe the spontaneous emission of light from a material when excited by an optical source [90]. Quantum mechanically, photoluminescence can be defined as the excitation of electron to a higher energy state and subsequent return to the ground state which is accompanied by the emission of photon [91]. The major characteristic of photoluminescence relies on the ability of electrons to be excited with light and photons being emitted in turn. Photoluminescence can be either phosphorescence or fluorescence depending on the period of emission after excitation.

Table. 1.1: Types of luminescence

Phenomenon	**Mode of excitation**
Photoluminescence (fluorescence and phosphorescence)	Light (photon) absorption
Cathodoluminescence	Cathode rays (electron beams)
Radioluminescence	Ionizing radiation (X-rays, α, β, and γ and rays)
Electroluminescence	Electric field
Thermoluminescence	Heating after pre-storage of energy (e.g. radioactive irradiation)
Chemiluminescence	Chemical processes (e.g. oxidation)
Sonoluminescence	Ultrasounds
Triboluminescence	Frictional and electric forces
Bioluminescence	Biochemical processes

1.7.2. Fluorescence and Phosphorescence

Introduced in the middle of the 19th century by G.G. Stokes [92], fluorescence can be basically distinguished from phosphorescence based on the duration of emission after the excitation source is switched off. While the emission of light disappears simultaneously at the end of excitation in fluorescence process, it persists after excitation in phosphorescence process. The mechanisms of fluorescence and phosphorescence can be explained by the Jablonski diagram [93] as shown in Fig. 1.3. Fluorescence basically involves two energy levels; the ground state and the excited state. Here an electron absorbs a photon of energy $h\nu_A$ and gets excited to S_1 (or S_2) level, after which it relaxes to the lowest vibrational level of S_1 (internal conversion) before emitting a photon of energy $h\nu_F$ and then returns to the ground state after vibrational relaxation. In fluorescence process, the spin multiplicity of the excited and the ground state are the same. On the other hand, three basic levels are involved in phosphorescence process: a ground state, an excited state and a metastable trapping state. Here, an electron excited to a S_2 vibrational level for instance undergo an intersystem crossing (ISC) to an electronic triplet excited state where it undergo series of transitions in the metastable states before it emits a photon of energy $h\nu_P$ and return to the ground state.

Unlike fluorescence, in phosphorescence process, the spin multiplicity of the excited and the ground state are different [94].

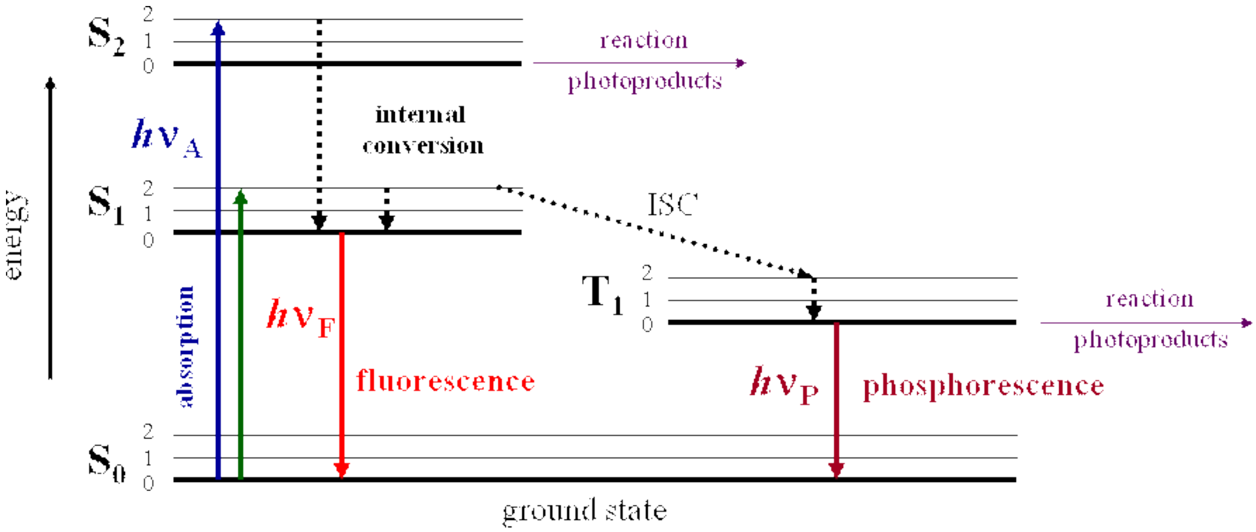

Fig. 1.3: Simplified Jablonski diagram. The sequence of events leading to fluorescence and phosphorescence are shown. S_0 is the ground state, S_1 and S_2 are excited singlet states; T_1 is an excited triplet state. 0, 1, 2 represent vibrational levels. Straight lines represent transitions involving photons, dotted lines represent vibrational or thermal transitions.

1.7.3. Luminescence centers

Luminescence centers are some point defect of any kind in crystal that can absorb and emit energy. Luminescence centers can be either extrinsic or intrinsic [95]. Extrinsic center also known as “impurity centers” are mostly activators incorporated intentionally into the crystal for some application purpose. Other forms of extrinsic luminescence centers are sensitizers and quenchers. Extrinsic centers are mainly rare earth elements or transitional metal ions. On the other hand, intrinsic centers also known as “defect center” are native of the host materials and can originate as a result of (i) structural imperfections – due to poor ordering, damage from radiation, or shock damage and (ii) impurities (non-activators), substitutional or interstitial that can cause distortion on the crystal lattice [96]. Intrinsic centers are responsible for band-to-band recombination of electron-hole pairs.

1.8. Applications of phosphors

Applications of phosphors can be classified based on the various devices they can be produced with as follows: (i) as light source e.g. fluorescent lamps; [97] (ii) as display devices e.g. cathode-ray tubes (CRT) [98] and light-emitting diode (LED); [99] (iii) as detector systems e.g. X-ray screen [100] and scintillators [101] and (iv) in other applications such as in luminous paints [102], optical lasers [103], optical amplifiers [104], and solar energy converters [105]. In this section however, we will only discuss in detail the applications of phosphors on LED since this is the area of interest in this work.

1.8.1. Light emitting diode (LED)

LEDs belong to family of solid state lighting (SSL) which emits light by solid state electroluminescence along with organic light-emitting diodes (OLED) and polymer light-emitting diodes (PLED) as opposed to incandescent bulbs (which uses thermal radiation as light source) or fluorescent tubes. Unlike incandescent bulbs, LEDs don't have filaments that burns out or gets hot, rather they are illuminated by electrons movement in a semiconductor [106].

In a narrow sense, LEDs are semiconductor diodes that permit the flow of current in one direction alone. It is well known that diodes consist of P- and N-type semiconductors with P-type having extra hole and the N-type having extra electron. Also a depletion zone is formed when no voltage is applied to the diode by the movement of electrons from the N-type material to the P-type material. However, when enough voltage is applied to the diode (N-type side is connected to the negative end of the circuit and P-type is connected to the positive end), the depletion zone disappears and hence charge can move across the diode. As the free electrons from the N-type material moves across the diode, they fall into the empty holes in the P-type material and this results in the emission of photons as shown in Fig. 1.5 [107]. This process is analogous to the transition of electron from the conduction to the valence band of a material and consequently emits a photon.

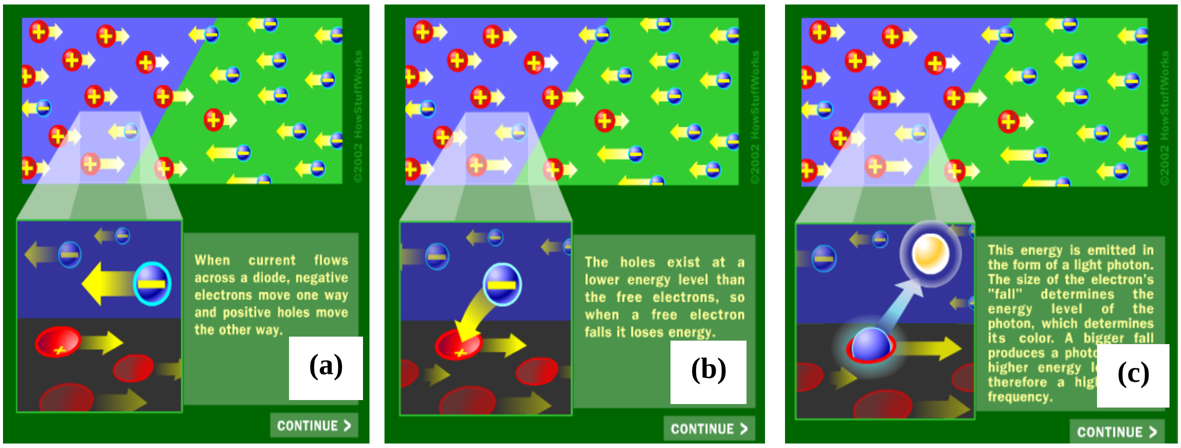

When current flows across a diode, negative electrons move one way and positive holes move the other way.

The holes exist at a lower energy level than the free electrons, so when a free electron falls it loses energy.

This energy is emitted in the form of a light photon. The size of the electron's "fall" determines the energy level of the photon, which determines its color. A bigger fall produces a photo higher energy l therefore a hig frequency.

Fig. 1.5: Illustration of how free electrons from N-type material move across the diode junction (a), and fall into the empty holes from the P-type material (b), leading to the emission of photons (c).

Recently, LEDs, especially white LEDs have attracted much attention because of their economic advantages over other solid-state light sources. As a result, many researchers have put extra efforts on phosphors converted LEDs; making this area the most active research field in phosphors. White LEDs can be constructed in three different ways as discussed below:

(i) **Mixed-coloured white light**: This involves the combination of the three primary coloured (red, blue and green) LEDs in a single device and this combination gives white light through colour addition (Fig. 1.6). Phosphors are not used in this type of arrangement. This type of LEDs have high colour rendering index and can provide a wide range of colour reproducibility (>100% NTSC colour region) when used as light source for backlight of a liquid crystal display (LCD) [108]. Conversely, this approach of construction of LEDs has suffered some drawbacks because of the difference in the life time of the various light sources. This results in low luminescence efficiency resulting from strong absorption of the blue light by the red and the green light.

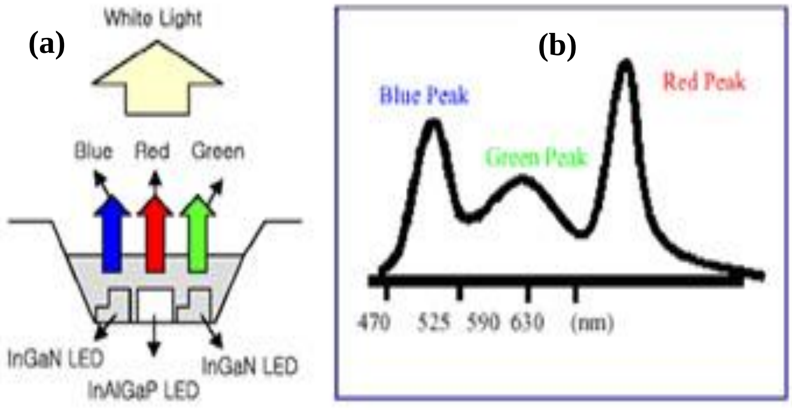

Fig. 1.6: (a) Illustration of how combination of three primary colours, red, green and blue yields white light. (b) The luminescence emission spectrum of red, green and blue LEDs [109].

(ii) **UV- pumped phosphor-based white LEDs**: In this arrangement, white LEDs are fabricated by optical excitation of phosphors using ultraviolet (UV) based LEDs (Fig. 1.7 (a)). The UV-LEDs (usually AlGaInN based) excitation source has been reported in the near-UV (320−390 nm) [110] and in the violet, close to visible spectrum (390−410 nm) [111].

In the UV-pumped white LEDs, the UV-emitting LED is coated with red, green and blue light emitting phosphors, resulting in an emission which covers almost the whole range of the visible spectrum (Fig. 1.7 (b)).

Advantages of UV- pumped phosphor-based white LEDs

(a) High colour rendering-index (up to 97%) [112].

(b) High chromatic stability under different driving currents.

Disadvantages of UV- pumped phosphor-based white LEDs

(a) The major drawback of UV-pumped white LEDs is the loss of energy during conversion of UV light to white light. As a result, UV-pumped white LEDs have lower luminous efficiency compared to white LEDs based on yellow phosphor excited with blue LED.

(b) Due to the high energy of UV-light, the resin used for packaging the LEDs is solarized, leading to light output degradation over time.

(c) Change in emission colour may be observed since combination of two or more kind of phosphors with different properties such as life time, temperature dependent and durability are required.

(d) In case of any leakage in the LEDs, the UV-light can be hazardous to the user [108].

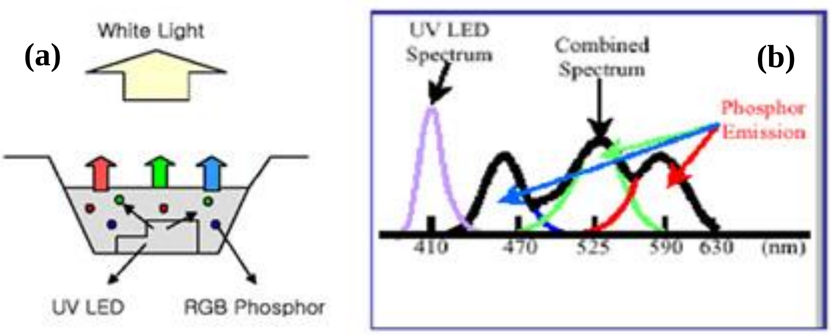

Fig. 1.6: (a) Illustration of how UV-light shone through red, green and blue phosphors yield white light. (b) The luminescence emission spectrum of UV-light excited red, green and blue emitting phosphors [109].

(iii) **Yellow phosphor-converted white light**: White light emitting LED can also be constructed by a combination of phosphors and short-wavelength LED. Here a blue LED is usually coated with yellow emitting phosphor (Fig. 1.8 (a)). When the phosphor is illuminated by the LED, part of the blue light will be used for the excitation of the yellow light while some will contribute to the blue component of the white emission [106]. A typical example of this type of white LED is the combination of blue LED (based on InGaN/GaN) and yellow-emitting YAG:Ce ($Y_3Al_5O_{12}:Ce^{3+}$) phosphor. The YAG:Ce phosphor absorbs part of the blue LED emission at 460 nm and convert it to broad-band yellow emission while the remaining part of the blue emission contributes to the blue component of the white light (Fig. 1.8 (b)). The quantum efficiency of 90% has been reported for this phosphor [113]. This type of arrangement has some advantages and disadvantages listed below.

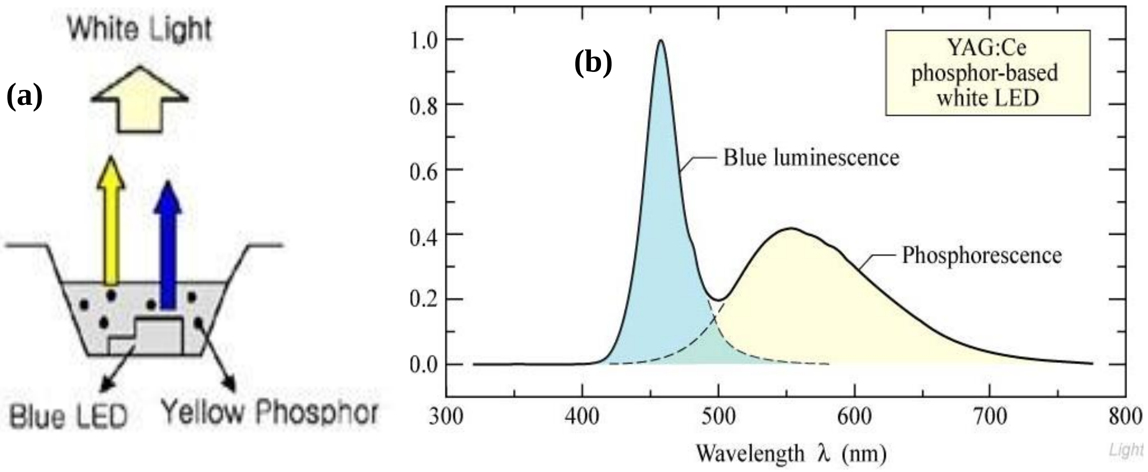

Fig. 1.8: (a) Illustration of how blue LED light, shone through its complementary yellow phosphor, yields white light. (b) The luminescence emission spectrum of YAG:Ce phosphor excited blue LED [109].

Advantages of yellow phosphor-converted white light LED based on YAG:Ce

(a) Tunable emission colour over wide wavelength range: This can be achieved by partial substitution of Y with Gd and Al with Ga which results in shifting of the emission wavelength of Ce between 510 and 590 nm without significant reduction in the efficiency [108].

(b) High chemical stability: The robust crystal structure of YAG:Ce phosphor helps it to only deteriorates slightly even under severe conditions [114].

(c) Short persistence of the Ce^{3+} luminescence: The life time of Ce^{3+} in YAG is very small (10^{-7}-10^{-8} s) which make it a good light source for display applications [115].

(d) Inexpensive and easy manufacturing process: YAG has been used as host material for several years in applications such as laser, CRTs and fluorescent lamps. As a result, its manufacturing process has been well established [116].

Disadvantages of yellow phosphor-converted white light LED based on YAG:Ce

(a) Because the excitation source (blue LED) has higher energy than the yellow emitting phosphor, energy is lost due to the absorption of part of the blue light by the phosphor.

(b) Low colour rendering index.

(c) Low luminous efficacy.

1.9. Statement of Problem

In section 1.8.1, we discussed the three major ways through which white light can be generated: by combination of red, blue and green LED, combination of blue LED and a yellow phosphor or excitation of red, blue and green phosphor using UV-light. We also listed some of the problems associated with each method for construction of white LED. Some of these problems are a result of combination of different phosphors or different LEDs in a single chip. To address these inefficiencies, there is a need to develop a single host white light emitting phosphors that can be excited by either ultraviolet (UV) or blue LED.

1.10. Objectives of this study

In a quest to find solutions to the problems associated with the various ways of generation of white light, we aimed to develop white light emitting and tunable phosphors by using solution combustion synthesis to produce:

(a) $GdYSiO_5$, $LaYSiO_5$ and $LaGdSiO_5$ doped Dy^{3+} and choose the one that gives the highest photoluminescence (PL) emission intensity.

(b) $La_{2-x}Gd_xSiO_5$ doped Dy^{3+} ($x = 0, 0.5, 1, 1.5$ and 2) and choose the mole ratio of La and Gd which give the maximum PL emission intensity

(c) Synthesize $LaGdSiO_5$:Dy^{3+} x mol% ($x = 0.05, 0.1, 0.25, 0.75, 1.0, 1.5, 2.0, 3.0$ and 5.0) by varying the mole concentration of Dy^{3+} to optimize the emission intensity.

1.11. Layout of the thesis

This thesis is divided into nine chapters

Chapter 1: Chapter one is divided into two sections. Section one gives background on nanoscience and nanotechnology and the applications of nanotechnology while section two is about phosphors, terminology of some luminescence processes and the aim of the study.

Chapter 2: This chapter describes the crystallographic properties of rare earth oxyorthosilicates, the properties of dysprosium and luminescence related to intrinsic defects in silicon dioxides.

Chapter 3: This chapter discusses combustion synthesis, its types and solution combustion synthesis of rare earth oxyorthosilicates.

Chapter 4: This chapter describes the various techniques used for characterization of our materials.

Chapter 5: Here, we report the structural, optical properties and the elemental analysis of both single and mixed rare earth oxyorthosilicates doped Dy^{3+}.

Chapter 6: This chapter reports the effects of the variation of the molar ratio of La and Gd on the structure, optical properties and the chemical composition of $La_{2-x}Gd_xSiO_5:Dy^{3+}$.

Chapter 7: The dynamics of Dy^{3+} in $LaGdSiO_5$ host matrix are discussed and the ToF-SIMS and the XPS analysis are also reported.

Chapter 8: The photoluminescence spectra of $LaGdSiO_5:Dy^{3+}$ recorded using blue light as the excitation source is discussed.

Chapter 9: The thesis summary, conclusion and the future work.

1.12. References

[1] R.P. Feynman, in Miniaturization, ed. H. D. Gilbert, (Reinhold, New York), 282-296 (1961).

[2] N. Taniguchi, Proc. of International Conference on Precision Engineering (ICPE), Tokyo, Japan, 18-23 (1974).

[3] T.J. Webster, Int. J. Nanomed. 2, 1 (2007).

[4] K.E. Drexler. Molecular engineering: An approach to the development of general capabilities for molecular manipulation. Proc. Natl. Acad. Sci. USA 78, 5275-5278, (1981)

[5] K.E. Drexler. Engines of Creation: The Coming Era of Nanotechnology. Anchor Books USA, ISBN 0-385-19973-2(pbk) (1986).

[6] G. Binnig and C.F. Quate. Atomic Force Microscope. Phy. Rev. Lett. 56, 9 (1986).

[7] Human Frontier Science Program (HFSP). Retrieved April, (2014) from http://www.hfsp.org/

[8] H. Bedouelle and G. Winter. A model of synthetase/transfer RNA interaction as deduced by protein engineering. Nature. 320, 371-373 (1986)

[9] R.T. Bate. Nanoelectronics. Nanotechnology 1, 1 (1990).

[10] I. Sumio. "Helical microtubules of graphitic carbon". Nature 354, 56–58 (1991).

[11] K.E. Drexler. Nanosystems: Molecular Machinery, Manufacturing, and Computation. Wiley Interscience (1992).

[12] Foresight Institute (1993). First Feynman Prize in Nanotechnology Awarded. Retrieved April, (2014) from http://www.foresight.org/Updates/Update17/Update17.1.html.

[13] Foresight Institute (1993). White House Science Office on Nanotechnology. Retrieved April, (2014) from http://www.foresight.org/Updates/Update16/Update16.5.html#anchor372539.

[14] Foresight Institute (1993). Rice University to Build Nanotech Lab. Retrieved April, (2014) from http://www.foresight.org/Updates/Update17/Update17.1.html#RiceNanotechnology.

[15] Foresight Institute (1994). First Nanosystems Course. Retrieved April, (2014) from http://www.foresight.org/Updates/Update18/Update18.1.html#FirstCourse.

[16] Foresight Institute (1994). US Science Advisor advocates nanotechnology. Retrieved April, (2014) from http://www.foresight.org/Updates/Update20/Update20.1.html#anchor57200.

[17] M. Nelson and C. Shipbaugh. The potential of Nanotechnology for Molecular Manufacturing. RAND Corporation (1995).

[18] T. McKendree Revolution in Military Affairs, with Mine Hagen, Hughes Aircraft, 145 pages (1995).

[19] Zheng, et al. "From molecular to macroscopic via the rational design of a self-assembled 3D DNA crystal". Nature 461, 74 (2009).

[20] Foresight Institute (1996). Feynman grand prize. Retrieved April, (2014) from www.foresight.org/GrandPrize.1.html.

[21] Foresight Institute (1996). First European Nanotech conference. Retrieved April, (2014) from http://www.foresight.org/Updates/Update24/Update24.1.html#anchor575761.

[22] Foresight Institute (1996). NASA Invest in Nanotechnology. Retrieved April, (2014) from http://www.foresight.org/Updates/Update26/Update26.1.html#anchor383866.

[23] Foresight Institute (1996). IBC Conference on Molecular Nanotechnology. Retrieve April (2014) from http://www.foresight.org/Updates/Update27/Update27.5.html#anchor598145.

[24] Foresight Institute (1997). First Nanotech Development Company Formed. Retrieved April, (2014) from http://www.foresight.org/Updates/Update29/Update29.3.html#anchor588503.

[25] Foresight Institute (1997). Breakthrough-Scale Design. Retrieved April, (2014) from http://www.foresight.org/Updates/Update28/Update28.1.html#anchor1228823.

[26] Foresight Institute (1997). 1997 Feynman Prize in Nanotechnology. Retrieved April, (2014) from http://www.foresight.org/about/1997Feynman.html.

[27] Foresight Institute (1998). First NSF forum. Retrieved April, (2014) from http://www.foresight.org/Conferences/MNT6/NSF.html.

[28] C. Mao, W Sun, Z. Shen and N.C. Seeman. A nanomechanical device based on the B - Z transition of DNA. Nature, 397. 144-146 (1999).

[29] Foresight Institute (1998). 1998 Feynman Prize in Nanotechnology. Retrieved April, (2014) from http://www.foresight.org/about/1998Feynman.html.

[30] R.A. Freitas Jr. Nanomedicine, Vol I: Basic Capabilities. Landes Bioscience;1 edition, ISBN-10: 1570596808 (1999).

[31] Foresight Institute (1999). Foresight Guidelines for Responsible Nanotechnology. Retrieved April, (2014) from http://www.foresight.org/guidelines/current.html.

[32] Foresight Institute (1999). Nanotechnology: the coming revolution in manufacturing. Retrieved April, (2014) from http://www.merkle.com/papers/nanohearing1999.html.

[33] Foresight Institute (2000). California Nanotechnology Research Initiative. Retrieved April, (2014) from http://www.foresight.org/Updates/Update43/Update43.2.html#CNSI.

[34] K. Hickman. Nanomaterials: It’s a small, small world. CSA (2002). http://www.csa.com/discoveryguides/nano/overview.php.

[35] National Nanotechnology Initiative (NNI). What’s so special about the nanoscale? http://www.nano.gov/nanotech-101/special.

[36] Nanodic.com (2011). Dictionary of nanotechnology – Nanotechnology. Retrieved May, (2014) from http://www.nanodic.com/general/Nanotechnology.htm.

[37] Nanotechproject.org. Introduction to Nanotechnology. Retrieved May, (2014) from http://www.nanotechproject.org/topics/nano101/introduction_to_nanotechnology/.

[38] A. Phaedon and C. Philip. Nanotubes for electronics. Sci. Ame. (2000).

[39] H. Alexander. (2001). “Nanotubes make tiny diodes”. Retrieved May, (2014) from http://www.academicpress.com/inscight/11181999/grapha.htm.

[40] C. Vincent (2001). Nanotubes. Retrieved May, (2014) from http://www.phys.psu.edu/~crespi/

[41] B. Perman. (2012). “10 uses of carbon nanotubes”. Retrieved May, (2014) from http://dsc.discovery.com/technology/tech-10/carbon-nanotubes-uses.html.

[42] Ascribe Newswire. Nanotubes Hold Promise for Groundbreaking Technological Change in Products from TVs to Computer Memory to Velcro.” Ascribe Newswire (February 29, 2000)

[43] Two-bit heroes - Computing with quanta. The Economist Volume 338 Issue 7948

[44] Cue the qubits: Quantum computing - How to make a quantum computer. The Economist Volume 342 Issue 8005

[45] D. Deutsch. Quantum computation. Physics World (1992).

[46] M. Steve. “Tantalizing Tubes.” Scientific American (2000).

[47] H. Hank. “Buckeyballs: Making Full Use of Fullerenes.” Westech (1998).

[48] D.V. Talapin, J.S. Lee, M.V. Kovalenko, E.V. Shevchenko, Chem. Rev. 110, 389(2010).

[49] Z. Yang et al. Experimental Observation of an Extremely Dark Material Made by a Low- Density Nanotube Array. Nano Lett., Vol. 8, No. 2 (2008).

[50] J. Ready. Nano-Manhattan: 3D Solar Cells Boost Efficiency While Reducing Size, Weight and Complexity of Photovoltaic Arrays. Retrieved May, (2014) from http://www.gtri.gatech.edu/casestudy/3d-solar-cells-boost-efficiency.

[51] S. Vlad, C. Ciobanu, M. Butnaru, D. Macocinschi, D. Filip, L.M. Gradinaru and M. Mandru. Preparation of polyurethane microspheres by electrospray technique. Digest J. of Nanomat. & Biostru. 6, 624-652 (2011).

[52] T. Kubik, K. Bogunia-Kubik and M. Sugisaka. Nanotechnology on duty in medical applications. Current Pharmaceutical Biotechnology 6, 17-33 (2005).

[53] T. Vo-Dinh, B. Cullum. Biosensors and biochips: advances in biological and medical diagnostics (Review). Frensenius J. Analy. Chem. 366, 540-551 (2000).

[54] J. Wang. Carbon-Nanotube Based Electrochemical Biosensors: A Review. Electroanalysis 17, No. 1 (2005).

[55] E. Duane et al. Quantum Dot Peptide Biosensors for Monitoring Caspase 3 Proteolysis and Calcium Ions. Acsnano. 4, 5487-5497 (2010).

[56] R.R.K. Reddy, I. Basu, E. Bhattacharya and A. Chadha. Estimation of triglycerides by a porous silicon based potentiometric biosensor. Curr. Appl. Phys. 3, 155–61 (2003).

[57] E. Hutter and D. Maysinger. Gold-nanoparticle-based biosensors for detection of enzyme activity. Trends in Pharmacological Sciences, 34, No. 9 (2013).

[58] Y. Cui, Q. Wei, H. Park, and C.M. Lieber. Nanowire nanosensors for highly sensitive and selective detection of biological and chemical species. Science 293, 1289–92 (2001).

[59] V.D. Tuan. Nanobiosensors: probing the sanctuary of individual living cells. J Cell Biochem, Suppl. 39, 154–61 (2002).

[60] M.R. Leyden et al. Increasing the detection speed of an all-electronic real-time biosensor. Lab. Chip. 7, 954-959 (2012).

[61] The Industrial Physicist. pp. 26–29 (February 2001).

[62] MITechNews.com. (January, 2014). Wearable biosensors detect illness. Retrieved May, (2014) from http://www.mitechnews.com/articles.asp?id=16665.

[63] K. Cho, X. Wang and S. Nie et al. Therapeutic Nanoparticles for Drug Delivery in Cancer. Clin. Cancer Res 14, 1310-1316 (2008).

[64] D. Hieu, S. Kayla and W. Teri. Grafting Aptamers onto Gold Nanostars Increases in Vitro Efficacy in a Wide Range of Cancer Cell Types. ACS. 11, 580-587 (2014).

[65] Y. Amir et al. Universal computing by DNA origami robots in a living animal. Nat. Nanotch. DOI: 10.1038/NNANO.2014.58 (2014).

[66] A. Scroeder et al. Remotely Activated Protein-Producing Nanoparticles. Nano Lett. 12, 2685−2689 (2012).

[67] CanIndian.com. (March, 2014) . Laser-activated drug delivery boon to tackle cancer. Retrieved May, (2014) from http://www.canindia.com/4iax9.

[68] A. Ashkin. Optical trapping and manipulation of neutral particles using lasers. Proceedings of the National Academy of Sciences 94, 4853-4860 (1997).

[69] E. Mazur et al. The role of the AFD neuron in C. elegans thermotaxis analyzed using femtosecond laser ablation. BMC Neuroscience, 7, 30 (2006).

[70] J. Baumgart et al. Off-resonance plasmonic enhanced femtosecond laser optoporation and transfection of cancer cells. Biomaterials 33, 2345-2350 (2012).

[71] G.D.M. Jeffries et al. Using Polarization-Shaped Optical Vortex Traps for Single-Cell Nanosurgery. Nano Lett., 7, 415-420 (2007).

[72] T. Vo-Dinh, B.M. Cullum. Fluorescence spectroscopy for biomedical diagnostics. In: Biomedical Photonics Handbook, Vo-Dinh T (Ed), V. Biomedical Diagnostics II Optical Biopsy, CRC Press, Orlando (FL), (2003).

[73] R. Rotomskis. Optical biopsy of cancer: nanotechnological aspects. Tumori, 94. 200-205 (2008).

[74] S. H. Joo, J. Y. Park, C.–K. Tsung, Y. Yamada, P. Yang and G. A.Somorjai, Nat. Mater. 8, 126 (2009).

[75] B. D. Chandler and J. D. Gilbertson, Top. Organomet. Chem. 20, 97 (2006).

[76] C. Chen et al. Mesoporous multicomponent nanocomposite colloidal spheres: ideal high-temperature stable model catalysts. Angew. Chem. Int. Ed. 50, 3725 – 3729 (2011).

[77] D. I. Enache, J. K. Edwards, P. Landon, B. Solsona-Espriu, A. F. Carley, A. A. Herzing, M. Watanabe, C. J. Kiely, D. W. Knight and G. J. Hutchings, Science, 311, 362 (2006).

[78] Q. Zhang. A highly active titanium dioxide based visible-light photocatalyst with nonmetal doping and plasmonic metal decoration. Angew. Chem. Int. Ed. 50, 7088 – 7092 (2011).

[79] S. Mostafa et al. Shape-dependent catalytic properties of Pt nanoparticles. J. Am. Chem. Soc. 132, 15714 – 15719 (2010).

[80] M. Sanles-Sobrido et al. Highly catalytic single-crystal dendritic Pt nanostructures supported on carbon nanotubes. Chem. Mater. 21, 1531 – 1535 (2009).

[81] P. Dutta and S. Gupta. Understanding of Nano Science and Technology. Global vision, (2006).

[82] W. B. Sherman and N. C. Seeman. A precisely controlled dna biped walking device. Nano. Lett. to appear (2004).

[83] Military uses of nanotechnology: the future of war. Retrieved May, (2014) from http://nano--tech.blogspot.com/p/military.html.

[84] Military. Retrieved May, (2014) from http://www.thenanoage.com/military.htm.

[85] W.M. Yen, S. Shionoya and H. Yamamoto. Phosphor hand book, 2nd edition. CRC Press, Florida. ISBN 0-8493-3564-7, Section 1.1 (2007).

[86] C. Ronda. Luminescence: From Theory to Applications. WILEY-VCH Verlag GmbH & Co. KGaA, Weinheim. ISBN: 978-3-527-31402-7 (2008).

[87] H. Zhu. Materials design and synthesis for desirable magnetic and optical properties. ProQuest LLC (2008).

[88] A. Shalav, B. S. Richards and M. A. Green. Sol. Energy Mater. Sol. Cells, 91, 829 (2007).

[89] B. Valeur. Molecular Fluorescence: Principle and Applications. Wiley-VCH Verlag GmbH, ISBN: 3-527-29919-X (2001).

[90] T.H. Gfroerer. Photoluminescence in Analysis of Surfaces and Interfaces. Encyclopedia of Analytical Chemistry R.A. Meyers (Ed.) 9209 – 9231 John Wiley & Sons Ltd, Chichester, (2000)

[91] Photoluminescence. Retrieved May, (2014) from http://en.wikipedia.org/wiki/Photoluminescence

[92] G. G. Stokes. Philos. Trans. 142, 463–562 (1852).

[93] A. Jabłoński. "Efficiency of Anti-Stokes Fluorescence in Dyes" Nature 131, 839-840 (1933).

[94] A.P. Luiza et al. Fluorescence and Chemiluminescence: Teaching Basic Principles by Simple Demonstration Experiments. Retrieved May, (2014) from http://chem.sci.utsunomiya-u.ac.jp/v13n2/22alp-nery/alpnery.html.

[95] G. Walker and S. Burley. Luminescence petrography and spectroscopic studies of diagenetic minerals. In Luminescence Microscopy and Spectroscopy: Quantitative and Qualitative Applications, SEPM Short Course 25, 83–96 (1991).

[96] D. J. Marshall, J. H. Giles, and A. Marino. Combined instrumentation for EDS elemental analysis and cathodoluminescence studies of geological materials. In Hagni, R. D. (ed.), Process Mineralogy VI, Warrendale, PA, The Metallurgical Society Inc., 117–35 (1988).

[97] T. Justel, H. Nikol, and C. Ronda. New developments in the field of luminescent materials for lighting and displays, Angew. Chem., Int. Ed., 37, 3085, (1998).

[98] H. Yamamoto and H. Matsukiyo. Problems and progress in cathode-ray phosphors for high-definition displays, J. Lumin., 48&49, 43, (1991).

[99] E.F. Schubert. Light-emitting diodes 2nd edition. Cambridge University Press New York, (2006).

[100] E. Zych, J. Trojan-Piegza, and L. Kepinski. Homogeneously precipitated Lu_2O_3:Eu nanocrystalline phosphor for X-ray detection, Sens. Actuators, B, 109, 112, (2005).

[101] G. Blasse. Scintillator materials. Chem. Mater., 6, 1465, (1994).

[102] R. Felix and E. Shapiro. Self-Luminous Paints. US Patent Office, 3,033,797, (1962).

[103] A.A. Kaminskii. Modern developments in the physics of crystalline laser materials. Phys. Status Solidi A, 200, 215, (2003).

[104] D.B. Barber et al., Amplification by optical composites, Optics Lett., 22, 1247, (1997).

[105] K. Kawano et al. Application of rare-earth complexes for photovoltaic precursors, Sol. Energy Mater. Sol. Cells, 48, 35, (1997).

[106] J.D. Bullough et al. Lighting Answers: Light emitting Diode Lighting Systems. Lighting Answers: Light Emitting Diode Lighting Systems (2003).

[107] T. Harris and W. Fenlon. How Light Emitting Diodes Work. Retrieved May, (2014) from http://electronics.howstuffworks.com/led.htm

[108] W.M. Yen, S. Shionoya and H. Yamamoto. Phosphor hand book, 2nd edition. CRC Press, Florida. ISBN 0-8493-3564-7, Section 5.92. (2007).

[109] OLEDNET (2009). Red + Green + Blue LED, UV LED + RGB Phosphor, Retrieved May, (2014) from http://www.ecse.rpi.edu/~schubert/Light-Emitting-Diodes-dot-org/chap21/chap21.htm

[110] R.F. Karlicek Jr. Personal communication (1999)

[111] D. Morita, M. et al. Watt-class high-output-power 365 nm ultraviolet light-emitting diodes. J. Appl. Phys. 43, 5945 (2004).

[112] E. Radkov, A. Setlur, Z. Brown and J. Reginelli. High CRI phosphor blends for near UV LED lamps. Proc. SPIE 5530, 260 (2003).

[113] F.S. Galasso. Structure and Properties of Inorganic Solids, Pergamon Press, New York, (1970).

[114] S. Shionoya and W. M. Yen. Phosphor Handbook. CRC Press, Florida, pp. 187, (1998).

[115] S. Shionoya and W. M. Yen. Phosphor Handbook. CRC Press, Florida, pp. 440, (1998).

[116] H.A. Hoppe, H. Lutz, P. Morys, W. Schnick and A. Seilmeier. J. Phy. Chem. Solids, 61, (2001, 2000).

CHAPTER TWO

Literature Review

2.1. Introduction

This chapter focuses on the review of the structural properties of rare earth oxyorthosilicate (basically La_2SiO_5, Gd_2SiO_5 and Y_2SiO_5), general properties of rare earth ions, electronic configuration of dysprosium, its properties such as physical properties and luminescence properties in different host matrices and their general applications. Also a brief review of luminescence associated with impurities in SiO_2 is given.

2.2. Rare Earth Oxyorthosilicates

Rare earth oxyorthosilicates (R_2SiO_5, R = La, Gd or Y) are generally good host for luminescent ions [1] due to their high stability which is as a result of their high density, high atomic number, high quantum efficiency, fast decay time, good energy resolution, minimal self-absorption and most importantly reasonable production cost [2]. The monoclinic R_2SiO_5 crystal could be stably formed according to the phase diagram of R_2O_3-SiO_2 [3].

2.2.1. The crystal structure of rare earth oxyorthosilicate

Rare earth oxyorthosilicates have two basic types of crystal structures. The monoclinic crystallographic point group with space group *P21/c* and *I2/a* corresponding respectively to low temperature phase ($X1$) and the high temperature phase ($X2$) and are found in large ionic radius rare earth ions in rare earth oxyorthosilicates (La–Tb). The second type is the monoclinic crystallographic point group with space group *C2/c* and *B2/b* (*C2/c* correspond to the low temperature phase while *B2/b* corresponds to the high temperature) found in small ionic radius rare earth ions in rare earth oxyorthosilicates (Dy-Lu, Y, Sc) [4-6]. La_2SiO_5 and Gd_2SiO_5 fall into the *P21/c* space group while Y_2SiO_5 fall into the *C2/c* space group. A phase-transformation temperature of about 1190℃ and 1250°C has been reported from $X_1$to X_2 for Y_2SiO_5 [4, 7]

2.2.1.1. Crystal structure of La_2SiO_5

Trivalent lanthanum ion (La^{3+}) in the monoclinic La_2SiO_5 crystal has two nonequivalent crystallographic sites, La1 and La2 as shown in Fig. 2.1. La1 sites are coordinated to 9 oxygen atoms which forms a tricapped trigonal prism having the bond lengths between 0.237 to 0.305 nm. La2 sites are coordinated to 7 oxygen atoms with a bond length of 0.251 nm. The ionic radii of La^{3+} in the nine and sevenfold coordinates are respectively 0.1216 nm and 0.110 nm with the corresponding interatomic distances of 0.264 and 0.250 nm for La1-O and La2-O. The lattice parameters of a = 0.93329(5) nm, b = 0.75087(3) nm, c = 0.70337(4) nm, β = 108.675(6)^0 and V = 0.4669 nm^3 have been reported for La_2SiO_5 [8].

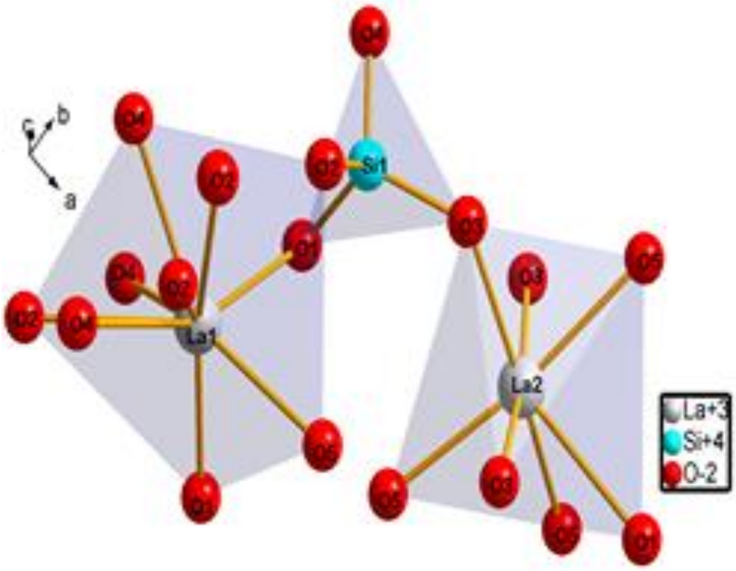

Fig. 2.1: Crystal structure of La_2SiO_5

The crystal structure of (X_1) phase of La_2SiO_5 consist of three types of polyhedron: $La1O_9$, $La2O_7$ and SiO_4. $La1O_9$ and $La2O_7$ polyhedral are connected together through SiO_4 groups and non-silicon-bonded oxygen atoms (O5) to form three dimensional structures [9].

2.2.1.2. Crystal structure of Gd_2SiO_5

Gd_2SiO_5 is isostructural with La_2SiO_5 with the Gd^{3+} having crystallographic sites, Gd1 and Gd2 as shown in Fig. 2.2. Similar to those of La_2SiO_5, the X_1 phase of Gd1 is coordinated with 9 oxygen atoms and the Gd2 with 7 oxygen atoms [10]. The $Gd1O_9$ and $Gd2O_7$ polyhedron are connected via SiO_4 group with all oxygen atoms creating bonds to silicon except for the O5 which link with only the gadolinium atoms. The Gd-Gd1 and Gd2-Gd1 distance of 0.3734 nm and 0.3781 nm respectively are much longer than the Gd2-Gd2 distance of 0.3499 nm. The average Gd2-Oxygen bond length (Gd2-O) of 0.249 nm is longer than the average Gd1-O of 0.239 nm [11] but the ionic radius of Gd^{3+} in Gd1 (0.1107 nm) [12] is bigger than that of Gd2 (0.10 nm) [8]. The lattice parameters of a = 0.91105 nm, b = 0.69783 nm, c = 0.68544 nm, β = 107.1411^0 and V = 0.41642 nm^3 has been reported for Gd_2SiO_5 [13].

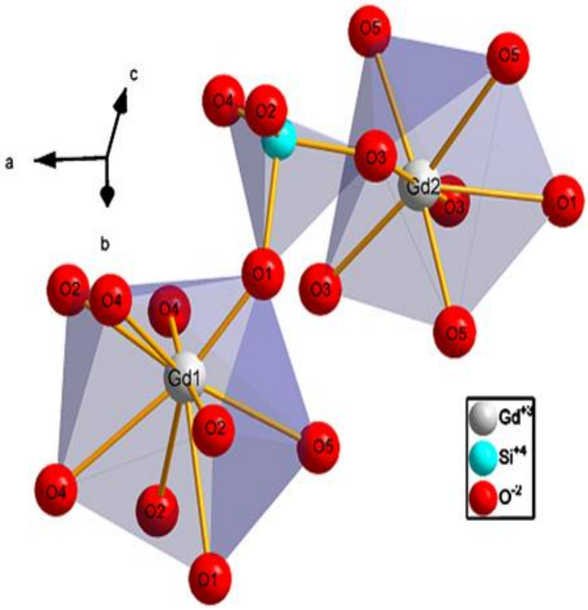

Fig. 2.2: Crystal structure of Gd_2SiO_5.

2.2.1.3. Crystal Structure of Y_2SiO_5

Although Y_2SiO_5 have monoclinic structure just like La_2SiO_5 and Gd_2SiO_5, it has a different space group and different number of oxygen coordinating the yttrium (Y) crystallographic sites. Y_2SiO_5 belong to C2/c space group [14] with Y1 and Y2 crystallographic sites as shown in Fig. 2.3. Coordinated by 7 oxygen atoms, the Y1 crystallographic site forms polyhedron having 5 oxygen atoms in common with the tetrahedron SiO_4 and 2 non-silicon-bonded oxygen atoms. On the other hand, Y2 crystallographic site consists of reticular formation of pseudo octahedron comprising of 4 oxygen atoms common with that in the tetrahedron SiO_4 and 2 non-silicon-bonded oxygen atoms [15]. Y^{3+} in Y1 and Y2 crystallographic sites have ionic radius of 0.096 and 0.090 nm respectively [8] with average Y2-O distance of 0.237 nm and average Y1-O distance of 0.227 nm. The lattice parameter of Y_2SiO_5 are a = 1.443 nm, b = 1.041 nm, c = 0.6733 nm, β = 122.13° and V = 0.3974 nm^3 [11].

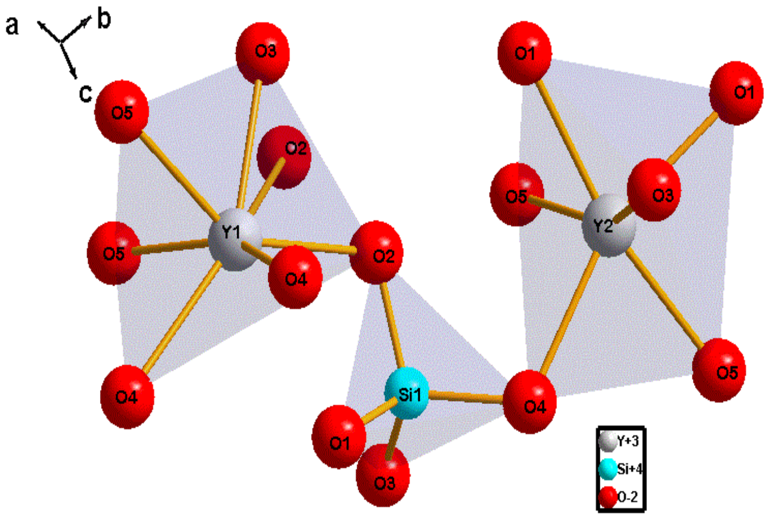

Fig. 2.3: Crystal structure of Y_2SiO_5

2.3. Lanthanide ions

Lanthanides are seldom thought to consist of element from cerium (Ce) (Z = 58) to lutetium (Lu) (Z = 71) because of the absence of 4f electron in lanthanum (La) (Z = 57) which in general occupies a position in the periodic table that open the lanthanide series (Note that all lanthanides are f-block elements except La). However, lanthanides consist of 15 elements from La to Lu and they have general electronic configuration denoted by $[Xe]4f^n5d^16s^2$, with [Xe] the electronic configuration of xenon gas while n represents the number of electrons ranging from 0 for La to 14 for Lu [16]. These 15 elements together with chemically identical scandium and yttrium are called rare earth elements (Fig.2.4). Furthermore, the electronic configurations of lanthanides can be divided into $[Xe]4f^{n-1}5d^16s^2$ and $[Xe]4f^n6s^2$ (n = 1-14) depending on the relative energy levels of the atom. Lanthanum, cerium, gadolinium and lutetium belong to former group while the rest of the lanthanides belong to the latter. However, both types of configuration can be adopted for terbium since they are energetically close to each other. Generally, lanthanides are triply ionized (Ln^{3+}) in the solid state except for europium and cerium which can exist as Ln^{2+} and Ln^{4+} respectively.

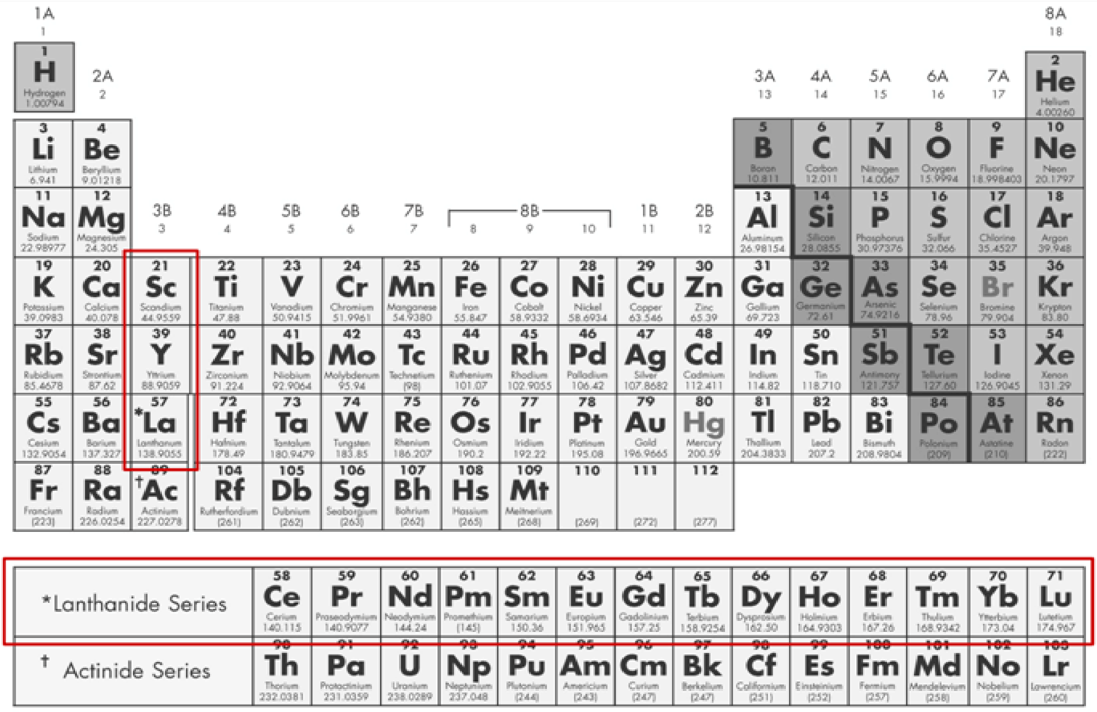

Fig. 2.4: Periodic table of elements

Except from La^{3+} and Lu^{3+} which respectively have empty and filled 4f electrons, all the other Ln^{3+} have partially filled 4f shell which is shielded from the chemical environment by the filled 5s and 5p shells. As a consequence of this shielding, 4f electrons have negligible interaction with the chemical environment leading to all the lanthanides having similar chemical properties [17, 18]. The transitions between the f orbitals of Ln^{3+} are strictly parity-forbidden as well as spin-forbidden but the latter is attenuated by spin-orbit coupling. The shielding of the 4f shells also causes the 4f-4f transitions of the Ln^{3+} to have sharp emission spectra and narrow absorption peaks usually observed in the ultra-violet, visible and near-infrared regions. Nevertheless, each Ln^{3+} has its own characteristic emission and absorption spectrum. It is imperative to note that because of the empty and filled 4f shell of La^{3+} and Lu^{3+} respectively, they do not have electronic energy levels to induce excitation in/or near the visible region.

Furthermore, unlike the 4f-4f electronic transitions, 4f-5d electronic transitions are parity allowed and as such they yield a broader spectrum and their energy is tremendously dependent on the environment of the ion since 5d orbitals is outer orbital and has direct contact with ligand ions. The 4f-5d electronic transitions are commonly observed in Ce^{3+}, Pr^{3+} and Tb^{3+} and they have high energy (Fig. 2.5).

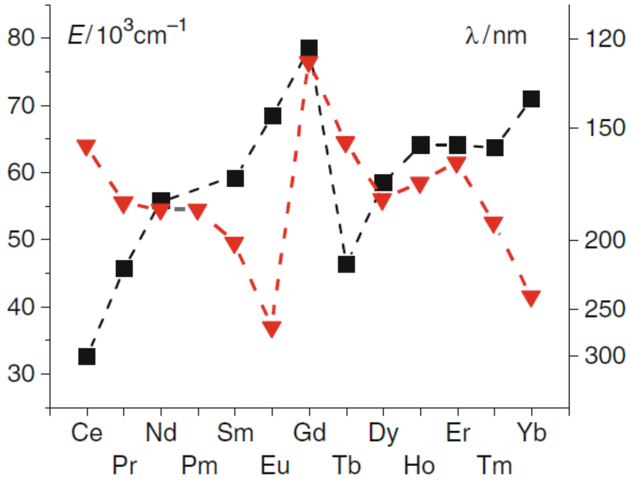

Fig. 2.5: Energy of 4f-5d transitions of Ln^{3+}:CaF2 (squares, [19]) and of the 2p (O)-4f LMCT transitions (triangles, [20]).

2.4. Dysprosium

Dysprosium with the chemical symbol Dy discovered in 1886 by French chemist Paul Émile Lecoq de Boisbaudran when he separated dysprosium oxide from holmium oxide is the ninth element out of the fourteen elements in the lanthanide series and also a rare earth metal [21]. It has atomic number 66, atomic weight 162.50 g.mol^{-1} and its electronic configuration is $(1s)^2$ $(2s)^2$ $(2p)^6$ $(3s)^2$ $(3p)^6$ $(4s)^2$ $(3d)^{10}$ $(4p)^6$ $(5s)^2$ $(4d)^{10}$ $(5p)^6$ (4f)9 $(5d)^1$ $(6s)^2$ normally written in the form $[Xe]4f^95d^16s^2$ with [Xe] the electronic configuration of xenon. Some of the properties of Dy are summarized in table 2.1.

Dy^{3+} has outer shell of $4f^9$ indicating that it has 9 valence f electrons, so by applying Hund's rules [22], one can determine the ground state of its 4f shell. Since for f electrons the orbital quantum number l = 3 (l = 0, 1, 2,3,… which can be represented as *s*, *p*, *d*, *f*,…shells) and there are 9 4f electrons in Dy^{3+} with seven electrons having spin down and two having spin up as shown in table 2.2. The magnetic quantum number, m_l takes values from $-l\ldots0\ldots l$ and the *S*-value is given by 1/2 multiply by the total number of unpaired electrons (5 in this case) [23]. Hence the maximum value of *S* is 5/2 and the maximum value of *L* = -3 -2 -1 0 +1 +2 +3 +2 +3 = 5. So the total angular momentum given by $J = L + S$ (since the shell is more than half filled) is 15/2. *L*, *S* and *J* which are usually called spectroscopic term is written as

$^{(2S+1)}L_J$, where (2S+1) is called spin multiplicity and L usually represented as (S, P, D, F, G, H…) takes values from 0, 1, 2, 3, 4…. By and large, the ground state of Dy^{3+} can be written as $^6H_{15/2}$ where H corresponds to L-value which 5, the spin multiplicity (2S+1) is 6 and J-value is 15/2. In fact, the ground term of Dy^{3+} splits into $^6H_{15/2}$, $^6H_{13/2}$, $^6H_{11/2}$, $^6H_{9/2}$, $^6H_{7/2}$ and $^6H_{5/2}$.

Table 2.1: Properties of Dy

Colour	Silvery-white
Structure	Hexagonal
Density	8.559 g/cm^3
Melting point	1441 ^{0}C
Boiling point	2560 ^{0}C
State	Solid
Solubility	Soluble in dilute acids
Atomic volume	19. 032 cm^3/g
Atomic radius	0.1773 nm
Ionic radius	0.0908 nm

Table 2.2: Electronic spins of Dy^{3+}

m_l	↑	↓
3	●	●
2	●	●
1	●	-
0	●	-
-1	●	-
-2	●	-
-3	●	-

2.4.1. The luminescence properties of Dy^{3+} doped in different host matrices and their applications

The luminescence properties of Dy^{3+} ions have been studied in difference host matrices and also in different wavelength regions. The choice of the host matrix or the wavelength region basically depends on the application of the material. By and large, two dominant emission bands are usually observed in Dy^{3+} emission spectra irrespective of the host matrix. The emission band usually observed around 485 nm (blue) which is as a result of $^4F_{9/2} \rightarrow {}^6H_{15/2}$ f-f electronic transition of Dy^{3+} and the second band observed around 575 nm (yellow) due to $^4F_{9/2} \rightarrow {}^6H_{13/2}$ f-f electronic transition of Dy^{3+}. Defined as hypersensitive, the yellow emission which is electric dipole transition is highly sensitive to the crystal field around Dy^{3+} ions. On the other hand, the blue emission is a magnetic dipole transition and hardly varies with the crystal field around Dy^{3+} ions [24]. Dy^{3+} doped matrices have found applications in white light emitting phosphors [25-29], field emission display (FED) [30, 31], scintillation [32] solid state laser and optical amplifier [33-36] and optical waveguide and optical sensors [36, 37].

Although Dy^{3+} doped matrices has been reported as a potential phosphor for the generation of white light as a result of the prominent blue and yellow emissions [38, 39], the choice of host matrix plays important role in accomplishing this goal. Because of the hypersensitive nature of the yellow emission, it is very difficult to balance its emission intensity with that of the blue emission. However, this is only applicable when Dy^{3+} ions are located at low symmetry (without inversion center) in the host matrix. On the other hand, the blue emission can yield stronger emission if Dy^{3+} ions are situated at a higher symmetry (with an inversion center) in the host matrix. But in a case where the ligand field is situated in or very close to the inversion symmetry in the host matrix, both the blue and yellow emissions gives equivalent emission intensities. The aforementioned case has been reported in Dy^{3+} doped gadolinium phosphate ($GdPO_4$) [40] and Dy^{3+} doped lanthanum phosphate ($LaPO_4$) [25] while the case where Dy^{3+} ions are located in the higher symmetry has been reported in Dy^{3+} doped lead fluorophosphate glasses (PbF_2) [27]. Moreover, these two cases are seldom reported compared to the case where Dy^{3+} ions are located in the low symmetry. To generate white light in the low symmetry case, a single host matrix that can emit in the blue region such as calcium molybdate ($CaMoO_4$) also known as Powellite can be used [29] or Dy^{3+} can be co-doped with another rare earth ion which can emit in the blue region [28,41].

Unlike in the white emitting application, the laser applications based on Dy^{3+} doped matrices focused on the $^6H_{13/2}$→$^6H_{15/2}$ transition of Dy^{3+} for mid-IR laser and on $^4F_{9/2}$ → $^6H_{13/2}$ (yellow) transition for yellow (visible) laser. Mid-IR lasers within the range of 3-4 μm has found many applications such as in medicine and environmental sensing The choice of host materials is vital in Mid-IR laser application since the lattice vibration of the host material affects the lasing properties of material due to multiphonon relaxation. Materials with high lattice vibration (high phonon energy) such as silica glass (with phonon energy of 1100 cm^{-1}) are not recommended since their high phonon energy impedes their use at source wavelength longer than 2.3 μm. Mid-IR laser application has been reported in Dy^{3+} doped ZBLAN glass (so termed because it contains fluorides of Zr, Ba, La, Al and Na) [42], fluoride fiber, tellurites [36] and germinates [36,37] with respective emission wavelengths of 2.96 μm, 3.0 μm, 3.4 μm, 3.4 μm and 4.35 μm. However, for visible laser applications, $^4F_{9/2}$ → $^6H_{13/2}$ (yellow) transition of Dy^{3+} has attracted more attention and has been reported in $Gd_2SiO_5{:}Dy^{3+}$ [43], $(Lu_xGd_{1-x})_2SiO_5{:}Dy^{3+}$ [44] and xerogel doped with $Gd_{1.6}Dy_{0.4}(WO_4)_3$ [45].

2.5. Luminescence related to intrinsic defects in silicon dioxide

Strong luminescence observed in silicon cluster usually in the blue and UV region can be explained by quantum confinement effect. This can be observed at very small crystallite size (2-10 nm) [46]. However, in some cases, the emission can be observed in the red and yellow region due to the formation of Si−O bonds on the surface of the crystal which lead to mid-band gap trapped electrons and holes excited states hence affecting the dependency of luminescence on crystallite size.

The structural, electrical and optical properties of silica matrix can be affected drastically by the presence of defects. Defects can result from mechanical stress, temperature change, manufacturing processes, impurities, and irradiation. These parameters can also lead to the transformation of an existing defect to another form. Defects can be classified based on their size and structure as dislocation or linear defects, point defects and plane defects [47, 48]. Point defects can be either intrinsic or extrinsic depending on its origin. Defects that originate from the atoms of the host matrix alone are referred to as intrinsic point defects. Examples of this type of defects include vacancies (missing host atoms), and self-interstitials (additional host atoms occupying an interstitial position). Extrinsic point defects refer to atoms of foreign material present in the host crystal. These types of defects are usually as a result of doping. Intrinsic point defects in silica could be oxygen or silicon vacancies and their interstitials, Si−Si or O−O homobonds or under-coordinated silicon or oxygens. In this section, we will discuss few of the defects in silica network, for detailed information and other types of defects in silica, consult ref. [46].

2.5.1. Oxygen-deficiency center (ODC)

Oxygen deficiency center (ODC) is a term used to describe the optical and electrical properties of neutral oxygen vacancies [49]. ODC is generally indicated as ≡Si−Si≡. Two type of diamagnetic ODCs has been observed in pure silica, neutral oxygen vacancy ODC(I) and the two coordinated silicon ODC(II) commonly symbolized by =Si●●. In ODC(I), two Si atoms can be in their relaxed state and form a silicon-silicon bond (relaxed oxygen vacancy ≡Si−Si≡) or they can be in an unstable interaction state and form an unstable oxygen vacancy (unstable oxygen vacancy ≡Si···Si≡), see Fig. 2.7. ODC(I) has been observed around 7.6 eV (163 nm) absorption band [50]. Furthermore, photoluminescence emission band have also been reported around 4.4 eV (282 nm) and 2.7 eV (459 nm) under 5 eV (248 nm), 6.9 eV (178 nm) or 7.6 eV (163 nm) band which was ascribed to the interaction of ODC(II) with ODC(I) [51, 52].

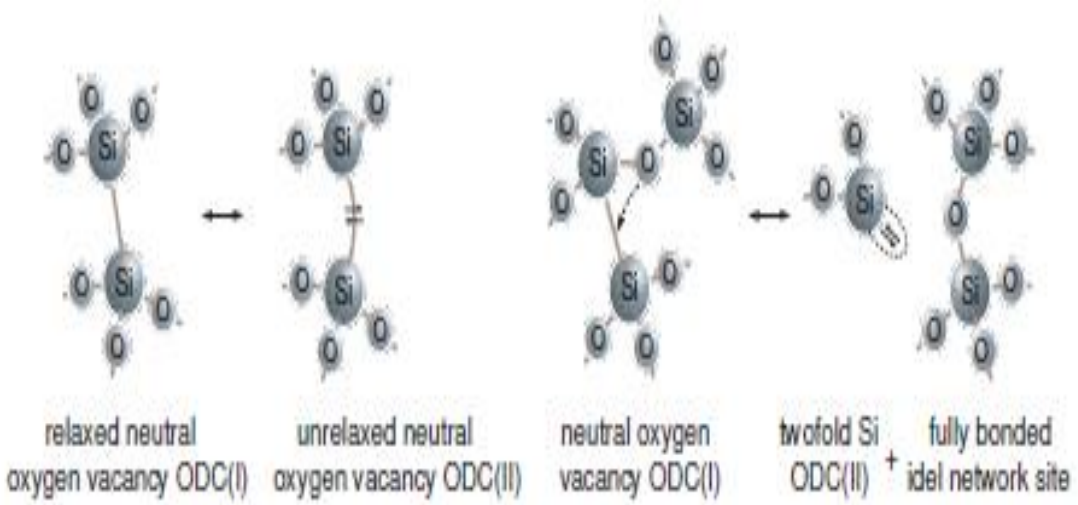

Fig. 2.7: Schematic illustration of the transformation between ODC(I) and ODC(II) visualizing two possible models for the ODC(II), the unrelaxed oxygen vacancy and the twofold coordinated silicon.

2.5.2. Self-trapped excitons (STE)

An electron or a hole inserted into an insulator can couple to the phonon field of the material resulting to it getting "self-trapped" by deforming the lattice structure of the material around itself. A self-trapped exciton (STE) is often referred to as an excitonic polaron [53]. The formation of STE create a localized bound state which form a lower energy than an electron or a hole inserted into the valence or conduction band. In other words, STE lead to the formation of transient (short living) defects created by the combination of electronic excitation energy of electron-hole pairs and electron-phonon interaction. Either radiative or non-radiative transition can be produce by these electron-holes and electron-phonon interaction, however, the recombination of the defect pair can lead to the annihilation of the non-radiative transient defects [54].

STE luminescence emission spectrum has been observed between 2 eV (620 nm) and 3 eV (413 nm) in silica [55, 56]. The blue luminescence emission in crystalline SiO_2 has also been ascribed to STE. This same emission however has been observed in emission spectra of amorphous SiO_2 but with much lower intensities compare to other characteristic bands. Furthermore, when STE is perturbed by a little deformation owing to structural defects, it also gives emission in this energy range. For instance, luminescence emission band has been observed at 2.5 eV (496 nm) for Ge implanted quartz and at 2.8 eV (443 nm) for non-implanted quartz [57].

2.6. References

[1] C. Li, C. Wyon, R. Moncorge, IEEE J. Quant. Electron. 28, 1209 (1992)

[2] K.J. McClellan et al. Crystalline Rare-earth Activated Oxyorthosilicate phosphor (2003)

[3] N.A. Toropov and I. A. Bondar. Rare-Earth Silicates Communication 1. Phase Diagram of the System La_2SiO_3-SiO_2. Institute of Silicate Chemistry, Academy of Sciences, USSR Translated from Izvestiya Akademii Nauk SSSP, Otdelenie Khimicheskikh Nauk, No. 2, pp. 153-156, (1960)

[4] J. Felsche. Structure and Bonding.13, 99 (1973).

[5] D. Meiss,W.Wischert and S.Kemmler-Sack: Phys. Status Solidi A 133, 575 (1992).

[6] M. Yin, C. Duan, W. Zhang, L. Lou, S. Xia and J. C. Krupa: J. Appl. Phys. 86, 3751 (1999).

[7] E. M. Rabinovich, J. Shmulovich, V. J. Fratello, and N. J. Kopylov, Am. Ceram. Soc. Bull., 66, 1505 (1987).

[8] R.D. Shannon. "Revised effective ionic radii and systematic studies of interatomic distances in halides and chalcogenides," Acta Crystallogr.32, 751–767 (1976).

[9] K. Fukuda, T. Iwata and E. Champion. Crystal Structure of Lanthanum Oxyorthosilicate, La_2SiO_5. Power Diffr. 21,4 (2006).

[10] L. Fornasiero, K. Petermann, E. Heumann. & G. Huber. Spectroscopic properties and laser emission of Er^{3+} in scandium silicates near 1.5 μm, Optical Materials,.10, 9-17 (1998).

[11] J. Felsche. The crystal chemistry of the rare-earth silicates, Structure and Bonding, pp.99-197, ISSN 0081-5993 (Print), Springer-Verlag, New York (1973)

[12] A.A. Bosak, C. Dubourdieu, J.P. Sénateur, O. Yu. Gorbenko and A.R. Kaul. Hexagonal rare earth (R = Eu-Dy) magnites: XRD study of epitaxially stabilized films. Crystal Engineering 5, 355-364 (2002).

[13] R. Lisiecki, G. Dominiak-Dzik, P. Solarz, W. Ryba-Romanowski, M. Berkowski, and M. Glowacki. Optical Spectra and Luminescence of the Dy-doped Gd_2SiO_5 Single Crystal. Appl Phys B 98, 337-346 (2010).

[14] J. Felsche. Structure and Bonding 13, 99 (1973).

[15] IEM Databases and Datasets. Retrieved March, (2014) from http://database.iem.ac.ru/.

[16] R D Cowan the Theory of Atomic Structure and Spectra (California, USA: Univ. of California Press) (1981).

[17] M.H. Werts. Making sense of lanthanide luminescence Sci. Prog. 88, 101 (2005).

[18] S. Cotton. Lanthanide and Actinide Chemistry (Chichester: Wiley) (2006).

[19] P. Dorenbos. The f-d transitions of the trivalent lanthanides in halogenides and chalcogenides. J. Lumin. 91, 91–106 (2000).

[20] S. Shionoya, W.M. Yen (1999). Principal phosphor materials and their optical properties. In: Shionoya S, Yen WM (eds) Phosphor handbook. CRC, Boca Raton, Ch. 235

[21] Slashdocs (2009). Dysprosium. Retrieved March, (2014) from http://www.slashdocs.com/hohohohohohohohok/Atomic%20Symbol.html.

[22] G.L. Miessler and D.A. Tarr, Inorganic Chemistry (Prentice-Hall, 2nd edn 1999) [ISBN 0138418918], pp. 358–360

[23] J.-C.G. Bu¨nzli and S.V. Eliseeva. Basics of Lanthanide Photophysics. Laboratory of Lanthanide Supramolecular Chemistry,E ´ cole Polytechnique Fe´de´rale de Lausanne, Switzerland (2011).

[24] J. C. Zhang and Y. H. Wang. Chin. Phys. Lett. 25, 1453 (2008).

[25] G. Han, Y. Wanga, C. Wua,and J. Zhang. Hydrothermal synthesis and vacuum ultraviolet-excited luminescence properties of novel Dy^{3+}-doped $LaPO_4$ white light phosphors. Mater. Res. Bull. 44, 2255–2257 (2009).

[26] P. Bahu, K. J. Jang, E. S. Kim, L. Shi and H. J. Sed. Optical Properties and White-Light Emission in Dy^{3+}-Doped Transparent Oxyfluoride Glass and Glass Ceramics Containing CaF_2 Nanocrystals. J. Korean Phy. Soc. 54, 1488-1491 (2009).

[27] C.R. Kesavulu, C.K. Jayasankar. White light emission in Dy^{3+}-doped lead fluorophosphate glasses. Mat. Chem. & Phy. 130, 1078-1085 (2011).

[28] C.H. Yang, Y.X. Pan and Q.Y. Zhang. Enhanced white light emission from Dy^{3+}/Ce^{3+} codoped $GdAl_3(BO_3)_4$ phosphors by combustion synthesis. Mat. Sci. & Eng. B 137, 195-199 (2007).

[29] S. Dutta, S. Som and S. K. Sharma. Luminescence and photometric characterization of K^+ compensated $CaMoO_4:Dy^{3+}$ nanophosphors. Dalton Trans., 42, 9654 (2013).

[30] Y. Zhang et al. Soft-chemical synthesis and tunable luminescence of Tb^{3+}, Tm^{3+}/Dy^{3+}-doped SrY_2O_4 phosphors for field emission displays. Dalton Trans., 42, 4799 (2013).

[31] G. Li, C. Li, C. Zhang, Z. Cheng, Z. Quan, C. Peng and J. Lin. Tm^{3+} and/or Dy^{3+} doped LaOCl nanocrystalline phosphors for field emission displays. J. Mater. Chem. 19, 8936-8943 (2009).

[32] X.Y. Sun et al. Synthesis and luminescent properties of $BaGd_2O_4:Dy^{3+}$, a novel scintillating phosphor. Appl. Phys. B 110, 27-34 (2013).

[33] G. Lakshminarayana, R. Yang, M. Mao, J. Qiu and I.V. Kityk. Photoluminescence of Sm^{3+}, Dy^{3+} and Tm^{3+} -doped transparent glass ceramics containing CaF_2 nanoparticles. J. Non-Crystalline Solids. 355, 2668-2673 (2009).

[34] J.S. Kumar, K. Pavani, A.M. Babu, N.K. Giri, S.B. Rai and L.R. Moorthy. Fluorescence Characteristics of Dy^{3+} ions in Calcium fluoroborate glasses. J. Lumi., 130, 1916-1923 (2010).

[35] S. Yang, X. Wang, H. Guo, G. Dong, B. Peng, J. Qiu, R. Zhang and Y. Shi. Broadband near-infrared emission in Tm^{3+}-Dy^{3+} codoped amorphous chalcohalide films fabricated by pulsed laser deposition. Opt. Exp. 19, 26531 (2011).

[36] B.D.O. Richards, T.T. Fernandez, G. Jose, D. Binks and A. Jha. Mid-IR (3–4 μm) fluorescence and ASE studies in Dy^{3+} doped tellurite and germanate glasses and a fs laser inscribed waveguide. Laser Phys. Lett. 10, 085802 (6pp) (2013).

[37] F. Charpentier, F. Starecki, J.L. Doualan, P. Jóvári, P. Camy, J. Troles, S. Belin, B. Bureau and V. Nazabal. Mid-IR luminescence of Dy^{3+} and Pr^{3+} doped $Ga_5Ge_{20}Sb_{10}S(Se)_{65}$ bulk glasses and fibers. Mat. Lett.101, 21-24 (2013).

[38] P. Babu, K.H. Jang, E.S. Kim, L. Shi, H.J. Seo, F. Rivera-Lopez, U.R. Rodriguez-Mendoza, V. Lavin, R. Vijaya, C.K. Jayasankar, L. Rama Moorthy, J. Appl. Phys. 105, 013516 (2009).

[39] G. Dominiak-Dzik, P. Solarz, W. Ryba-Romanowski, E. Beregi, L. Kovács, J. Alloys Compd. 359, 51 (2003).

[40] C. Cao, H.K. Yang, B.K. Moon, B.C. Choi and J.H. Jeong. Host Sensitized White Luminescence of Dy^{3+} Activated $GdPO_4$ Phosphors. J. Electrochem. Soci. 158, J6-J9 (2011).

[41] X. Zhang, F. Meng, W. Li, S. Il Kim, Y.M. Yu and H.J. Seo. Investigation of energy transfer and concentration quenching of Dy^{3+} luminescence in $Gd(BO_2)_3$ by means of fluorescence dynamics. J. Alloy & Compounds 578, 72-76 (2013).

[42] Y.H. Tsang, A.E. El-Taher, T.A. King and S.D. Jackson. Efficient 2.96 μm dysprosium-doped fluoride fibre laser pumped with a Nd:YAG laser operating at 1.3 μm Opt. Express 14, 678–85 (2006).

[43] R. Lisiecki, G. Dominiak-Dzik, P. Solarz, W. Ryba-Romanowski, M. Berkowski and M. Głowacki. Optical spectra and luminescence dynamics of the Dy-doped Gd_2SiO_5 single crystal. Appl. Phys. B 98, 337-346 (2010).

[44] Czochralski Growth and Optical Properties of $(Lu_xGd_{1-x})_2SiO_5$ Solid Solution Crystals Single Doped with Sm^{3+} and Dy^{3+}. W. Ryba-Romanowski, A. Strzep, M. Glowacki, R. Lisiecki, P. Solarz and J.Z. Domagala. Acta Physica Polonica No. 2, Vol. 124 (2013).

[45] B. Grobelna, A. Synak and P. Bojarski. The luminescence properties of dysprosium ions in silica xerogel doped with $Gd_{1.6}Dy_{0.4}(WO_4)_3$. Optica Appplicata. No. 2, Vol. XLII (2012).

[46] R. Salh. Defect Related Luminescence in Silicon Dioxide Network: A Review. Institute of Physics, Faculty of Science and Technology, Umeå University, Umeå Sweden, (2011).

[47] P. Kofstad. High Temperature Corrosion, ELSEVIER, London and New York, (1988).

[48] M.A. Stevens-Kalceff and J. Wong. Distribution of defects induced in fused silica by ultraviolet laser pulses before and after treatment with a CO_2 laser, J. Appl. Phys. 97, 113519, (2005).

[49] N. Richard et al. Oxygen deficient centers in silica: optical properties within many-body perturbation theory J. Phys.: Condens. Matter 25, 335502, (2013).

[50] H. Imai, K. Arai, H. Imagawa, H. Hosono, and Y. Abe. Two types of oxygen-deficient center in synthetic silica glass, Phys. Rev. B 38, 12772 (1988).

[51] H. Nishikawa, E. Watanabe, D. Ito and Y. Ohki. Decay kinetics of the 4.4 eV photoluminescence associated with the two states of oxygen-deficient-type defect in amorphous SiO_2, Phys. Rev. Lett. 72, 2101 (1994).

[52] K. S Seol, Y. Ohki, H. Nishikawa, M. Takiyama and Y. Hama. Effect of implanted ion species on the decay kinetics of 2.7 eV photoluminescence in thermal SiO_2 films, J. Appl. Phys. 80, 6444 (1996).

[53] G. Mladen and M. Lubomir. Exciton self-trapping processes. Pure & Appl. Chern., 67, 447-456, (1995).

[54] Hayes W. and Stoneham A. M. Defects and Defect Processes in Nonmetalic Solids, John Wiley, New York, (1985).

[55] C. Itoh, K. Tanimura and N. Itoh. Optical studies of self-trapped excitons in SiO_2, J. Phys. C. Solid State Phys. 21, 4693 (1988).

[56] D.L. Griscom. Proc. 33rd Frequency Control Symposium (Elrctronic Industrial Association, Washington, DC, p.98 (1979b).

[57] W. Hayes and T.J.L. Jenkin. Optically detected magnetic resonance studies of exciton trapping by germanium in quartz, J. Phys. C 21, 2391 (1988).

CHAPTER THREE

Combustion Synthesis

3.1. Introduction

Combustion synthesis (CS) also known as self-propagation high-temperature synthesis (SHS), fire or furnaceless synthesis uses high exothermic redox reactions between metals and nonmetals, metathetical reaction (a process involving the exchange of bonds between the two reacting chemical species) between reactive compounds or reactions comprising redox compounds and redox mixtures for production of materials. Combustion synthesis can be represented by a simple chemical equation of the form $mX + nY \rightarrow XmYn$. Where X is the fuel (metal) and Y is the oxidizers (nonmetal) [1]. The fuel should be able to attain compositional homogeneity with the other constituents and should undergo combustion at low ignition temperature with the oxidizer [2]. Some of the fuel used are glycine, acid, citric ascorbic acid, urea, etc. Combustion synthesis involves three main phases which includes flaming (gas-phase), smoldering (heterogeneous-phase) before explosive reaction. The flaming temperature promotes crystallization and phase formation. But a very high flame temperature however, can have adverse effect on the powders, such as increasing of the crystallite size, and formation of hard agglomerate which in turn will lead to reduction in the surface area and sinterability. The flaming temperature is reduced by the evolution of gaseous products during combustion through heat dissipation. The nature of the powder heavily depends on the flaming temperature and gas evolution, and these parameters also depend on the type of fuel used and the ratio of the oxidant-to-fuel [3]. This technique has been used in the synthesis of advanced ceramics, catalysts, alloys, composites, intermetallics and nanomaterials. Combustion reaction is self-propagating which once ignited can occur at adiabatic temperature (Tad) within the range of 1500-3000 K (1226 – 2726 ^{o}C). Other advantages of combustion synthesis include:

(i) No sophisticated equipment are required
(ii) High purity products are produced
(iii) Any size or shape of particle can be produced
(iv) Stabilization of metastable phases
(v) Very low cost of production
(vi) Fast heating rate and short reaction times

3.2. Redox reaction

All combustion reactions are redox reactions, but all redox reactions are not necessarily combustion reactions. Redox is a term derived from two words: reduction and oxidation, which describes the concepts of electron transfer between species [4]. A classical definition of oxidation is the addition of oxygen or any other electronegative element (nonmetal) while reduction refers to the addition of hydrogen or any other electropositive element (metal), e.g.,

$$4Fe + 3O_2 \rightarrow 2Fe_2O_3 \text{ (oxidation)} \tag{3.1}$$

$$CuO + H_2 \rightarrow Cu + H_2O \text{ (reduction).} \tag{3.2}$$

Contemporarily, oxidation reaction refers to increase in oxidation state which is prompted by the loss of electrons by a molecule, atom or ion. Conversely, reduction reaction refers to the decrease in the oxidation state due to gaining of electrons by a molecule, atom or ion [5]. The reductant or the reducing agent is the electron donor, and the oxidant or the oxidizing agent is the electron acceptor, e.g.

$$14H^+ + Cr_2O_7^{2-} + 6Fe^{2+} + 6e = 6Fe^{3+} + 2Cr^{3+} + 7H_2O. \tag{3.3}$$

In eq. (3.3), Cr^{6+} is reduced to Cr^{3+} while Fe^{2+} is oxidized to Fe^{3+}. Hence, in combustion reactions, the fuel acts as the electron donor and the oxidizer an electron acceptor.

3.3. Types of combustion synthesis

Combustion synthesis can be classified based on the state of the reactants (solid, liquid or gas) and the adiabatic temperature as (i) self-propagating high temperature synthesis (SHS), (ii) low-temperature combustion synthesis (LCS), (iii) solution combustion synthesis (SCS), (iv) gel-combustion, (v) sol-gel combustion, (vi) volume combustion (thermal explosion), (vii) emulsion combustion, etc. [6]. However, in this work we are going to focus on solution combustion synthesis since it was the method we used in the synthesis of our nanophosphors.

3.3.1. Solution combustion synthesis (SCS)

Solution combustion method can be used in the synthesis of oxide materials. It is basically the combination of CS and reactive solution such as metal nitrites and different fuels such as urea/hydrazides, oxalyl dihydrazide (ODH), malonic acid dihydrade (MDH), tera formal tris azine (TFTA), etc. [7]. The desired high-temperature required for ignition is generated by the reaction between the fuel and the oxygen containing species which is formed during the decomposition of the nitrite species. Some oxide materials and fuels used for their synthesis including their applications are listed in table 3.1. These fuels perform two basic functions:

(i) They produce C and H which form CO_2 and H_2O during combustion and release heat.

(ii) They accelerate homogeneous mixing of the cations solution through the formation of complexes with the metal ions.

Table 3.1: Fuels used in the synthesis of some oxide materials

Phosphor material	Fuel used	Crystallite size (nm)	Application	Ref.
$Eu^{3+}/Y_3Al_5O_{12}$	U	60-90	Red phosphor.	[8]
$Ce_{1-x}Tb_xMgAl_{11}O_9$	CH	10-20	Green phosphor.	[9]
Eu^{3+}/Y_2O_3	GLY	20-30	Red phosphor.	[10]
Eu^{3+}/Y_2O_3	CA	25	Red phosphor.	[11]
Y_2SiO_5:Ce, Lu_2SiO_5:Ce, Gd_2SiO_5:Ce	HM	20–80	Detection of ionizing radiation and dense scintillators.	[12]
$SrAl_2O_4:Eu^{2+},Dy^{3+},Tb^{3+}$	U + BAF	50-80	Long lasting phosphorescence materials.	[13]
Eu^{3+} activated $YAlO_3$ and $LaAlO_3$	NH_4NO_3 + U	-	Red phosphors.	[14]
$Gd_3PO_7:Eu^{3+}$	GLY	40	Red phosphors.	[15]
$CaWO_4:Eu^{3+}$	CA,	50–100	Fluorescent	[16]

	NH_4NO_3		lamps, colored lightning for advertisement industries and other optoelectronic devices.	
MAl_2O_4:Eu^{3+}, R^{3+} (M = Sr, Ba, Ca, R = Dy, Nd and La)	U	21–40	Long persistent luminescent material.	[17]
Pr^{3+}, Tm^{3+} doped $Gd_3Ga_5O_{12}$	U	30	Magneto optical films and materials for solid state lasers.	[18]
Y_2O_3:Eu^{3+}	S	30-50	Red emitting phosphor used in CRT screens, plasma displays, fluorescent lamps	[19]

U, Urea; CH, Carbohydrazide; HM, Hexamine; GLY, Glycine; BAF, Boric acid flux; CA, Citric acid; S, Sucrose; NH_4NO_3, Ammonium nitrate.

3.3.2. Solution combustion synthesis of rare earth oxyorthosilicates

The typical steps involved in SCS which we employed in the synthesis of our nanophosphors are shown in Fig.3.1. In our case, urea ($CO(NH_4)_2$ and ammonium nitrate (NH_4NO_3) were used as fuel while the oxidizers were lanthanum nitrate hexahydrate ($La(NO_3)_3.6H_2O$), gadolinium nitrate hexahydrate ($Gd(NO_3)_3.6H_2O$), yttrium nitrate hexahydrate ($Y(NO_3)_3.6H_2O$) and silicic acid ($SiO_2.xH_2O$). Appropriate amount of these compounds were added into a glass beakers after which 2 ml of distilled water was added. The mixture was stirred vigorously using magnetic stirrer set at 100℃ for 15 min to obtain a homogenous solution. The solution was then transferred directly into a ceramic crucible boat and immediately into muffle furnace pre-heated to 600 ± 10℃. 3 min after placing the solution into the furnace, oxidation took place resulting to the evaporation of gasses (CO_2, N_2 and H_2O). A typical example of oxidation reaction in one of our cases is shown in eq. (3.4).

$$2La(NO_3)_3(H_2O)_6 + 5CH_4N_2O + (SiO_2)(H_2O) = La_2SiO_5 + 5CO_2 + 23H_2O + 8N_2 \qquad (3.4)$$

The crucible is then remove from the furnace and the foam-like crispy end product is allowed to cool down to room temperature before it is gently ground into fine powder using agate mortar and pestle by hand.

With the procedures described above, we were able to prepare different nanophosphor materials with single host matrices (La_2SiO_5, Gd_2SiO_5 and Y_2SiO_5) and mixture of these host matrices doped with Dy^{3+}.

Advantages of solution combustion synthesis

(i) The crystallite size can be controlled by varying parameters such as fuel and oxidizer ratio and composition

(ii) Low energy requirement: Since the thermal energy required for the reaction is provided by the reaction itself. Also no additional annealing is necessary.

(iii) Time saving: The entire process takes just few minutes.

(iv) Environmental friendliness: The chemical natures of the by-product (N_2, CO_2 and H_2O) are environmental friendly.

(v) Wide variety of fuel can be used.

(vi) High purity of the end-product.

Disadvantages of solution combustion synthesis

(i) The end-product is about 20% of the precursor.

(ii) It is very challenging when used in the synthesis of high temperature metals such as chromites and alumina.

(iii) When a wrong choice of fuel is made, it leads to rough surfaced end-product and may also lead to its contamination.

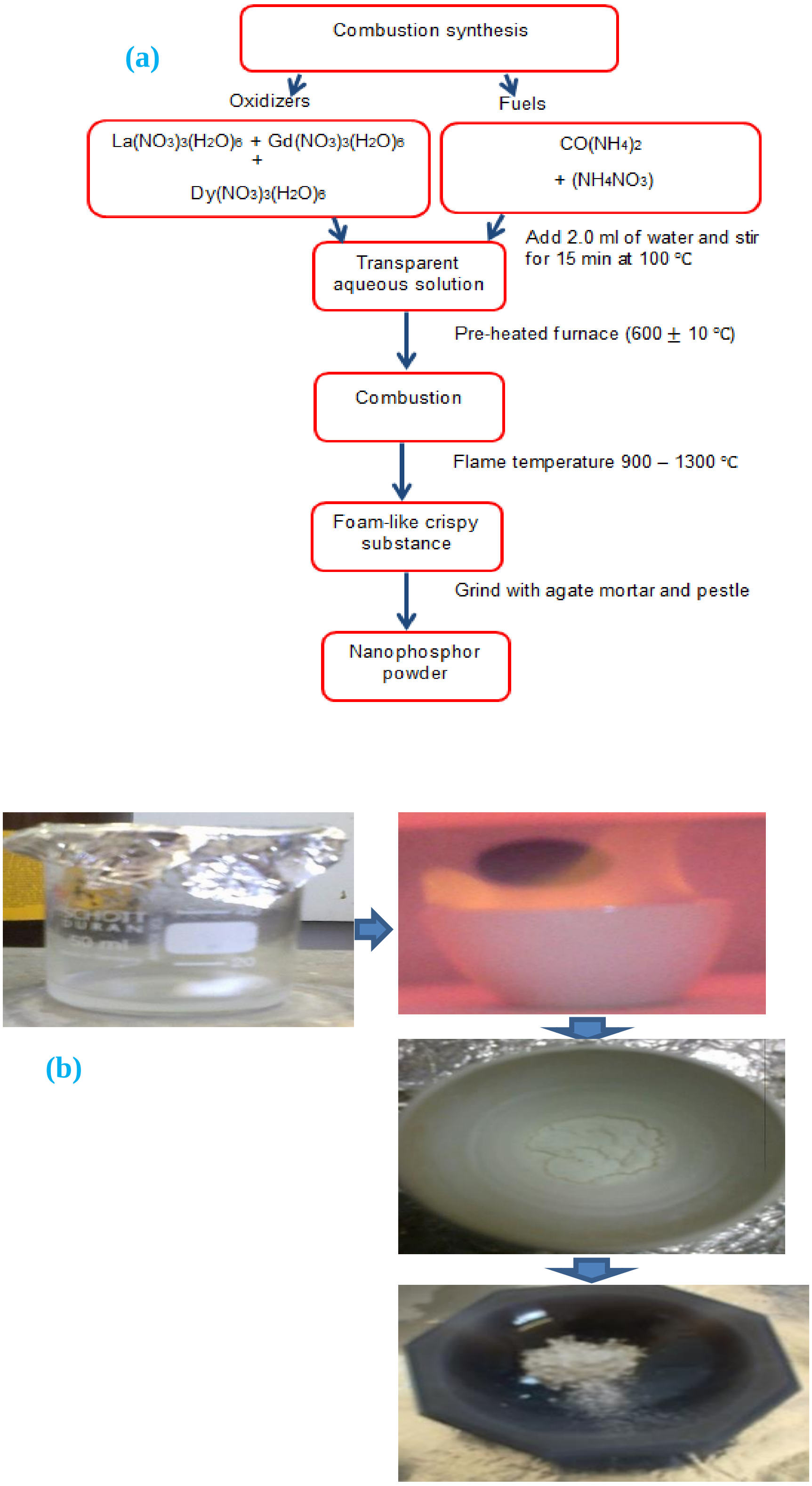

Fig. 3.1: Illustration of the steps involved in SCS using (a) flow chart and (b) snapped shots.

3.4. Reference

[1] K.C. Patil, S.T. Aruna and S. Ekambaram. Combustion Synthesis. Current option in solid state & material science 2, 158-165 (1997).

[2] R. D. Purohit and A. K. Tyagi, J. Mater. Chem. 2, 312 (2002).

[3] S. V. Chavan and A. K. Tyagi, J. Mater. Res., 19, 3181(2004).

[4] Redox Reactions. Retrieved May, (2014) from http://www.wiley.com/college/boyer/0470003790/reviews/redox/redox.htm

[5] A.A. Borisov, L.T. De Luca, A.G. Merzhanov. Self-Propagating High-Temperature Synthesis of Materials CRC Press, pp. 198 (2002).

[6] C.K. Patila, S.T. Arunab, T. Mimania. Combustion synthesis: an update. Current Opinion in Solid State and Materials Science 6, 507–512 (2002).

[7] K.C. Patil, S.T. Aruna, S. Ekambaram. Combustion synthesis. Curr Opin Solid State Mater Sci. 2, 158–165 (1997).

[8] S. Shikao, J. Wang. Combustion synthesis of Eu^{3+} activated $Y_3Al_5O_{12}$ phosphor nanoparticles. J Alloys Comp 327, 82–86 (2001).

[9] D. Ravichandran, R. Roy, P. Ravindranathan and W.B. White. Combustion synthesis of hexaluminate phosphors. J Am Ceram Soc. 82, 1082–1166 (1999).

[10] G. Fagherazzi, S. Polizzi, M. Bettinelli, A. Speghini. Yttria based nanosized powders: a new class of fractal materials obtained by combustion synthesis. J Mater Res. 15, 586–589 (2000).

[11] S. Roy, W. Sigmund, F. Aldinger. Nanostructured yttria powders via gel combustion. J Mater Res. 14, 1524–1531 (1999).

[12] R.E. Muenchausen, E.A. McKigney, L.G. Jacobsohn, M.W. Blair, B.L. Bennett and D.W. Cooke. Science and application of oxyorthosilicate nanophosphors. IEEE Trans Nucle Sci. 55, 1532–1535 (2008).

[13] H. Song and D. Chen. Combustion synthesis and luminescence properties of $SrAl_2O_4$:Eu^{2+}, Dy^{3+}, Tb^{3+} phosphor. Lumin. 22, 554–558 (2007).

[14] Z. Qiu, Y. Zhou, M. Lü, A. Zhang and Q. Ma. Combustion synthesis of three dimensional reticular -structured luminescence $SrAl_2O_4$:Eu, Dy nanocrystals. Solid State Sci. 10, 629–633 (2008).

[15] S. Ekambaram. Solution combustion synthesis and luminescent properties of perovskite red phosphors with higher CRI and greater lumen output. J Alloys Comp. 390, L7–9 (2005).

[16] Y. Jin, W.P. Qin, J.S. Zhang, Y. Wang and C.Y. Cao. Synthesis of $Gd_3PO_7:Eu^{3+}$ nanospheres via a facile combustion method and optical properties. J Solid State Chem. 181, 724–729 (2008).

[17] X.M. Lou and D.H. Chen. Synthesis of $CaWO_4$: Eu^{3+} phosphor powders via a combustion process and its optical properties. Mater Lett, 62. 1681–1684 (2008).

[18] Z. Qiu, Y. Zhou, M. Lu, A. Zhang and Q. Ma. Combustion synthesis of long-persistent luminescent $MAl_2O_4:Eu^{2+}$, R^{3+} (M = Sr, Ba, Ca, R = Dy, Nd and La) nanoparticles and luminescence mechanism research. Acta Mater 55, 2615–2620 (2007).

[19] R. Krsmanovi´c, V.A. Morozov, O.I. Lebedev, S. Polizzi, A. Speghini, M. Bettinelli, et al. Structural and luminescence investigation on gadolinium gallium garnet nanocrystalline powders prepared by solution combustion synthesis. Nanotech. 18, 325604–325613 (2007).

CHAPTER FOUR

Experimental Techniques

4.1. Introduction

In this chapter, we give brief discussion of various techniques used for characterization of our samples. These techniques can be grouped according to the type of information they can give about the samples as structural and surface characterization, and optical techniques. The former include X-ray diffraction (XRD), X-ray photoelectron spectroscopy (XPS), scanning electron microscope (SEM) and time-of-flight secondary ion mass spectroscopy (TOF-SIMS). While the later include UV-Vis spectrometer, photoluminescence spectrometer and Fourier transform infrared (FTIR) spectroscopy.

4.2. Structural and Surface Characterization Techniques

4.2.1. X-Ray Diffraction (XRD)

4.2.1.1. Introduction

Accidentally discovered in 1895 by a German physicist Wilhelm Conrad Roentgen while studying cathode rays in high-voltage gaseous-discharge tube, X-rays lies between ultra-violet and gamma radiation in the electromagnetic spectrum [1, 2]. X-rays have extremely short wavelength ranging from 10 to 0.1 nm or 120 eV to 120 keV in the electromagnetic spectrum (Fig. 4.1). Because it has wavelength comparable to the size of atoms, X-rays are used for probing atomic and molecular structure in variety of materials. They can be produced in two ways: (i) by X-ray tubes or (ii) synchrotron radiations. X-ray tubes are generally the source of X-ray used in the laboratory X-ray instruments. In the tube, X-rays are generated by bombarding a solid target, either rotating or stationary, with a focused beam of electrons accelerated across a high voltage field. Targets commonly used are Cu and Mo, which emit 8 and 14 keV or 1.54 and 0.8 Å X-ray respectively. X-ray is emitted when the accelerated electrons are slowed down by colliding with the solid target [3].

Max von Laue was the first to discover X-ray diffraction during his study of the internal structure of opaque objects (radiography) in 1912 [4]. In the same year W.H. Bragg and his son, W.L. Bragg gave the accurate mathematical interpretations of Laue experiment, the necessary conditions that must be met for diffraction to occur.

When an incident X-ray interact with electrons in atoms of a material, part of the beam are scattered coherently, some incoherently while others are transmitted through the material. Coherent scattering takes place when there is no change in the wavelength of the scattered X-ray beam (elastic scattering), hence only momentum transfer takes place. Elastically scattered X-rays are measured to obtain information about the crystal structure of the material since they carry information about distribution of electrons in the materials. The interference of the diffracted waves from different atoms gives rise to intensity distribution. If the atoms are arranged in a periodic fashion, (as in perfect crystal), the diffracted waves will show sharp interference maxima with the same symmetry as in distribution of atoms [5].

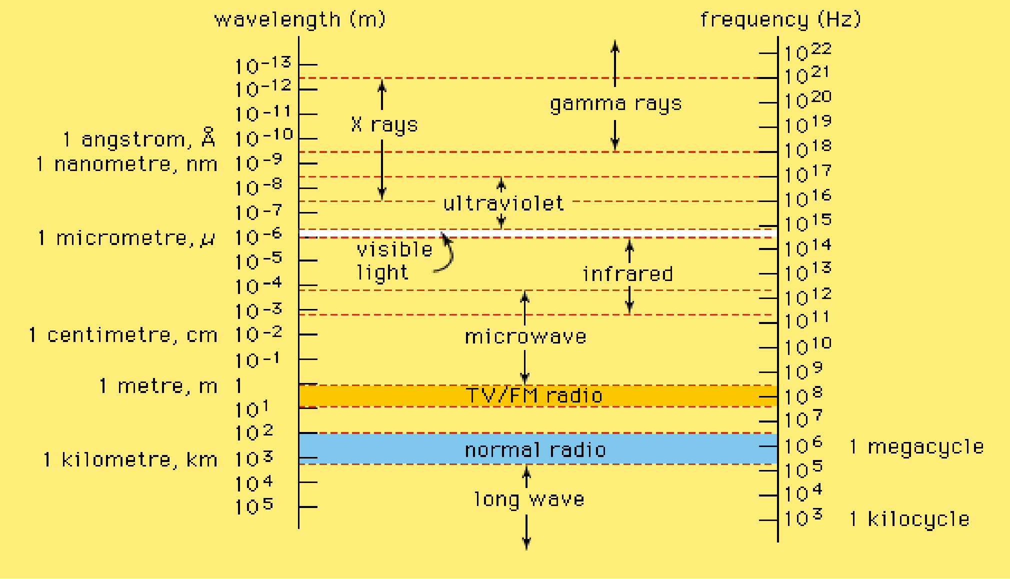

Fig. 4.1: The electromagnetic spectrum [2].

4.2.1.2. Bragg's Law

Bragg's law gives the coherent and incoherent angles of scattering from a crystal lattice. Bragg's law is represented schematically in Fig. 4.2 from which the law can be derived. Consider the interaction of X-ray beam with a perfect crystal in which all the atoms lie on a cubic lattice. The point *A* and *B* represent individual atoms. The incident beams I is coherent, and hence all individual X-ray are in phase until the point the first beam strikes atom *A*. However, the second beam travelled an extra distance *BC* + *BD* before it strikes the atom *B*. The scattered wave at J will be in phase if the path length (IAJ and ICBDJ) differ by an integral (n) multiple of wavelengths (λ). Hence the extra path travelled by the second beam must be integral multiple of wavelength. i.e.

$$n\,\lambda = BC + BD \tag{4.1}$$

It is clear that d (interatomic distance) is the hypotenuse of the right angled triangle ABC, hence we can write

$$BC = d\,Sin\,\theta \tag{4.2}$$

From eq. (4.1), BC = BD, therefore

$$\lambda = 2BC \tag{4.3}$$

Substituting eq. (4.2) into (3.3) gives

$$n\,\lambda = 2\,d\,Sin\,\theta \tag{4.4}$$

Eq. 4.4 is known as Bragg's law [6]. By analogy, n denotes the order of reflection and can take any positive integer e.g. $n = 1$ is the "first order" reflection, $n = 2$ the "second order" reflection. However, conventionally, n can be set to 1. d is the interplanar spacing.

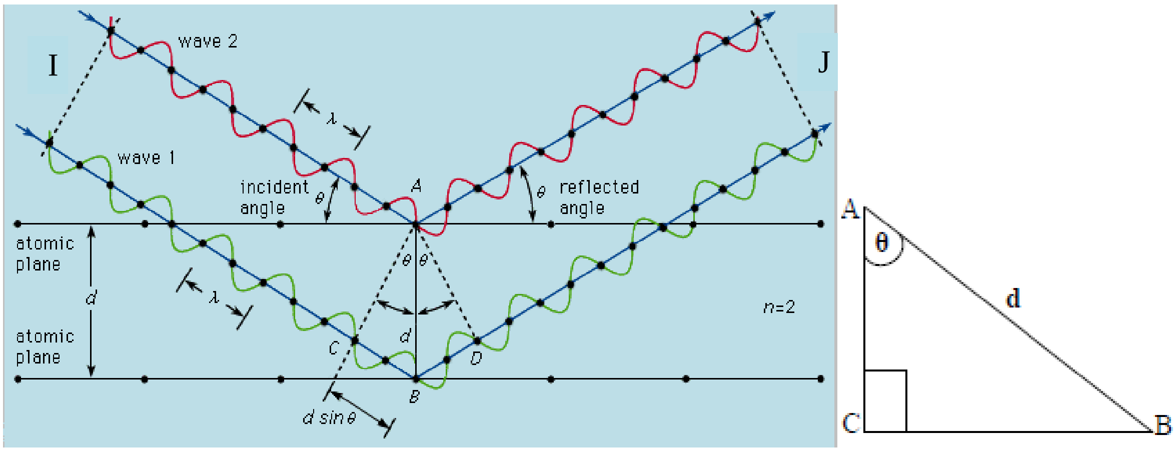

Fig. 4.2: Bragg's Diffraction Scheme [2].

4.2.1.3. Experimental Techniques for X-ray Diffraction

X-ray diffraction is a general-purpose analytical technique employed in analysis and quantitative resolution of various crystalline phases of powdered or solid samples of any compound [8]. The sample should be displayed in a plane or flattened surface. An outstanding characteristic of X-ray diffraction is its non-destructive nature. The principle of operation of X-ray diffractometer is based on the Bragg-Brentano geometry. The basic setup of the Bragg-Brentano geometry is depicted in Fig. 4.3.

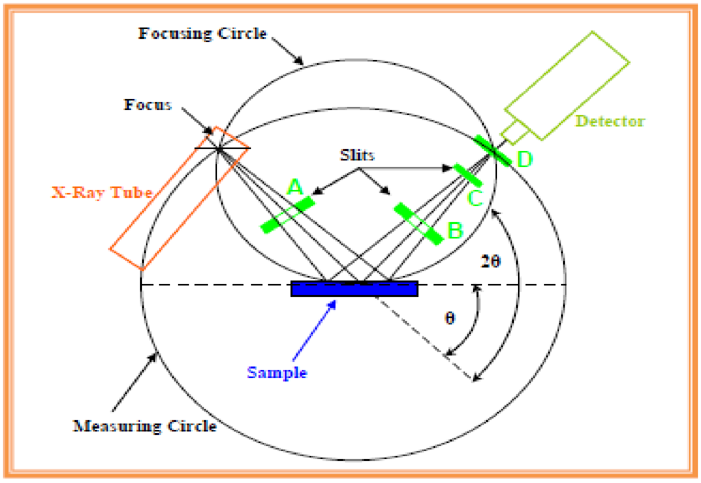

Fig. 4.3: Basic setup for the D8 Advance X-ray Diffractometer, Bragg-Brentano Geometry [7]. A: aperture, B: scattered radiation slit, C: Kα filter, D: detector slit.

In the Bragg-Brentano geometry, X-ray diffraction can be in either $\theta - \theta$ or $\theta - 2\theta$ configuration. In $\theta - \theta$ configuration, the sample is fixed at stationary position at the center of the goniometer while the X-ray source and the detector are made to rotate around a common axis located at the center of the goniometer. Here the sample lies on a horizontal plane which forms vertical planes at angle θ with both the X-ray source and the detector. The X-ray source and the detector rotate at the same angular velocity enabling them to maintain equal angles with the surface of the sample. With this condition, the reflected beam can be captured once diffraction occurs at the Bragg angle.

In $\theta - 2\theta$ configuration, the source of the X-ray is fixed at stationary position forming an angle θ with the non-stationary sample. Thus, the variation in the angle of the incident X-ray beam is due to the sample's movement. The sample rotate in the same axis with the detector but the detector move at twice the speed of the sample, hence the diffraction angle 2θ, is always twice the glancing angle, θ.

In this work, Bruker AXS D8 Advanced X-ray diffractometer was used for the XRD measurements. The diffractometer was equipped with monochromatic CuKα radiation with wavelength (λ) =1.54056 Å. The scans were measured in the $\theta - 2\theta$ configuration in the range of 10 – 70 ° in a step size of 0.00945054° while the X-ray generator was set at standard setting of 40 kV at 40 mA.

4.2.2. X-ray Photoelectron Spectroscopy (XPS)

4.2.2.1. Introduction

First named electron spectroscopy for chemical analysis (ESCA), by a Swedish scientist K. Siegbahn and his research group in 1954, X-ray photoelectron spectroscopy (XPS) is one of the instrumental in-situ surface analytical techniques for studying the surface of solid phase substances [9]. XPS gives qualitative and quantitative information about the elemental composition, chemical state, electronic state and empirical formula of elements contained in a material. XPS is based on photoelectric effect principle [10]. The energies of incident photons used in XPS are generally greater than 1000 eV. The standard laboratory sources for the XPS are Mg$K\alpha$ (1253.3 eV) and Al$K\alpha$ (1486.6 eV). In XPS, a special case which involves the ejection of a characteristic electron from the core level of an atom by incident X-ray photon is used to obtain information about the sample. The kinetic energy of the ejected photoelectrons can be determined using a high sensitive electron energy analyzer and electron detector, which gives information about the binding energy of the photoelectrons. The distribution of the binding energies gives information on the chemical composition of the sample, since binding energies are characteristic for each element. All XPS measurements are performed under ultra-high vacuum (UHV) chamber ($\sim 10^{-11}$mbar).

4.2.2.2. Experimental Set-up for XPS

A typical setup for XPS experiment is shown schematically in Fig. 4.4. The photon source can be X-ray, UV-light, laser light or synchrotron. Photons with known energy are used to excite the atoms slightly below the sample surface. The ejected electrons from the surface are then filtered by the hemispherical analyser (HSA) depending on their energies before their intensity is finally recorded by the detector. However, for incident photons that penetrate deep into the sample, the ejected electrons have low probability of escaping from the sample's surface without losing energy and hence mainly contribute to the background signal rather than well-defined primary photoelectron peaks.

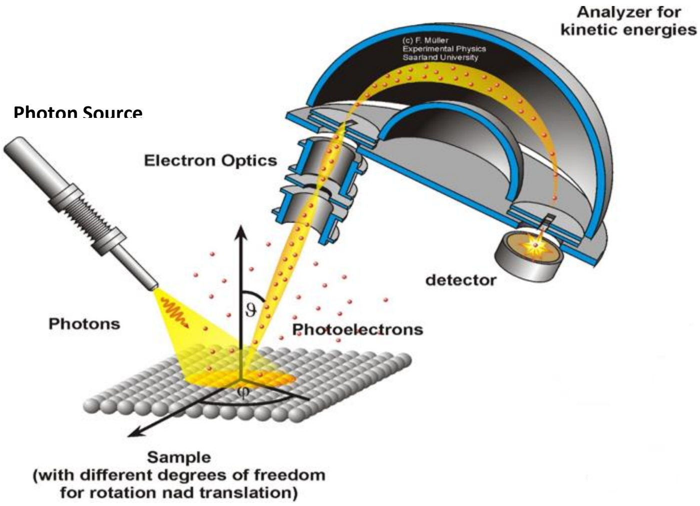

Fig. 4.4: Schematic of a typical XPS setup [11].

4.2.2.3. Basic Principle of XPS

The basic principle of XPS is shown in Fig. 4.5. An incident X-ray beam is shone on the surface of a sample and the X-ray photon is absorbed completely by the core electron of an atom. If the absorbed photon energy is sufficiently to overcome the surface energy barrier of the sample, core electron (photoelectron) will be ejected from the atom. The photoemission process can be considered as a one particle excitation which has no effect on the electronic structure of the atom [12]. The XPS technique involves three basic steps: the absorption of photon and excitation of electron, the hurl of the excited electron through the sample to the surface and the escape of the electron through the surface energy barrier into the vacuum. The photoelectrons are then detected in the vacuum and their energy distribution is measured. The energy levels involved in the XPS spectrometer is shown in Fig. 4.6.

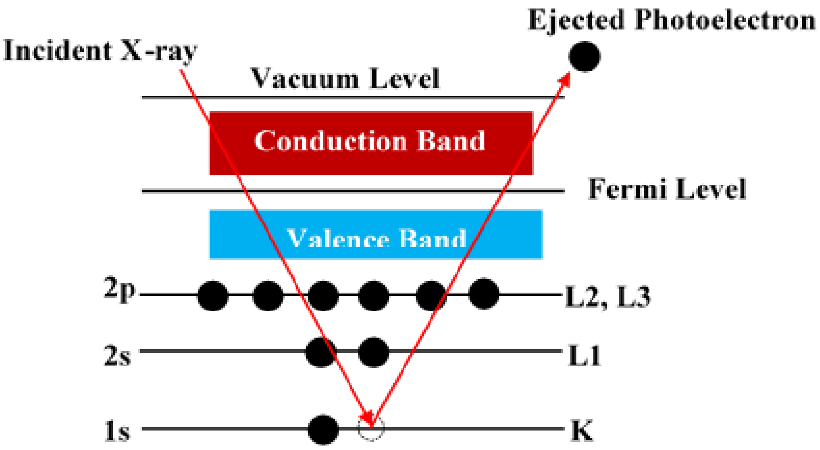

Fig. 4.5: Schematic diagram of the XPS process, showing photo-ionization of an atom by the ejection of a 1s electron.

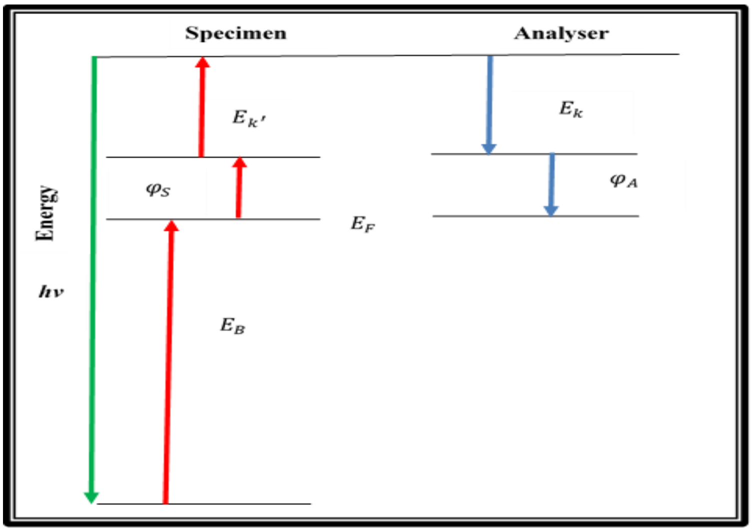

Fig. 4.6: The energy levels involved in the XPS spectrometer.

It is evident from Fig. 4.6 that the work function of the spectrometer plays role in the energy equation which relates the kinetic energy of the photoelectron to the binding energy. Therefore, it is of great important to calibrate the energy scale of the spectrometer before each experiment using standard such as Cu and Au [13]. Binding energy of the photoelectron can be derived as shown in table 4.1.

Table 4.1: Derivation of the binding energy of photoelectron

Specimen side	**Analyzer side**
$hv = E_B + \varphi_s + E_{k'}$ (4.6)	$E_k + \varphi_A = \varphi_s + E_{k'}$ (4.7) $E_{k'} = E_k + \varphi_A - \varphi_s$ (4.8)
hv = energy of primary X-ray beam	E_k = kinetic energy of the photoelectron measured by analyser
E_B = binding energy of the photoelectron φ_s = work function of the specimen $E_{k'}$ = kinetic energy of the photoelectron in vacuum	φ_A = work function of the analyser

Since the Fermi level of the analyzer is in the same potential with that of the specimen, eq. (4.8) can be substituted into eq. (4.6) thus: Eq. (4.6) can be written as

$$
\begin{aligned}
E_B &= hv - \varphi_s - E_{k'} \\
&= hv - \varphi_s - E_k - \varphi_A + \varphi_s \\
&= hv - E_k - \varphi_A \qquad (4.9)
\end{aligned}
$$

It can be seen from eq. (4.9) that the binding energy of the photoelectron is independent of the work function of the specimen. Hence once the kinetic is measured by the XPS spectrometer and the X-ray energy and the work function of the analyzer are known, the binding energy of the photoelectron can be determined.

4.2.3. Scanning Electron Microscope (SEM)

4.2.3.1. Introduction

Invented in 1937 by a German Physicist Manfred von Ardenne [14], SEM creates high magnified images of objects by focusing energetic electron beam onto a sample surface in a raster scan pattern and the signals that arises from the interaction of the sample's surface and the incident electron beam is detected. This signal gives information about the sample's external morphology, chemical composition, crystalline structure and the orientation of materials the sample is made up of. During data acquisition, data can be collected within a selected area of the sample's surface [15]. The generated signals include secondary electrons, backscattered electrons, diffracted backscattered electrons, Auger electrons, photons, visible light and heat. SEM is primarily used for detection of the secondary electrons (for topographical image and morphology). To detect other signals, SEM is usually equipped with equipment such as energy-dispersive X-ray spectroscopy (EDS) for elemental maps or chemical analysis, back-scattered electron Detector (BSE) for phase identification and cathodoluminescence (CL) for compositional mapping. Resolution better than 1 nm can be achieve using SEM and it can operate under high vacuum, low vacuum, in wet conditions and at wide range of cryogenic (low temperature) or elevated temperatures.

4.2.3.2. The Principle of SEM

The basic principle of SEM is shown in Fig. 4.7. Electrons from an electron gun composed of electron source of either thermionic, Schottky or field-emission cathode are accelerated through a voltage difference (typically 0.1−50 keV) between cathode and anode. The electron depending on the electron beam source can generate beam with different diameters. Thermionic emission can generate beam with diameter in the order of 10−50 μm and beam diameter in the order of 10−100 nm can be generated using Schottky or field emission gun. The magnetic lenses further narrowed the electron beam to the diameter of 1−10 nm before they arrive onto the surface of the specimen with electron-probe current in the range of 10^{-9}−10^{-12} A [16]. By placing sets of plates (final lens) around the beam and varying the potential difference between them, the electron beam can be deflected such that it can scan lines across the sample surface. The scanned beam can do three things when they hit the surface of the sample: They can pass through the sample without colliding with any atom. Conversely, they can collide with electrons in the atoms of the sample and create secondary electrons or they can collide with the nucleus of the atom of the sample, creating backscattered electrons.

The secondary electrons are relatively weak in energy (about 100 V). If they are close enough to the surface of the sample, they can be collected by the secondary electron detector to form SEM image. If the incident beam interacts with the nucleus of the sample’s atoms, it reflects back out of the sample as a backscattered electron. These types of electrons have high energy and are detected using the backscattered electron detector to form backscattered electron images. The electron detectors are usually placed in the chamber and they have high positive potential (about 10 keV) on their face which they use to attract the electrons ejected from the sample [17].

In secondary electron imaging mode, the incident electron beam ejects secondary electrons from the sample's surface as it is scanned across the surface topography of the sample. When the beam scan across area with low topography, the amount of secondary electrons ejected from the sample decreased and this shows a dark spot on the SEM image. Conversely, for area of high topography, much secondary electron is emitted resulting to bright spot on the image. However, in backscattering imaging mode, area of the sample constituting low atomic weight elements will emit less backscattered electrons than area composed of high atomic elements [18].

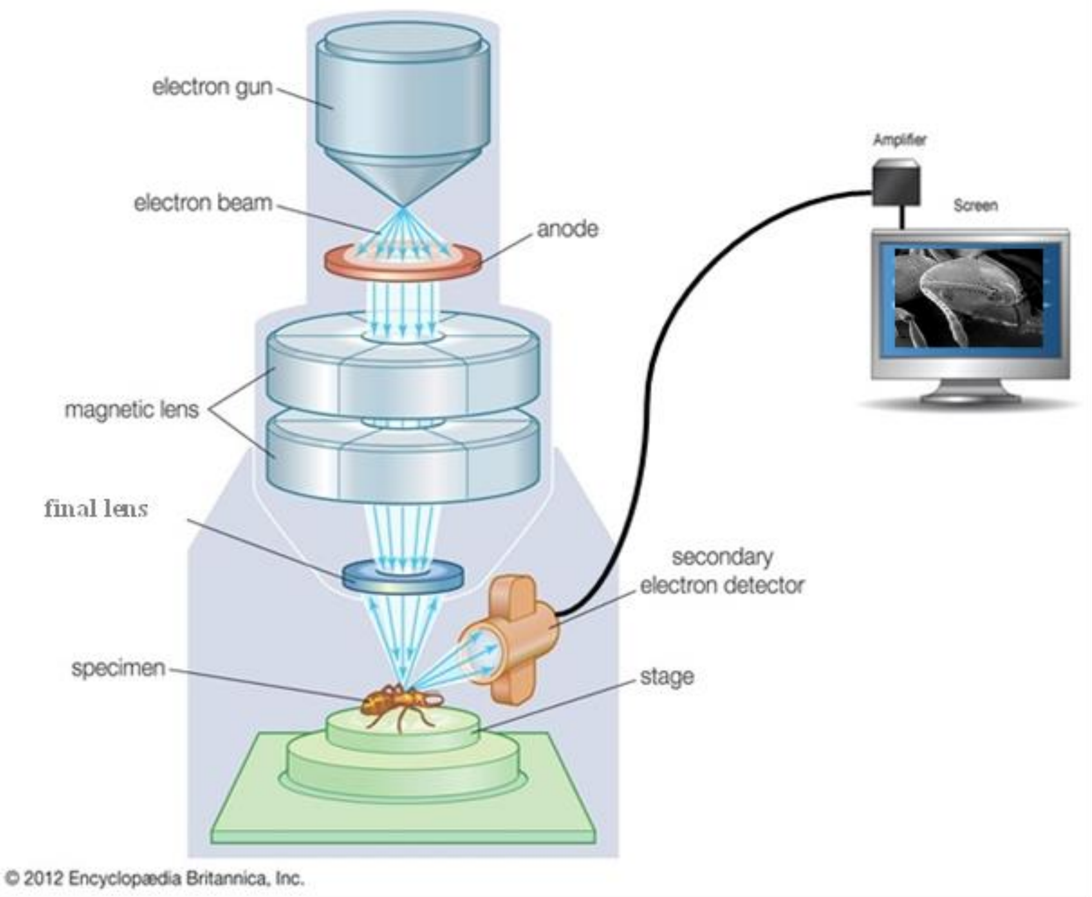

Fig. 4.7: A schematic of scanning electron microscopy.

The signal collected by the detector are converted to photons using a scintillator, amplified in a photomultiplier, and then converted to electrical signal which is used to modulate the intensity of the image on the screen.

4.2.4. Time of Flight Secondary Ion Mass Spectroscopy (ToF-SIMS)

4.2.4.1. Introduction

Time-of-Flight Secondary Ion Mass Spectroscopy (TOF-SIMS) is a surface-sensitive analytical technique that uses a pulse primary ion beam (Cs or micro-focused Ga) to probe the surface of a solid material [19]. The momentum transfer from the primary ion to the target initiates a ‘collision cascade’ within the solid, much like a microscopic billiards game. A portion of this momentum is redirected back towards the surface resulting in the ejection of atomic or molecular ions (secondary ions) from the surface. More than 95% of these secondary ions originate from the outermost 1-2 layers of the solid thus defining TOF-SIMS surface analysis as an extremely surface sensitive technique [20].

Because of its surface sensitivity, TOF-SIMS has been utilized to characterize a variety of conducting and non-conducting surfaces. Common applications include metals, semiconductors, biomaterials, ceramics, lubricants, polymers, glasses, catalysts, pharmaceuticals, thin films and paper [20]. Depth profiling can also be performed by TOF-SIMS. A low energy ion gun is operated in DC mode for sputtering with high depth resolution. Data acquisition is accomplished using the same or a second ion gun operated in pulsed mode. Depth profiling by TOF-SIMS allows monitoring of all species of interest simultaneously with high-mass resolution to remove any interferences [21].

4.2.4.2. Theory

The basic equation governing TOF separation can be derived as follow; the kinetic energy of the secondary ion is related to its charge and applied voltage by

$$KE = QV \qquad (4.10)$$

Therefore,

$$\frac{1}{2}mv^2 = QV$$

$$v^2 = \frac{2QV}{m}$$

(4.11)

The measured time-of-flight (t) of the ion is given by d/v where d is the length of the tube.

Hence it follows that $t = \frac{d}{v}$ and $\frac{t}{d} = \frac{1}{v}$. Therefore eq. (4.11) can be written as

$$\left(\frac{t}{d}\right)^2 = \frac{1}{v^2} = \frac{m}{2QV}$$

Hence

$$\frac{m}{Q} = 2V\left(\frac{t}{d}\right)^2 \qquad (4.12)$$

But Q is related to the elementary particle e by $Q = ze$. Where z is the number of the elementary charges. Therefore eq. (4.12) becomes

$$\frac{m}{z} = 2eV\left(\frac{t}{d}\right)^2 \tag{4.13}$$

Also the extraction pulse potential E is related to the applied voltage by $E = \frac{V}{s}$, where s is the length of the tube over which E is applied. Therefore eq. (4.13) becomes

$$\frac{m}{z} = 2eEs\left(\frac{t}{d}\right)^2 \tag{4.14}$$

m/z is the mass-to-charge ratio of the ions [22]. Theoretically, this implies that all the ions are given the same initial kinetic energy by the extraction pulse and then drift along the field free drift zone where they will be separated so that all ions of the same m/z arrive at the detector at the same time. In practice, the pulse is not felt by all ions to the same intensity and so a kinetic energy distribution for each discrete m/z exists. This lowers the resolution by creating a time-of-flight distribution for each m/z [23]. This is relatively easily corrected by the application of a reflectron at the end of the drift zone [24]. The reflectron consists of a series of electric fields which repulse the ions back along the flight tube - usually at a slightly displaced angle (see Fig. 4.7) - resulting in a refocusing of ions with the same m/z value on the reflectron detector. The ions are introduced either directly from the source of the instrument or from a previous analyzer as a pulse. This results in the ions receiving the same initial kinetic energy. As they pass along the field free drift zone, they are separated by their masses, lighter ions traveling faster.

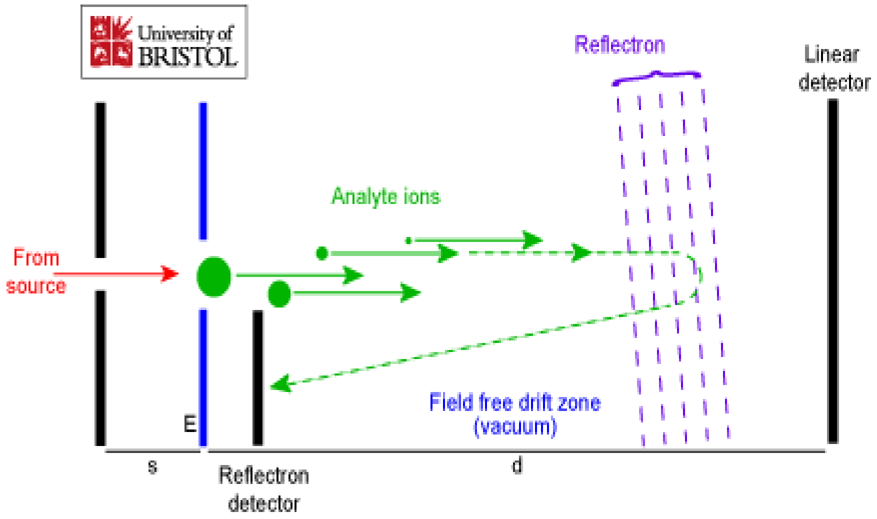

Fig. 4.7: A schematic of a ToF mass spectrometer operating in Reflectron Mode.

4.2.4.3. Principle of Operation of ToF-SIMS

Fig. 4.8 shows the basic set-up for a typical TOF-SIMS instrument, of the pulsed primary ion beam and single stage reflectron analyzer design [25]. A pulse of ion beam bombards the specimen and sputters it. This produces a cloud of atoms and molecules among which some are ionized. The ionized particles of one polarity, atomic and molecular secondary ions, are accelerated into a reflectron type spectrometer. They travel two meters through a tube to arrive at ion detection and counting system. However, because they all depart from the sample at the same time and were subjected to the same accelerating voltage, the lighter ones arrive at the detection system before the heavier ones. The "Time-of-Flight" of an ion is proportional to the square root of its mass (see eq. 4.14), so that all the different masses are separated during the flight and can be detected individually. The next pulse of primary ions cannot start until the secondary ions of the first pulse have cleared the analyzer. Otherwise the slower heavy ions of the first pulse are overtaken by the faster light ions of the second pulse. Once extracted into the mass spectrometer, the secondary ions travel through a field free region where they are separated in time based on their mass to charge ratio. For each primary ion pulse, a full mass spectrum is obtained by measuring the arrival times of the secondary ions at the detector and performing a simple time to mass conversion. Chemical images can also be generated by collecting a mass spectrum at every pixel (256 x 256) as the finely focused, primary ion beam is rastered across the sample surface.

Sample integrity is preserved during analyses by operating under “static” conditions. This mode dictates $\leq 1\text{x}10^{13}$ ions/cm^2 impinge on a surface ensuring that ≤ 1% of the characterized region is consumed. Using pulse primary ion source ($\leq 1\ ns$) in conjunction with the TOF-analyser help to maximize the secondary ion detection sensitivity. For insulating samples, charge compensation is necessary by using an electron flood gun during analysis. This delivers low energy (~ 20 eV) electrons to the sample surface to neutralize any charging by the positive primary ion beam [26].

4.2.4.4. The primary ion beam

Typically, the primary ion beam is accelerated by around 20-30 kV, pulsed with a typical pulse width of 25 ns and then further bunched so that it arrives at the sample within $\sim 1\ ns$. The primary ion pulse contains several hundred of primary ions which sputters the secondary ions from the sample surface. The primary ion pulse provides a reference for $t = 0$ for the time-of-flight measurement of the secondary ion [27].

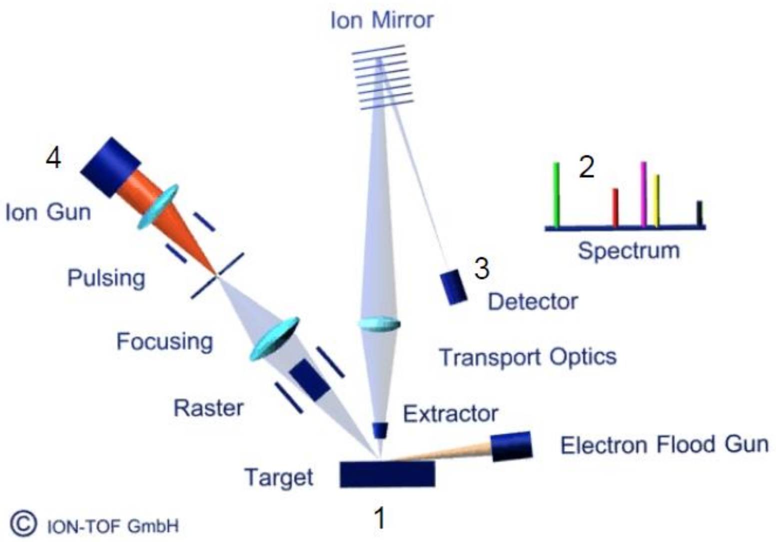

Fig. 4.8: Schematic diagram of the ION-TOF TOF-SIMS IV mass spectrometer, provided by ION-TOF GmbH (Muenster, Germany).

4.2.4.5. The secondary ions

The secondary ions are extracted into the time-of-flight mass analyzer through the application of an extraction voltage (typically -2000V for positive secondary ions and +2000V for negative secondary ions). The extraction voltage determines the energy of the secondary ions as they drift through the analyzer along a flight path which is roughly 2 m in length. Secondary ions are separated by their mass since heavier ions have lower velocity than lighter ones with the same kinetic energy. At some distance into the flight path, the secondary ions are reflected by an ion mirror which provides first order energy compensation. Since secondary ions are typically emitted with a small spread of kinetic energies of several electron volts [24, 28], the reflectron analyzer provides improved time-focus at the detector for different ions of the same species. At the end of the flight path, the secondary ions are detected by a single ion counting detector, consisting of a microchannel plate (MCP) detector coupled to time-to-digital convertor (TDC) electronics.

4.2.4.6. The spectrum

The spectrum obtained with each primary ion pulse is collected and summed over many pulses (typically 105 – 107). Finally, the spectrum is converted from a ‘time-of-flight’ scale into a mass scale via mass calibration using a number of known secondary ions [26].

4.3. Optical Characterization Techniques

4.3.1. Ultraviolet-Visible (UV-Vis) Spectroscopy

4.3.1.1. Introduction

Ultraviolet-Visible (UV-Vis) spectroscopy is a very handy and useful technique use for measurement of absorbance, transmittance and reflectance of variety of materials [29]. From these quantities, the optical and electronic properties of a material can be determined. The ultraviolet (UV) region lies between 100−400 nm in the electromagnetic spectrum while the visible light region lies between 400−800nm. In other words, UV-Vis spectroscopy can be used to scan the absorbance, transmittance or reflectance of a material between the range of 100−800 nm. However, the technique is usually designed to scan between 200−800 nm due to application reasons. In the absorbance mode, this technique is used to measure the concentration of substance in liquid solution in agreement with the Beer-Lambert law [30]. In a nutshell, in absorption spectroscopy, a liquid sample is placed between a light source and a photodetector and the light intensity is compared before and after passing through the sample. The transmission spectroscopy is a bit similar to the absorption spectroscopy but it can be used for solid, liquid or gas samples. Here light that passed through the sample is compared with the light which does not pass through it [29]. Solid samples are usually measured in the reflectance mode. Depending on the equipment used, reflectance measurement can be specular or diffuse. Although absorption, transmission and reflection spectroscopy can be used for the measurement of a sample in different states, the set-ups for these techniques are the same.

4.3.1.2. The Basic Set-up for UV-Vis Spectroscopy

The set-up for UV-Vis spectrometer is depicted schematically in Fig. 4.9. The basic parts of the spectrometer includes: a light source (D_2 lamp or Tungsten lamp), a sample holder, a diffraction grating, a monochromator and a detector. Light from the light source splits into several beams in different direction by the diffraction grating (filter) [31]. The monochromator transmits a selected range of wavelength of light which is later split into two paths by the half-mirrored device (beam splitter). One path of the light passes through the sample and other path passes through the reference. The intensity of the reference beam which may suffer insignificant or no absorption and that of the sample are detected by the photo diodes and compared and the output is shown at the data output.

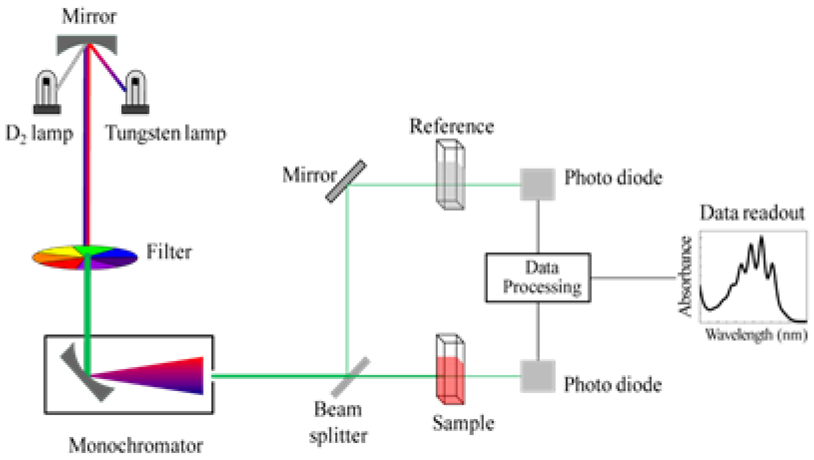

Fig. 4.9: Schematic of UV- visible spectrophotometer [32]

4.3.1.3. The Tauc Plot

The Tauc plot is a known method for the calculation of the band gap of materials. The absorption coefficient for interband transitions is related to the band gap by

$$(\alpha h v)^{1/n} = A(hv - E_g) \tag{4.15}$$

where α is the absorption coefficient, h is Planck's constant, v is the frequency of vibration, E_g the band gap and A is a constant which is almost independent of the chemical composition of the material [33].

Steps involved in obtaining band gap from transmittance curve using Tauc Plot

(i) In eq. (4.15), the value of the exponent n denotes the nature of the sample transition.

- For direct allowed transitions…………..$n = 1/2$
- For direct forbidden transitions…………..$n = 3/2$
- For indirect allowed transitions…………...$n = 2$
- For indirect forbidden transitions…………$n = 3$

If we consider an indirect band gap material having $n = 2$,

(ii) The acquired diffuse reflectance spectrum is converted to Kubelka-Munk function given by $FR_\infty = (1 - R_\infty)^2/(2R_\infty)$, hence the vertical axis is converted to $F(R_\infty)$

which is proportional to the absorption coefficient. The α in the Tauc equation is then substituted by $F(R_\infty)$ such that we have

$$[h\nu FR_\infty]^{1/2} = A(h\nu - E_g) \tag{4.16}$$

(iii) The wavelength in nm is converted to the photon energy $(h\nu)$ in electron volt (eV) using the relation $h\nu = {}^{1240}/_{\lambda(nm)}$. The function $[h\nu FR_\infty]^{1/2}$ is then plotted against $(h\nu)$.

(iv) A line is drawn tangent to the point of inflection on the $(h\nu) - [h\nu FR_\infty]^{1/2}$ curve to the $(h\nu)$ axis and the point of the intersection of the line to the $(h\nu)$ axis is the band gap.

4.3.2. Photoluminescence (PL) Spectroscopy

Photoluminescence (PL) spectrometer is an instrument used to record both excitation and emission spectra. An emission spectrum can be measured at a given excitation wavelength. On the contrary, an excitation spectrum depends on the emission intensity and can be measured at a given emission wavelength. Both spectra can be represented in either wavelength or wavenumber scale with units in nanometers (nm) or per centimeter (cm^{-1}) respectively [34]. Wavenumber can be converted to nanometer by taking the inverse and multiplying by 10^7. For detailed information on PL and its principles, see section 1.8.1.

In PL Spectrometer, light shone on a sample is absorbed leading to excitation process and the excess energy is emitted in the form of photon (luminescence process) [35]. The schematic of a typical photoluminescence spectrometer is shown in Fig. 4.10. The source of the excitation is a xenon lamp. The instrument shown has monochromators which is used to select the excitation and emission wavelengths. The shutter is used to eliminate the exciting light or to block the emission channel. The beam splitter in the excitation light path is used to reflect part of the excitation light to the reference sample. Two gratings in the excitation monochromator are used to decrease the stray light (light having different wavelength with the chosen light). The concave grating is used for further reduction of the stray light. The photomultiplier tubes (PMT) is used for detection of photoluminescence which is then quantified using the appropriate electronics devices. The output is display graphically on a screen and also stored digitally [34].

In this report, the photoluminescence measurement was taken with: (i) Cary Eclipse fluorescence spectrometer equipped with 150 W xenon lamp as the source and scanning wavelength of 241 nm at the average time of 0.01s and sampling interval of 1.0 nm and (ii) a PL system consisting of a 325 nm He-Cd gas laser as an excitation source, a spectrometer, a photomultiplier tube (PMT) detector and a lock-in amplifier.

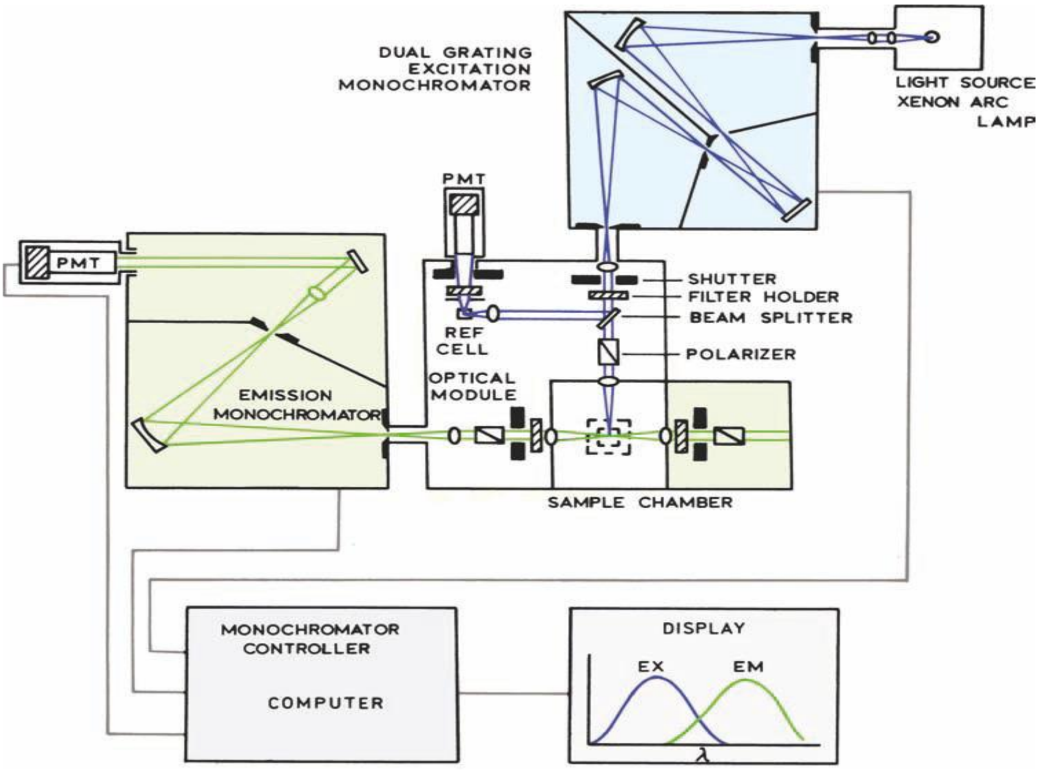

Fig. 4.10: Schematic of photoluminescence spectrometer [34]

4.3.3. Fourier Transform Infrared (FTIR) Spectroscopy

Fourier transform infrared (FTIR) spectroscopy uses infrared (IR) radiation to give molecular analysis of materials. Its principle is based on the use of the molecular vibration of materials to measure their absorbance and transmittance. This technique exploits the fact that molecules absorb specific frequencies that are characteristic of their structure. FTIR can be used for the analysis of solid, liquid or gas samples. This technique has verse applications which include: emission spectra [36], photocurrent spectra [37], micro-samples [38], gas chromatograph-infrared spectrometry [39] and thermogravimetry-infrared spectrometry [40]. The schematic of the basic FTIR spectrometer principle is shown in Fig. 4.11. A collimated infrared (IR) light is focused on the beam splitter commonly made of a very thin film of germanium. About 50% of the light passes through the film and is reflected back along its path by the fixed mirror, and half of the reflected light (25% of the original light) is reflected by the same beam splitter through the sample cell to the infrared sensor. The remaining 50% of the incident light (the reference beam) is reflected at right angles to its incident path onto a moving mirror. The light from the moving mirror is reflected back along its original path and half of it is transmitted through the beam splitter, through the sample cell, to the infrared sensor. Therefore, in total, 25% of the incident collimated light from the source reaches the sensor from the fixed mirror and 25% from the movable mirror. The system work in the form of the Michelson interferometer, and as such the path of the two light beams striking the IR sensor will be different hence forming constructive and destructive interference.

When the movable mirror traverses its programmed path and constructive and destructive interference occurs, a series of maxima and minima signals will be monitored by the sensor. The interferometer takes a Fourier transform of the incoming signal since the frequency of the waveform is determined by the velocity of the moving mirror [41].

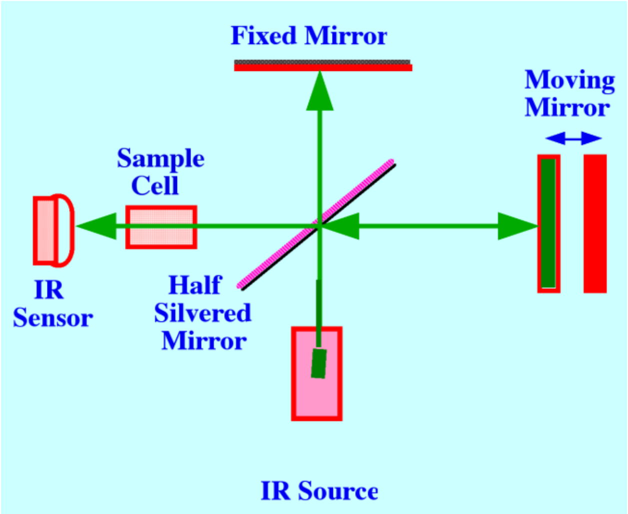

Fig. 4.11: Schematic of FTIR spectrometer

If the initial intensity of the reference beam is I_0 and I is the intensity of the beam that passes the sample, then the absorbance (A) is related to the transmittance (T) by Beer's law [42] given as

$$A = log_{10}\ (1/T)$$

Where T is I_0/I, hence

$$A = log1_{10}\ (I/I_0) \qquad (4.17)$$

4.4. References

[1] H. A. Enge, M. R. Wehr and J. A. Richards. Introduction to Atomic physics. Addison-Wesley Publishing Company. ISBN: 0201018799 (1972).

[2] M. M. Alam; M. Phil Thesis, "Synthesis and Optical Properties of Semiconductor Nanostructures" Islamic University, Kushtia, Bangladesh (2008).

[3] L.V. Azaroff. X-Ray diffraction, McGraw Hill company (1974).

[4] B. D. Cullity and S. R. Stock. Elements of X-ray Diffraction, 3rd ed. Prentice Hall pp. 1 (2001).

[5] B.D. Cullity. Elements of X-ray diffraction, Addison-Wesley Publishing Co.Inc. (1978).

[6] B. D. Cullity and S. R. Stock Elements of X-ray Diffraction, 3rd ed. Prentice Hall pp. 95 (2001).

[7] A. Monshi, M. Foroughi, and M. Monshi. Modified Scherrer Equation to Estimate More Accurately Nano-Crystallite Size Using XRD. World Journal of Nano Science and Engineering, 2, 154-160 (2012).

[8] Bruker Advanced X-Ray Solutions, D8 X-Ray Diffractometer User's Manual Volume I, pp. 1-2

[9] K. Siegbahn, et al. ESCA: Nova Acta Regiae, Soc, Sci. Ser. 20 (1967).

[10] H. Hertz; Ann. Physik 31, 983 (1887).

[11] Ultra High Vacuum Lab. Photoelectron spectrometer, ESCA-Mk II by Vacuum Generators. Retrieved June, (2014) from http://jacobs.physik.uni-saarland.de/instrumentation/uhvl.htm.

[12] Surface Physics Group. Principles of photoemission spectroscopy (PES). Retrieved June, (2014) from http://physics.mff.cuni.cz/kfpp/povrchy/method/xps-ma

[13] W.D. Roos. An Introduction to X-ray Photoelectron Spectrometer (XPS). Dept. of Physics, UFS (2012).

[14] M. von Ardenne. Improvements in electron microscopes. GB 511204, convention date (Germany) 18 February 1937.

[15] S. Swapp. Scanning Electron Microscopy (SEM). Retrieved June, (2014) from http://serc.carleton.edu/research_education/geochemsheets/techniques/SEM.html.

[16] L. Reimer. Scanning Electron Microscopy: Physics of Image Formation and Microanalysis. Springer. ISBN: 3540639764. Pp 1 (1998).

[17] Basic principles of the SEM. Retrieved June, (2014) from Ammrf http://www.ammrf.org.au/myscope/sem/practice/principles/layout.php#detail.

[18] How SEM Works. Retrieved June, (2014) from Seallabs http://www.seallabs.com/how-sem-works.html.

[19] A. Benninghoven. Chemical Analysis of Inorganic and Organic Surfaces and Thin Films by Static Time-of-Flight Secondary Ion Mass Spectrometry (TOF-SIMS), Angewandte Chemie International (in English), 33, 1023-1043 (1994).

[20] L.VanVaeck, A. Adriaens and R. Gijbels. Static Secondary Ion Mass Spectrometry: (S-SIMS) Part 1. Methodology and Structural Interpretation, Mass Spectrometry Reviews. 18, 1-47 (1999).

[21] A. Adriaens, L. VanVaeck and F. Adams. Static Secondary Ion Mass Spectrometry (S-SIMS) Part 2: Material Science Applications, Mass Spectrometry Reviews. 18, 48-81 (1999).

[22] W.C. Wiley & I.H. MacLaren. The Review of Scientific Instruments. 26, p1150 (1995).

[23] R.J. Cotter. Analytical Chemistry. 64, p1027A (1992).

[24] Mamyrin et al. Soviet Physics - JETP, 37, p45 (1973) and International Journal of Mass Spectrometry and Ion Processes. 131, p1. (1994).

[25] J. Schwieters, H. G. Cramer, T. Heller, U. Jurgens, E. Niehuis, J. Zehnpfenning, and A. Benninghoven. Journal of Vacuum Science & Technology a-Vacuum Surfaces and Films 9, 2864 (1991).

[26] F. M. Green, I. S. Gilmore, and M. P. Seah, Journal of the American Society for Mass Spectrometry 17, 514 (2006).

[27] A. Delcorte and P. Bertrand. Surface Science 97, 412-413 (1998).

[28] A. Delcorte, C. Poleunis and P. Bertrand. Applied Surface Science 252, 6542 (2006).

[29] Absorption / Transmission / Reflection Spectroscopy. Retrieved June, (2014) from Andor http://www.andor.com/learning-academy/absorption-transmission-reflection-spectroscopy-an-introduction-to-absorption-transmission-reflection-spectroscopy.

[30] M. Fox. Optical Properties of Solids. Oxford University Press, ISBN: 0198506139, p. 3 (2001).

[31] H. H. Perkampus. UV-Vis Spectrosopy and its Application. Springer laboratory 1 (1992).

[32] Ultraviolet–visible spectroscopy. Retrieved June, (2014) from Wikipedia, the free encyclopedia http://en.wikipedia.org/wiki/Ultraviolet%E2%80%93visible_spectroscopy.

[34] J. Tauc. The optical properties of solids (North-Holland, Amsterdam, 1970) Young, PA. J. Phys. C: Solid State Phys. 4, 93 (1971).

[35] J.R. Lakowicz. Principles of Fluorescence Spectroscopy, 3rd edition. Springer p. 28, ISBN: 100387312781 (2010).

[36] M. Gaft, R. Reisfeld and G. Panczer. Luminescence spectroscopy of minerals and materials. Springer p. 263. ISBN 3-540-21918-8 (2005).

[37] J. Poortmans and V. Arkhipov. Thin film solar cells: fabrication, characterization and applications. John Wiley and Sons. p. 189. ISBN 0-470-09126-6 (2006).

[38] J.P. Beauchaine, J.W. Peterman, R.J. Rosenthal. "Applications of FT-IR/microscopy in forensic analysis". Microchimica Acta 94 (1-6): 133–138. doi:10.1007/BF01205855 (1988).

[39] R. White. Chromatography/Fourier transform infrared spectroscopy and its applications. Marcel Dekker. ISBN 0-8247-8191-0 (1990).

[40] K. Nishikida, E. Nishio, R.W. Hannah. Selected applications of FT-IR techniques. Gordon and Breach. p. 240. ISBN 2-88449-073-6 (1995).

[41] R.P. Scott. The Fourier Transform IR Spectrometer. Retrieved June, (2014) from http://www.analyticalspectroscopy.net/ap3-8.htm.

[42] Beer "Bestimmung der Absorption des rothen Lichts in farbigen Flüssigkeiten" (Determination of the absorption of red light in colored liquids), Annalen der Physik und Chemie, 86, pp. 78–88 (1852).

CHAPTER FIVE

Structure, Optical Properties and Elemental Analyses of Mixed rare earth oxyorthosilicate (R_2SiO_5, R = La, Gd and Y) doped Dy^{3+} phosphors.

5.1. Introduction.

Rare earth oxyorthosilicate of the form R_2SiO_5 (R = La, Gd, Y) doped with rare earth elements, has been of a special interest for the past decades due to their wide band gap, fast decay times, high quantum efficiency, high density and minimal self-absorption [1]. The quantum efficiency of some R_2SiO_5 has been reported to be twice that of bismuth germanium oxide (BGO) [2], and their life time is about five times smaller than that of BGO [3]. They are regarded as good host lattices [4] for rare-earth dopant ions to prepare light emitting materials (phosphors) due to their relatively high chemical stability. Rare-earth doped oxyorthosilicate phosphors are used in different types of light emitting devices and scintillators [5-11].

Rare earth oxyorthosilicates have two basic types of crystal structures. These are the monoclinic crystallographic point group with space group *P21/c* and *I2/a* corresponding respectively to the low temperature phase ($X1$) and high temperature phase ($X2$). These groups are found in large ionic radii rare earth ions (La–Tb) in rare earth oxyorthosilicates. The second type is the monoclinic crystallographic point group with space group *C2/c* (low temperature phase) and *B2/b* (high temperature phase). These groups are found in small ionic radii rare earth ions (Dy-Lu) in rare earth oxyorthosilicates [12-14]. La_2SiO_5 and Gd_2SiO_5 fall into the *P21/c* space group while Y_2SiO_5 fall into the *C2/c* space group. A phase-transformation temperature of about 1190 °C and 1250 °C has been reported from $X_1$to X_2 for Y_2SiO_5 [12, 15]. The lattice parameters of La_2SiO_5, Gd_2SiO_5 and Y_2SiO_5 are shown in table 5.1.

Table 5.2: Lattice parameters of La_2SiO_5, Gd_2SiO_5 and Y_2SiO_5 reference in their respective JCDPS files

Compound	a (nm)	b (nm)	c (nm)	β (°)
La_2SiO_5	0.9326	0.7510	0.7032	108.69
Y_2SiO_5	1.041	0.6721	1.249	102.650
Gd_2SiO_5	0.912	0.706	0.673	107.580

The recent increasing interest in the luminescence of Dy^{3+} doped matrices in the visible region is supported by some practical applications in lighting. The two prominent emission peaks around 486 nm (blue emission) and around 573 nm (yellow emission) are promising for application in white-light emitting phosphors [16, 17]. However, a more promising application of Dy^{3+}-doped matrices is found in visible laser as a result of the dominance of the yellow emission from the hypersensitive $^4F_{9/2} \rightarrow {}^6H_{13/2}$ electronic transition [18].

Although much work has been reported on the luminescence of La_2SiO_5, Gd_2SiO_5 and Y_2SiO_5 doped rare earth elements [19-24], there is still a need to improve their luminescence properties for practical applications. In this work, we tried to improve the luminescence properties of rare-earth oxyorthosilicate by incorporating lanthanum, gadolinium and yttrium ions. La_2SiO_5, Gd_2SiO_5 and Y_2SiO_5 are known to have two crystallographic sites [12-15], therefore incorporating La, Gd and Y is expected to provide more sites in the crystal lattice to be occupied by the Dy^{3+} dopant ions.

5.2. Experimental

Preparation

Nanoparticulate Dy^{3+} doped $LaGdSiO_5$, $LaYSiO_5$ and $GdYSiO_5$ phosphors were prepared by urea-assisted solution combustion method using the analytical reagents, lanthanum nitrate hexahydrate $La(NO_3)_3.6H_2O$, gadolinium nitrate hexahydrate $Gd(NO_3)_3.6H_2O$, yttrium nitrate hexahydrate $Y(NO_3)_3.6H_2O$ and silicic acid (SiO_2H_2O). Stoichiometric amounts of $La(NO_3)_3.6H_2O$, $Gd(NO_3)_3.6H_2O$ and $Y(NO_3)_3.6H_2O$ were added in different beakers and stoichiometric amounts of SiO_2H_2O, urea $CO(NH_4)_2$ and ammonium nitrate (NH_4NO_3) were added to each glass beaker after which 2.0 ml of distilled water was added. All the hosts were doped with 1.0 mol% of Dy^{3+}. For 1.0 mol% of Dy^{3+} doped $LaGdSiO_5$, 0.6696 g of $La(NO_3)_3.6H_2O$, 0.6980 g of $Gd(NO_3)_3.6H_2O$, 0.0109 g of $Dy(NO_3)_3.6(H_2O)$, 0.1000 g of SiO_2H_2O, 0.6251 g of $CO(NH_4)_2$ and 0.4691 g of NH_4NO_3 were used. Similarly, for 1.0 mol% of Dy^{3+} doped $LaYSiO_5$ and $GdYSiO_5$ the same quantity of chemicals used above were used except the variations in the mass of $Y(NO_3)_3.6H_2O$ (0.4251 g). Each mixture was stirred vigorously using a magnetic stirrer on a hot plate set to 100 ℃ for 15 min until a homogenous solution was obtained. The homogenous solution was transferred to a ceramic crucible boat and immediately into a muffle furnace pre-heated to 600 ± 10 ℃. 2 min after placing the solution into the furnace, oxidation took place resulting in the evaporation of gasses (CO_2, N_2

and H_2O) and giving a foam-like crispy end product. The product was allowed to cool down to room temperature and it was then gently ground into fine powder using an agate mortar and pestle. The powders were then stored in samples holders for characterization. The procedure for the synthesis of our powder phosphors is illustrated schematically in Fig. 5.1.

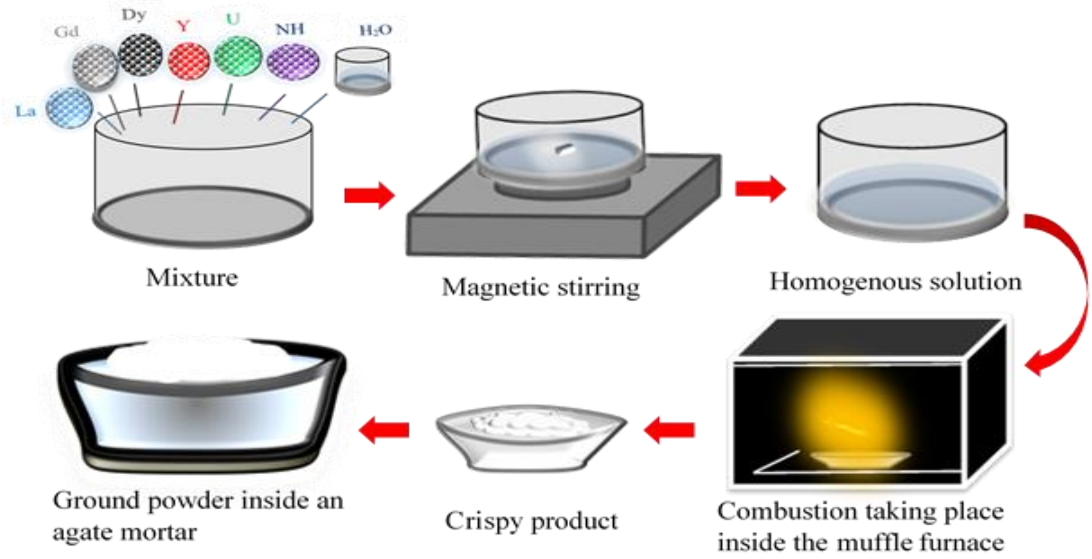

Fig. 5.1: A schematic illustration of the synthesis procedure of our powders. (La = $La(NO_3)_3.6H_2O$, Gd = $Gd(NO_3)_3.6H_2O$, Dy = $Dy(NO_3)_3.6(H_2O)$, Y = $Y(NO_3)_3.6H_2O$, U = $CO(NH_4)_2$ and NH = NH_4NO_3)

Characterization

The structure of our materials was analysed using a Bruker D8 Advanced X−ray diffractometer (XRD) equipped with monochromatic $CuK\alpha$ radiation of wavelength$(\lambda) = 1.54056$ Å. The morphology study was carried out using Jeol JSM-7800F field emission scanning electron microscope (FE-SEM). The photoluminescence (PL) spectra were measured with two instruments: (i) Cary Eclipse fluorescence spectrometer equipped with 150 W xenon lamp used as the excitation source and scanning wavelength of 241 nm at the average time of 0.01s and sampling interval of 1.0 nm and (ii) a PL system consisting of a 325 nm He-Cd gas laser as an excitation source, a spectrometer, a photomultiplier tube (PMT) detector and a lock-in amplifier. The UV-Vis measurements were taken using Lambda 950 UV-Vis spectrometer. The identification of the atomic and molecular ionic species and the distribution of the dopant ions in the host lattices were examined using iontof ToF-SIMS[5] in positive secondary ion polarity (+SIMS) mode in both spectroscopic and imaging mode. In each case, the pulsed primary ion source (Bi^{3+}) was set at 30 keV and the DC current was

11.0 pA. The analytical area was 100 × 100 μm with pixels resolution of 512 × 512 and 50 scans were taken at the scan rate of 26.21 sec/scan. The base pressure was pumped down to 10^{-9} mbar and Ar^+ dual-beam flood gun was in the switch on mode in order to compensate for charge.

5.3. Results and discussion

The XRD patterns of $GdYSiO_5$, $LaGdSiO_5$, and $LaYSiO_5$ all doped with 1.0 mol% of Dy^{3+} together with standard monoclinic structures of La_2SiO_5, Gd_2SiO_5 and Y_2SiO_5 referenced in the standard JCDPS files no: 40-0234, 74-1795 and 74-2011 are shown in Fig. 5.2. The crystallographic planes corresponding to La_2SiO_5, Gd_2SiO_5 and Y_2SiO_5 are indicated respectively with the symbols *, ¤ and ♦ and the corresponding indexes are listed in table 5.2. Also included in table 5.2 are the calculated and theoretical d-spacing corresponding to each crystallographic plane. The d-spacings were calculated using the d-spacing equation for monoclinic systems [25] given by

$$\frac{1}{d^2} = \frac{h^2}{a^2 \sin^2\beta} + \frac{k^2}{b^2} + \frac{l^2}{c^2 \sin^2\beta} - \frac{2hl \cos\beta}{ac \sin^2\beta} \qquad [5.1]$$

where *hkl* are the Miller indices and *a*, *b*, *c* and β are lattice parameters shown in table 5.1.

The XRD pattern of $LaYSiO_5$ show peaks that are consistent with the peaks from the standard monoclinic structures of La_2SiO_5 and Y_2SiO_5 represented respectively by * and ♦. This result indicates that $LaYSiO_5$ is an admixture of La_2SiO_5 and Y_2SiO_5. Similarly, $LaGdSiO_5$ is an admixture of La_2SiO_5 and Gd_2SiO_5, while $GdYSiO_5$ Gd_2SiO_5 is an admixture of Gd_2SiO_5 and Y_2SiO_5. It is therefore reasonable to conclude that we have successfully crystallized mixed rare-earths oxyorthosilicates. Dy^{3+} will preferentially substitute either La^{3+} or Gd^{3+} in their crystal sites, but it will be unlikely to substitute Y^{3+} due to the difference in the ionic radii. La^{3+} (ionic radii 0.110 nm and 0.1216 nm for seven and nine-fold coordinated sites) [26] and Gd^{3+} (ionic radii 0.10 nm and 0.1107 nm for seven and nine-fold coordinated sites) [27, 28] can easily be substituted by Dy^{3+} (ionic radii 0.1052 nm and 0.1167 nm for six and eightfold coordinated sites) but it cannot easily substitute Y^{3+} (ionic radii 0.090 nm and 0.096 nm for seven and six-fold coordinated sites) [26] because of its comparatively small ionic radius [29].

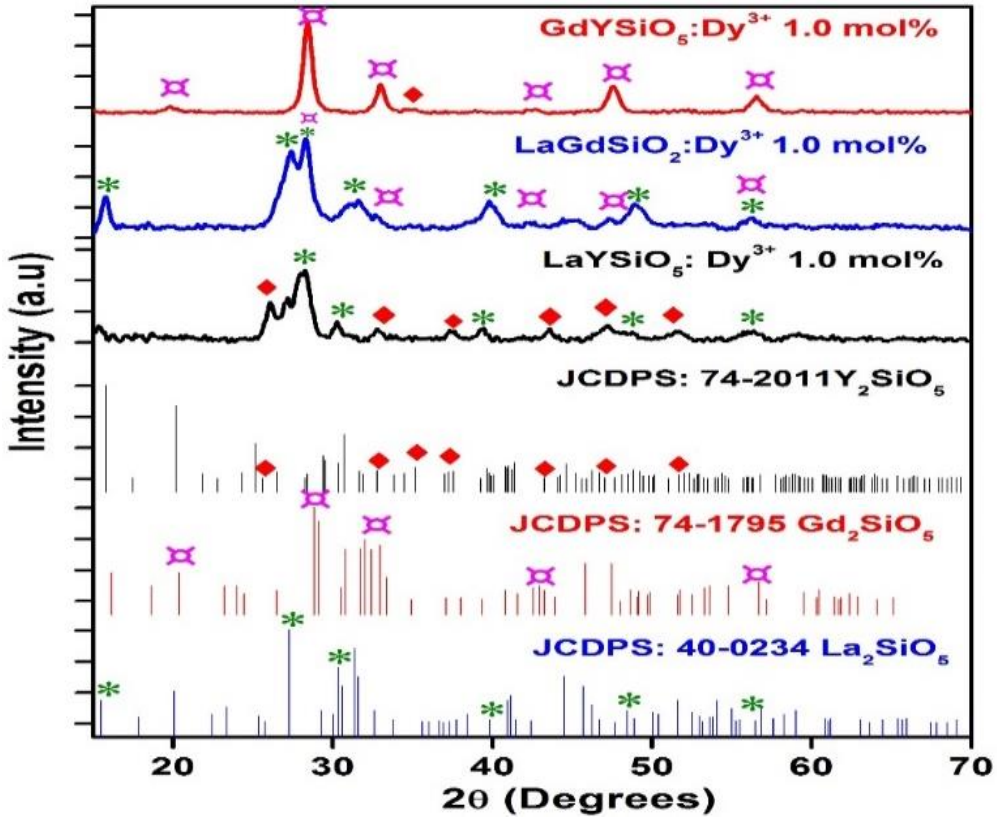

Fig. 5.2: The XRD patterns of $LaGSiO_5$, $LaYSiO_5$ and $GdYSiO_5$ doped with 1.0 mol% of Dy^{3+}.

The average crystallite size (L) and the lattice strain (ε) induced by defects and related crystal imperfections were calculated using the Williamson-Hall equation [30, 31] given by

$$\beta_{hkl} Cos\theta = 4\varepsilon\ Sin\theta\ +\ \frac{K\,\lambda}{L} \qquad [5.2]$$

where λ is the X-ray wavelength in nanometer (nm), β_{hkl} is the peak width of the diffraction peaks profile at half maximum height, θ is the Bragg angle and K is a constant related to the crystallite shape, usually taken as 0.9 or 0.89 for full width half maximum (FWHM) of spherical crystals with cubic unit cells. The average crystallites sizes and the lattice strains of both the undoped and Dy^{3+} doped host lattices were estimated and the values obtained are listed in table 5.3. The increase in the lattice strain observed in the doped samples could be attributed to distortion induced by the dopants in the host matrices [32]. The peak widths were not corrected for the instrumental broadening therefore the actual crystallite sizes may be bigger than the values listed in table 5.3.

Fig. 5.3 (a)–(f) shows the FE-SEM images of $LaYSiO_5:Dy^{3+}$, $LaGdSiO_5:Dy^{3+}$ and $GdYSiO_5:Dy^{3+}$ powders. Fig. 5.3 (b) is the high magnification image of the encircled area in Fig. 5.3 (a) while Fig. 5.3 (d) and (f) respectively show the high magnification of the areas encircled in Fig. 5.3 (c) and (e). The images show that the powders were made up of an agglomeration of plate-let and flake like nanoparticles. The magnified

Table 5.2: The crystallographic planes corresponding to various Bragg angles and the calculated and theoretical d-spacing for La_2SiO_5, Gd_2SiO_5 and Y_2SiO_5

2θ	La_2SiO_5	Y_2SiO_5	Gd_2SiO_5	La_2SiO_5 d-spacing (nm)		Y_2SiO_5 d-spacing (nm)		Gd_2SiO_5 d-spacing (nm)	
(Degree)	Planes	Planes	Planes	Calculated	theoretical	Calculated	theoretical	Calculated	theoretical
15.80	$(\bar{1}10)$	-	-	0.57474	0.57230				
20.08	-	-	(200)			0.33606	0.33605	0.42861	0.43470
26.50	-	(020)	-						
27.47	(021)	-		0.37322	0.32709				
28.50	$(\bar{1}12)$	(310)	(021)	0.32217	0.31800	0.34899	0.30238	0.33175	0.30927
30.35	$(\bar{3}12)$	-	-	0.28178	0.29421				
32.62	(310)	-	(102)	0.27675	0.27431			0.27964	0.29205
35.16	-	$(\bar{4}02)$	-			0.23892	0.25506		
37.30	(130)	$(\bar{3}21)$	-	0.24243	0.24083	0.29814	0.24119		
39.83	(122)	(015)	$(\bar{3}21)$	0.24577	0.22611	0.22323	0.22913	0.21978	0.22874
42.58	-	-	$(\bar{4}02)$					0.23853	0.21213
43.24	-	$(\bar{1}32)$	-			0.22400	0.20902		
47.40	-	$(\bar{4}15)$	(421)			0.160421	0.19077	0.18723	0.19142
48.80	(312)	-	-	0.19667	0.18626				
51.59	$(\bar{5}12)$	(233)	-	0.17595	0.17703	0.18404	0.17682		
56.20	$(\bar{5}13)$	$(\bar{6}04)$	(240)	0.16113	0.16183	0.14259	0.16401	0.15410	0.16353
59.00	(142)	$(\bar{5}25)$	-	0.16528	0.15647	0.15659	0.15603		

Table 5.3: The average crystallites sizes and the lattice strains of the doped and undoped samples

Nano-phosphors	Strain of undoped ($\times 10^{-3}$)	Strain 1.0 mol% Dy^{3+} doped ($\times 10^{-2}$)	Crystallite size of undoped (nm)	Crystallite size 1.0 mol% Dy^{3+} doped (nm)
$LaGdSiO_5$	1.7	1.42	8.0	14.0
$LaYSiO_5$	8.9	1.29	9.0	14.0
$GdYSiO_5$	5.6	6.20	10.0	13.0

images (Fig 5.3 (b), (d) and (f)) show pores and hollows on the surface resulting from gases that evolved during the combustion reaction.

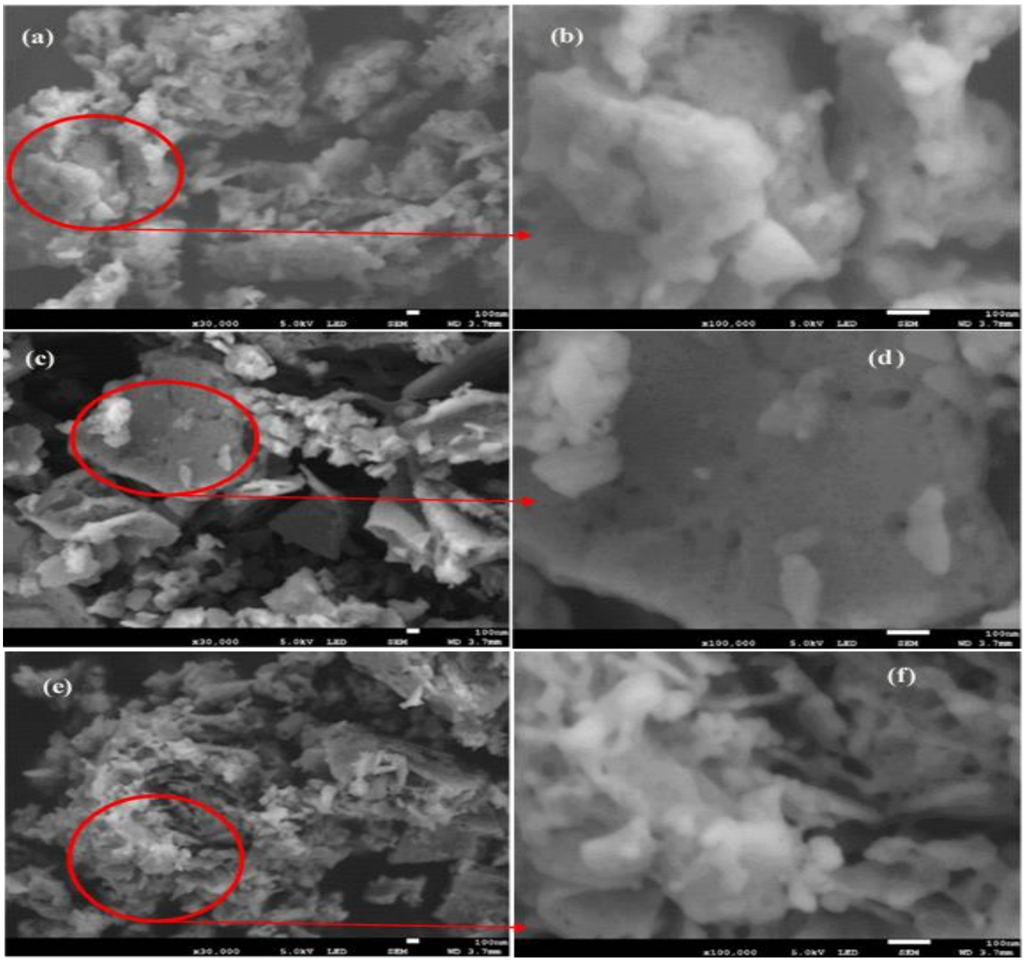

Fig. 5.3: FE-SEM images of (a) low and (b) high magnification of $LaYSiO_5:Dy^{3+}$, (c) low and (d) high magnification of $LaGdSiO_5:Dy^{3+}$ and (e) low and (f) high magnification of $GdYSiO_5:Dy^{3+}$ nanophosphors.

Fig. 5.4 (a), (b) and (c), depict the positive secondary ion ToF-SIMS spectra of $LaYSiO_5:Dy^{3+}$, $LaGdSiO_5:Dy^{3+}$ and $GdYSiO_5:Dy^{3+}$ phosphors, respectively, in the range of 14-185 atomic mass units. All the atomic ionic species present in our materials were detected. In addition CH_3^+, Na^+ and K^+ were detected in all the spectra, which we assign to incidental contaminants from the atmosphere and sample holders. All the spectra show positive and molecular ions associated with our materials. For example, in Fig. 5.4 (a) the positive atomic ions associated with our materials are Si^+, Y^+, La^+, Dy^+ and the corresponding molecular ions are SiH^+, SiO^+, $SiOH^+$, YH^+, YO^+, YOH^+, LaH^+, LaO^+, $LaOH^+$, DyH^+, DyO^+ and $DyOH^+$. A similar trend was observed in Fig. 5.4 (b) and (c). The molecular ions were probably formed as a result of the reaction between atomic species from our materials and atmospheric oxygen and water. A summary of the positive atomic ions and the corresponding molecular ions, and the associated atomic mass units are presented in table 5.4.

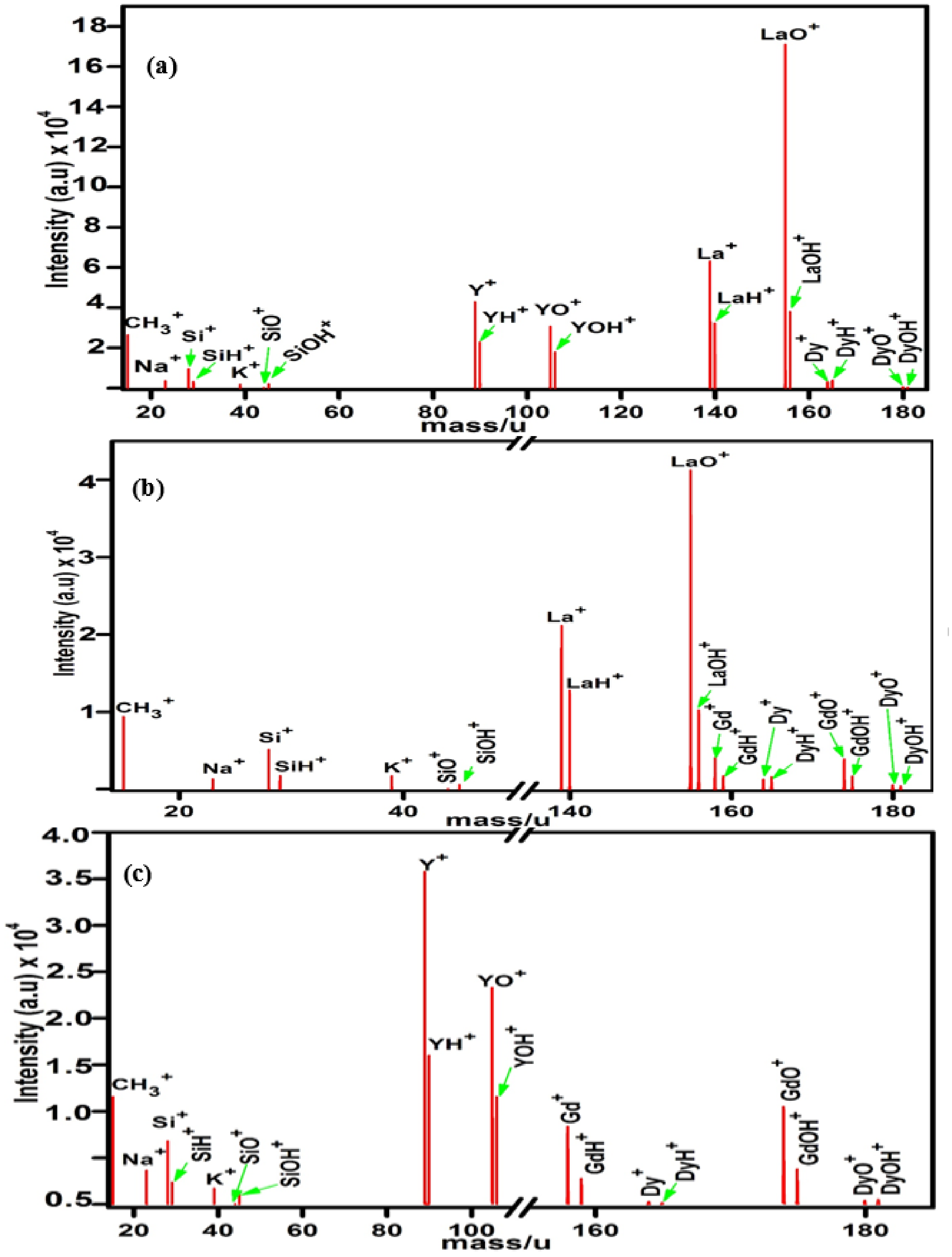

Fig. 5.4: The Positive ToF-SIMS spectra of (a) $LaYSiO_5:Dy^{3+}$ (b) $LaGdSiO_5:Dy^{3+}$ and (c) $GdYSiO_5:Dy^{3+}$ nanophosphors.

Table 5.4: Atomic/molecular ions and their atomic mass units

Atomic/molecular ions	Mass/u	Atomic/molecular ions	Mass/u
CH_3^+	15	LaH^+	140
Na^+	23	LaO^+	155
Si^+	28	$LaOH^+$	156
SiH^+	29	Gd^+	158
K^+	39	GdH^+	159
SiO^+	44	GdO^+	174
$SiOH^+$	45	$GdOH^+$	175
Y^+	89	Dy^+	164
YH^+	90	DyH^+	165
YO^+	105	DyO^+	180
YOH^+	106	$DyOH^+$	181
La^+	139		

The secondary ions images were generated by scanning the primary ion beam over 100 × 100 μm^2 area of the samples and collecting secondary ions at each point within the area. Fig. 5.5 (a - c) show the positive ToF-SIMS images of La^+, DyO^+ and Y^+ from $LaYSiO_5:Dy^{3+}$, Fig. 5.5(d - f) are the images of La^+, DyO^+ and Gd^+ from $LaGdSiO_5:Dy^{3+}$ and Fig. 5.5(g - i) are the images of Gd^+, DyO^+ and Y^+ taken from $GdYSiO_5:Dy^{3+}$. The vertical scale bar in all the images represents the signal intensities of each ion. High intensity indicates region with high ionic concentration of the element in question and region of low intensity indicates low ionic concentration. The best image sharpness was obtained by setting the banning at 4.0 pixels.

Fig. 5.6 (a) shows the overlay image of La^+ (purple), DyO^+ (green) and Y^+ (blue) taken from $LaYSiO_5:Dy^{3+}$, Fig. 5.6 (b) shows the overlay image of La+ (purple), DyO^+ (green) and Gd^+ (blue) taken from $LaGdSiO_5:Dy^{3+}$ and Fig. 5.6 (c) shows that of Gd^+ (purple), DyO^+ (green) and Y^+ (blue) taken from $GdYSiO_5:Dy^{3+}$. In all the images the dopant (DyO^+) ions are evenly distributed over the entire 100 × 100 μm^2 analytical area.

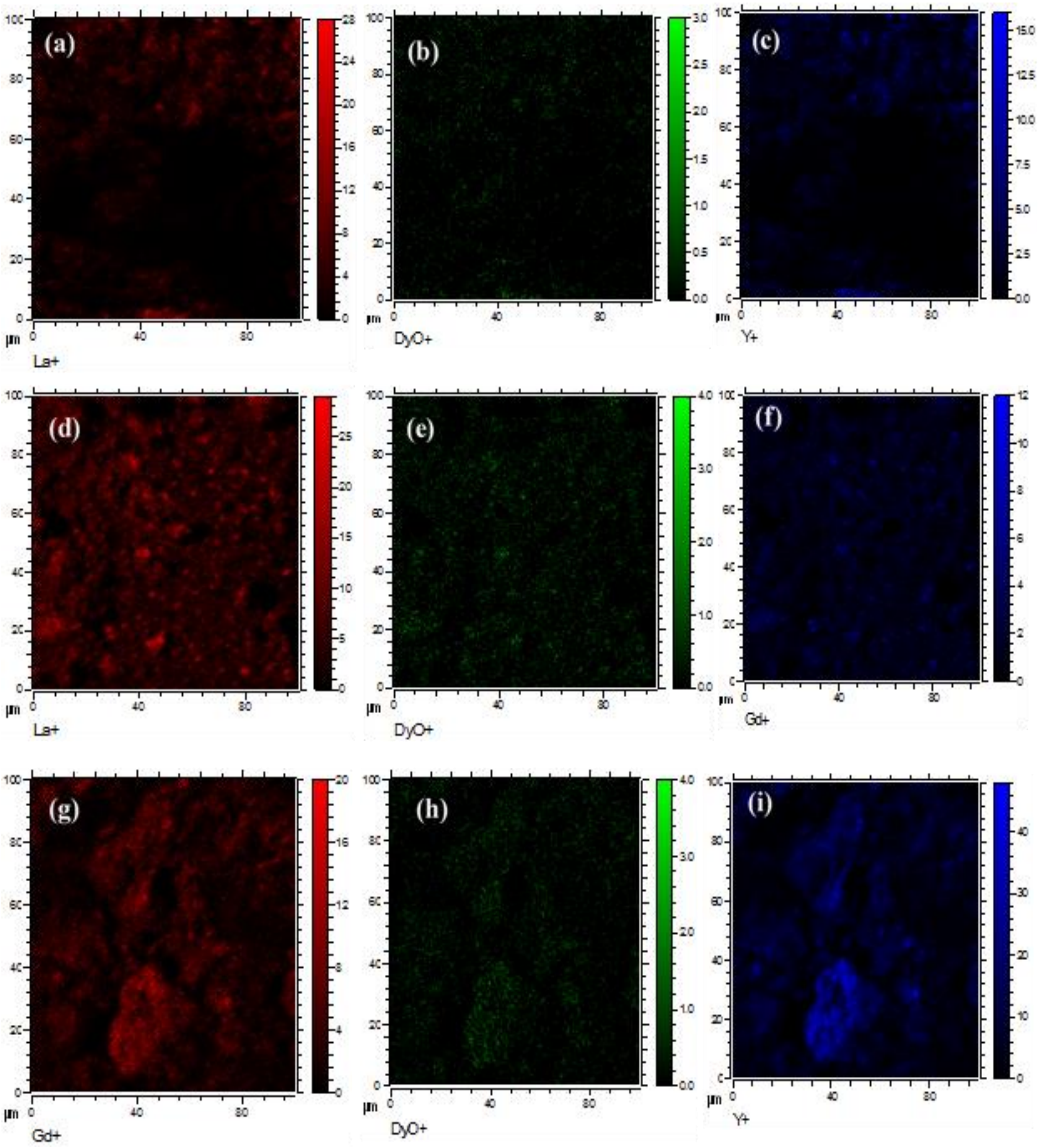

Fig. 5.5: The positive ToF-SIMS images of (a) La$^+$, (b) DyO$^+$ and (c) Y$^+$ taken from LaYSiO$_5$:Dy^{3+}, (d) La$^+$, (e) DyO$^+$ and (f) Gd$^+$ taken from LaGdSiO$_5$:Dy^{3+} and g) Gd$^+$, (h) DyO$^+$ and (i) Y$^+$ taken from GdYSiO$_5$:Dy^{3+}.

The PL excitation and emission spectra recorded when the samples were excited using a monochromatized xenon lamp are shown respectively in Fig. 5.7 and Fig. 5.8. Fig. 5.7 shows the excitation spectra recorded when monitoring the emission at 573 nm. The excitation spectrum consists of narrowband emission peaks in the range of 260 to

400 nm, and a combination of broad band and comparatively narrow bands protruding from the broad band in the range of 200 to 260 nm. The excitation peaks at 275 and

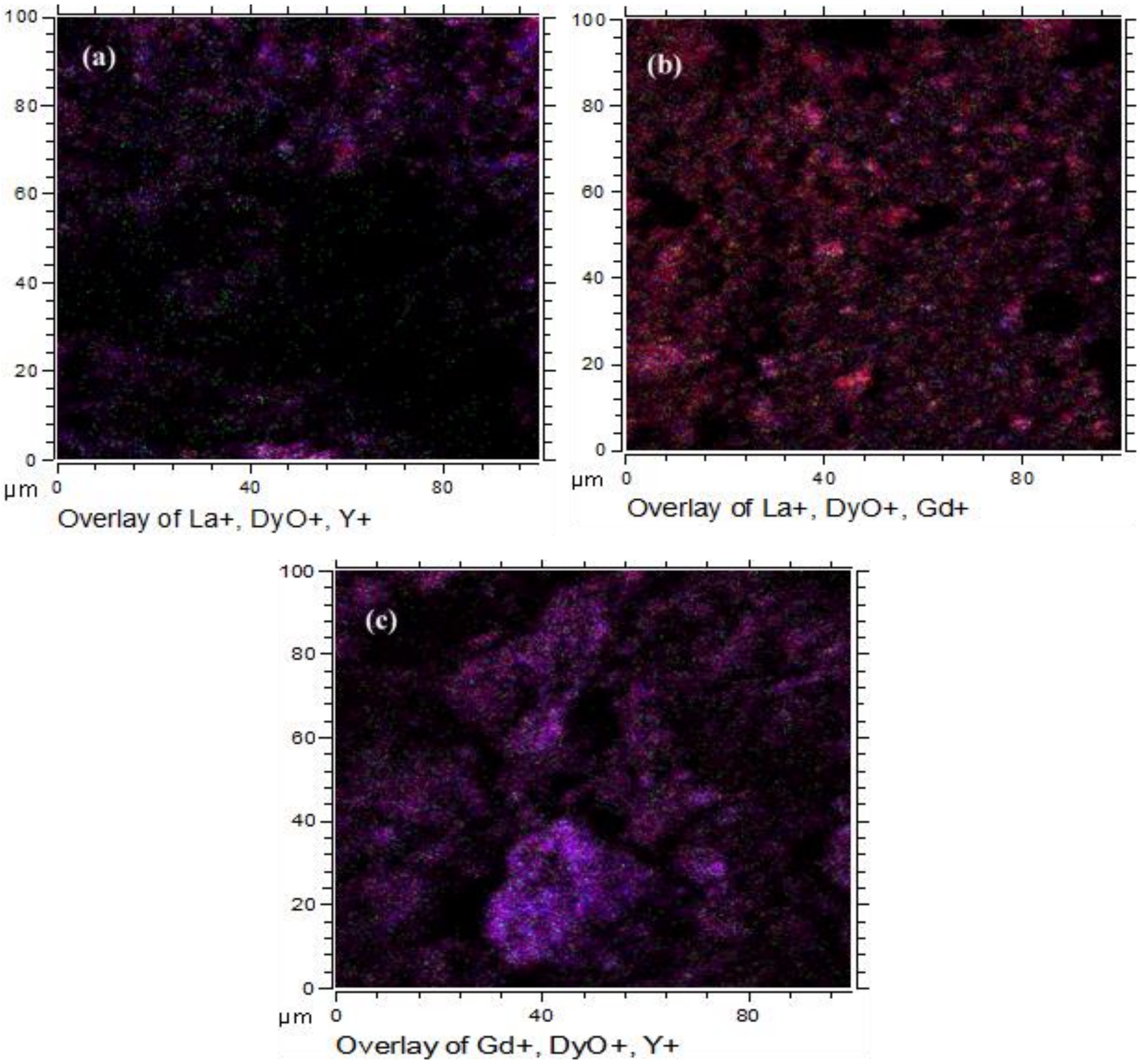

Fig. 5.6: The overlay ToF-SIMS images of (a) La^+, DyO^+ and Y^+, (b) La^+, DyO^+ and Gd^+ and (c) Gd^+, DyO^+ and Y^+ taken respectively from $LaYSiO_5{:}Dy^{3+}$, $LaGdSiO_5{:}Dy^{3+}$ and $GdYSiO_5{:}Dy^{3+}$ nanophosphors.

313 nm are attributed to ${}^8S_{7/2}\rightarrow{}^6I_J$ and ${}^6P_J\rightarrow{}^8S_{7/2}$ transitions of Gd^{3+} [33] and the 351 and 386 nm peaks correspond to the ${}^6H_{15/2}\rightarrow{}^6P_{7/2}$ and ${}^6H_{15/2}\rightarrow{}^4I_{13/2}$ transitions of Dy^{3+} respectively [34]. Notice that the peak at 241 nm was not observed in $GdYSiO_5{:}Dy^{3+}$, hence it cannot be attributed to either the allowed 4f→5d transitions of Dy^{3+} or $O^{2-}\rightarrow Ln^{3+}$ (Ln = La, Y, Gd or Dy) charge transfer states. Furthermore, the $O^{2-}\rightarrow Ln^{3+}$ charge transfer states of Dy^{3+} and Gd^{3+} and their 4f→5d allowed electronic transitions are observed below 200 nm [35, 36] and neither La^{3+} nor Y^{3+} can induce excitation in/or

near the visible region since they have no 4f electrons [37, 38]. We attribute the excitation peaks at 241 nm to La_{Gd}^{3+} and La_{Y}^{3+}isoelectronic impurities [39, 40] and the 227 nm excitation peaks to electronic transitions from the O2p valence band to the La (5d6s) or Gd (5d6s) or Y (4d5s) conduction band as the case may be [41, 42]. This result suggests that the host absorbed the primary excitation energy and transferred it to Dy^{3+}. The shapes and the peak intensity of these broad absorption bands are different simply because the hosts were different. For example, the peak intensity of the $LaGdSiO_5$ is higher than those of $LaYSiO_5$ and $GdYSiO_5$, suggesting that it absorbed the primary excitation energy efficiently and transferred it to Dy^{3+}. The absence of the excitation lines at 275 and 313 nm in $LaYSiO_5:Dy^{3+}$ in Fig. 5.6 suggests that those peaks are from Gd^{3+} and not Dy^{3+}.

The changes observed in the excitation intensities of the phosphors can be related to the differences between the ionic radii of each element and that of Dy^{3+} as discussed in the XRD data. The similarities between the ionic radii of La^{3+} and Gd^{3+} suggests that more La^{3+} and Gd^{3+} crystal sites will be occupied by Dy^{3+} more than Y^{3+} crystal sites. As a result the peak intensity of $LaGdSiO_5:Dy^{3+}$ is higher than that of $LaYSiO_5:Dy^{3+}$ and $GdYSiO_5:Dy^{3+}$. Furthermore, we attribute the higher PL emission intensity to comparatively efficient absorption of the primary excitation energy by $LaGdSiO_5$ that was subsequently transferred to Dy^{3+}. The corresponding emission spectra for the excitation spectra shown in Fig. 5.7 when exciting at the wavelength of 241 nm are shown in Fig. 5.8. The PL emission lines observed at 485, 573, 668 and 756 nm are assigned respectively to the $^4F_{9/2}\rightarrow{}^6H_{15/2}$, $^4F_{9/2}\rightarrow{}^6H_{13/2}$, $^4F_{9/2}\rightarrow{}^6H_{11/12}$ and $^4F_{9/2}\rightarrow{}^6H_{9/2}$ transitions of Dy^{3+}. The $^4F_{9/2}\rightarrow{}^6H_{13/2}$ transition is a forced electric dipole transition while the $^4F_{9/2}\rightarrow{}^6H_{15/2}$ is magnetic dipole transition. The forced electric dipole transition is supersensitive while the magnetic dipole transition hardly varies with the crystal field strength for the Dy^{3+} ions [18]. This explains why the yellow emission at 573 nm ($^4F_{9/2}\rightarrow{}^6H_{13/2}$) is more intense than the blue emission at 668 nm ($^4F_{9/2}\rightarrow{}^6H_{15/2}$). The small peak observed around 613 nm is ascribed to $^8G_{7/2}\rightarrow{}^6P_{5/2}$ electronic transition of Gd^{3+} [43]. The inset in Fig. 5.8 shows the PL spectra in 550 nm to 620 nm region. It can be seen from the inset that the 613 nm emission was not observed in the $LaYSiO_5:Dy^{3+}$ spectrum and this further confirms our assignment of this peak to Gd^{3+}. From the excitation and the emission spectra (see Fig. 5.7 and 5.8), it is clear that the peak intensities of $LaGdSiO_5:Dy^{3+}$ are ~2 times higher than those of

$GdYSiO_5:Dy^{3+}$ and ~3 higher than those of $LaYSiO_5:Dy^{3+}$ for the excitation and emission wavelengths of 241 and 573 nm respectively.

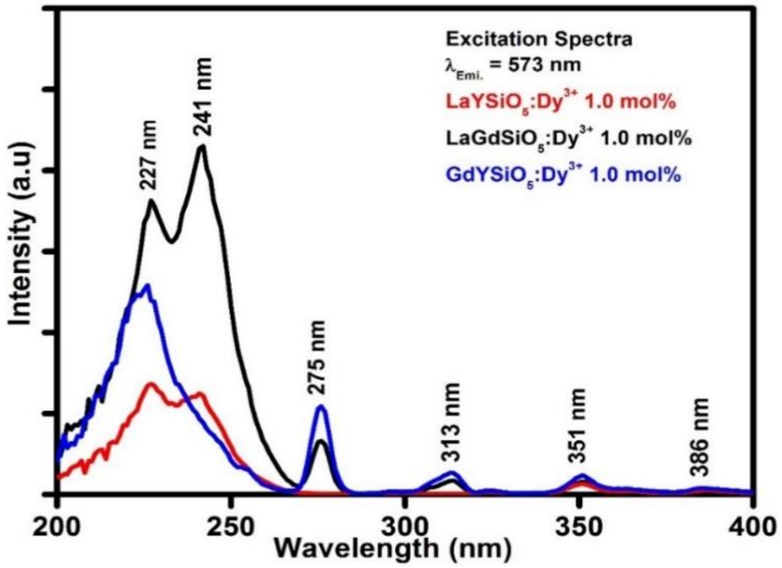

Fig. 5.7: Excitation spectra of $LaGdSiO_5:Dy^{3+}$, $LaYSiO_5:Dy^{3+}$ and $GdYSiO_5:Dy^{3+}$ monitored under 573 nm emission wavelength.

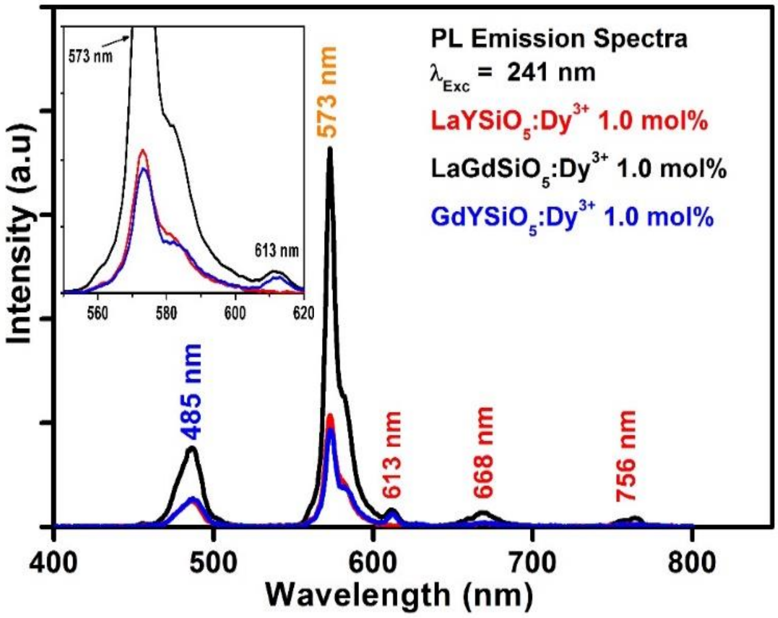

Fig. 5.8: Emission spectra of $LaGdSiO_5:Dy^{3+}$, $LaYSiO_5:Dy^{3+}$ and $GdYSiO_5:Dy^{3+}$ monitored under the excitation wavelength of 241 nm. The inset is the magnification showing the spectra region from 550 nm to 620 nm.

The PL emission spectra recorded when exciting the phosphors using the 325 nm He-Cd laser as the excitation source are shown in Fig. 5.9. In addition to the emission peaks similar to those shown in Fig. 5.8, a broad emission peak was observed in the blue region (400 to 460 nm). This peak is ascribed to self–trapped excitons (STE) in SiO_2 [44]. This peak was not observed when the samples were excited using the monochromatized xenon lamp (Fig. 5.8). This is probably due to the fact that different types and modes of excitations were used, among other things. The emission spectra in Fig. 5.8 were recorded when the samples were excited in phosphorescence mode, while those in Fig. 5.9 were recorded when exciting in fluorescence mode. Therefore, owing to its short lifetime (0.125-5.000 ns) [45], SiO_2 cannot be detected in phosphorescence mode. The photoluminescence emission peaks observed at 485, 573, 668, and 756 nm are respectively assigned to $^4F_{9/2}\rightarrow{}^6H_{15/2}$, $^4F_{9/2}\rightarrow{}^6H_{13/2}$, $^4F_{9/2}\rightarrow{}^6H_{11/12}$ and $^4F_{9/2}\rightarrow{}^6H_{9/2}$ f→f electronic transition of Dy^{3+} ions [18]. From the PL emission spectra in Fig. 5.9 the spectrum of $GdYSiO_5:Dy^{3+}$ appears to be more intense than those of $LaGdSiO_5:Dy^{3+}$ and $LaYSiO_5:Dy^{3+}$. This could be due to the absence of 4f electrons in La^{3+} and Y^{3+} and small ionic radius of Y^{3+} (as discussed in the XRD data). Since Y^{3+} have smaller ionic radius than Dy^{3+}, most of the Dy^{3+} ions will occupy the Gd^{3+} sites in $GdYSiO_5$ host. Similarly, most of the Dy^{3+} ions will prefer to occupy La^{3+} sites in $LaYSiO_5$. In $LaGdSiO_5$, most of the Dy^{3+} ions will occupy La^{3+} sites since La^{3+} have bigger ionic radius than Gd^{3+} (although the ionic radius of Gd^{3+} is bigger than that of Dy^{3+}). By and large, because of lack of 4f electrons in La^{3+} and Y^{3+}, they will not contribute to the excitation of Dy^{3+} in the near visible region. This causes the lower emission intensity of $LaYSiO_5:Dy^{3+}$. Because most of the Dy^{3+} ions will occupy La^{3+} sites in $LaGdSiO_5:Dy^{3+}$ and La^{3+} will not contribute to Dy^{3+} excitation, it (La^{3+} sites) will only create more distance between Dy^{3+} ions in $LaGdSiO_5$ matrix and hence decrease the emission intensity. Gd^{3+} is the favourite site of Dy^{3+} in $GdYSiO_5$ and Gd^{3+} have 4f electrons and hence will improve Dy^{3+} emission intensity.

Fig. 5.10 shows the optical reflectance spectra as a function of wavelength of $LaYSiO_5:Dy^{3+}$, $GdYSiO_5:Dy^{3+}$ and $LaGdSiO_5:Dy^{3+}$ phosphors. The absorption peaks observed at 275 nm and 313 nm are assigned to the f→f transitions of Gd^{3+} while the absorption observed at 351 nm is assigned to the f→f transition of Dy^{3+}. The 275 and 313 nm absorptions are , respectively, due to the $^8S_{7/2}\rightarrow{}^6J$ and $^6P_J\rightarrow{}^8S_{3/2}$ transitions of Gd^{3+} [33], while the 351 nm absorption is due to the $^6H_{15/2}\rightarrow{}^6P_{7/2}$ transition of Dy^{3+} [34].

The band gap was determined using Tauc plot. The Tauc plot is a well-known method for the calculation of the band gap of semiconducting and insulating materials. The absorption coefficient for interband transitions is related to the band gap by the expression:

$$(\alpha h v)^{1/n} = A(hv - E_g) \tag{5.3}$$

where α is the absorption coefficient, h is Planck's constant, v is the frequency of vibration, E_g the band gap, n denotes the nature of the sample transition and A is a constant independent of the chemical composition of the material [46].

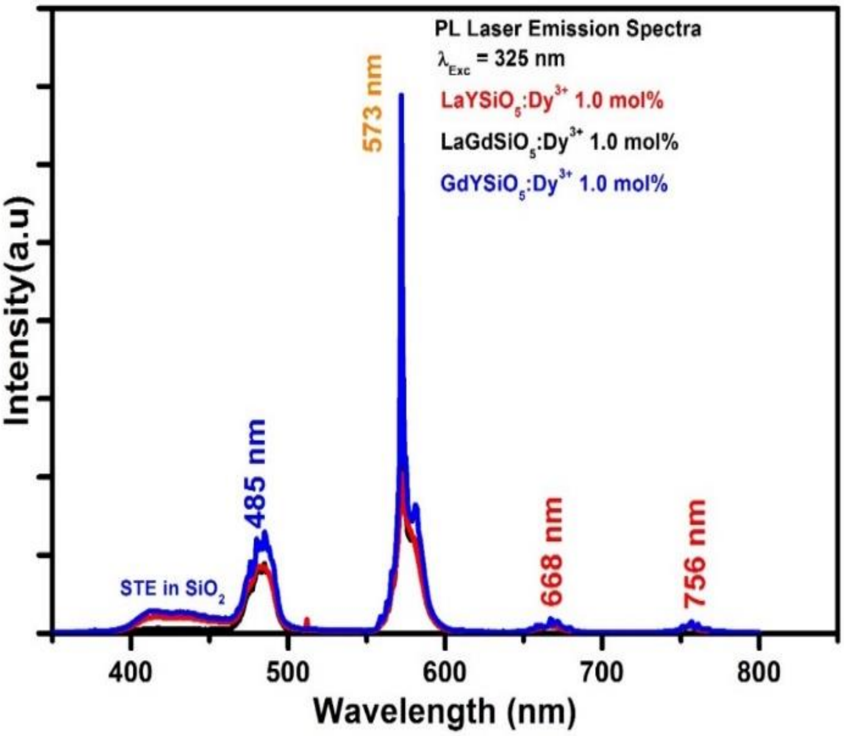

Fig. 5.9: Emission spectra of $LaGdSiO_5:Dy^{3+}$, $LaYSiO_5:Dy^{3+}$ and $GdYSiO_5:Dy^{3+}$ monitored under excitation wavelength of 325 nm.

Fig. 5.11 shows the $(hv) - [hvF(R_\infty)]^{1/2}$ curves of 1.0 mol% of Dy^{3+} doped $LaYSiO_5$, $GdYSiO_5$ and $LaGdSiO_5$ with estimated band gaps of 4.85 eV, 5.00 eV and 4.63 eV respectively. These values are less than the reported band gap values of Gd_2SiO_5 and Y_2SiO_5 (6.10 eV) [47, 48]. The observed decrease in the band gaps can be attributed to the strains (see Table 5.3) induced by incorporation of cations and Dy^{3+} dopant ions in the lattice [32].

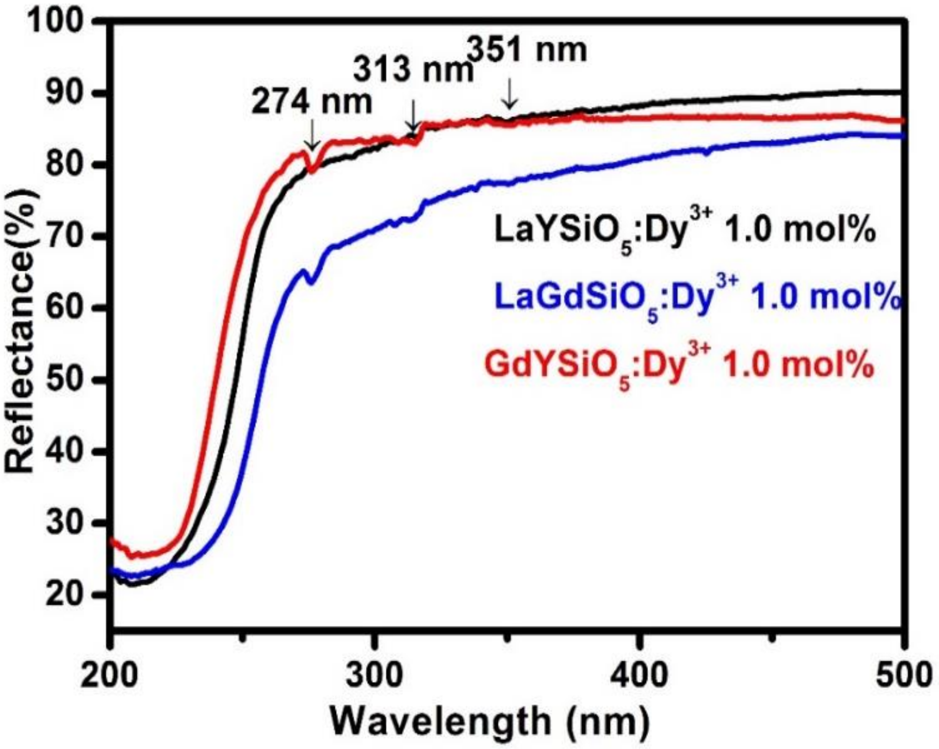

Fig. 5.10: The reflectance spectra of $LaYSiO_5:Dy^{3+}$, $GdYSiO_5:Dy^{3+}$ and $LaGdSiO_5:Dy^{3+}$.

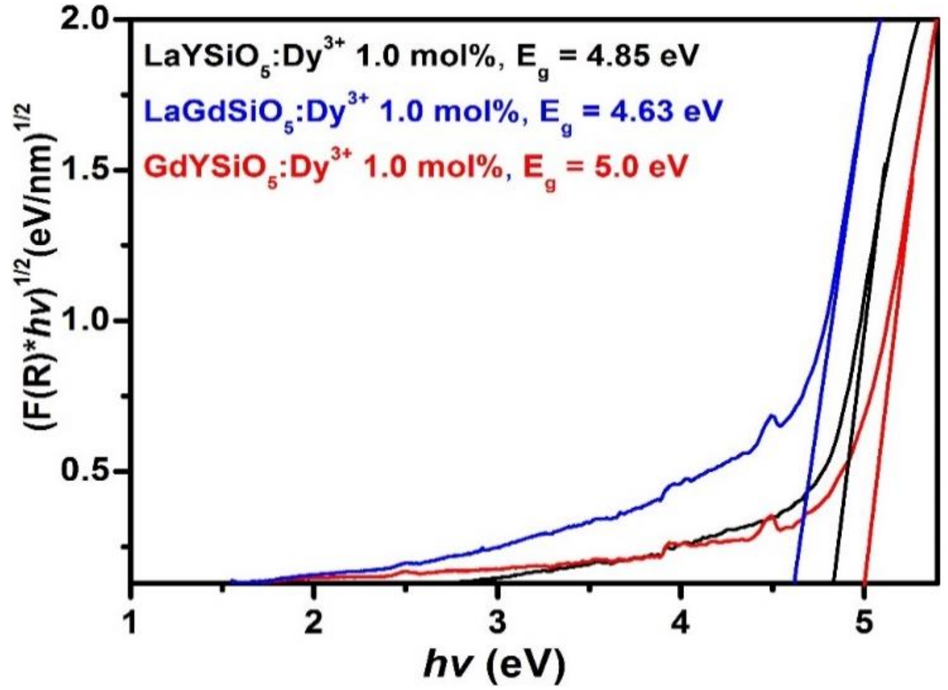

Fig. 5.11: $(F(R)*hv)^{1/2}$ versus hv curve of $LaYSiO_5:Dy^{3+}$ $LaGdSiO_5:Dy^{3+}$ and $GdYSiO_5:Dy^{3+}$.

5.4. Conclusion

Dy^{3+} doped mixed rare-earth oxyorthosilicates phosphors, namely $LaGdSiO_5:Dy^{3+}$ $LaYSiO_5:Dy^{3+}$, and $GdYSiO_5:Dy^{3+}$ were successfully prepared by urea-assisted combustion method. The structure, chemical composition, UV-visible absorption and photoluminescent properties of the phosphors were examined. Our materials exhibited slightly different bandgaps estimated from the absorption data and the differences were attributed to lattice strains most likely caused by the incorporation of Dy^{3+} ions. When excited with the monochromatized xenon lamp, the phosphors showed only line emission peaks associated with the f→f transitions of Dy^{3+}. The PL intensity from $LaGdSiO_5:Dy^{3+}$ was comparatively higher than that from $LaYSiO_5:Dy^{3+}$ and $GdYSiO_5:Dy^{3+}$ when the samples were excited in phosphorescence mode. But $GdYSiO_5:Dy^{3+}$ gave the highest intensity when the samples were excited in fluorescence mode. It is therefore safe to conclude that $LaGdSiO_5$ and $GdYSiO_5$ are better host of Dy^{3+}. When excited with the 325 nm He-Cd laser, however, our phosphors exhibited PL emission peaks consisting of a broad emission band at 400–460 nm associated with the self-trapped excitons in SiO_2 and line emissions associated with the f→f transitions of Dy^{3+}. This result indicates that the emission colour of our phosphors can be tuned depending on the type of excitation. Furthermore, it is reasonable to conclude that $LaGdSiO_5$ and $GdYSiO_5$ have emerged as better host for Dy^{3+} than $LaYSiO_5:Dy^{3+}$ because they provide more lattice sites for occupation by Dy^{3+} and hence improved PL intensity.

5.5. References

[1] D.W. Cooke, E.A. McKigney, R.E. Muenchausen, B.L. Bennett, Nanocomposite scintillators, detector, and method, 1 9, US Pat., (2008).

[2] K. Takagi, T. Fukazawa, Cerium-activated Gd_2SiO_5 single crystal scintillator, Appl. Phys. Lett., 42 (1983) 43−45.

[3] H. Ishibashi, K. Shimizu, K. Susa, Cerium doped GSO scintillators and its application to position sensitive detectors, IEEE Trans. Nucl. Sci., 36 (1989) 170−172.

[4] C. Li, C. Wyon, R. Moncorge, Spectroscopic properties and fluorescence dynamics of Er^{3+} and Yb^{3+} in Y_2SiO_5 IEEE J. Quant. Electron, 28 (1992) 1209−1221.

[5] T.E. Peters, Cathodoluminescent $Ln_y (SiO_2)_x$:Tb phosphors J. Electrochem. Soc., 116 (1969) 985−989.

[6] J. Wang, S. Tian, G. Li, F. Liao, X. Jing, Influence of Rare Earth Elements (Sc, La Gd, and Lu) to the Luminescence Properties of FED Blue Phosphor Y_2SiO_5:Ce, J. Electrochem. Soc., 148 (2001) h61−66.

[7] R. Y. Lee, F.L. Zhang, J. Penczek, B.K. Wagner, P.N. Yocom, C.J. Summers, Investigation of Ce-doped silicates for low voltage field emission diplay, J. Vac. Sci. Technol., 16 (1998) 855−857.

[8] C.M Michail, A. Toutountzis, I.G. Valais, I. Seferis, M. Georgousis, G. Fountos, I.S. Kandarakis, G.S. Panayiotakis, Luminescence Efficiency of Gd_2O_2S:Eu Powder Phosphors as X-ray to Light Converter, e-JST., 2 (2010) 5.

[9] T. Kamae Y. Fukazawa, N. Isobe, M. Kokubun, A. Kubota, S. Osone, T. Takahashi, N. Tsuchida, H. Ishibashi, Improvement on the light yield of a high-Z inorganic scintillator GSO:Ce Nucl. Instr. Meth. Phys. Res., A 490, (2002) 456−464.

[10] V. Avdeichikov, B. Jakobsson, V. A. Nikitin, V. Nomokonov, A. Wegner, Systematics in the light response of BGO, CsI(Tl) and GSO(Ce) scintillators to charged particles Nucl. Instr. Meth. Phy. Res., A 484 (2002) 251−258.

[11] W. Mangesha, T.D. Taulbee, J.D. Valentine, B.D. Rooney, $Gd_2SiO_5(Ce^{3+})$ and BaF_2 measured electron and photon responses Nucl. Instr. Meth. Phys. Res., A 486 (2002) 448−452.

[12] J. Felsche, Structure and Bonding, Springer, 13 (1973) 99.

[13] D. Meiss, W. Wischert, S. Kemmler-Sack, Luminescence of the system (Y, Gd, $Tb)_2 SiO_5:Eu^{3+}$, Phys. Status Solidi., A 133 (1992) 575−584.

[14] M. Yin, C. Duan, W. Zhang, L. Lou, S. Xia, J.C. Krupa, Site selectively excited luminescence and energy transfer of X_1-Y_2SiO_5:Eu at nanometric scale, J. Appl. Phys., 86, (1999) 3751−3757.

[15] E.M. Rabinovich, J. Shmulovich, V.J. Fratello, N.J. Kopylov, Sol-gel deposition of Tb^{3+}:Y_2SiO_5 cathodoluminescent layers, Am. Ceram. Soc. Bull., 66 (1987) 1505−1509.

[16] P. Babu, K.H. Jang, E.S. Kim, L. Shi, H.J. Seo, F. Rivera-Lopez,U.R. Rodriguez-Mendoza, V. Lavin, R. Vijaya, C.K. Jayasanka, L. Rama Moorthy, Spectral investigations on Dy^{3+}-doped transparent oxyfluoride glasses and nanocrystalline glass ceramics, J. Appl. Phys., 105, (2009) 013516.

[17] G. Dominiak-Dzik, P. Solarz, W. Ryba-Romanowski, E. Beregi, L. Kovács, Dysprosium-doped $YAl_3(BO_3)_4$(YAB) crystals: an investigation of radiative and non-radiative processes, J. Alloys Compd., 359 (2003) 51−58.

[18] G. Dominika-Dzik, P. Solarz, W. Ryba-Bomanowski, E. Beregi, E. Harmann, L. Kovacs, Optical properties and laser potential of dysprosium doped $YAl_3(BO_3)_4$(YAB) crystal, Radiat. Eff. Defect. S., 157 (2002) 1161−1165.

[19] R. Lisiecki, G. Dominiak-Dzik, P. Solarz, W. Ryba-Romanowski, M. Berkowski, M. Glowacki, Optical Spectra and Luminescence of the Dy-doped Gd_2SiO_5 Single Crystal, J. Appl. Phys., B 98 (2010) 337−346.

[20] L.G. Jacobsohn, S.C. Tornga, M.W. Blair, B.L. Bennett, R.E. Muenchausen, R. Wang, P.A. Crozier, D.W. Cooke, Synthesis, structure, and scintillation of Ce-doped gadolinium oxyorthosilicate nanoparticles prepared by solution combustion synthesis, J. Appl. Phys., 110 (2011) 083515.

[21] Y. Chen, B. Liu, C. Shi, M. Kirm, M. True, S. Vielhauer, G. Zimmerer, Luminescent properties of Gd_2SiO_5 powder doped with Eu^{3+} under VUV–UV excitation, J. Phys. Condens. Matter, 17 (2005) 1217−1224.

[22] J. Wang, S. Tian, G. Li, F. Liao, X. Jing, Influence of Rare Earth Elements Sc, La, Gd, and Lu to the Luminescent Properties of FED Blue Phosphor Y_2SiO_5:Ce, J. Electrochem. Soci., 2001, 148 (2001) h61−66.

[23] M. Yin, C. Duan, W. Zhang, L. Lou, S. Xia, J.C Krupa, Site selectively excited luminescence and energy transfer of X_1-Y_2SiO_5:Eu at nanometric scale, J. Appl. Phys., 86 (1999) 7.

[24] O. Sidletskiy, Scintillation crystals based on solid solutions of oxyorthosilicates, Func. Mat., 17 (2010) 4.

[25] W. Massa, Crystal structure determination, Springer-Verlag Berlin Heidelberg New York (2000) 25.

[26] R. D. Shannon, Revised effective ionic radii and systematic studies of interatomic distances in halides and chalcogenides, Acta. Cryst., 32 (1976) 751−769.

[27] J. Felsche, The crystal chemistry of the rare-earth silicates, Springer, 1st edn, (1973) 99−197.

[28] A. A. Bosak, C. Dubourdieu, J.P. Se´nateur, O. Yu. Gorbenko, A.R. Kaul, Hexagonal rare earth (R = Eu-Dy) magnites: XRD study of epitaxially stabilized films, Cry. Engi., 5 (2002) 355−364.

[29] R. D. Shannon, C. T. Prewitt, Effective ionic radii in oxides and fluorides, Acta. Cryst., B 25 (1969) 925.

[30] G. K. Williamson, W. H. Hall, X-ray line broadening from filed aluminium and wolfram, Acta. Metallurgica, 1 (1953) 22−31.

[31] V. D. Mote, Y. Purushotham, B.N. Dole, J. Theo., Williamson-Hall analysis in estimation of lattice strain in nanometer-sized ZnO particles, J. Appl. Phys., 6 (2012) 6.

[32] R. C. Aguielera, Z. Han, Y. Cai, L.C. Kimerling, Direct Band Gap Narrowing in Highly Doped Ge, J. Michel, Appl. Phys. Lett., 102 (2013) 152106.

[33] Y. Li, Chang, Y. Chang, Y. Lin, C Laing., Luminescence and Energy Transfer Properties of Gd^{3+} and Tb^{3+} in $LaAlGe_2O_7$, J. Phys. Chem., 111 (2007) 10682−10688.

[34] X. Liu, W. Xiang, F. Chen, Z. Hu, W. Zhang, Synthesis and photoluminescence characteristics of Dy^{3+} doped $NaY(WO_4)_2$ phosphors, Mater. Res. Bull., 48 (2013) 281−285.

[35] A.K. Gulnar, V. Sudarsan, R.K.Vasta, R.C. Hubli, U.K Gautam, A. Vinu, A.K. Tyagi, $CePO_4$:Ln (Tb^{3+} and Dy^{3+}) nano-leaves dispersible in methanol and water and having bright luminescence, Crystal Growth & Design 9 (2009) 2451-2456.

[36] I.N. Ogorodnikov, V.A. Pustovarov, S.I. Omelkov, D.O. Vostrov, L.I. Isaenko, Optical and Luminescence spectroscopy studies of electronic structure of $Li_6GdB_3O_9$ single crystals, Opt. Mat. 36 (2014) 1060-1064.

[37] K. N. Shinde, S.J. Dohoble, H.C. Swart, K. Park, Phosphate phosphors for solid-state lighting, Springer Ser. Mat. Sci., 174 (2013) 54.

[38] K. A. Gschneidner, R. M. Valletta., Concerning the crystal structure sequence in the lanthanide metals and alloys; evidence for 4f contribution to the bonding, Acta Met., 16 (1968) 477−484.

[39] Y.V. Zorenko, Luminescence of Sc^{3+} and La^{3+} isoelectronic impurities in $Lu_3Al_5O_{12}$ single-crystal films, Optics and spectroscopy, 100 (2006) 572-580.

[40] Y. Zorenko, V. Gorbenco, V. Savchyn, T. Voznyack, M. Nikl, J.A. Mares, A. Winnacker, Novel UV-emitting single crystalline film phosphors grown by LPE method, Radiation measurements 45 (2010) 444-448.

[41] G. Li, C. Li, C. Zhang, Z. Cheng, Z. Quan, C. Peng and J. Lin, Tm_{3+} and/or Dy^{3+} doped LaOCl nanocrystalline phosphors for field emission displays, J. Mater. Chem., 19 (2009) 8936-8943.

[42] M. Jia, J. Zhang, S. Lu, J. Sun, Y. Luo, X. Ren, H. Song, X. Wang, UV. Excitation properties of Eu^{3+} at the S6 site in bulk and nanocrystalline cubic Y_2O_3, Chem. Phy. Lett. 384 (2004) 193-196.

[43] C. R. Ronda, ed., Luminescence: From theory to application, Wiley-VCH Verlag GmbH and Co. KGaA, Weinheim, (2008) 93.

[44] C. Itoh, K. Tanimura, N. Itoh, Optical studies of self-trapped excitons in SiO_2, J. Phys. C. Solid State Phys., 21 (1988) 4693.

[45] A. Uedono, L. Wei, S. Tanigawa, R. Suzuki, H. Ohgaki, Characterization of silicon dioxide deposited by low-temperature CVD using TEOS and ozone by monoenergetic position beams, Hyperfine Interactions, 84 (1994) 231−236.

[46] J. Tauc, ed., The optical properties of solids, Academic Press, New York, (1966).

[47] K. Mori, M. Nakayama, H. Nishimura, Role of the core excitons formed by 4f−4f transitions of Gd^{3+} on Ce^{3+} scintillation in Gd_2SiO_5:Ce^{3+}, Phys. Rev., B 67 (2003) 165206.

[48] H. Pang, G. Zhao, M. Jie, J. Xu, X. He, Study on the growth, etch morphology and spectra of Y_2SiO_5 crystal, Material Lett., 59 (2005) 3539−3542.

CHAPTER SIX

Structure, scanning electron microscopy, and spectroscopy of $La_{2-x}Gd_xSiO_5:Dy^{3+}$ nanophosphors

6.1. Introduction

Rare-earth oxyorthosilicate (R_2SiO_5) are created from binary rare-earth silicate (R_2O_3-SiO_2) system with 1:1 composition. Based on the size of the radius of the rare-earth ion, they can be classified into two groups of monoclinic structures, namely small and large ionic radius rare-earth ions. Both lanthanum oxyorthosilicate (La_2SiO_5) and gadolinium oxyorthosilicate (Gd_2SiO_5) belong to the small ionic radius rare-earth ions in rare-earth oxyorthosilicates crystals. They fall into the monoclinic crystallographic point group with space group *P21/c* and *I2/a* corresponding to low temperature phase ($X1$) and the high temperature phase ($X2$) respectively [1]. Both La_2SiO_5 and Gd_2SiO_5 have two non-equivalent crystallographic sites coordinated by 7 and 9 oxygen atoms. These crystals have demonstrated excellent properties like wide band gap, fast decay time, high quantum efficiency, high density and minimal self-absorption and they also possess a great ability to accommodate rare-earth ions [2]. They have been used as host to prepare light emitting materials or phosphors for different applications [3-9]. In rare earth oxyorthosilicates ($Re_2O_3.SiO_2$), SiO_2 can give broad blue emission from self-trapped excitons (STE) [10, 11]. Mixing of La_2SiO_5 and Gd_2SiO_5 can leverage the best properties of these materials. For instance, varying the molar ratio of La to Gd in $La_{2-x}Gd_xSiO_5$ matrix has the potential to tune the band gap of the material and hence influence its optical properties. Several works have been reported on mixed compound rare-earth oxyorthosilicates but mostly for scintillation and laser applications [12-17].

Dy^{3+}-doped matrices have shown a promising application as a white light emitting phosphors because of the occurrence of two intense photoluminescence due to simultaneous emission of bluish-green (at ~485 nm) and yellowish (at ~575 nm) colours. The blue-green and the yellowish emissions are respectively due to $^4F_{9/2} \rightarrow {}^6H_{15/2}$ and $^4F_{9/2} \rightarrow {}^6H_{13/2}$ f-f electronic transition of Dy^{3+}. Defined as hypersensitive, the yellow emission which is electric dipole transition is highly sensitive to the crystal field around Dy^{3+} ions. On the other hand, the bluish emission is a magnetic dipole transition and hardly varies with the crystal field around Dy^{3+} ions [18].

In the present study, by varying the molar ratio of La to Gd in $La_{2-x}Gd_xSiO_5:Dy^{3+}$ (x = 0, 0.5, 1.0, 1.5 and 2) phosphors, we were able to tune the colour of the emitted light from blue to yellow and white when the phosphors where excited using 325 nm He-Cd laser as excitation source. These results suggest that our materials can be used as single host phosphors for UV-pumped multicolour and white light emitting diodes.

6.2. Experimental

Preparation

Urea ($CO(NH_4)_2$) and ammonium nitrate (NH_4NO_3) assisted solution combustion method was used to prepare $La_{2-x}Gd_xSiO_5:Dy^{3+}$ 1.0 mol% (x = 0, 0.5, 1.0, 1.5 and 2.0) nanophosphors. The precursors used were lanthanum nitrate hexahydrate ($La(NO_3)_36H_2O$), gadolinium nitrate hexahydrate ($Gd(NO_3)_36H_2O$), dysprosium nitrate hexahydrate ($Dy(NO_3)_36H_2O$) and silicic acid (SiO_2H_2O). The quantity of SiO_2H_2O, $CO(NH_4)_2$, NH_4NO_3 and $Dy(NO_3)_36H_2O$ were fixed at 0.1 g, 0.4691 g 0.6251 g and 0.0109 g respectively in all the samples, while the quantity of $La(NO_3)_36H_2O$ and $Gd(NO_3)_36H_2O$ were varied. For x = 0 (i.e. $La_2SiO_5:Dy^{3+}$), the quantity of $La(NO_3)_36H_2O$ was 1.3392 g. For x = 0.5, 1.0 and 1.5. The quantities of $La(NO_3)_36H_2O$ and $Gd(NO_3)_36H_2O$ were respectively 1.0078 g and 0.3455 g, 0.6696 g and 0.698 g, and 0.3314 g and 1.0505 g. For x = 2.0 (i.e. $Gd_2SiO_5:Dy^{3+}$), the quantity of $Gd(NO_3)_36H_2O$ was 1.3959 g. These quantities were added in five different glass beakers and each was dissolved in 2.0 ml of distilled water. The solutions were stirred with magnetic stirrer on a hot plate set at 100 ℃ for about 15 min to obtain homogenous solutions. Each solution was transferred into separate ceramic crucible boat and then into a muffle furnace pre-heated to 600 ± 10℃, one at a time. After about 2 min oxidation took place (producing flame which lasted for ~ 60 s) which was accompanied by release of large smoke from the furnace. It took about 5 min for the combustion process to complete, resulting to foam-like crispy end products. The products were allowed to cool to room temperature and were gently ground into fine powders using agate mortar and pestle and the powders were then transferred into sample holders for characterization.

Characterization

The structure and molecular vibration of the samples were analyzed using: Bruker D8 advanced X-ray diffractometer and Nicolet 6700 Fourier transform infrared (FT-IR) spectrometer respectively. The morphology study and the elemental analysis were carried out using Jeol JSM-7800F field emission scanning electron microscope (FE-SEM) fitted with Oxford Aztec 350 X-Max80 energy-dispersive X-ray spectroscopy (EDS). The electronic and chemical states were investigated using PHI 5000 Versaprobe-scanning ESCA microprobe X-ray photoelectron spectroscopy (XPS). The photoluminescence (PL) spectra were measured in the phosphorescence and fluorescence modes, respectively, using Cary Eclipse fluorescence spectrophotometer and a PL system consisting of a 325 nm He-Cd gas laser as an excitation source, a spectrometer, a photomultiplier tube (PMT) detector and a lock-in amplifier, while the ultraviolet visible (UV-Vis) measurements were taken using Lambda 950 UV-Vis spectrometer.

6.3. Results and Discussion

Fig. 6.1 shows the XRD spectra of $La_{2-x}Gd_xSiO_5$:Dy^{3+} (x = 0, 0.5, 1.0, 1.5 and 2.0) nanoparticulate phosphors. The spectra match with the standard monoclinic phases of La_2SiO_5 and Gd_2SiO_5 referenced in the standard JCDPS file no: 40-0234 and 74-1795 respectively. For x = 0 only a pure phase of La_2SiO_5 was observed, while the pure phase of Gd_2SiO_5 was observed when x = 2. For any other value of x (i.e. x = 0.5, 1.0 and 1.5) the XRD patterns consist of diffraction peaks from La_2SiO_5 and Gd_2SiO_5 implying that admixtures of the two phases were crystallized. There is a noticeable shift in the peak position when the molar ratio of La to Gd was varied. For example, (102) and (033) peaks shifted to the right as amount of La decreases while the (132) peak shifted to the left. The shifting could be attributed to substitution induced lattice strains. Observe that none of the peaks in La_2SiO_5 lie in the same plane with the Gd_2SiO_5 peaks, although few of the peaks have the same 2θ values. For instance, ($\bar{1}12$) and (012) peaks from La_2SiO_5 respectively have the same 2θ values with (021) and ($\bar{4}21$) peaks from Gd_2SiO_5. These results indicate that we either crystallized pure La_2SiO_5/Gd_2SiO_5 or an admixture of both La_2SiO_5 and Gd_2SiO_5.The average crystallite size (L) and the lattice strain (ε) of our nanophosphors were calculated using the Williamson-Hall equation [19, 20] given in eq. 6.1 and the results are shown in table 6.1.

$$\beta_{hkl}\mathrm{Cos}\theta = 4\varepsilon\ \mathrm{Sin}\theta + \frac{K\lambda}{L} \tag{6.1}$$

where λ is the X-ray wavelength in nanometer (nm), β_{hkl} is the peak width of the diffraction peaks profile at half maximum height, θ is the Bragg angle and K is a constant related to the crystallite shape, usually taken as 0.9 or 0.89 for full width half maximum (FWHM) of spherical crystals with cubic unit cells.

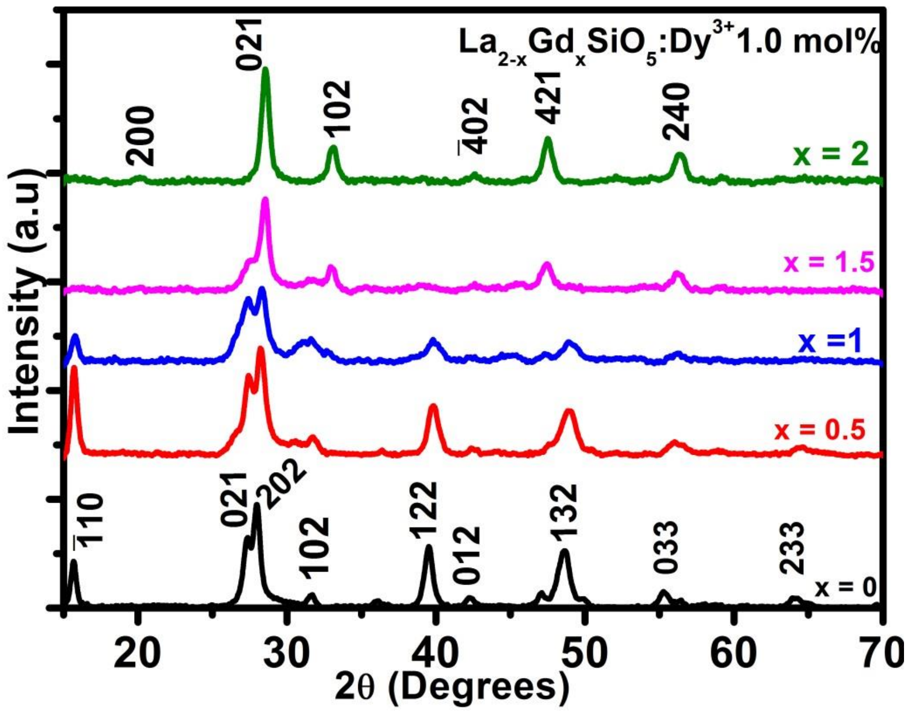

Fig. 6.1: XRD pattern of $La_{2-x}Gd_xSiO_5:Dy^{3+}$ (x = 0, 0.5, 1.0, 1.5 and 2.0) nanophosphors.

Table 6.1: The crystallite sizes and the lattice strains of $La_{2-x}Gd_xSiO_5:Dy^{3+}$ nanophosphors.

$La_{2-x}Gd_xSiO_5:Dy^{3+}$	Crystallite size (*L*) (nm)	Strain (ε) (× 10^{-2})
x = 0	19.0	7.20
x = 0.5	21.0	6.40
x = 1.0	13.0	10.60
x = 1.5	10.0	10.29
x = 2.0	15.0	8.90

The FE-SEM images of $La_2SiO_5:Dy^{3+}$ (x = 0), $Gd_2SiO_5:Dy^{3+}$ (x = 2) and $LaGdSO_5:Dy^{3+}$ (x =1) nanophosphors are shown in Fig. 6.2 (a-f) respectively. Fig. 6.2 (a), (c) and (e) show the low magnification images while Fig. 6.2 (b), (d) and (f) show the corresponding high magnification images respectively. The image of $La_2SiO_5:Dy^{3+}$ (Fig. 6.2 (a)) shows agglomerated nanoparticles with no definite shapes while that of $Gd_2SiO_5:Dy^{3+}$ (Fig. 6.2 (c)) shows agglomerated plate-like nanostructure lying in different orientations with pores on the surfaces. The image of the mixture of the two compounds, $LaGdSiO_5:Dy^{3+}$ (Fig. 6.2 (e)), shows large and small plate-like structures.

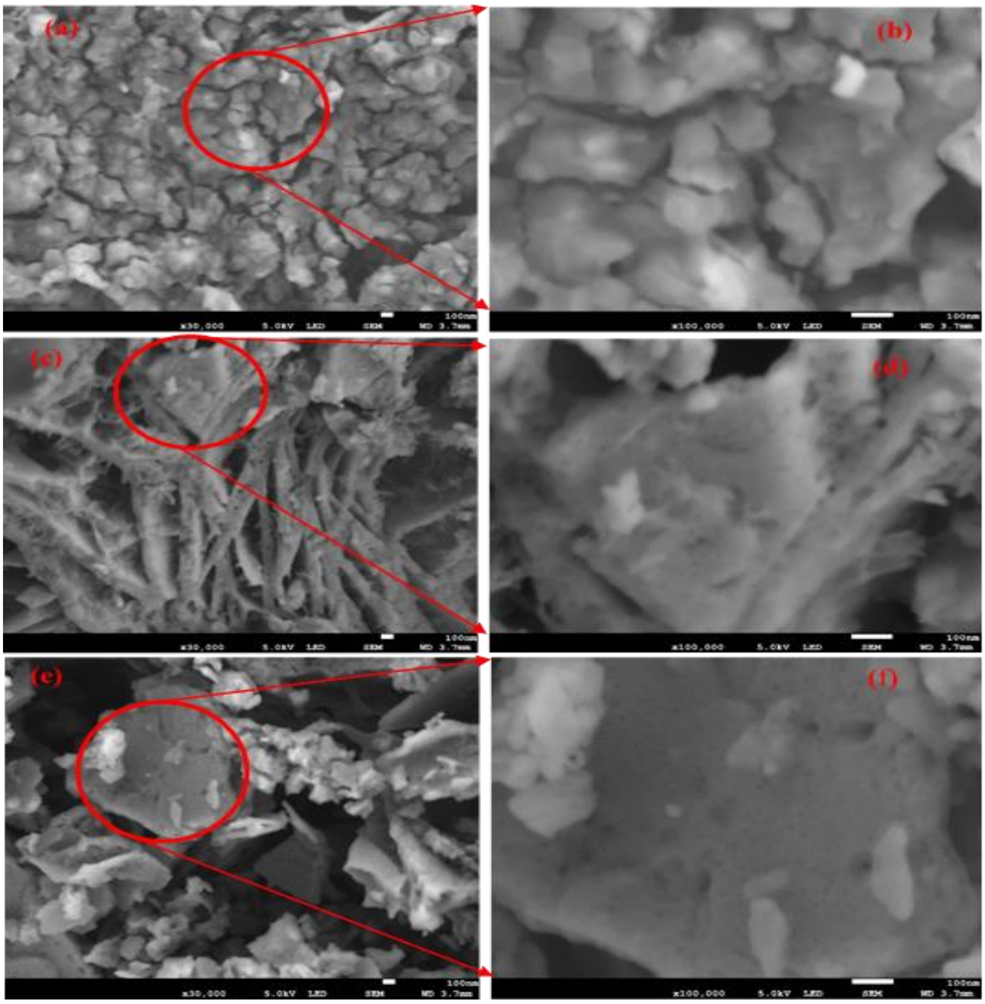

Fig. 6.2: FE-SEM images of (a) low and (b) high magnification of $La_2SiO_5:Dy^{3+}$ (x =0), (c) low and (d) high magnification of $Gd_2SiO_5:Dy^{3+}$ (x = 2) and (e) low and (f) high magnification of $LaGdSiO_5:Dy^{3+}$ (x =1).

The EDS was used to investigate the elemental composition of $La_{2-x}Gd_xSiO_5:Dy^{3+}$ (x = 0, 2 and 1) nanophosphors and the results are shown in Fig. 6.3 (a-c) respectively. Carbon (C) was probably from the atmospheric hydrocarbons and the carbon tape on which the samples were mounted. La, Gd, Dy, Si and O were observed in the samples as expected. Low count of Dy in the spectra is due to its low concentration in the samples. The insets are the elemental maps corresponding to each sample. It can be seen from the maps that all the elements were evenly distributed on the sample surfaces.

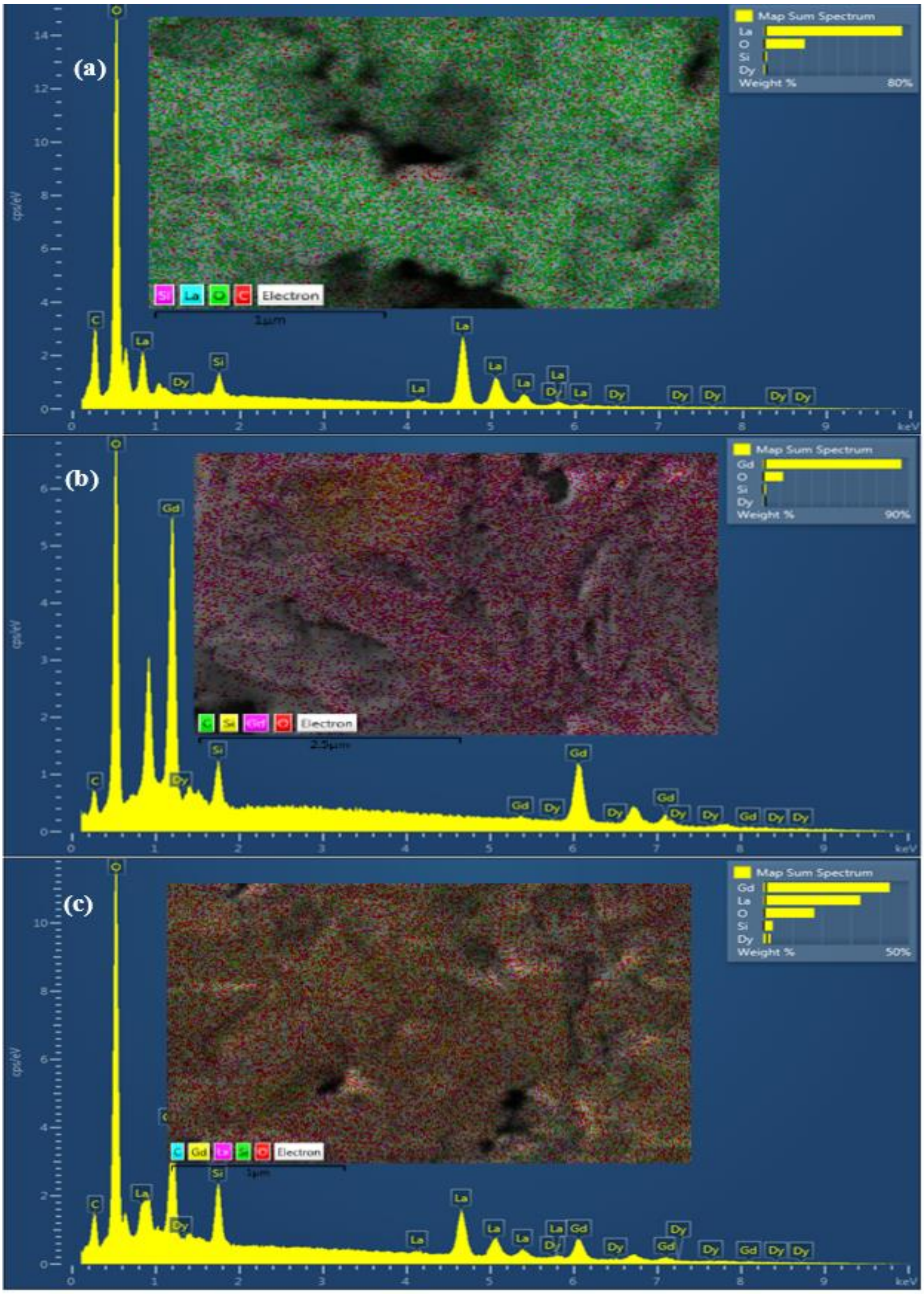

Fig. 6.3: EDS spectra of $La_{2-x}Gd_xSiO_5:Dy^{3+}$, (a) x = 0, (b) x = 2 and (c) x = 1. The insets are the elemental maps of the corresponding samples.

Fig. 6.4 shows the FTIR spectra measured from samples with the values of x = 0 and 2. Three spectral ranges were considered in the measurements: (i) 3000-3650 cm^{-1} region where the OH groups and the stretching vibration of water were observed, (ii) 1350-1700 cm^{-1}, where bending mode of water was observed and (iii) 400-1100 cm^{-1} where Si-O-Si, La-O and Gd-O vibrations occurred. It is apparent from the spectra that no shift was observed in the peak positions of the two samples. The absorption peak around 506 cm^{-1} is assigned to La-OH and Gd-OH bending modes in La(OH)$_3$ and Gd(OH)$_3$ [21-24]. The three peaks observed at 665, 880 and 1100 cm^{-1} are assigned to the characteristics stretching modes of Si-O-Si group, while the one at 3605 cm^{-1} is associated with the stretching mode of the OH group [25, 26]. The bands at 1380, 1500 and 1655 cm^{-1} are associated with the bending modes of water while those at 3120 and 3430 cm^{-1} are associated with the stretching modes of water [22, 27, 28]. The peak observed at the center of the spectra around 2350 cm^{-1} is assigned to stretching vibration of CO$_2$ [29, 30].

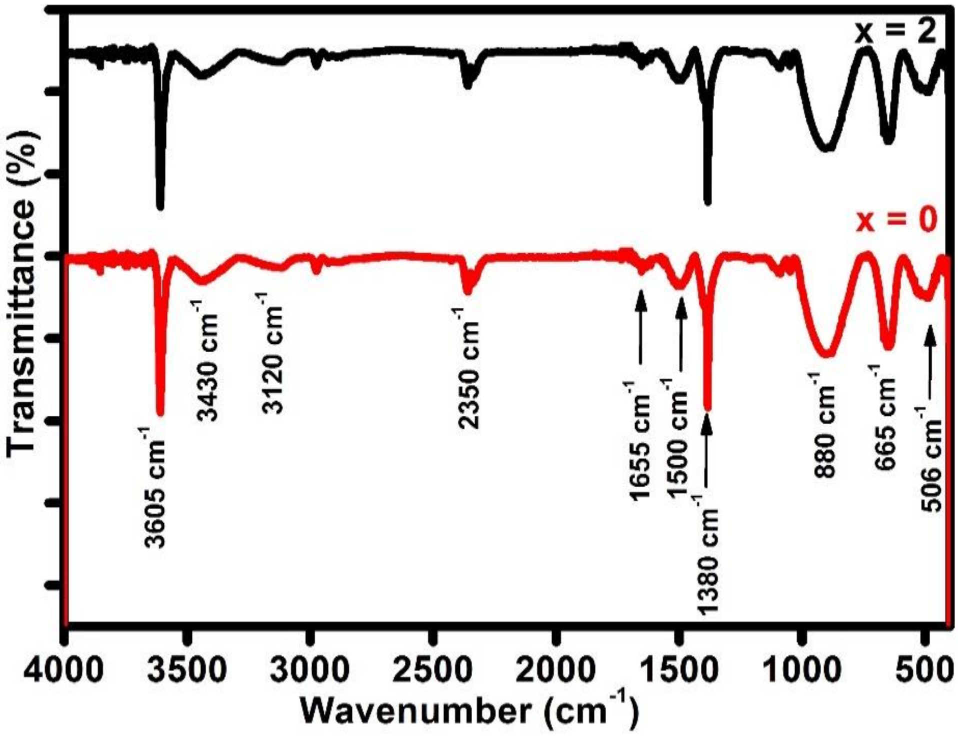

Fig. 6.4: FTIR spectra of La$_{2-x}$Gd$_x$SiO$_5$:Dy^{3+} (x = 0 and 2) nanophosphors.

The electronic and chemical states of La$_2$SiO$_5$:Dy^{3+} (x =0), Gd$_2$SiO$_5$:Dy^{3+} (x = 2) and LaGdSiO$_5$:Dy^{3+} (x = 1) were analyzed using the XPS technique. Fig. 6.5 (a) shows the O 1s spectrum of La$_2$SiO$_5$:Dy^{3+}. The fitted spectrum exhibits three peaks which are ascribed to La$_2$O$_3$ (530.10 eV), La$_2$SiO$_5$ (530.75 eV) and SiO$_2$ (531.61 eV) [31-35]. Similarly, the fitted

O 1s spectrum of Gd_2SiO:Dy^{3+} shown in Fig. 6.5 (b) exhibits three peaks ascribed to Gd_2O_3 (528.14 eV), Gd_2SiO_5 (530.46 eV) and SiO_2 (532.16 eV) [35-37]. In the O 1s spectrum of $LaGdSiO_5$:Dy^{3+} shown in Fig. 6.5 (c), the $LaGdO_3$ peak consists of the La_2O_3 and Gd_2SiO_3 peaks resulting in the shift of the binding energy to 529.02 eV which lies between the other two peaks. The other peaks are ascribed to $LaGdSiO_5$ (530.62 eV) and two SiO_2 peaks at 531.60 and 532.58 eV. The $LaGdSiO_5$ peak consists of the La_2SiO_5 and the Gd_2SiO_5 peaks resulting in the shift of the binding energy. Fig. 6.5 (d) shows the fitted XPS spectrum of Si 2p peak of La_2SiO_5:Dy^{3+}. The Si 2p peak position for Si, SiO_x ($x < 2$), La_2SiO_5, SiO_2 and SiO_4 were measured at 99.89 eV, 100.88 eV, 102.10 eV, 103.30 eV and 104.65 eV respectively. Fig. 6.5 (e) shows the fitted XPS spectrum of Si 2p peak of Gd_2SiO_5:Dy^{3+}. Five peaks observed are Si, SiO_x ($x < 2$), Gd_2SiO_5, SiO_2 and SiO_4 were observed at 99.82, 100.71, 102.20 eV 103.17 eV and 104.38 eV respectively [35, 38, 39]. Fig. 6.5 (f) shows the spectrum of Si 2p peak of $LaGdSiO_5$:Dy^{3+}. Five peaks assigned to Si, SiO_x ($x < 2$), $LaGdSiO_5$, SiO_2 and SiO_4 were observed at 99.86 eV, 100.80 eV, 102.06 eV, 103.24 eV and 104.16 eV respectively. The $LaGdSiO_5$ peak consists of the La_2SiO_5 and the Gd_2SiO_5 peaks which led to the shift in the binding energy.

The 3d core-levels XPS spectra of all rare earth compounds consist of double-peak structures of 3d $_{5/2}$ and $3d_{3/2}$ which are as a result of spin-orbit splitting and their plasmon satellites [40]. The major XPS peaks (which are due to the photoexcitation of core-level electron) are due to electrons which travel through the solid without energy loss. The plasmon satellite peaks can be either intrinsic or extrinsic. Satellites are extrinsic when they occur as a result of interaction of photoelectron with other electrons when they are coming from the inner shell to the surface of a solid. Intrinsic satellites occur from de-excitation of photohole neutralized by an electron that moved into the site of the photoemission process and lead to change in the energy of the state from which the photoemission occurred [41]. Fig. 6.6 (a) show the fitted XPS spectrum of La 3d core level peaks. The peak split into $3d_{5/2}$ ($J = 5/2$) and $3d_{3/2}$ ($J = 3/2$) components with a spin-orbit splitting of 16.8 eV. Each state can under photoionization split into two final states I ($3d^1 4f^0$) (a core hole) and II ($3d^1 4f^1$) (a core hole with the transfer of an electron from the O_{2p} valence band to an empty 4f orbital). The final state I is assigned to the La-O bond in La_2O_3 and is observed at 835.92 and 852.30 eV in the $3d_{5/2}$ and $3d_{3/2}$ states respectively. The final state II is assigned to the La-OH bond in $La(OH)_3$. In the final states II, electron-hole exchange further create a $J = 1$ term (a strong signal) and a $J \neq 1$ terms (a cluster of weak signals) in each spin-orbit with the J ≠ 1 terms having lower binding energy than the J = 1 term.

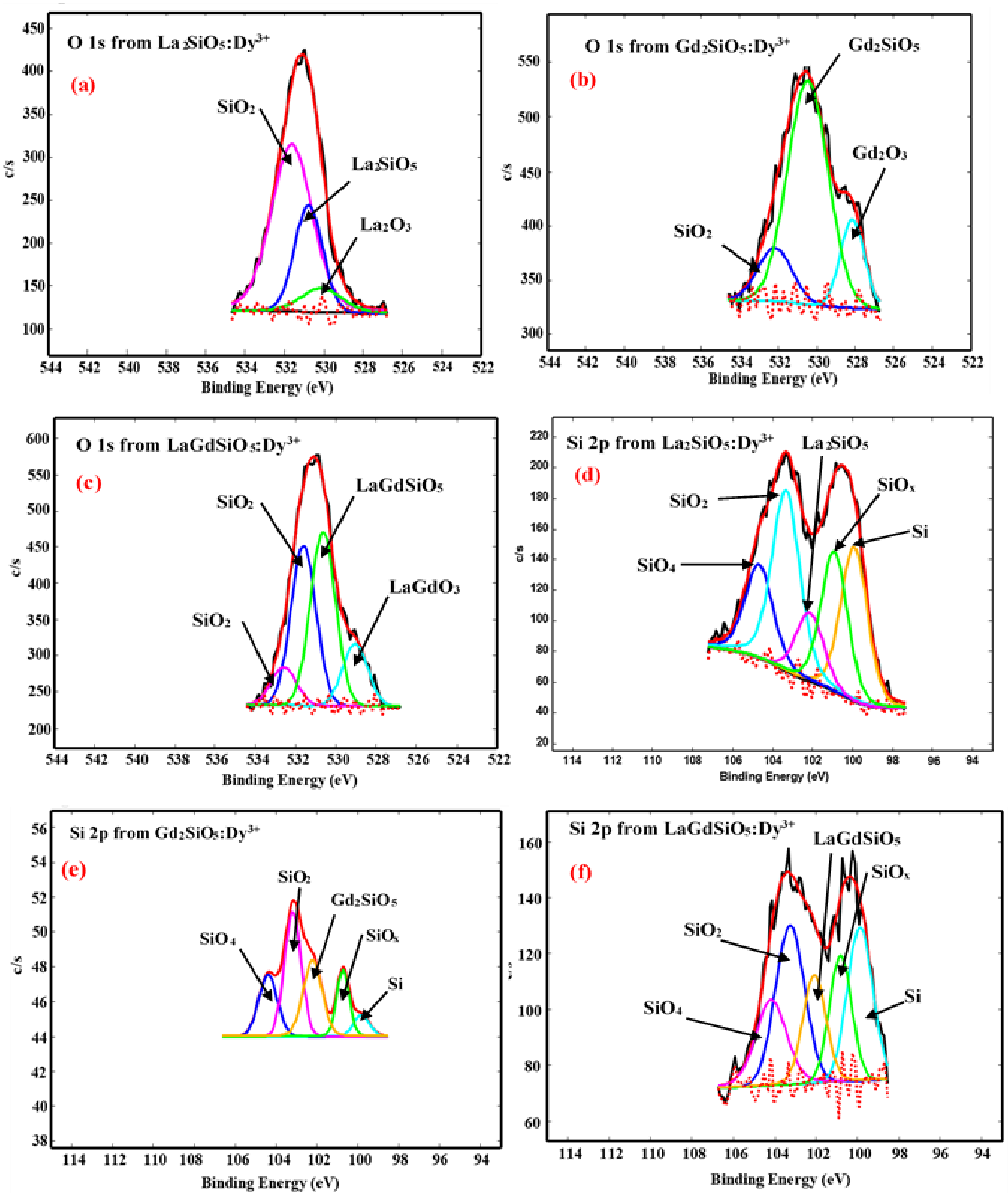

Fig. 6.5: XPS spectra of (a) O 1s peak from $La_2SiO_5:Dy^{3+}$, (b) O 1s peak from $Gd_2SiO_5:Dy^{3+}$, (c) O 1s peak from $LaGdSiO_5:Dy^{3+}$, (d) Si 2p peak from $La_2SiO_5:Dy^{3+}$, (e) Si 2p peak from $Gd_2SiO_5:Dy^{3+}$ and Si 2p peak from $LaGdSiO_5:Dy^{3+}$ nanophosphors.

The J = 1 terms lines are observed at 839.74 and 856.51 eV respectively in the $3d_{5/2}$ and $3d_{3/2}$ states whereas the J ≠ 1 terms lines are observed at 837.94 and 854.93 eV for the $3d_{5/2}$ and $3d_{3/2}$ states respectively [42-44]. The two broad peaks at 848.20 and 863. 88 eV corresponds to the La $3d_{3/2}$ plasmon satellite components [31, 42, 44, 45]. Fig. 6.6 (b) shows the fitted XPS spectrum of Gd 3d core level peaks. The spin-orbit splitting of the $3d_{5/2}$ and $3d_{3/2}$ is 32.0 eV. In the $3d_{5/3}$ state of Gd 3d core levels, two peaks were observed at 1186.84 eV and 1184.51eV. These peaks correspond to elemental Gd and its plasmon satellite peak respectively. Similarly, in the $3d_{3/2}$ state, the two peaks observed at 1219.21 eV and 1216.35 eV corresponds respectively to Gd-O bond in Gd_2O_3 and its satellite peak [46-48]. The small broad peak at 1198.28 eV is also due to the plasmon satellite component of the Gd $3d_{3/2}$ state. The peak observed at 1195.41 eV corresponds to the $4f^7 \rightarrow 3d^9 4f^7$ electronic configuration which is normally observed in trivalent Gd compounds and it is due to the $3d4f^7$ final state multiplet structure [49]. Fig. 6.6 (c) shows the fitted XPS spectrum of Dy 4d core level peaks. The 4d levels of lanthanides often show additional structure (a phenomenon known as multiplet splitting) due to the electrostatic interaction between a core level and the partially filled 4f levels [40]. In Dy 4d core level, the multiplet splitting arises due to the interaction of the 4d and 4f state since these two shells have the same principle quantum number [50, 51]. The peaks observed at 152.30 eV and 154.17 eV in Fig. 6.6 (c) are due to Dy in Dy_2O_3 and the multiplet splitting respectively. The broad band centered at 166.16 eV is attributed to the Dy-O bond in Dy_2O_3 which arises due to final states with 4d and 4f spins parallel and anti-parallel respectively [52]. The backgrounds observed in Fig. 6.5 (d) and (e) and Fig. 6.6 (b) is known as intrinsic background noise (IBN) and it is caused by inelastic scattered electrons [53]. It increases with the binding energy because it includes all the inelastically scattered electrons from the beginning to the end of the analysis.

The optical reflectance spectra and the band gap of $La_{2-x}Gd_xSiO_5:Dy^{3+}$ are shown in Fig. 6.7 (a) and (b) respectively. In Fig 6.7 (a) the absorption peaks at 275 and 313 nm are assigned to $^8S_{7/2} \rightarrow {}^6I_J$ and $^6P_J \rightarrow {}^8S_{7/2}$ electronic transitions of Gd^{3+} [54] while the one at 351 nm is assigned to $^6H_{15/2} \rightarrow {}^6P_{7/2}$ transitions of Dy^{3+} [55]. The values of the interband transitions vary with the molar ratio of La to Gd in the $La_{2-x}Gd_xSiO_5:Dy^{3+}$ matrix, increasing from 207 nm for

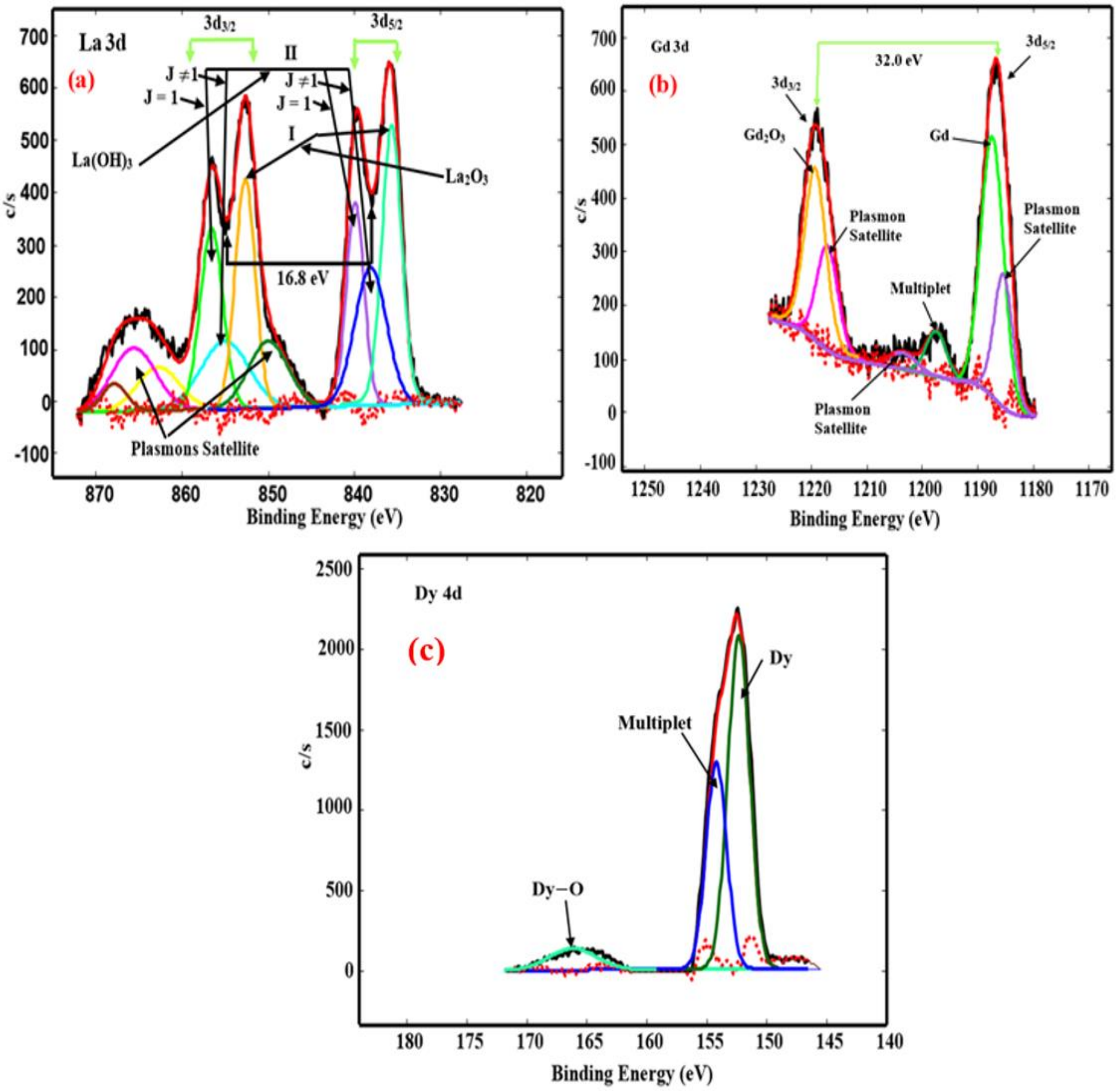

Fig. 6.6: XPS spectra of (a) La 3d peak, (b) Gd 3d peak and (c) Dy 4d peak.

x = 0, to 231 nm for x = 2. These changes can be explained by taking a close look at the estimated band gap values presented in Fig. 6.7 (b). It can be seen that the band gap can be tuned by varying the molar ratio of La to Gd. The band gaps were calculated with Tauc plot [56] and the values obtained are shown in table 6.2. The change in the band gap is attributed to lattice mismatch in the $La_{2-x}Gd_xSiO_5:Dy^{3+}$ matrix probably due to the difference in the lattice parameters of La_2SiO_5 and Gd_2SiO_5 [57].

Fig. 6.8 (a) and (b) shows the PL excitation and emission spectra of $La_{2-x}Gd_xSiO_5:Dy^{3+}$ nanophosphors recorded when the monochromatized xenon lamp was used as the excitation source. The excitation spectra were monitored at the emission wavelength of 573 nm.

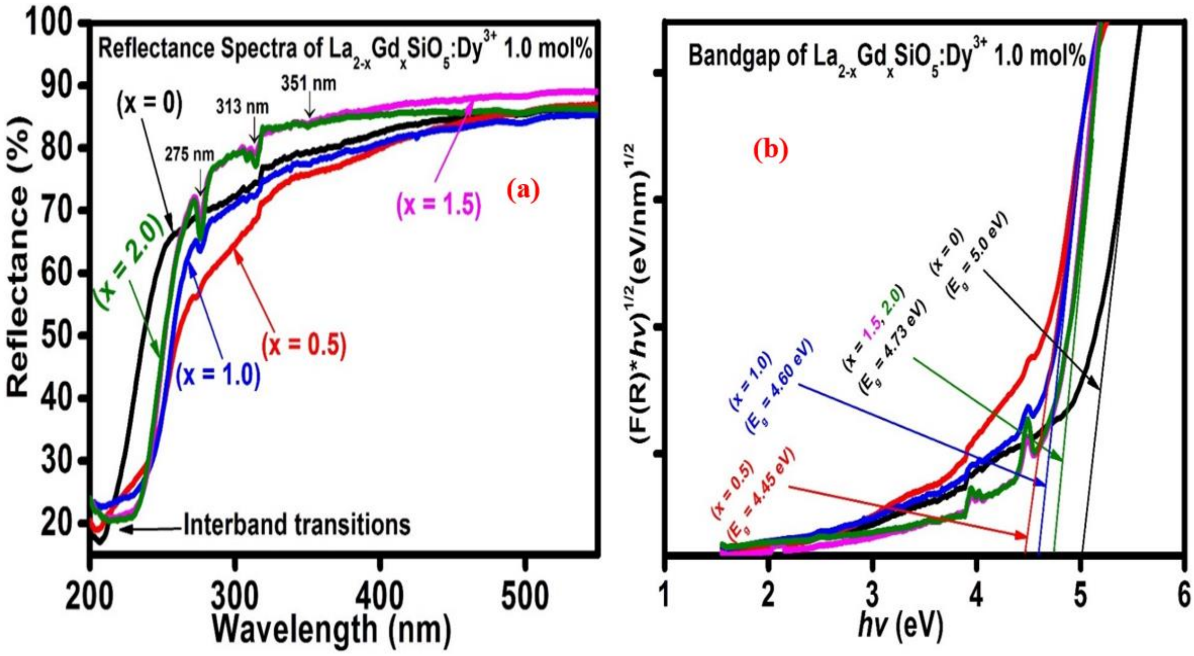

Fig. 6.7: Reflectance spectra (a) and band gap (b) of $La_{2-x}Gd_xSiO_5:Dy^{3+}$ (x = 0, 0.5, 1.0, 1.5 and 2.0).

The excitation spectrum consists of peaks in the range of 200 to 400 nm. The broad bands in the 200 to 260 nm range are attributed to host related absorptions and they depend on the malar ratio of La:Gd. For instance, the excitation peaks at 241 nm were not observed when x = 0 ($La_2SiO_5:Dy^{3+}$) and when x = 2 ($Gd_2SiO_5:Dy^{3+}$), but they were observed when La and Gd were intermixed. Therefore the excitation peaks at 227 and 241 nm cannot be as a result of either $O^{2-}\rightarrow Ln^{3+}$ (Ln = Dy, Gd, La) charge transfer states nor as a result of 4f→5d electronic transition of Ln^{3+}. Furthermore, the $O^{2-}\rightarrow Ln^{3+}$ charge transfer states and the 4f→5d electronic transition of Dy^{3+} and Gd^{3+} are observed below 200 nm [58-62] and La^{3+} cannot induce excitation in/or near the visible region since it has no 4f electrons [63]. We attributed the excitation peaks at 227 nm to the electronic transition from the O2p valence band to the La (5d6s) and Gd (5d6s) conduction bands [64, 65], while the 241 nm peaks are attributed to the La_{Gd}^{3+} isoelectronic impurities [66, 67]. The other excitations peaks at 275, 313, 351 and 386 nm are ascribed to $^8S_{7/2}\rightarrow{}^6I_J$ and $^6P_J\rightarrow{}^8S_{7/2}$ f-f forbidden transition of Gd^{3+} [54] and $^6H_{15/2}\rightarrow{}^6P_{7/2}$ and $^6H_{15/2}\rightarrow{}^4I_{13/2}$ f→f transition of Dy^{3+} [55] respectively. The inset in Fig. 6.8 (a) is the magnified excitation spectrum recorded in the 300 to 375 nm region. The excitation peak observed at 325 nm in the inset is assigned to $^6H1_{5/2}\rightarrow{}^6P_{3/2}$ f→f transition of Dy^{3+} [68, 69]. It can be seeing from Fig. 6.8 (a) that the maximum excitation intensity in the wavelength range from 200 to 260 nm was obtained when x = 1, but in the wavelength range from 260 to 450 nm, x = 2 gave the maximum excitation intensity. Since La^{3+} cannot induce excitation in/or near the visible region, Dy^{3+} ions sitting on La^{3+} sites (surrounded by La^{3+} ions) cannot contribute to the excitation near the visible regions. Rather, they will increase the distance between Dy^{3+}-Dy^{3+} ions in the $LaGdSiO_5$ matrix and hence causing decrease in the excitation intensity near the visible region. In the 200 to 260 nm region, equal La:Gd ratio will provide more O2 sites in the host and also more La_{Gd}^{3+} isoelectronic impurities, and hence the excitation intensity in this region is maximum when x = 1.

Table 6.2: Band gap of $La_{2-x}Gd_xSiO_5:Dy^{3+}$ nanophosphors

$La_{2-x}Gd_xSiO_5:Dy^{3+}$ 1.0 mol%	Band gap (eV)
x = 0	5.0
x = 0.5	4.45
x = 1.0	4.60
x = 1.5	4.73
x = 2.0	4.73

The PL emission spectra recorded when the samples were excited at the wavelength of 241 nm is shown in Fig. 6.8 (b). The two prominent emission peaks observed at 485 nm (blue) and 573 nm (yellow) and the other two small peaks around 668 and 756 nm are ascribed to the $^4F_{9/2}\rightarrow{}^6H_{15/2}$, $^4F_{9/2}\rightarrow{}^6H_{13/2}$, $^4F_{9/2}\rightarrow{}^6H_{11/12}$ and $^4F_{9/2}\rightarrow{}^6H_{9/2}$ f-f electronic transition of Dy^{3+} respectively [70]. The weak emission line peaking at around 613 nm is assigned to $^8G_{7/2}\rightarrow{}^6P_{5/2}$ electronic transition of Gd^{3+} [71]. It can be seeing from Fig. 6.8 (b), that the emission intensities followed a similar trend with the excitation intensities shown in Fig. 6.8 (a).

Fig. 6.9 (a) shows the emission spectra of the $La_{2-x}Gd_xSiO_5:Dy^{3+}$ when the 325 nm He-Cd laser was used as the excitation source. All the emission lines are the same as the ones in the emission spectra presented in Fig. 6.8 (b), except for the broad emission observed in the blue region of the spectra, (around 400 to 460 nm) with maximum at 415 nm. This peak is ascribed to the self-trapped excitons (STE) in SiO_2 [11]. The absence of the blue emission in the PL spectra in Fig. 6.8 (b) can be explained by considering the modes/types of excitation used. The emission spectra in Fig. 6.8 (b) were excited in phosphorescence mode while the one in Fig. 6.9 (a) was excited in the fluorescence mode. Phosphorescence is after-glow that persists longer than 0.1 s, while fluorescence is light emission during excitation (the life time is normally less than 10 ms) [72]. The reported life time of SiO_2 is between 0.125-5.000 ns

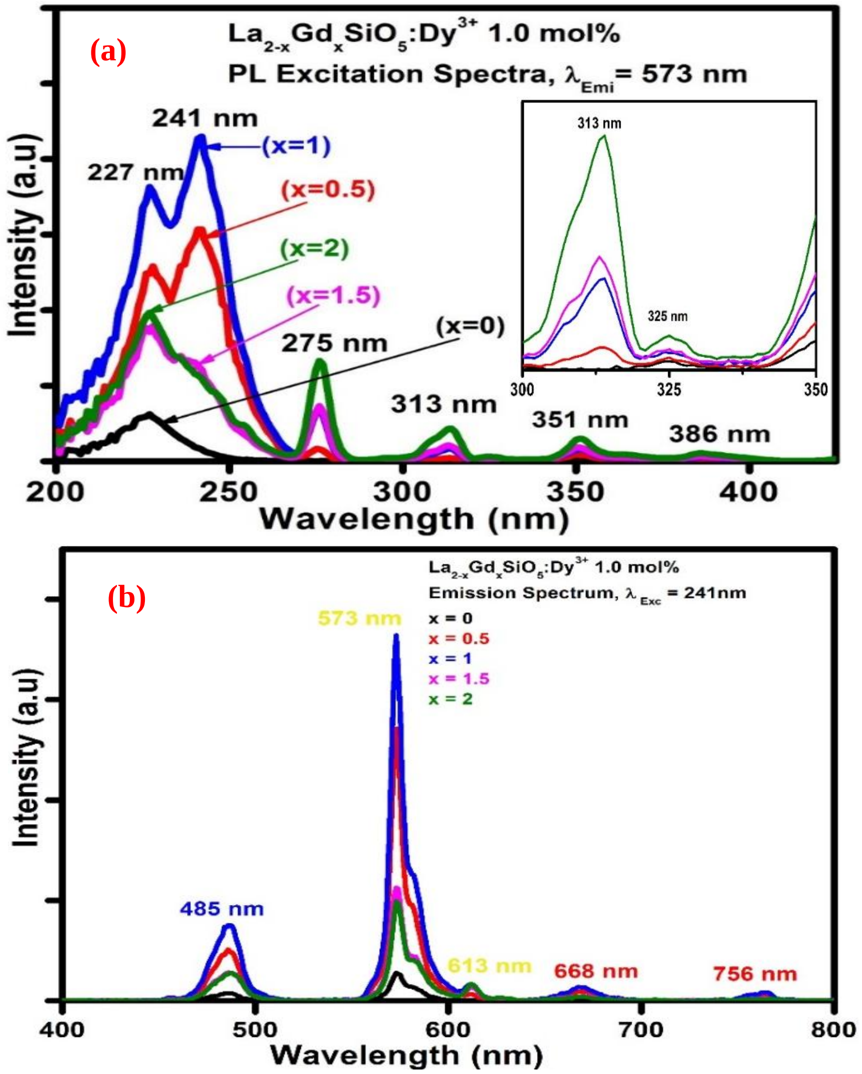

Fig. 6.8: Excitation spectra (a) and the emission spectra (b) of $La_{2-x}Gd_xSiO_5$:Dy^{3+} (x = 0, 0.5, 1.0, 1.5 and 2.0) monitored under 573 nm emission and 241 excitation wavelengths respectively using a PL system using xenon lamp as excitation source. The inset in (a) show the magnified excitation spectra from 300 to 375 nm wavelength range.

[73], so as a result of its smaller life time SiO_2 could not be detected in the phosphorescence mode. It can be observed from Fig. 6.9 (a) that the highest emission intensity of the 573 nm emission was obtained when x = 2, which is different from that in Fig. 6.8 (b), which was obtained when x = 1. The reason for this can be seeing from the excitation spectra shown in Fig. 6.8 (a), and the inset in the excitation spectra. From Fig. 6.8 (a) and its inset, it is clear that the excitation intensity is maximum at 325 nm when x = 2. Fig. 6.9 (b) show the

emission spectra when x = 0.5 where the yellow emission (573 nm) and two blue emissions (415 and 485 nm) have comparable intensities which results in the generation of white light shown in the inset with CIE coordinates of (0.347, 0.356). Fig. 6.9 (c) and (d) shows respectively how the broad blue and the yellow (573 nm) emission intensities vary with x. The blue emission gave maximum emission intensity when x = 0, i.e. when the host matrix was pure La_2SiO_5. However, a sharp decrease was observed in the intensity immediately when x = 0.5, after which there was a steady decrease as x increases from 0.5 to 2. Conversely, the intensity of the yellow emission increases gradually with x and gave sharp increase and the maximum emission intensities when x = 1.5 and 2 respectively. The decrease in the blue emission could be as a result of decrease in the impurity level in our material with increasing value of x. As seen in the XPS spectra peak intensity of Si 2p peak of $La_2SiO_5:Dy^{3+}$ is about four times higher than the Si 2p peak of $Gd_2SiO_5:Dy^{3+}$ (see Fig. 6.5 (d) and (e)). These suggest that La_2SiO_5 contain more SiO_x which is the major source of impurity in our materials than Gd_2SiO_5. In general, the decrease in the blue emission is a result of the decrease in the level of impurity in the nanophosphors which lead to an increase in the yellow emission since the traps due to the impurities in the samples will decrease [74].

Fig. 6.10 is an illustration of the energy level diagram of Dy^{3+} inside the host matrix. When the samples were excited using 325 nm (3.81 eV) He-Cd laser the excitation wavelength is equivalent to the $^6H15_{5/2} \rightarrow {}^6P_{3/2}$ excitation band of Dy^{3+} [68, 69]. So when the nanophosphors are excited using 325 nm He-Cd laser, Dy^{3+} electrons are excited from $^6H15_{5/2}$ to $^6P_{3/2}$ energy level of Dy^{3+} and holes are generated in the ground state. As can be seen from Fig. 6.10, this energy band of Dy^{3+} is smaller than the band gap of each host matrix (i.e. x = 0, 0.5, 1, 1.5 and 2). This implies that the electrons are not excited up to the conduction band of the host materials. In the excited state, the electrons are free electrons and can move around, likewise the holes in the ground state. Some of the free electrons can move into the host matrix and are trapped by defects in the host. The recombination of the excited electrons in the conduction band and the holes in the valence band can occur in different ways. It can occur through band-to-band transition or step-by-step through localized energy levels within the forbidden gap. In band-to-band transition, recombination occur directly from the excited state of Dy^{3+} to the ground states and give emissions after undergoing non-radiative transition to $^4F_{9/2}$ state of Dy^{3+} as shown at point (a) in Fig. 6.10. The recombination through localized energy levels within the forbidden gap can occur as a result of electrons trapped during excitation or in the process of recombination [75, 76]. The trapped electron can either transit into the $^4K_{15/2}$

excited state of Dy^{3+} or it can relax to the ground states of Dy^{3+} and give emissions after undergoing non-radiative transition to $^4F_{9/2}$ state of Dy^{3+} as shown in position (b) in Fig. 6.10. Position (c) in Fig. 6.10 represents the emission from self-trapped excitons (STE) in SiO_5. If field or temperature is not sufficient enough, excited electron and hole can couple together by a Coulomb attraction. STE occurs in structures when an excited electron and a hole spontaneously create a localized distortion in the lattice resulting to the lowering of their total energy and they are localized and trapped in the distortion [77].

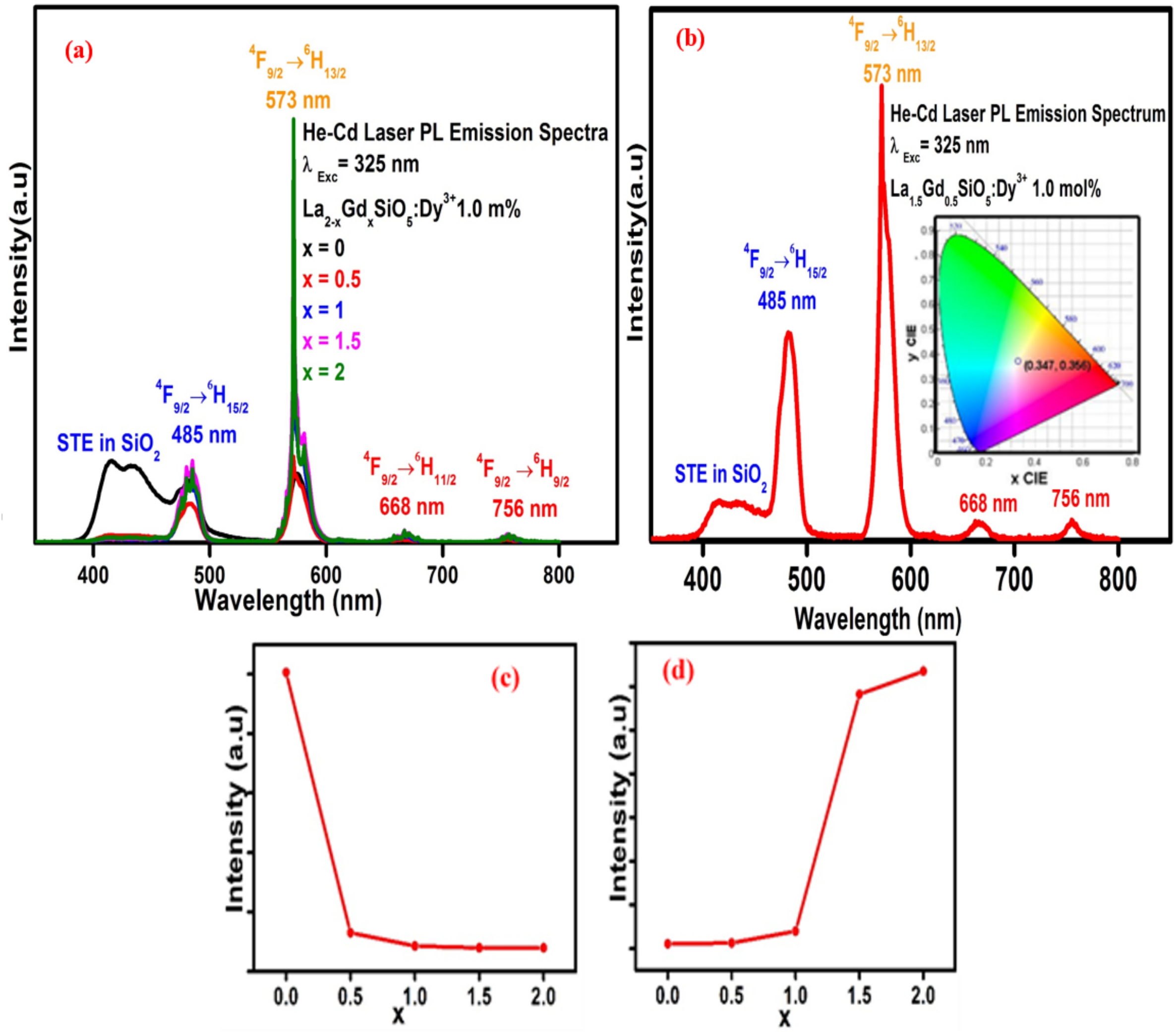

Fig. 6.9: Emission spectra of $La_{2-x}Gd_xSiO_5:Dy^{3+}$ (a) x = 0, 0.5, 1.0, 1.5 and 2.0, (b) x = 0.5 when monitored with a PL system using 325 nm He-Cd gas laser as excitation source. The inset in (b) is the CIE coordinate when x = 0.5. (c) Show the variation of the blue emission intensity with x and (d) show the variation of the yellow (573 nm) emission intensity with x.

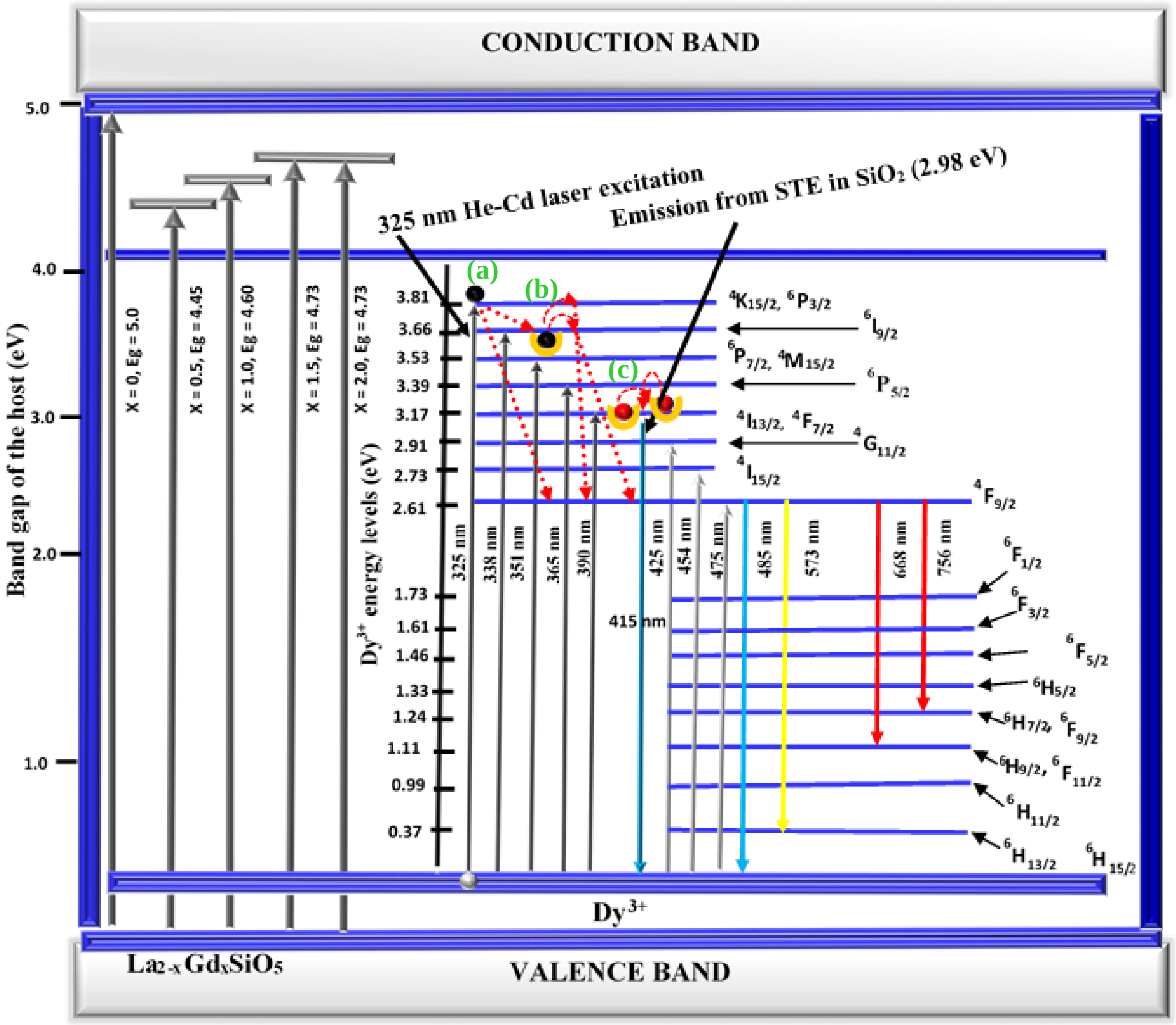

Fig. 6.10: Energy level diagram showing the energy level diagram of Dy^{3+} between the bands of the $La_{2-x}Gd_xSiO_5$ host matrices.

Fig. 6.11 shows the CIE chromaticity coordinates diagram of $La_{2-x}Gd_xSiO_5:Dy^{3+}$ for the PL emission obtained when the samples were excited using the 325 nm He-Cd laser. The CIE coordinates can be tuned from blue, through white, to yellow by varying the molar ratio of La and Gd in the $La_{2-x}Gd_xSiO_5:Dy^{3+}$ matrix. The CIE coordinates are represented with different letters and are shown in table 6.3.

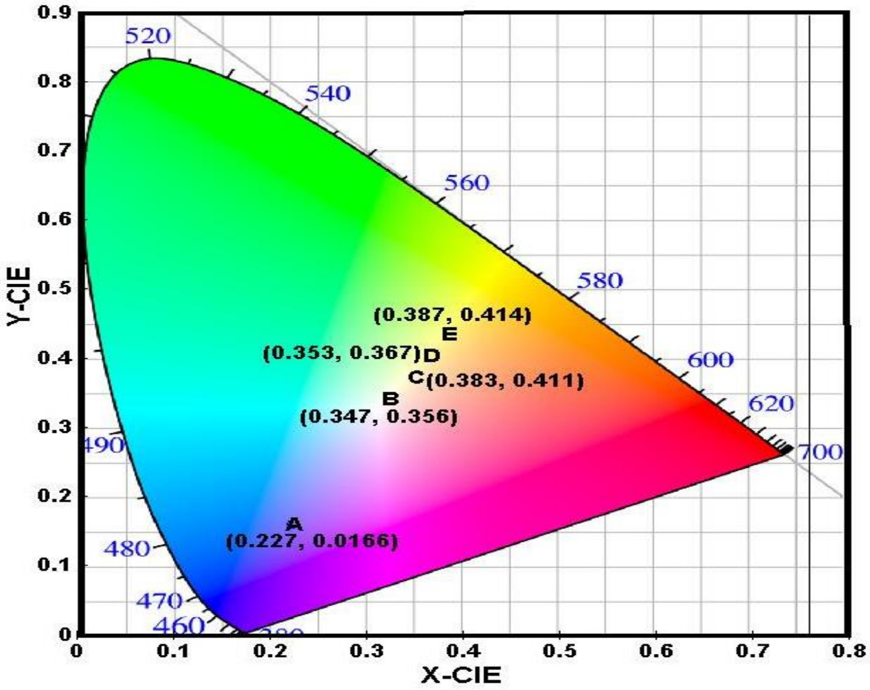

Fig. 6.11: CIE coordinates diagram of $La_{2-x}Gd_xSiO_5:Dy^{3+}$ studied with a PL system using 325 nm He-Cd gas laser as excitation source.

Table 6.3: CIE coordinates of $La_{2-x}Gd_xSiO_5:Dy^{3+}$ and the corresponding colours.

$La_{2-x}Gd_xSiO_5:Dy^{3+}$	Letters	CIE Coordinates	Colours
x = 0	**A**	(0.227, 0.166)	Blue
x = 0.5	B	(0.347, 0.356)	White
x = 1.0	**C**	(0.353, 0.367)	Yellowish-white
x = 1.5	**D**	(0.383, 0.411)	Yellow
x = 2.0	**E**	(0.387, 0.414)	Yellow

6.4. Conclusion

Using urea- and ammonium nitrate-assisted solution combustion method, we were able to prepare a novel $La_{2-x}Gd_xSiO_5$ (x = 0, 0.5, 1.0, 1.5 and 2.0) doped with 1.0 mol% of Dy^{3+} nanophosphors for UV-pumped multicolour and white light emitting diode applications. The crystallite size calculated from the XRD peaks varies from 10 to 21 nm. The photoluminescence properties were studied in phosphorescence and fluorescence mode using Cary eclipse spectrophotometer and 325 nm He-Cd laser system respectively. The phosphorescence emission showed the two characteristic peaks of Dy^{3+} at 485 nm (blue) and 573 nm (yellow) while the fluorescence emission showed an additional broad blue emission with maximum around 415 nm which is ascribed to STE in SiO_2. The blue emission from SiO_2 decreases with increasing molar ratio of Gd_2SiO_5 while the yellow emission increases. Hence by varying the mol ratio of La and Gd, we were able to tune the colour of the emitted light from blue, via white to yellow. Similarly, the band gap was tuned from 5.00 to 4.45 eV.

6.5. References

[1] J. Felsche. Springer Berlin Heidelberg, 13(1973) 99–197.

[2] D.W. Cooke, E.A. McKigney, R.E. Muenchausen, B.L. Bennett. Nanocomposite scintillators, detector, and method. U.S. Patent. Sr. No. 60/752,981 (2005).

[3] T.E. Peters. J. Electrochem. Soc. 116 (1969) 985-989.

[4] J. Wang, S. Tian, G. Li, F. Liao, X. Jing. J. Electrochem. Soc. 148 (6) (2001) H61-H66.

[5] R.Y. Lee, F.L. Zhang, J. Penczek, B.K. Wagner, P.N. Yocom, C.J. Summers. J. Vac. Sci. Technol. B, 16 (1998) 855.

[6] C.M Michail, A. Toutountzis, I.G. Valais, I. Seferis, M. Georgousis, G. Fountos, I.S. Kandarakis , G.S. Panayiotakis. e-JST 2 (2010) 25-32.

[7] T. Kamae, Y. Fukazawa, N. Isobe, M. Kokubun, A.Kubota, S. Osone, T. Takahashi, N. Tsuchida, H. Ishibashi. Nucl. Instr. Meth. Phys. Res. A, 490 (2002) 456-464.

[8] V. Avdeichikov, B. Jakobsson, V. A. Nikitin, V. Nomokonov, A. Wegner. Nucl. Instr. Meth. Phys. Res. A., 484 (2002) 251-258.

[9] W. Mangesha, T.D. Taulbee, J.D. Valentine, B.D. Rooney. Nucl. Instr. Meth. Phys. Res. A., 486 (2002) 448-452.

[10] I. Warshaw, R. Roy. Am. Ceram. Soc. Bull., 38 (1959) 169.

[11] C. Itoh, K. Tanimura, N. Itoh. J. Phys. C: Solid State Phys. 21 (1988) 4693-4702.

[12] G.B. Loutts, A.I. Zagumennyi, S.B. Lavrishev, Yu.D. Zavartsev, P.A. Studenikin. J. Crystal Growth 174 (1997) 331-336.

[13] G.D. Dominiak, W. R. Romanowski, R. Lisiecki, P. Solarz, B. Macalik, M. Berkowski, M. Gzowacki, V. Domukhovski. Crystal Growth & Design10 (2010) 3522-3530.

[14] W. Drozdowski, K. Brylew, A. J. Wojtowicz, J. Kisielewski, M. Świrkowicz, T. Łukasiewicz, J. T.M. de Haas, P. Dorenbos. Opt. Matt. Exp. 4 (2014) 1207-1212.

[15] W. Li, S. Xu, H. Pan, L. Ding, H. Zeng. Opt. Expr. 14 (2006) 6681-6686.

[16] O. Sidletskiy. Funct. Mat. 14 (2010) 414-420.

[17] W. Tian, J. Zhu, Z. Wang, J. Wang, Z. Wei. Chinese Opt. Lett. 12 (2014)1-3.

[18] J.C. Zhang, Y H. Wang. Chin. Phys. Lett. 25 (2008) 1453.

[19] G.K. Williamson, W.H. Hall. Acta Metallurgica, 1 (1953) 22-31.

[20] V.D. Mote, Y. Purushotham, B.N. Dole. J. theoretical and Applied Phys. 6 (2012) 6.

[21] S. Bernal, F.J. Botana, R. Garcia, J.M. Rodriguez-Izquerdo. React. Solids 4 (1987) 23-40.

[22] R. Krsmanovic Z. Andric, M.M. Cincovic, I. Zekovic, M.D. Dramicanin.. Acta Physica Polonnica 112 (2007) 975-980.

[23] M.P. Rosynek, D.T. Magnuson. J. Catal. 46 (1977) 402-413.

[24] C. Louis, R. Bazzi, M.A. Flores, W. Zheng, K. Lebbou, O. Tillement, B. Mercier, C. Dujardin, P. Perriat. J. Solid State Chem., 173 (2003) 335-341.

[25] G. Liu, G. Hong, D. Sun. J. Colloid Interface Sci., 278 (2004) 133-138.

[26] S. Bernal, F.J. Botana, R. Garcia, J.M. Rodriguez-Izquerdo. React. Solids 4 (1987) 23-40.

[27] S. Bernal, J.A. Diaz, R. Garcia, J.M. Rodriguez-Izquerdo, J. Mater. Sci. 20 (1985) 537-541.

[28] S. Bernal, F.J. Botana, R. Garcia, J.M. Rodriguez-Izquerdo. Thermochim. Acta 66 (1993) 139-145.

[29] P.A. Jacobs, F.H. van Cauwelaert, E.F. Vansant, J.B. Uytterhoeven. J. Chem. Soc. Faraday Trans. I 69 (1973) 1056-1068.

[30] V. Rakic, V. Dondur, R. Hercigonja. J.Serb.Chem.Soc. 68 (4-5) (2003) 409-416).

[31] F.S. Aguirre-Tastado, M. Milojevic, B. Lee, J. Kim, R.M. Wallace. Appl. Phys. Lett. 93 (2008) 172907.

[32] T. Gougousi, M.J. Kelly, D.B. Terry, G.N. Parsons. J. Appl. Phys. 93(2003) 1691-1696.

[33] W.S. Kim, S.K. Park, D.Y. Moon, B.W. Kang, H.D. Kim, J.W. Park. J. Korean Phys. Soc. 55 (2009) 590-593.

[34] C. Li, Y. Shen, S. Zhu, S. Shen. RSC Adv., 4 (2014) 29107-29119.

[35] E. Coetsee. J.J. Terblans, H.C. Swart. Appl. Surf. Sci. 256 (2010) 6641-6648.

[36] J.L. Her, M.H. Wu, Y.B. Peng, T.M. Pan, W.H. Weng, S.T. Pang, L. Chi. Int. J. Electrochem. Sci., 8 (2013) 606-620.

[37] H. Gang, S. Zhaoqi (eds). High-k gate dielectric for CMOS technology. Wiley-VCH, Weinheim, ISBN: 978-3-527-33032-4 (2012).

[38] C. Logofatu, C.C. Negrila, R.V. Ghita, F. Ungureanu, C. G. Manea, M.F. Lazarescu. Study of SiO_2/Si interface by surface techniques. Intech. ISBN: 978-953-307-587-7 (2011).

[39] E. Coetsee, J.J Terblans, H.C. Swart. J. Lumi. 126 (2007) 37-42.

[40] A.J. Signorelli, R.G. Hayes. Phys. Rev. B 8 (1973) 81-86.

[41] S. Hufner. Photoelectron Spectroscopy: Principles and Applications. Springer-Verlage Berlin Heideberg, pp. 173 (2003).

[42] D.F. Mullica, C.K. Lok, H.O. Perkins. Phy. Rev. B. 31 (1985) 4039-4042.

[43] T.H. Yang, Y.W. Harn, K.C. Chiu, C.L. Fan, J.M. Wu. J. Mater. Chem. 22 (2012) 17071-17078.

[44] S. Mickevicius, S. Grebinskij, V. Bondarenka, H. Tvardauskas, B. Vengalis, K. Sliuzienne, B.A. Orlowski, W. Drube.. Opt. Appl. XXXVI (2006) 235-243.

[45] L.A. Qian, P.T. Lai, W.M. Tang. Appl. Phys. Lett. 104 (2014)123505-5.

[46] D. Raiser, J.P. Deville. J. Electron Spectrosc. Relat. Phenom. 57 (1991) 91-97.

[47] M. Ahren, L. Selegard, F. Soderlind, M. Linares, J. Kauczor, P. Norman, P. Kall, K. Uvdal. J. Nanopart. Res. 14 (2012) 1006.

[48] P.P. Mokoene, I.M. Nagpure, V. Kumar, R.E. Kroon, E.J. Olivier, J.H. Neethling, H.C. Swart, O.M. Ntwaeaborwa. J. Phys. & Chem. Sol. 75 (2014) 998-1003.

[49] J. Chung, J. Park, J.G. Park, B.H. Choi, S.J. Oh, E.J. Cho, H.D. Kim, Y.S. Known. J. Korean Phys. Soci. 38 (2001) 744-749.

[50] H. Ogasawara, A. Kotani, B.T. Thole. Phys. Rev. B 50 (1994) 12332-12341.

[51] V.A. Mode, G.S. Smith. J. Inorg. & Nucl. Chem. 31(1969) 1857-1859.

[52] A.P. Milanov, R.W. Seidel, D. Barreca, A. Gasparotto, M. Winter, J. Feydt, S. Irsen, H.W. Becker, A. Devi. Dalton Trans. 40 (2011) 62-78.

[53] M.A. Tshabalala, F.B. Dejene, S.S. Pitale, H.C. Swart, O.M. Ntwaeaborwa. Physica B 439 (2014) 126–129.

[54] Y. Li, Y. Chang, Y. Chang, Y. Lin, C. Laing. J. Phys.Chem C, 111 (2007) 10682-10688.

[55] X. Liu, W. Xiang, F. Chen, Z. Hu, W. Zhang. Mater. Res. Bull. 48 (2013) 281-285.

[56] J. Tauc. The optical properties of solids (North-Holland, Amsterdam, 1970) Young, PA. J. Phys. C: Solid State Phys. 4, 93 (1971).

[57] M.A. Humayun, M.A. Rashid, F.A. Malek, A.N. Hussain. Journal of Russian Laser Research, 33 (2012) 387-394.

[58] Y. Li, Y. Chang, Y. Lin, Y. Shin, Y. Lin, J. Alloy and Comp. 439 (2007) 367-375

[59] J. Gou, Y. Wang, F. Li, J. Lumin. 128 (2008) 728.

[60] H. Liang, Q. Zeng, Y. Tao, S. Wang, Q. Su. Mat. Sci. & Eng: B. 98 (2003) 213-219.

[61] W. Zhao, S. An, B. Fan, S. Li. Opt. Mater. 35 (2013) 1748-1751.

[62] I.N. Ogorodnikov, V.A. Pustovarov, S.I. Omelkov, D.O. Vostrov, L.I. Isaenko. Opt. Mater. 36 (2014) 1060-1064.

[63] K.N. Shinde, S.J. Dhoble, H.C. Swart, K. Park, Springer Series in Materials Science 174 (2013) 54.

[64] G. Li, C. Li, C. Zhang, Z. Cheng, Z. Quan, C. Peng, J. Lin. J. Mater. Chem. 19 (2009) 8936-8943.

[65] M. Jia, J. Zhang, S. Lu, J. Sun, Y. Luo, X. Ren, H. Song, X. Wang. Chem. Phy. Lett. 384 (2004) 193-196.

[66] Y.V. Zorenko. Optics and spectroscopy 100 (2006) 572-580.

[67] Y. Zorenko, V. Gorbenco, V. Savchyn, T. Voznyack, M. Nikl, J.A. Mares, A. Winnacker. Radiation measurements 45 (2010) 444-448.

[68] G.V. Reddy, L.R. Moorthy, T. Chengaiah, B.C. Jamalaiah. Adv. Mat. Lett. 4 (2013) 841-848.

[69] W.T. Camal, P.R. Fields, K. Rajnak. J. Chem. Phys. 49 (1968) 4424-4442.

[70] R. Lisiecki, G. Dominiak-Dzik, P. Solarz, W. Ryba-Romanowski, M. Berkowski, M. Glowacki. Appl Phys. B 98 (2010) 337-346.

[71] C. Ronda (ed). Luminescence: from theory to application. Wiley-VCH Verlag GmbH and Co. KGaA, Weinheim. ISBN: 978-3-527-31402-7, pp 93 (2008).

[72] W.M. Yen, S. Shigeo, H. Yamamoto. Phosphor Handbook, 2nd edition. CRC Press laser and optical science and technology series. ISBN: 10: 0-8493-3564-7, p 83, (2007).

[73] A. Uedono, L. Wei, S. Tanigawa, R. Suzuki, H. Ohgaki. Hyperfine Interactions 84 (1994) 231-236.

[74] J.H. Hong, C.J. Cong, Z.G. Zhang, K.L. Zhang. Journal of Physics and Chemistry of Solids 68 (2007) 1359–1363.

[75] R. Salh. Defect Related Luminescence in Silicon Dioxide Network: A Review. ISBN: 978-953-307-587-7, InTech (2011).

[76] S. Soma, S. Dutta, Vijay Kumar, A. Pandey, V. Kumar, A.K. Kunti, J. Priya, S.K. Sharma, J.J. Terblans, H.C. Swart. J. Alloys & Comp. 622 (2015) 1068–1073.

[77] S.I. Beigi, S.G. Louie. Phy. Rev. Lett. 95 (2005) 156401.

CHAPTER SEVEN

The Influence of Dy^{3+} ions Concentration and Post-Annealing on the Properties of $LaGdSiO_5:xDy^{3+}$ (x = mol %) Nanophosphors

7.1 Introduction

Ordinarily, it would be expected that increase in activator concentration in phosphors would result to high luminescence intensity since luminescence are due to such impurities. However, a non-monotonic dependent of luminescence intensity on the activator concentration have been shown by many experiments. The luminescence intensity of a phosphor can increase with the activator concentration up to a certain maximum value, and then decrease beyond that value. This effect has been named concentration quenching. Concentration quenching can be as a result of: (i) loss of excitation energy from the emitting state due to cross-relaxation between the activators, (ii) excitation migration owing to resonance between the activator ions and (iii) coagulated or paired activator ions acting as quenching center [1]. The optimum activator concentration is a function of the nature of the host matrix and the activator since the number of lattice sites or nearest neighbors which may become quenching sites depends on the structure of the host and the degree of interaction depends on the activator ion [2]. Concentration quenching has been studied in Dy^{3+} doped in various host matrices [3-5].

In chapter six, we varied the molar ratio of La and Gd in $La_{2-x}Gd_xSiO_5$ (x = 0, 0.5, 1.0, 1.5 and 2.0) matrices while keeping the concentration of Dy^{3+} fixed at 1.0 mol %. The highest PL excitation and emission intensities were observed when x = 1.0, i.e. from $LaGdSiO_5:Dy^{3+}$ 1.0 mol %. In this chapter, we fixed the molar ratio of La and Gd at x = 1.0 and vary the molar concentration (x) of Dy^{3+} (x = 0.05, 0.1, 0.25, 0.75, 1.0, 1.5, 2.0, 3.0 and 5.0 mol%) and we studied the effect of Dy^{3+} concentration and post-preparation annealing on the structure and spectroscopic properties of our materials.

7.2. Experimental

The $LaGdSiO_5:Dy^{3+}$ nanophosphors were synthesized using solution combustion method as described in section 3.3.2. The starting materials were lanthanum (III) nitrate hexahydrate $La(NO_3)_3.6H_2O$, gadolinium (III) nitrate hexahydrate $Gd(NO_3)_3.6H_2O$, dysprosium (III) nitrate hexahydrate $Dy(NO_3)_3.6(H_2O)$ and silicic acid (SiO_2H_2O). Urea $CO(NH_4)_2$ and ammonium nitrate (NH_4NO_3) were used as fuel. For each of the nine set of samples, the masses of SiO_2H_2O, $CO(NH_4)_2$ and NH_4NO_3 are 0.1000 g, 0.4690 g, and 0.6251 g respectively. For $LaGdSiO_5$:Dy^{3+} 0.05 mol% (i.e. x = 0.05), the masses of $La(NO_3)_3.6H_2O$, $Gd(NO_3)_3.6H_2O$ and $Dy(NO_3)_3.6H_2O$ are respectively 0.6760 g, 0.7047 g and 0.0005 g. For x = 0.1, $La(NO_3)_3.6H_2O$ = 0.6757 g, $Gd(NO_3)_3.6H_2O$ = 0.7043 g and $Dy(NO_3)_3.6H_2O$ = 0.0011 g. For x = 0.25, $La(NO_3)_3.6H_2O$ = 0.6746 g, $Gd(NO_3)_3.6H_2O$ = 0.7035 g and $Dy(NO_3)_3.6H_2O$ = 0.0027 g. For x = 0.75 $La(NO_3)_3.6H_2O$ = 0.6712 g, $Gd(NO_3)_3.6H_2O$ = 0.6997 g and $Dy(NO_3)_3.6H_2O$ = 0.0081 g. For x = 1.0, $La(NO_3)_3.6H_2O$ = 0.6696 g, $Gd(NO_3)_3.6H_2O$ = 0.6980 g and $Dy(NO_3)_3.6H_2O$ = 0.0109 g. For x = 1.5, $La(NO_3)_3.6H_2O$ = 0.3331 g, $Gd(NO_3)_3.6H_2O$ = 0.3472 g and $Dy(NO_3)_3.6H_2O$ = 0.0082 g. For x = 2.0, $La(NO_3)_3.6H_2O$ = 0.3314 g, $Gd(NO_3)_3.6H_2O$ = 0.3455 g and $Dy(NO_3)_3.6H_2O$ = 0.0109 g. For x = 3.0, $La(NO_3)_3.6H_2O$ = 0.6560 g, $Gd(NO_3)_3.6H_2O$ = 0.6838 g and $Dy(NO_3)_3.6H_2O$ = 0.0326 g. For x = 5.0, $La(NO_3)_3.6H_2O$ = 0.6425 g, $Gd(NO_3)_3.6H_2O$ = 0.6697 g and $Dy(NO_3)_3.6H_2O$ = 0.0544 g. The structure and stretching modes of vibration of the samples were analyzed using: Bruker D8 advanced X-ray diffractometer and Nicolet 6700 Fourier transform infrared (FTIR) spectrometer respectively. The morphology study and the elemental analysis were carried out using Jeol JSM-7800F field emission scanning electron microscope (FE-SEM). The electronic and chemical states were investigated using PHI 5000 Versaprobe-scanning ESCA microprobe X-ray photoelectron spectroscopy (XPS). The identification of the atomic and molecular ionic species was examined using iontof ToF-SIMS^5 in positive secondary and negative ion polarity mode in the spectroscopic mode. The pulsed primary ion source (Bi^{3+}) was set at 30 keV and the DC current was 11.0 pA. The photoluminescence (PL) spectra were measured in the phosphorescence and fluorescence modes, respectively, using Cary Eclipse fluorescence spectrophotometer and a PL system consisting of a 325 nm He-Cd gas laser as an excitation source, a spectrometer, a photomultiplier tube (PMT) detector and a lock-in amplifier, while the ultraviolet visible (UV-Vis) measurements were taken using Lambda 950 UV-Vis spectrometer.

7.3. Results and Discussion

Lanthanum oxyorthosilicate (La_2SiO_5) and gadolinium oxyorthosilicate (Gd_2SiO_5) belong to the family of rare earth oxyorthosilicates (R_2SiO_5). They fall into the monoclinic crystallographic point group belonging to the *P2I/c* and the *I2/a* space groups. These space groups respectively corresponds to the low temperature phase *(X1)* and high temperature phase *(X2)*. The *X1* phase has two non-equivalent crystallographic sites, R1 (R1 = La1 or Gd1) sites coordinated by nine oxygen atoms and R2 (R2 = La2 or Gd2) sites coordinated by seven oxygen atoms [6-9]. The crystal structure of the *X1* phase consists of three types of polyhedra: $R1O_9$, $R2O_7$ and SiO_4. The $R1O_9$ and the $R2O_7$ polyhedra are connected through the SiO_4 groups and non-silicon-bonded oxygen atoms (O5) to form three dimensional structures as shown in Fig. 7.1 (a) and (b) for La_2SiO_5 and Gd_2SiO_5 respectively. The crystal structure of the *X2* phase consists of two crystallographic sites R1 coordinated by six oxygen atoms and R2 coordinated by seven oxygen atoms with a tetrahedra SiO_4 linking them [10] as shown schematically in Fig. 7.1 (c). A phase-transformation temperature of about 1190 ℃ and 1250 ℃ have been reported from X_1 to X_2 for Y_2SiO_5 [6, 11].

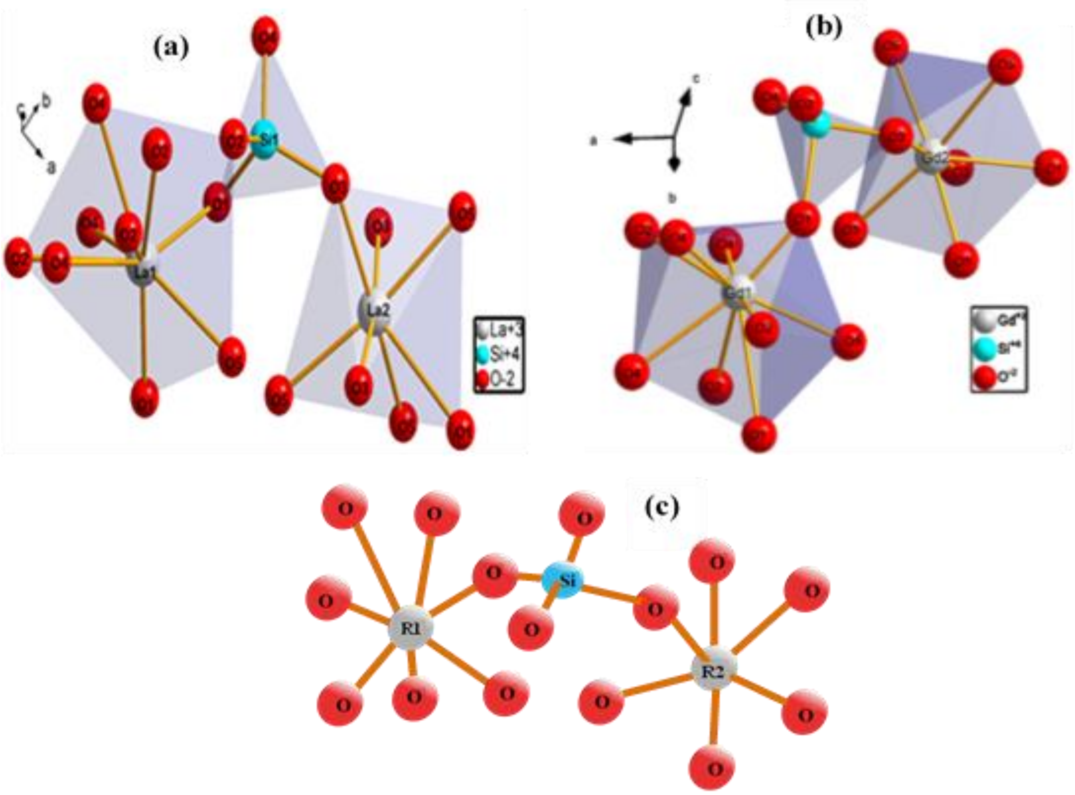

Fig. 7.1: The crystal structures of (a) *X1* phase of La_2SiO_5, (b) *X1* phase Gd_2SiO_5 and (c) schematic of the *X2* phase of R_2SiO_5 (R = La or Gd).

The XRD patterns of the least and the highest concentration of Dy^{3+} (i.e. x = 0.05 and x = 5.0 mol %) of the as-prepared and annealed samples were measured to study the effect of Dy^{3+} concentration and the annealing temperature on the structure of the host matrix and the results are shown in Fig. 7.2. It can be seen from Fig. 7.2 that Dy^{3+} ion did not have any effect on the main structure of the hosts, probably due to their relatively low concentration. In addition, this can be as a result of the similarities in the ionic radii of La^{3+} and Gd^{3+} and that of the

Dy^{3+} dopant. La^{3+} has ionic radii of 0.110 nm and 0.1216 nm in its seven and nine-fold coordinated sites respectively [12], while Gd^{3+} has atomic radii of 0.10 nm and 0.1107 nm in its seven and nine-fold coordinated sites respectively [6, 13]. Dy^{3+} has ionic radii of 0.1052 nm and 0.1167 nm in its six and eight-fold coordinated sites [12]. Due to these similarities, Dy^{3+} ions can easily displace any of the two ions without changing the main structure [14]. The XRD patterns match with the standard monoclinic structures of La_2SiO_5 and Gd_2SiO_5 referenced in JCDPS file no: 40-0234 and 74-1795 respectively. The peaks marked with the symbol "*" are from La_2SiO_5, while those marked with "♦" are from Gd_2SiO_5. Those marked with "●" are ascribed to both La_2SiO_5 and Gd_2SiO_5. In the annealed samples, the shapes of the (021) and ($\bar{1}12$) peaks marked with "♠" changed and the intensities of the (102) and (421) peaks increased slightly, suggesting that crystallinity improved. Also the (122) and (132) peaks marked with "♣" in the as-prepared samples disappeared in the annealed samples while the two peaks marked with "♥" appeared in the annealed samples. This could be due to phase transformation from the low temperature phase (*X1*) to the high temperature phase (*X2*). The average crystallite sizes (L) and the strain (ε) of the as-prepared samples calculated using the Williamson-Hall equation (Eqn. 7.1) [15, 16] and the results are shown in table 7.1.

$$\beta_{hkl}\mathrm{Cos}\theta = 4\varepsilon\ \mathrm{Sin}\theta + \frac{K\lambda}{L} \qquad [7.1]$$

where λ is the X-ray wavelength in nanometer (nm), β_{hkl} is the peak width of the diffraction peaks profile at half maximum height, θ is the Bragg angle and K is a constant related to the crystallite shape, usually taken as 0.9 or 0.89 for full width at half maximum (FWHM) of spherical crystals with cubic unit cells. Fig.7.3 shows the Williamson-Hall plot for $LaGdSiO_5:Dy^{3+}$ 5 mol %. A graph of $4\sin\theta$ along the x-axis and $\beta_{hkl}\mathrm{Cos}\theta$ along the y-axis was plotted. From the linear fit to the data points, the crystallite size was estimated by equating the y-intercept to $K\lambda/L$, and the strain was generated from the slope of the fit.

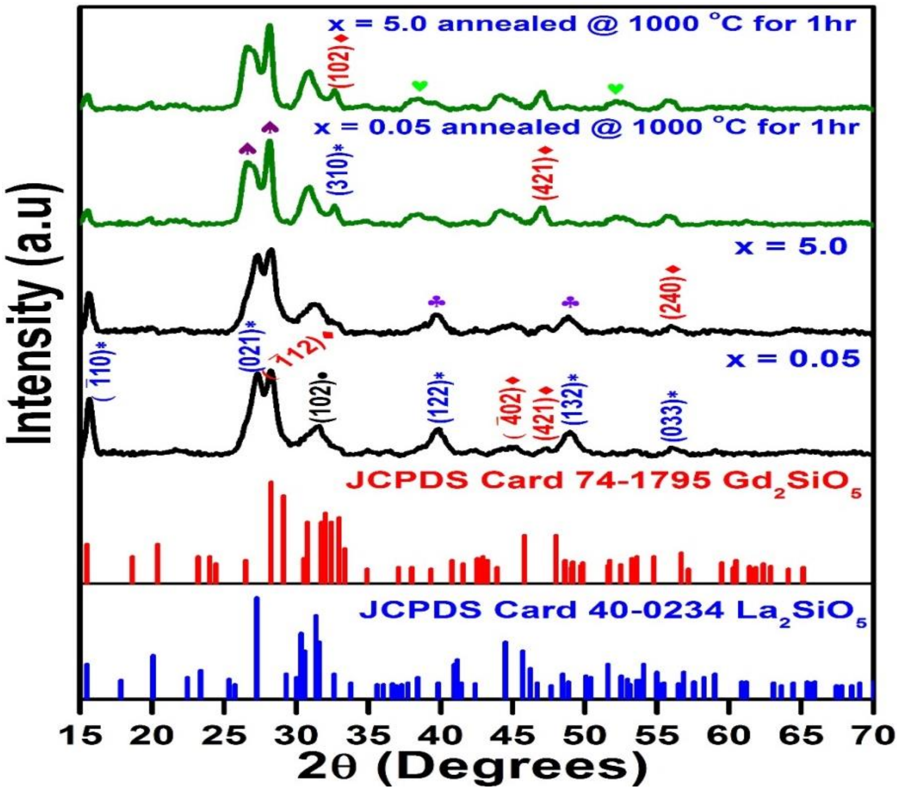

Fig. 7.2: The XRD patterns of as-prepared and annealed (at 1000 ℃ for 1hr) $LaGdSiO_5:Dy^{3+}$ x mol% (x = 0.05 and 5.0).

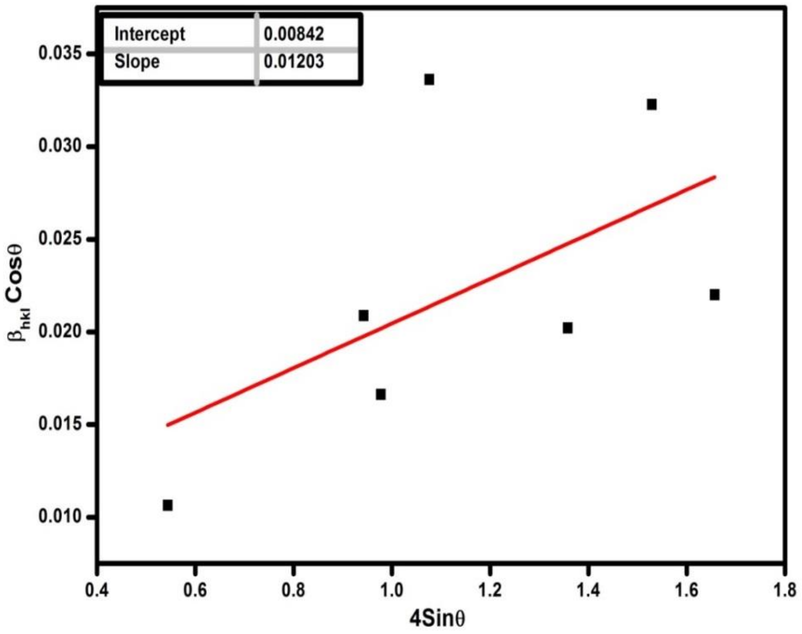

Fig. 7.3: The Williamson-Hall plot of $LaGdSiO_5:Dy^{3+}$ 5 mol%.

Table. 7.1: The crystallite sizes and lattice strain of $LaGdSiO_5:Dy^{3+}$ x mol % nanophosphors.

$LaGdSiO_5:Dy^{3+}$ x mol%	Crystallite size (L) (nm)	Strain (ε) ($\times 10^{-2}$)
x = 0.05	15	2.05
x = 0.1	12	1.82
x = 0.25	14	2.08
x = 0.75	16	1.95
x = 1.0	13	2.30
x = 1.5	14	2.43
x = 2	13	2.10
x = 3.0	12	1.64
x = 5.0	16	1.20

XPS was used to analyze the chemical states and composition of the samples. Fig. 7.4 (a) and (b) show the fitted high resolution XPS spectra of the O 1s peaks of $LaGdSiO_5:Dy^{3+}$ before (as-prepared) and after annealing at 1000 ℃ for 1 hr. The XPS spectra exhibit four peaks at 529.0 eV ($LaGdO_3$), 530.6 eV ($LaGdO_5$), 531.6 eV (SiO_2-La) and 532.5 eV (SiO_2-Gd) [17-21]. After annealing in Fig. 7.4 (b), there was a general reduction in the peak intensities and shifting of the binding energy values. For example, the binding energies for the four peaks observed in the as-prepared samples shifted 528.8 eV ($LaGdO_3$), 530.3 eV ($LaGdO_5$), 530.9 eV (SiO_2-La) and 531.5 eV (SiO_2-Gd) in the annealed sample. Consistent with the XRD data, these changes could be attributed to the post-preparation annealing induced phase transformation from *X1* to *X2*.

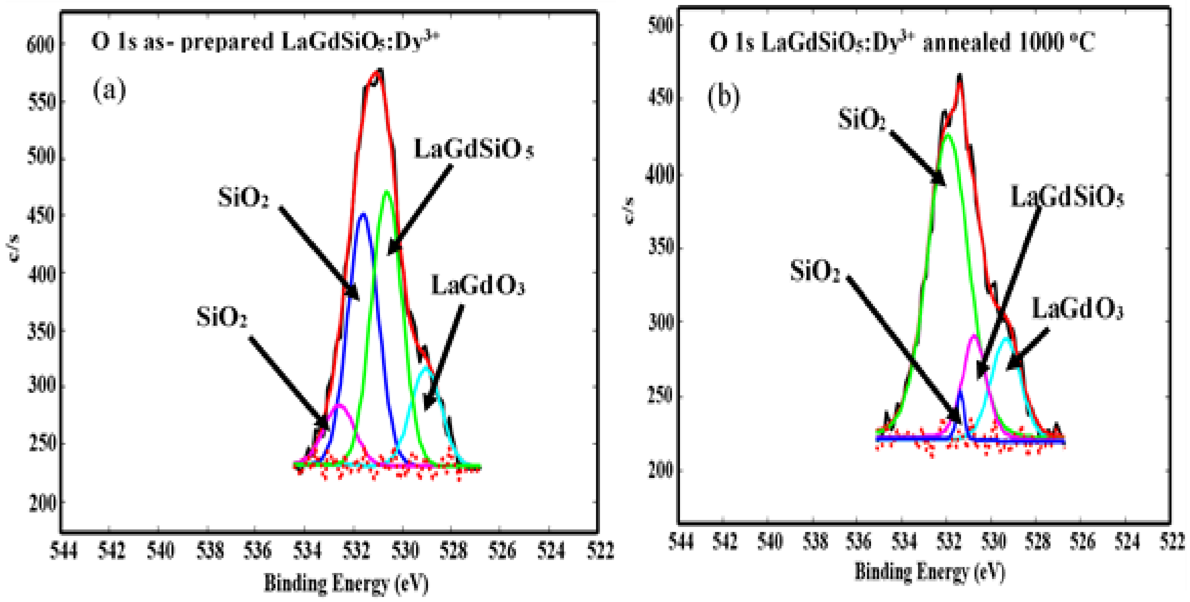

Fig. 7.4: XPS spectra of the O 1s peak of (a) as-prepared and (b) 1000 °C annealed LaGdSiO$_5$:Dy^{3+}.

Fig. 7.5 (a) and (b) show the positive mode secondary ions ToF-SIMS mass spectra of the as-prepared and the annealed sample respectively, while Fig. 7.5 (c) and (d) show the negative mode ions ToF-SIMS mass spectra of the as-prepared and the annealed sample. All the ionic and molecular species contained in the materials were presence, including C^-, CH_3^+, Na^+ and K^+ which we ascribed to contaminants from the atmosphere and sample holders. All the atomic and molecules species detected in the positive and negative modes are shown in table 7.2. Notice that the adventitious Na^+ and K^+ which were present in the spectrum of the as-prepared samples were not in the spectrum of the annealed samples. This could be as a result of the evaporation of these elements from the sample during annealing process. Na has a melting point of 97.72 °C and a boiling point of 883 °C [22] while K has a melting point of 63.4 °C and a boiling point of 765.6 °C [23], and hence they can easily evaporate before the annealing temperature of 1000 °C is reached. From the negative ToF-SIMS mass spectra for the as-prepared and the annealed samples shown in Fig. 7.5 (c) and (d) respectively, it can be seen that the intensity of O^-decreased by about 1000 after annealing. This is consistent with the XPS result (see Fig. 7.4).

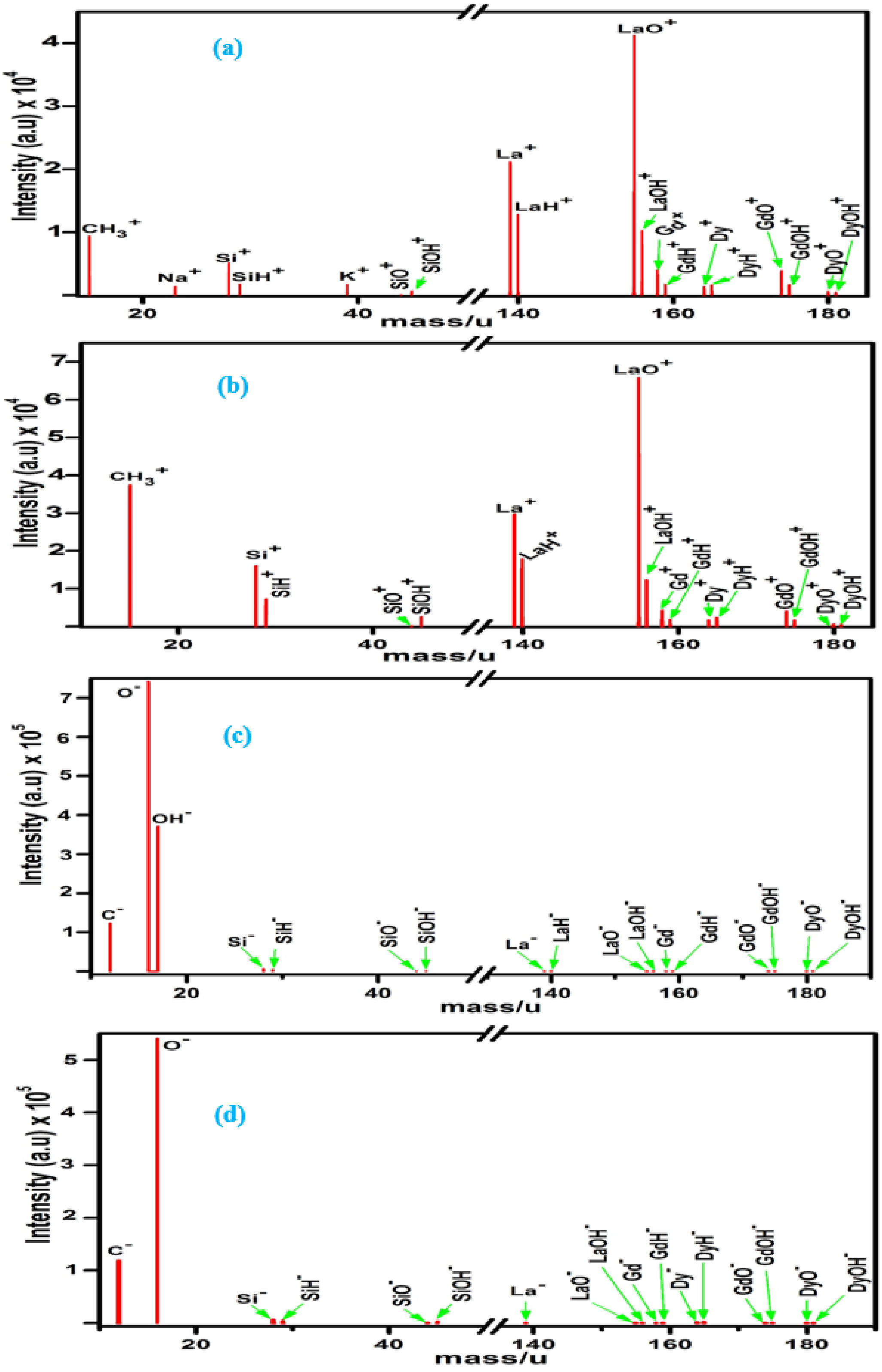

Fig. 7.5: ToF-SIMS mass spectra of LaGdSiO$_5$:Dy^{3+} nanophosphors for (a) positive ions analysis of as-prepared sample (b) positive ions analysis of sample annealed at 1000 °C for 1hr, (c) negative ions analysis of as-prepared sample and (d) negative ions analysis of sample annealed at 1000 °C for 1hr.

Table 7.2: Atomic/molecular ions and their atomic mass units

Positive atomic/molecular ions				Negative atomic/molecular ions			
Atomic/molecular ions	Mass/u	Atomic/molecular ions	Mass/u	Atomic/molecular ions	Mass/u	Atomic/molecular ions	Mass/u
CH_3^+	15	GdH^+	159	C^-	12	GdH^-	159
Na^+	23	GdO^+	174	O^-	16	Dy^-	164
Si^+	28	$GdOH^+$	175	OH^-	17	DyH^-	165
SiH^+	29	Dy^+	164	Si^-	28	GdO^-	174
K^+	39	DyH^+	165	SiH^-	29	$GdOH^-$	175
SiO^+	44	DyO^+	180	SiO^-	44	DyO^-	180
$SiOH^+$	45	$DyOH^+$	181	SiOH-	45	$DyOH^-$	181
La^+	139			La^-	139		
LaH^+	140			LaH^-	140		
LaO^+	155			LaO^-	155		
$LaOH^+$	156			$LaOH^-$	156		
Gd^+	158			Gd^-	158		

The PL excitation spectra of $LaGdSiO_5:Dy^{3+}$ x mol % (x = 0.05, 0.1, 0.25, 0.75, 1.0, 1.5, 2.0, 3.0, and 5.0) when monitoring emission at the wavelength of 573 nm using xenon lamp as the excitation source is shown in Fig. 7.6 (a). Two prominent peaks were observed at 227 and 241 nm. The $Ln^{3+} \rightarrow O^{2-}$ (Ln = Dy or Gd) charge transfer states and 4f→5d allowed electronic transitions of Dy^{3+} and Gd^{3+} are observed below 200 nm [24-28] and La^{3+} cannot induce excitation in/or near the visible region because it doesn't have 4f electrons. Hence, these excitation peaks cannot be assigned to any of these. In our previous report [29], the peak at 241 nm was not observed in $GdYSiO_5:Dy^{3+}$, but it was only observed in $LaYSiO_5:D^{3+}$ and $LaGdSiO_5:Dy^{3+}$. As a result, the excitation peak at 241 nm can be ascribed to La_{Gd}^{3+} isoelectronic impurities [30, 31]. The excitation band at 227 nm is host related and is ascribed to electronic transitions from the O2p valence band to the La (5d6s) and Gd (5d6s) conduction band [32, 33]. The excitation peaks intensities vary with the concentrations of Dy^{3+} ions. The 227 nm peak was more prominent at low concentration of Dy^{3+}, but the two peaks were almost equal at Dy^{3+} concentration of 0.25 mol %. For further increase in Dy^{3+} concentration however, the 241 nm peak intensities become more prominent. The decrease in the 227 nm peak with Dy^{3+} concentration could be due to the creation of more oxygen vacancies as the concentration of Dy^{3+} increases. Oxygen centers can act as luminescence enhancer or quencher [34, 35]. Doping with Dy^{3+} will disturbs the La_2SiO_5 and Gd_2SiO_5 lattices in the $LaGdSiO_5$ matrix, hence breaking the La-O and Gd-O bonds and generates more oxygen vacancies. Therefore, as the Dy^{3+} doping is increased, the amount of non-radiative oxygen vacancy centers around Dy^{3+} increases. The oxygen vacancies can trap and localize photoexcited electrons and hence decreasing their possibility to recombine with the holes. Since the increase in concentration of Dy^{3+} increases the non-radiative oxygen centers and the amount of trapped electrons, it will subsequently decrease the photoluminescence intensity. The excitation peaks observed at 275, 313, 351 and 386 nm are ascribed to $^8S_{7/2}\rightarrow{}^6I_J$ and $^6P_J \rightarrow{}^8S_{7/2}$ f-f transitions of Gd^{3+} [36] and $^6H_{15/2} \rightarrow{}^6P_{7/2}$ and $^6H_{15/2}\rightarrow{}^4I_{13/2}$ f-f transitions of Dy^{3+} [37] respectively. The graph of the excitation intensities as a function of Dy^{3+} concentration for the 227 and 241 nm excitation intensities of $LaGdSiO_5:Dy^{3+}$ x mol % are respectively shown in Fig. 7.6 (b) and (c). In both cases, the excitation intensity increased with Dy^{3+} concentration and reached maximum at x = 0.25 and x = 1.0 for 227 and 241 nm peaks respectively. Beyond these concentrations, the intensity decreases due to concentration quenching phenomena, which is probably as a result of non-radiative transitions among Dy^{3+} ions. Concentration quenching can be in the form of exchange interaction, multipole-multipole interaction or radiation re-absorption [38]. The type of interaction can be known by calculating the critical distance (R_c) between the neighbouring Dy^{3+} ions using Blasse equation [39] given by

$$R_c = 2\left(\frac{3V}{4\pi C_o Z}\right)^{1/3} \tag{7.2}$$

where V is the volume of the unit cell, Z is the number of ions per unit cell and C_o is the optimum concentration of the activator. $Z_{La2SiO5} = Z_{Gd2SiO5} = 4$, $V_{La2SiO5} = 0.46687$ nm^3, $V_{Gd2SiO5} = 0.41642$ nm^3 [40]. If we assume that Dy^{3+} ions are evenly distributed in the La and Gd sites in the $LaGdSiO_5$ host matrix, then we can take the average value of the volume of the unit cell (V). Taken $V = V_{La2SiO5} + V_{Gd2SiO5}$ and $C_o = 1.0$, then the R_c value between Dy^{3+}-

Dy^{3+} is 0.59 nm. Since the R_c value is close to 0.50 nm (5Å), it implies that the concentration quenching in $LaGdSiO_5$ is dominated by exchange interaction between Dy^{3+} ions.

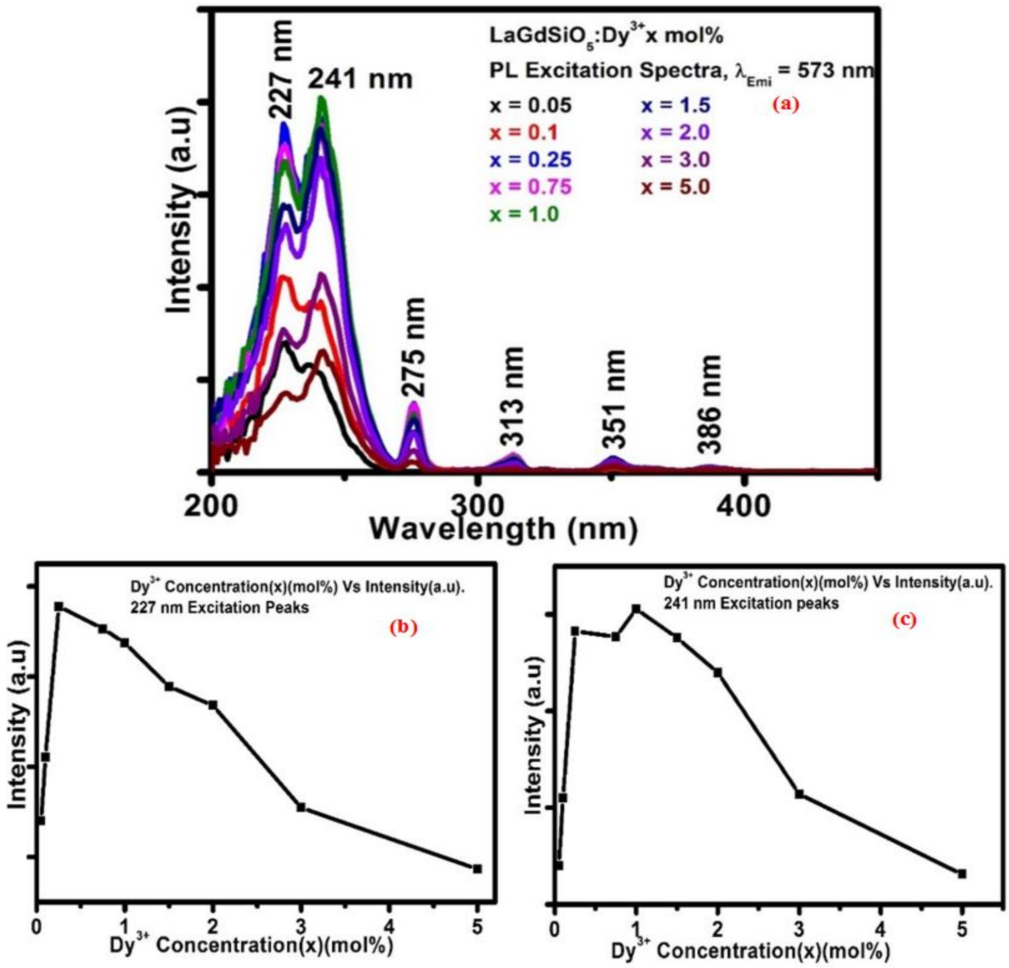

Fig. 7.6: (a) the excitation spectra of $LaGdSiO_5:Dy^{3+}$ x mol%. The graph of excitation intensities of $LaGdSiO_5:Dy^{3+}$ x mol % as a function of Dy^{3+} concentration for (b) 227 nm excitation peak and (c) 241 nm excitation peak (x = 0.025, 0.1, 0.25, 0.75, 1.0, 2.0, 3.0 and 5.0).

The PL emission spectra of $LaGdSiO_5:Dy^{3+}$ x mol % (x = 0.025, 0.1, 0.25, 0.75, 1.0, 2.0, 3.0 and 5.0) when exciting at the wavelengths of 227 and 241 nm are shown in Fig.7.7 (a) and (b) respectively. The emission peaks observed at 485, 573, 668 and 756 nm are ascribed to $^4F_{9/2}\rightarrow{}^6H_{15/2}$, $^4F_{9/2}\rightarrow{}^6H_{13/2}$ $^4F_{9/2}\rightarrow{}^6H_{11/12}$ and $^4F_{9/2}\rightarrow{}^6H_{9/2}$ f→f transition of Dy^{3+} respectively [40], while the small peak at 613 nm is ascribed to $^8G_{7/2}\rightarrow{}^6P_{5/2}$ electronic transition of Gd^{3+} [41]. In Fig. 7.7 (a) and (b), the maximum emission intensities for the 227 and 241 nm excitations were obtained when x = 0.25 and 1.0 respectively. Fig. 7.7 (c) shows the energy diagram of Dy^{3+} located between the valence and conduction bands of the host matrix. When excited with UV-light, electrons are promoted from the valence band of the host to its conduction band and holes are generated in the valence band. Some of the excited electrons relax at the higher energy levels of Dy^{3+}. After undergoing non-radiative transitions to $^4F_{9/2}$ level, the excited electron recombine to the various energy levels of Dy^{3+} and gives emission as shown in Fig. 7.7(c).

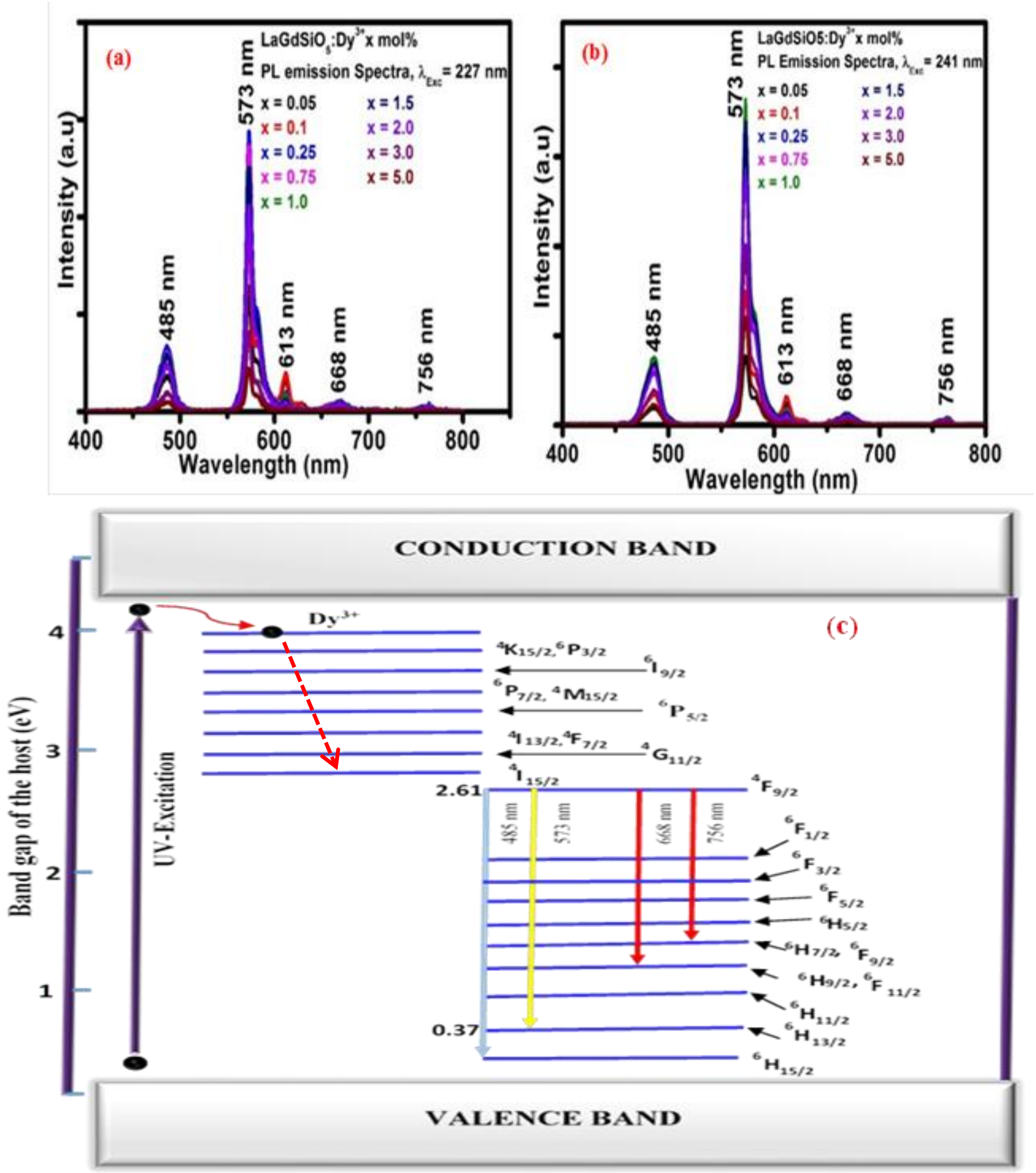

Fig. 7.7: PL emission spectra of $LaGdSiO_5{:}Dy^{3+}$ x mol % (x = 0.025, 0.1, 0.25, 0.75, 1.0, 1.5, 2.0, 3.0 and 5.0) monitored under (a) 227 nm excitation wavelength and (b) 241 nm excitation wavelength, (c) The energy diagram of Dy^{3+} between the bands of the host matrix.

Fig. 7.8 (a) and (b) show respectively the excitation and emission spectra of three of the samples (x = 0.25, 0.75 and 1.0 mol %) with highest intensities after annealing at 1000 °C for 1hr. A remarkable increase was observed on the excitation peaks at 227 nm when monitoring emission at the wavelength of 573 nm, but the excitation peaks at 241 nm reduced drastically. The decrease in the 241 nm excitation peak intensity could be attributed to reduction of concentration of the isoelectronic impurities after annealing. The highest excitation and emission intensities were obtained in Fig. 7.8 (a) and (b) when the Dy^{3+} concentration was 0.25 mol%. Using eqn. 7.2, the R_c value for the annealed sample is 0.94 nm. The R_c value being greater than 0.5 nm suggests that Dy^{3+}-Dy^{3+} interactions in the annealed samples could be dominated by multipole-multipole interaction [42].

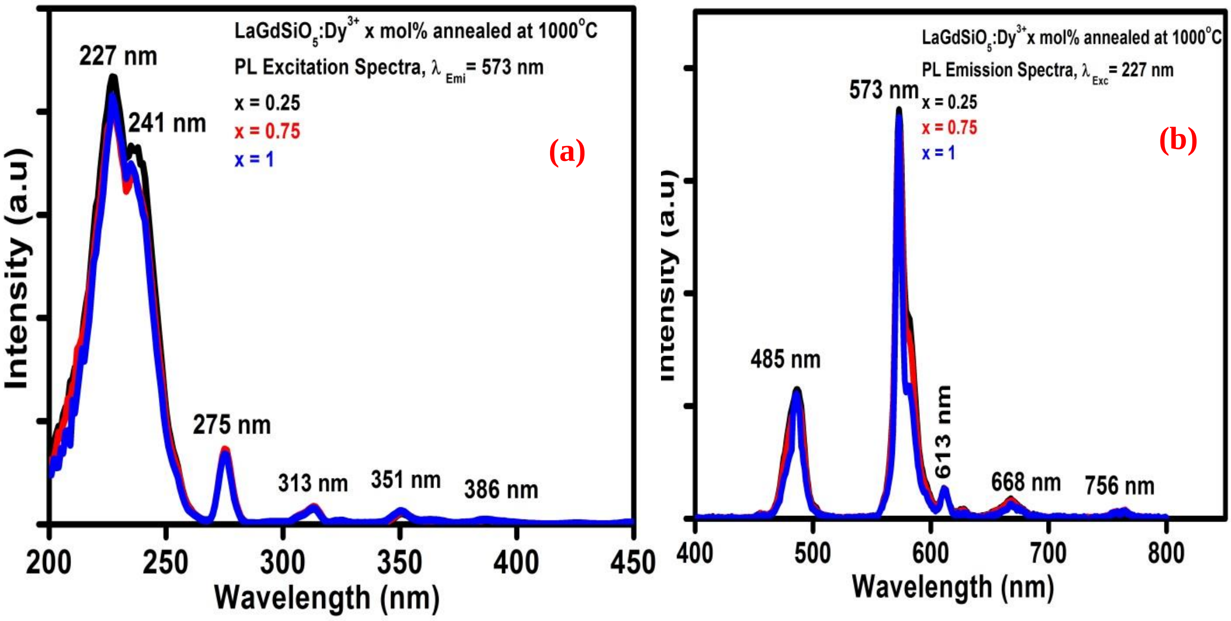

Fig. 7.8: The PL (a) excitation and (b) emission spectra of $LaGdSiO_5:Dy^{3+}$ x mol% (x = 0.25, 0.75 and 1.0) nanophosphors annealed at 1000 °C for 1hr studied under emission and excitation wavelengths of 573 nm and 227 nm respectively.

Fig. 7.9 (a) and (c) shows respectively the PL emission spectra of the as-prepared and annealed samples excited using a 325 nm He-Cd laser. The emission lines are similar to those shown in Fig. 7.7 (a) and (b) except for a broad blue emission bands in the 400 – 460 nm regions, with maximum at 415 nm. This emission is ascribed to the self-trapped excitons (STE) in SiO_2 [42]. The blue emission was not observed when xenon lamp was used as the excitation source because the measurement was taken in phosphorescence mode while the

325 nm He-Cd laser measurement was in fluorescence mode. Phosphorescence is light emission that persists (after-glow) longer than 0.1 s, while fluorescence emission occurs during excitation process, with a life time less than 10 ms [44]. In literature, the life time of SiO_2 is in the range of 0.125–5.000 ns [45], hence emission from SiO_2 cannot be detected in phosphorescence mode because of its smaller life time. The other PL emission lines observed at 485, 573, 668, and 756 nm are respectively assigned to $^4F_{9/2}\rightarrow{}^6H_{15/2}$, $^4F_{9/2}\rightarrow{}^6H_{13/2}$, $^4F_{9/2}\rightarrow{}^6H_{11/12}$ and $^4F_{9/2}\rightarrow{}^6H_{9/2}$ f→f electronic transitions of Dy^{3+} ions [46]. Fig. 7.9 (b) shows how the emission intensities varies with the molar concentrations (x) of Dy^{3+} in the as-prepared samples. The two emission peaks from Dy^{3+} (485 nm and 573 nm) varies in the same manner with Dy^{3+} molar concentration and reached maximum when $x = 1.0$. However, the emission peaks from STE in SiO_2 varies in a different manner with some having maxima at 415 nm and others at 438 nm. For the annealed samples, the blue emission from STE in SiO_2 decreased drastically as shown in Fig. 7.9 (c). This suggests that the number of traps in the material decreased after annealing. Fig. 7.9 (d) shows how the emission intensities vary with Dy^{3+} concentration for the annealed samples. For the 485 nm Dy^{3+} transition, the maximum emission intensity was obtained when $x = 3$, but for the 573 nm Dy^{3+} transition, the maximum emission intensity was obtained when $x = 1.5$. However, STE in SiO_2 showed broad peak with maxima at 415 nm and gave maximum emission intensity when $x = 1$. The dissimilarities observed in the intensity maxima of these peaks with the change in concentration of Dy^{3+} could be linked to the effect of oxygen vacancies created by Dy^{3+} ions on the crystal field of the host matrix [34, 35, 47]. The ratio at which the blue (485 nm) and the yellow (573 nm) emission of Dy^{3+} varies depends wholly on where Dy^{3+} ions are located in the symmetry of the host lattice. The yellow emission is hypersensitive to the chemical environment of the Dy^{3+} ions, and hence can vary easily with little change in the chemical environment. However, this is obtainable only when Dy^{3+} ions are located at low symmetry (without inversion center) in the host matrix. On the other hand, the blue emission can yield stronger emission intensity if Dy^{3+} ions are located at higher symmetry (with an inversion center) in the host matrix [48]. Furthermore, if the ligand fields is situated in or very close the inversion symmetry in the host matrix, both the blue and yellow emissions gives equivalent emission intensities [49, 50]. Therefore, if the ratio of the blue and yellow emission intensity of Dy^{3+} depends on where the Dy^{3+} ions are located in the symmetry of the host matrix and the oxygen vacancies created by the change in the concentration of Dy^{3+} ion can affect crystal field of the host matrix. It implies that the change in the concentration of Dy^{3+} can affect the ratio of the emission intensities of the blue and yellow emission of Dy^{3+}. The inset in Fig. 7.9

(d) is a magnified graph of Dy^{3+} concentrations versus the emission intensities of STE in SiO_2 for the annealed samples.

Fig. 7.10 shows the energy diagram of Dy^{3+} between the bands of the host matrix when monitoring the excitation using a 325 nm He-Cd lasers. Under 325 nm He-Cd lasers excitation, Dy^{3+} electrons were excited from $^6H_{15/2}$ ground state to $^4K_{15/2}$ excited state of Dy^{3+} and holes were generated in the ground state. The excited electrons become free electrons and move freely in the excited state and likewise the holes in the ground state. Some of the free electrons can escape into the host matrix and are trapped by defects in the host. The recombination of the excited electrons in the conduction band and the holes in the valence band can occur in different ways: it can occur through band-to-band transition or step-wisely through localized energy levels within the forbidden gap. In band-to-band transition, recombination occur directly from the excited state of Dy^{3+} to its ground states and give emissions after undergoing non-radiative transition to $^4F_{9/2}$ state of Dy^{3+} as shown at position (1) in Fig. 7.10. The recombination through localized energy levels within the forbidden gap can occur as a result of electrons trapped during excitation or in the process of recombination. The trapped electron can either transit into the $^4K_{15/2}$ excited state of Dy^{3+} or it can relax to the ground states of Dy^{3+} and give emissions after undergoing non-radiative transition to $^4F_{9/2}$ state of Dy^{3+} as shown in position (2) in Fig. 7.10. Position (3) in Fig. 7.10 is used to represent the emission from self-trapped excitons (STE) in SiO_2. Excited electron and hole can couple together by a Coulomb attraction. STE occurs in structures when an excited electron and a hole spontaneously create a localized distortion in the lattice, resulting in the lowering of their total energy, and they localizes and are trapped in the distortion [51]. This leads to breaking of bonds and thus resulting in the creation of dangling bonds in the system. In SiO_2, dangling bonds can be in the form of “non-bridging oxygen” or “silicon dangling bond”.

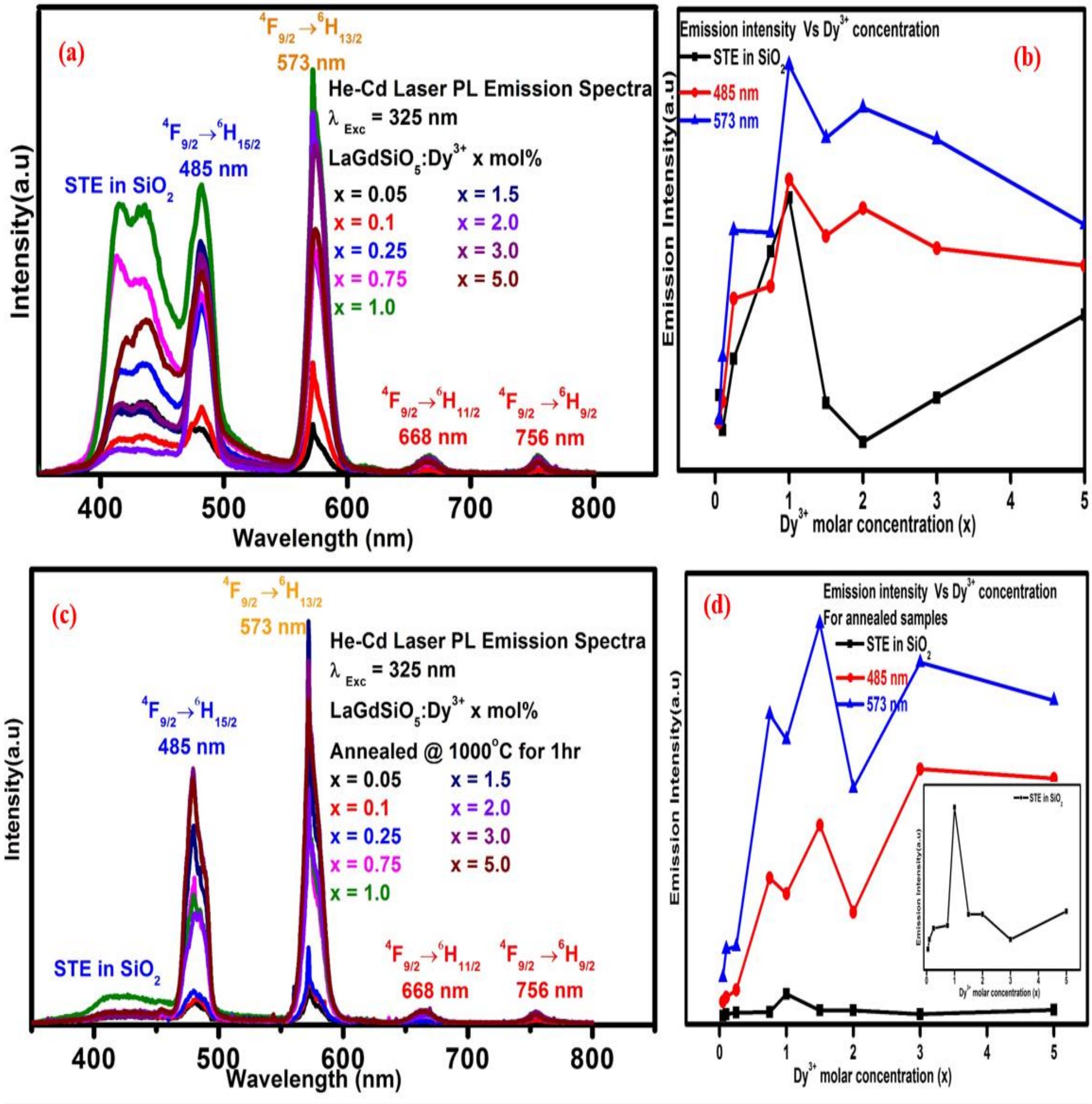

Fig. 7.9: (a) The PL emission spectra of LaGdSiO$_5$:Dy^{3+} x mol% (x = 0.05, 0.1, 0.25, 0.75, 1.0, 2.0, 3.0 and 5.0) monitored using the PL system with 325 nm He-Cd lasers as excitation source. (b) Variation of the emission intensity of the STE emission, 485 nm emission and 573 nm emission with the molar concentration of Dy^{3+}. (c) The PL emission spectra of the samples after annealing at 1000 ℃ for 1hr. (d) How the STE emission band, 485 nm and 573 nm emission lines varies with Dy^{3+} molar concentrations. The inset in (d) is a magnified graph of Dy^{3+} concentrations versus the emission intensities of STE in SiO$_2$ for the annealed samples.

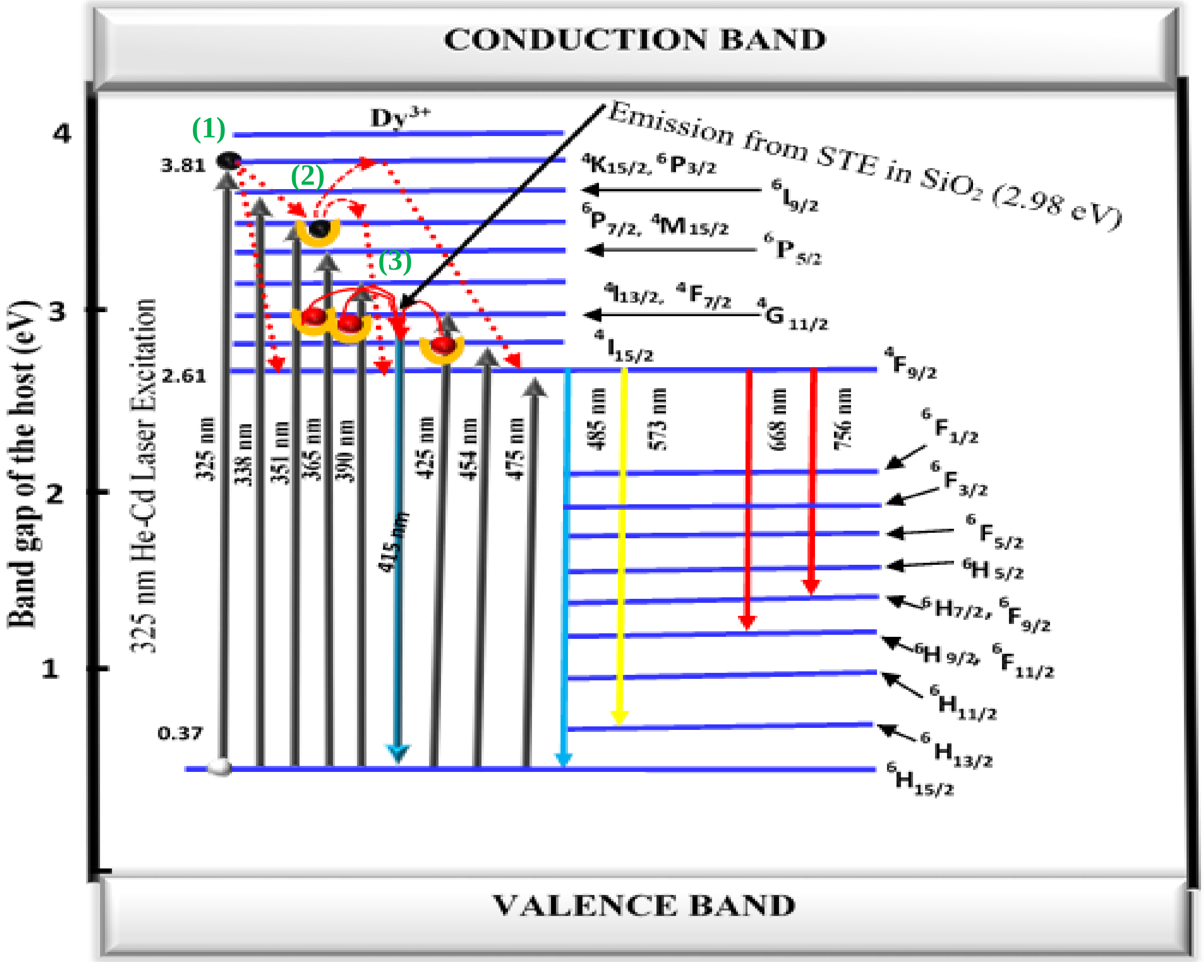

Fig. 7.10: Energy level diagram showing the energy level diagram of Dy^{3+} between the bands of the $LaGdSiO_5$ host matrix.

The CIE coordinates of the nanophosphors from the emission spectra of the as-prepared and the annealed samples shown in Fig. 7.9 (a) and (c) are shown respectively in Fig. 7.11 (a) and (b). For the as-prepared samples, the coordinates vary from blue to yellow through white with the variation of the concentration of Dy^{3+}. The coordinates of (0.343, 0.358) and (0.342, 0.357) were obtained at point F in Fig. 7.11 for x = 1.5 and 3.0 respectively and they are close to white light. The coordinates of the annealed samples vary with Dy^{3+} concentration as shown in Fig. 7.9 (c) and the coordinate of (0.326, 0.343) at point A were obtained when x = 1. The CIE coordinates and the corresponding Dy^{3+} concentration for the as-prepared and the annealed samples are shown in table 7.3.

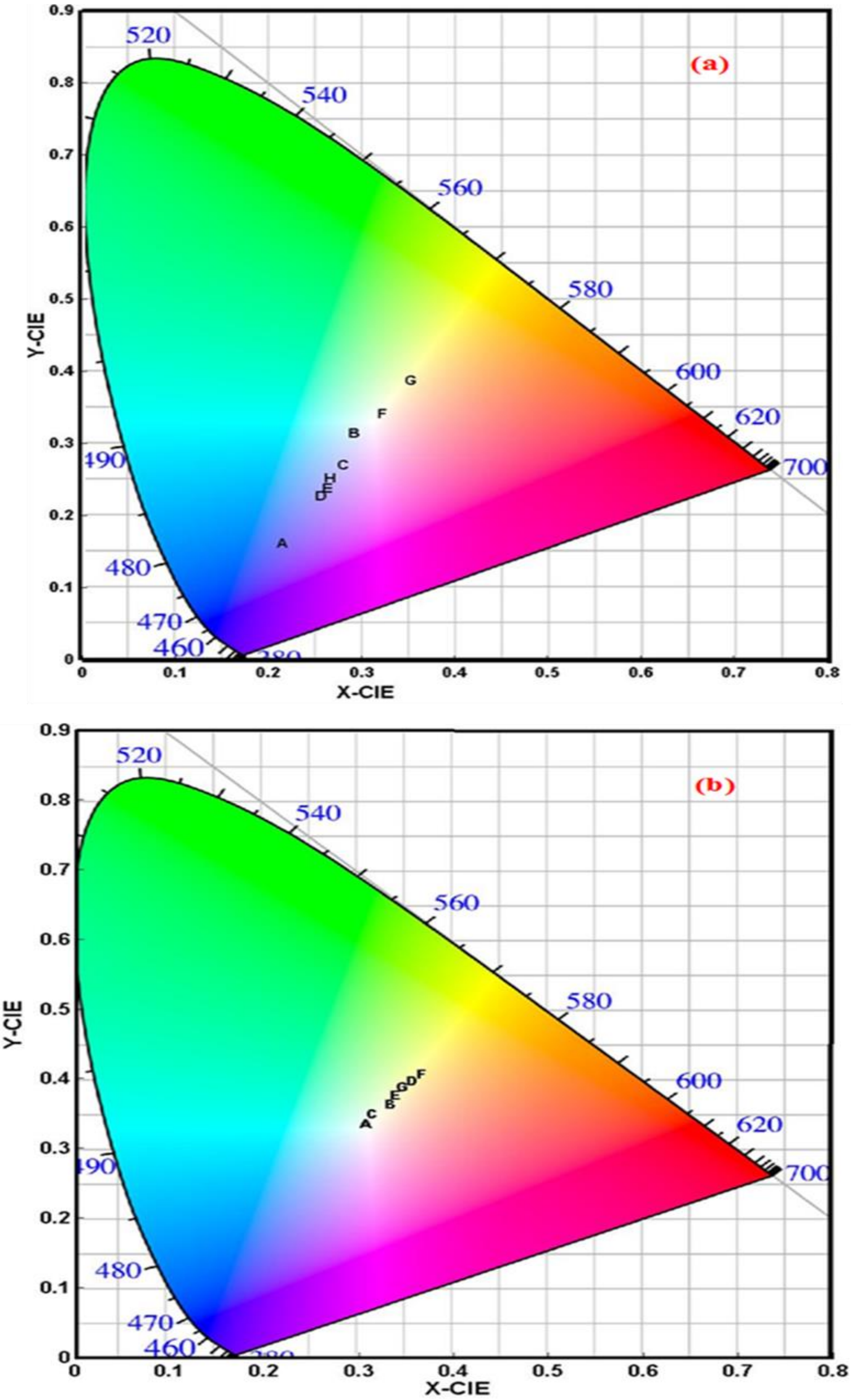

Fig. 7.11: CIE coordinates diagram of LaGdSiO$_5$:Dy^{3+} x mol% studied with a PL system using a 325 nm He-Cd laser as excitation source for (a) the as-prepared and (b) the annealed samples.

Table 7.3: CIE Coordinates of LaGdSiO$_5$:Dy^{3+} x mol

$LaGdSiO_5:Dy^{3+}$ x mol%	As-prepared samples		Annealed @ 1000 ºC for 1hr	
	Letters	CIE Coordinates	Letters	CIE Coordinates
x = 0.05	**A**	(0.222, 0.183)	**A**	(0.326, 0.343)
x = 0.1	**B**	(0.304, 0.315)	**B**	(0.348, 0.376)
x = 0.25	**C**	(0.295, 0.285)	**C**	(0.325, 0.347)
x = 0.75	**D**	(0.269, 0.246)	**D**	(0.369, 0.400)
x = 1.0	**E**	(0.277, 0.255)	**E**	(0.353, 0.380)
x = 1.5	**F**	(0.343, 0.358)	**D**	(0.369, 0.405)
x = 2.0	**G**	(0.376, 0.403)	**F**	(0.376, 0.407)
x = 3.0	**F**	(0.342, 0.357)	**D**	(0.365, 0.400)
x = 5.0	**H**	(0.281, 0.269)	**G**	(0.361, 0.392)

7.4. Conclusion

By varying the molar concentrations (x) of Dy^{3+} (x = 0.025, 0.1, 0.25, 0.75, 1.0, 1.5, 2.0, 3.0 and 5.0) in $LaGdSiO_5$ host matrix we prepared novel nanophosphors using urea- and ammonium nitrate-assisted solution combustion method. The XRD showed transition from low temperature to high temperature phase after annealing the samples at temperature of 1000 ℃ for 1hr. The excitation spectra when monitoring the emission at 573 showed two peaks at 227 and 241 nm. The 227 nm peak give the highest excitation intensity when x = 0.25 mol% while the 241 nm peak give the highest excitation intensity when x = 1 mol%. Therefore, the best luminescence intensities can be achieved from $LaGdSiO_5:Dy^{3+}$ when exciting at 227 nm at Dy^{3+} molar concentration of 0.25% or exciting at 241 nm at Dy^{3+} molar concentration of 1 mol%. The PL intensities of the 241 nm excitation line decreased drastically after annealing at 1000 ℃ for 1hr while the intensity of the 227 nm peaks increased. This suggests that a more stable luminescence can be generated from $LaGdSiO_5:Dy^{3+}$ by exciting at 227 nm. The emission spectra when monitoring the excitation at 227 and 241 nm showed two prominent peaks from Dy^{3+} appearing at 485 nm and 573 nm. When the phosphors were excited using a 325 nm He-Cd lasers, the emission spectra showed an extra broad blue emission ranging from 400 to 460 nm with a maximum around 415 nm which was ascribed to self-trapped excitons (STE) in SiO_2. This extra broad emission decreased after annealing, suggesting that the level of impurities in the samples was decreased. The CIE calculated from the emission spectra generated from the 325 nm He-Cd lasers showed coordinates which varied from blue to yellow through white with change in the molar concentration of Dy^{3+} in the as-prepared samples. The CIE of the annealed samples followed the same trend with the as-prepared samples but the CIE coordinates were shifted. We can therefore conclude that our material has a potential application in UV-pumped multicolour and white light emitting diodes.

7.5. References

[1] E. Nakazawa, Excitation energy transfer and cooperative optical phenomena, In: S. Shionoya, W.M. Yen, H. Yamamoto, (Eds), Phosphor handbook, 2nd Ed. CRC press, 2006, pp. 99-110.

[2] R.C. Ropp, Studies in inorganic chemistry 21 “Luminescence and the solid state” 2nd Ed; Elsevier. B.V. 2004, pp. 447-603.

[3] G.S.R. Raju, E. Pavitra, J.S. Yu, Facile template free synthesis of $Gd_2O(CO_3)_2.H_2O$ chrysanthemum-like nanoflowers and luminescence properties of corresponding $Gd_2SiO_3:RE^{3+}$ spheres, Dalton Trans. 42 (2013) 11400-11410.

[4] X. Zhang, F. Meng, W. Li, S. Kim, Y.M. Yu, H.J. Seo, Investigation of energy transfer and concentration quenching of Dy^{3+} luminescence in $Gd(BO_2)_3$ by means of fluorescence dynamics, J. Alloy & Comp. 578 (2013) 72-76.

[5] I.M. Nagpure, V.B. Pawade, S.J. Dhoble, Combustion synthesis of $Na_2Sr(PO_4)F:Dy^{3+}$ white light emitting phosphor, J. Bio. Chem. Lumi. 25 (1999) 9-13.

[6] J, Felsche, The crystal chemistry of the rare-earth silicates” in Structure and Bonding; Vol. 13, in: J.D. Dunitz, P. Hemmerich, J.A. Ibers, C.K. Jorgensen, J.B. Neilands, R.S. Sir Nyholm, D. Reinen, R.J.P. Williams (Eds.), Rare Earths, Springer-Verlag: New York, 1973, pp. 99-197.

[7] Y.I. Smolin, S.P. Tkachev, Determination of the structure of gadolinium orthosilicate $Gd_2O_3•SiO_2$ Kristalografiya. 14 (1969) 22–25.

[8] K. Fukuda, T. Iwata, Crystal structure of lanthanum oxyorthosilicate, La_2SiO_5, Powder Diffr. 21 (2006) 4. DOI: 10.1154/1.2383066

[9] R. Lisiecki, G. Dominiak-Dzik, P. Solarz, W. Ryba-Romanowski, M. Berkowski, M. Glowacki, Optical Spectra and Luminescence of the Dy-doped Gd_2SiO_5 Single Crystal, Appl. Phys. B. 98 (2010) 337-346.

[10] J. Wen, C.K. Duan, L. Ning, Y. Huang, S. Zhan, J. Zhang, M. Yin, Spectroscopic distinctions between two types of Ce^{3+} ions in X2-Y_2SiO_5: A theoretical investigation, J. Phys. Chem. A. 118 (2014) 4988-4994.

[11] E.M. Rabinovich, J. Shmulovich, V.J. Fratello, N.J. Kopylov, Am. Ceram. Soc. Bull. 66[10] (1987) 1505-1509.

[12] R.D. Shannon, Revised effective ionic radii and systematic studies of interatomic distances in halides and chalcogenides Acta. Crystallogr. A32 (1976) 751–767.

[13] A.A. Bosak, C. Dubourdieu, J.P. Sénateur, O. Yu, Hexagonal rare earth (R = Eu-Dy) magnites: XRD study of epitaxially stabilized films, Cryst. Eng. 5 (2002) 355-364.

[14] R.D. Shannon, C.T. Prewitt, Effective ionic radii in oxides and fluorides, Acta. Crystallogr. B25 (1969) 925- 946.

[15] G.K. Williamson, W.H. Hall, X-ray line broadening from filed aluminium and wolfram, Acta Metallurgica. 1 (1953) 22-31.

[16] V.D. Mote, Y. Purushotham, B.N. Dole, Williamson-Hall analysis in estimation of lattice strain in nanometer-sized ZnO particles, J. theor. Appl. Phys. 6, (2002) 6 (pp. 8).

[17] F.S. Aguirre-Tastado, M. Milojevic, B. Lee, J. Kim, R.M. Wallace, In situ study of surface reactions of atomic layer deposited $La_xAl_{2-x}O_3$ films on atomically clean $In_{0.2}Ga_{0.8}As$, Appl. Phys. Lett. 93 (2008)172907.

[18] T. Gougousi, M.J. Kelly, D.B. Terry, G.N. Parsons, Properties of La-silicate high-K dielectric films formed by oxidation of La on silicon, J. Appl. Phys. 93 (2003)1691-1696.

[19] W.S. Kim, S.K. Park, D.Y. Moon, B.W. Kang, H.D. Kim, J.W. Park, Characteristics of La_2O_3 Thin Films Deposited Using the ECR Atomic Layer Deposition Method, J. Korean Phys. Soc. 55 (2009) 590-593.

[20] C. Li, Y. Shen, S. Zhu, S. Shen, Supported Ni-La-O_x for catalytic decomposition of N_2O I: component optimization and synergy, RSC Adv. 4 (22014) 29107-29119.

[21] J.L. Her, M.H. Wu, Y.B. Peng, T.M. Pan, W.H. Weng, S.T. Pang, L. Chi, High performace $GdTi_xO_y$ electrolyte-insulator-semiconductor pH sensor and biosensor, Int. J. Electrochem. Sci. 8 (2013) 606-620.

[22] Sodium-Chemicool (online). Available chemicool.com (accessed August, 2014).

[23] Potassium-Chemicool (online). Available chemicool.com (accessed August, 2014).

[24] A.K. Gulnar, V. Sudarsan, R.K. Vasta, R.C. Hubli, U.K. Gautam, A. Vinu, A.K. Tyagi, $CePO_4$:Ln (Ln = Tb^{3+} and Dy^{3+}) Nanoleaves Incorporated in Silica Sols, Crystal Growth & Design. 9 (2009) 2451-2456.

[25] J. Gou, Y. Wang, F. Li, The luminescence properties of Dy^{3+}-activated SrB_4O_7 under VUV excitation, J. Lumin.128 (2008) 728- 731.

[26] H. Liang, Q. Zeng, Y. Tao, S. Wang, Q. Su, VUV-VU excited luminescent properties of calcium borophosphate doped with rare earth ions, Mat. Sci. & Eng. B. 98 (2003) 213-219.

[27] W. Zhao, S. An, B. Fan, S. Li, Photoluminescence properties of $MgY_4Si_3O_{13}$:Gd^{3+}, Tb^{3+} under vacuum ultraviolet excitation, Opt. Mat. 35 (2013) 1748-1751.

[28] I.N. Ogorodnikov, V.A. Pustovarov, S.I. Omelkov, D.O. Vostrov, L.I. Isaenko, Optical and Luminescence spectroscopy studies of electronic structure of $Li_6GdB_3O_9$ single crystals, Opt. Mat. 36 (2014) 1060-1064.

[29] S.N. Ogugua, S.K.K. Shaat, H.C. Swart, O.M. Ntwaeaborwa, Optical properties and chemical composition analyses of mixed rare earth oxyorthosilicate (R_2SiO_5, R = La, Gd and Y) doped Dy^{3+} phosphors prepared by urea-assisted solution combustion method, J. Phys. Chem. Soli. 83, (2015) 109–116.

[30] Y.V. Zorenko, Luminescence of Sc^{3+} and La^{3+} isoelectronic impurities in $Lu_3Al_5O_{12}$ single-crystal films. Opt. Spectrosc. 100 (2006) 572-580.

[31] Y. Zorenko, V. Gorbenco, V. Savchyn, T. Voznyack, M. Nikl, J.A. Mares, A. Winnacker, Novel UV-emitting single crystalline film phosphors grown by LPE method, Radiat. Meas. 45 (2010) 444-448.

[32] G. Li, C. Li, C. Zhang, Z. Cheng, Z. Quan, C. Peng, J. Lin, Tm_{3+} and/or Dy^{3+} doped LaOCl nanocrystalline phosphors for field emission displays, J. Mater. Chem. 19 (2009) 8936-8943.

[33] M. Jia, J. Zhang, S. Lu, J. Sun, Y. Luo, X. Ren, H. Song, X. Wang, UV. Excitation properties of Eu^{3+} at the S6 site in bulk and nanocrystalline cubic Y_2O_3, Chem. Phys. Lett. 384 (2004) 193-196.

[34] N. Serpone, Is the band gap of pristine TiO_2 narrowed by anion- and cation-doping of titanium dioxide in second-generation photocatalysts, J. Phys. Chem. B. 110 (2006) 24287-24293.

[35] B. Choudhury, A. Choudhury, Oxygen vacancy and dopant concentration dependent magnetic properties of Mn doped TiO_2 nanoparticle, Curr. Appl. Phys. 13 (2013) 1025-1031.

[36] Y. Li, Y. Chang, Y. Chang, Y. Lin, C. Laing, Luminescence and Energy Transfer Properties of Gd^{3+} and Tb^{3+} in $LaAlGe_2O_7$, J. Phys. Chem. C, 111 (2007) 10682-10688.

[37] X. Liu, W. Xiang, F. Chen, Z. Hu, W. Zhang, Synthesis and photoluminescence characteristics of Dy^{3+} doped $NaY(WO_4)_2$ phosphors Mater. Res. Bull. 48 (2013) 281-285.

[38] Q. Liu, Y. Liu, Z. Yang, Y. Han, X. Li, G. Fu, Multiwavelength excited white-emitting phosphor Dy^{3+}-activated $Ba_3Bi(PO_4)_3$ J. Alloys Compd. 515 (2012) 16-19.

[39] K. Banse, H. Boersch, G. Herziger, G. Schäfer, W. Seelig, Nonresonant continuous laser oscillation in the visible, Phys. Lett. A, 28 (1968) 6-7.

[40] R. Lisiecki, G. Dominiak-Dzik, P. Solarz, W. Ryba-Romanowski, M. Berkowski, M. Glowacki, Optical Spectra and Luminescence dynamics of the Dy-doped Gd_2SiO_5 Single Crystal, Appl. Phys. B. 98 (2010) 337-346.

[41] R.T. Wegh, A. Meijerink, First observation of visible luminescence from trivalent gadolinium, Acta Phys. Polonica. A. 90 (1996) 333-337.

[42] S. Xin, Y. Wang, Z. Wang, F. Zhang, Y. Wen, G. Zhu, An intense red-light phosphor $YBa_3(PO_4)_3$:Eu^{3+} for near-ultraviolet light emitting diode application, Electrochem. Soli. Stat. Lett. 14 (11) (2011) H438-H441.

[43] C. Itoh, K. Tanimura, N. Itoh, Optical studies of self-trapped excitons in SiO_2, J. Phys. C: Solid State Phys. 21(1988) 4693- 4702.

[44] E. Nakazawa, Transient characteristics of luminescence, in: S. Shionoya, W.M. Yen, H. Yamamoto (Eds.), Phosphor handbook, 2nd Ed ,CRC press, 2006, pp. 83-97.

[45] A. Uedono, L. Wei, S. Tanigawa, R. Suzuki, H. Ohgaki, Characterization of silicon dioxide deposited by low-temperature CVD using TEOS and ozone by monoenergetic positron beams, Hyperfine Interact. 84 (1994) 231-236.

[46] F. Zhang, Y. Wang, Y. Wen, D. Wang, Y. Tao, Photoluminescence properties of RE^{3+}-activated $Na_3GdP_2O_8$ (RE^{3+} = Tb^{3+}, Dy^{3+}, EU^{3+}, Sm^{3+}) under VUV excitation, Opt. Mat. 33 (211) 475-479.

[47] S. Yun-Bin, Z. Xiang-Qun, L. Guo-Ke, C. Zhao-Hua, Effects of oxygen vacancy location on the electronic structure and spin density of Co-doped rutile TiO_2 dilute magnetic semiconductors, Chin. Phys. B. 21 (2012) 047503-047508.

[48] C.R. Kesavulu, C.K. Jayasankar, White light emission in Dy^{3+}-doped lead fluorophosphate glasses, Mat. Chem. & Phys. 130 (2011) 1078-1085.

[49] C. Cao, H.K. Yang, B.K. Moon, B.C. Choi, J.H. Jeong, Host Sensitized White Luminescence of Dy^{3+} Activated $GdPO_4$ Phosphors J. Electrochem. Soci. 158(2) (2011) J6-J9.

[50] G. Han, Y. Wanga, C. Wua, Zhang, Hydrothermal synthesis and vacuum ultraviolet-excited luminescence properties of novel Dy^{3+}-doped $LaPO_4$ white light phosphors J. Mater. Res. Bull. 44 (2009) 2255–2257.

[51] S.I. Beigi, S.G. Louie, Self-Trapped Excitons in Silicon Dioxide: Mechanism and Properties, Phys. Rev. Lett. 95 (2005) 156401, DOI: 10.1103/PhysRevLett.95.156401

CHAPTER EIGTH

Blue Light excited $LaGdSiO_5$ doped x molar % Dy^{3+} white light-emitting nanophosphors for solid state lighting applications

8.1. Introduction

The most important property of any phosphor is its quantum efficiency (i.e. its brightness) which is the ratio of the number of photons that a phosphor absorbs to the number of photons it emits. Self-absorption, band gap, density, thermal and the chemical stability and decay time are other important properties of phosphors. Phosphors are often graded based on these properties with the superior ones having higher quantum efficiency, minimal self-absorption, wide band gap, high density, high thermal and chemical stability and fast decay time [1, 2]. Rare-earth oxyorthosilicates (R_2SiO_5, R = La or Gd) crystals have demonstrated outstanding characteristics of good host for various rare-earth ions. For instance, they have shown wide band gap of about 6.0 eV, high quantum efficiency, minimal self-absorption, high density, fast decay time [1], and good thermal and chemical stability [3, 4]. Some R_2SiO_5 has shown quantum efficiency twice as that of germanium oxide (BGO) [5], and life time about five times less than BGO [6]. These properties gives R_2SiO_5 the excellent host ability to accommodate many rare-earth ions for various phosphor applications [7-13].

R_2SiO_5 are produced from 1:1 composition of binary rare-earth silicate (R_2O_3-SiO_2) system. They are classified into two monoclinic structure groups (small and large ionic radius rare-earth ions) in accordance with the size of the ionic radius of the rare-earth ion. The small ionic radii rare-earth ions in R_2SiO_5 include all the light rare-earth elements and Tb (La-Tb) while the large ionic radii rare-earth ions in R_2SiO_5 include all the heavy rare-earth elements except Tb (Y, Dy-Lu). The small ionic radius radii rare-earth ions in R_2SiO_5 have monoclinic crystallographic point group with space group *C2/c* and *B2/b* belonging respectively to the low (*X1*) and high (*X2*) temperature phases. The large ionic radii rare-earth ions in R_2SiO_5 have monoclinic crystallographic point group with space group *P21/c* and *12/a* belonging to the low and high temperature phases respectively. Both La_2Sio_5 and Gd_2SiO_5 belong to the small ionic radii rare-earth ions in R_2SiO_5 crystals and they have two crystallographic sites R1 and R2 coordinated by 7 and 9 oxygen atoms respectively and linked together by tetrahedral SiO^{4-} ions [14-16].

Blue-light excited light emitting diodes (LEDs) have advantages over their UV-light excited counterparts due to the fact that the UV-converted LEDs suffers loss of energy during the conversion of UV-light to white light leading to low luminous efficiency of the LED. This approach also cause the solarization of the resin used for packaging the LED due to the high energy of the UV-light [17]. White light emitting phosphors can be achieved by co-doping a sensitizer and activator into the same host matrix. In this case, the constituents of the white light may be from a single activator at various crystal sites or from different activators [18, 19]. Zhang et al reported white light generated from $NaCaBO_3$:Ce^{3+}, Tb^{3+}, Mn^{2+} single phosphors [20]. Other reports on white light emitting single phosphors by Shaat et al [21], Lorbeer et al [22], Guo et al [23], and Chien-Hao et al [24]. The major disadvantage of co-doping sensitizer and activator into a single host is the high cost of the these materials, which are required at high concentration to get an efficient result since the distance between the sensitizer and the activator ions are required to be very small (about 1 nm) [25].

To overcome these challenges, a singly doped phosphor, which can generate white light when excited with blue light should be developed. Dy^{3+}-doped matrices can emit blue and yellow light [26] and this has made it one of the choices of an activator for white light emitting phosphors since a co-dopant is not required. The blue emission ($^4F_{9/2}\rightarrow{}^6H_{15/2}$) is a magnetic dipole transition and hardly varies with the crystal field around the Dy^{3+} ions. On the other hand, the yellow emission ($^4F_{9/2}\rightarrow{}^6H_{13/2}$) which is defined as hypersensitive is an electric dipole transition and highly sensitive to the crystal field around Dy^{3+} ions. As a result of the imbalance between the blue and the yellow emission, it is difficult to generate white light from Dy^{3+} doped matrices. Hence the host matrix and the excitation wavelength plays important role in accomplishing this goal. For host matrix without inversion center, Dy^{3+} ions are located in the low symmetry in the host matrix and the yellow emission ($^4F_{9/2}\rightarrow{}^6H_{13/2}$) of Dy^{3+} is stronger than the blue emission ($^4F_{9/2}\rightarrow{}^6H_{15/2}$) [27]. On the other hand, the blue emission can yield stronger emission if the Dy^{3+} ions are doped into a host matrix with inversion center and the Dy^{3+} ions are located in the higher symmetry [28]. Furthermore, when the Dy^{3+} ions are located at or close to the inversion symmetry of the host matrix, both the blue and the yellow emissions of Dy^{3+} yield equivalent emission intensities [29, 30]. The excitation wavelength can also influence the emission of Dy^{3+} [31].

Mixing La_2SiO_5 and Gd_2SiO_5 together can leverage the best qualities from these materials. We generated a single host $LaGdSiO_5$ by mixing La_2SiO_5 and Gd_2SiO_5 and doped it with different molar concentrations (x) of Dy^{3+} ions as activator (x = 0.05, 0.1, 0.25, 0.75, 1.0, 1.5, 2.0, 3.0 and 5.0). We monitored the photoluminescence (PL) emission with blue light excitation (425, 454 and 474 nm) and part of the incident blue light were absorbed and converted to emission. So, with the combination of the absorbed blue light and the blue emission from Dy^{3+}, we were able to balance the blue and the yellow emission which results in white emission. This is analogous to the InGaN-based YAG:Ce white LED, where InGaN LED is used to excite YAG:Ce yellow emitting phosphor and a portion of the blue light from InGaN LED is absorbed and re-emitted and combination of the blue emission from the InGaN LED and the yellow emission from YAG:Ce can yield white light [32].

8.2. Experimental

A detailed procedure for the samples preparation was discussed elsewhere [33]. The starting materials were lanthanum (III) nitrate hexahydrate $La(NO_3)_3.6H_2O$, gadolinium (III) nitrate hexahydrate $Gd(NO_3)_3.6H_2O$, dysprosium (III) nitrate hexahydrate $Dy(NO_3)_3.6(H_2O)$ and silicic acid (SiO_2H_2O). Urea $CO(NH_4)_2$ and ammonium nitrate (NH_4NO_3) were used as fuel. For each of the nine set of samples, the masses of SiO_2H_2O, $CO(NH_4)_2$ and NH_4NO_3 are 0.1000 g, 0.4690 g, and 0.6251 g respectively. For $LaGdSiO_5:Dy^{3+}$ 0.05 mol% (i.e. x = 0.05), the masses of $La(NO_3)_3.6H_2O$, $Gd(NO_3)_3.6H_2O$ and $Dy(NO_3)_3.6H_2O$ are respectively 0.6760 g, 0.7047 g and 0.0005 g. For x = 0.1, $La(NO_3)_3.6H_2O$ = 0.6757 g, $Gd(NO_3)_3.6H_2O$ = 0.7043 g and $Dy(NO_3)_3.6H_2O$ = 0.0011 g. For x = 0.25, $La(NO_3)_3.6H_2O$ = 0.6746 g, $Gd(NO_3)_3.6H_2O$ = 0.7035 g and $Dy(NO_3)_3.6H_2O$ = 0.0027 g. For x = 0.75 $La(NO_3)_3.6H_2O$ = 0.6712 g, $Gd(NO_3)_3.6H_2O$ = 0.6997 g and $Dy(NO_3)_3.6H_2O$ = 0.0081 g. For x = 1.0, $La(NO_3)_3.6H_2O$ = 0.6696 g, $Gd(NO_3)_3.6H_2O$ = 0.6980 g and $Dy(NO_3)_3.6H_2O$ = 0.0109 g. For x = 1.5, $La(NO_3)_3.6H_2O$ = 0.3331 g, $Gd(NO_3)_3.6H_2O$ = 0.3472 g and $Dy(NO_3)_3.6H_2O$ = 0.0082 g. For x = 2.0, $La(NO_3)_3.6H_2O$ = 0.3314 g, $Gd(NO_3)_3.6H_2O$ = 0.3455 g and $Dy(NO_3)_3.6H_2O$ = 0.0109 g. For x = 3.0, $La(NO_3)_3.6H_2O$ = 0.6560 g, $Gd(NO_3)_3.6H_2O$ = 0.6838 g and $Dy(NO_3)_3.6H_2O$ = 0.0326 g. For x = 5.0, $La(NO_3)_3.6H_2O$ = 0.6425 g, $Gd(NO_3)_3.6H_2O$ = 0.6697 g and $Dy(NO_3)_3.6H_2O$ = 0.0544 g. The structure was analyzed using (i) a Bruker D8 Advanced X-ray diffraction diffractometer (XRD) and (ii) a Nicolet 6700 Fourier transform infrared (FTIR) spectroscope. The ultraviolet visible (UV-Vis) spectrum was recorded using a Lambda 950 UV-Vis spectrometer, while the PL spectra were measured using a Cary Eclipse fluorescence spectrophotometer.

8.3. Results and Discussion

The XRD pattern of the highest and the least concentration of Dy^{3+} (i.e. x = 0.05 and x = 5.0 mol %) in the $LaGdSiO_5$ matrix were measured to monitor the effect of Dy^{3+} concentration on the structure of the host matrix. As can be seen from Fig. 8.1, the presence of Dy^{3+} in the host matrix has no significant effect on its structure. This can be as a result of the similarities in the ionic radii of the two host materials and that of the dopant. La^{3+} has ionic radii of 0.110 nm and 0.1216 nm in its seven and nine-fold coordinated sites respectively [34], while Gd^{3+} has atomic radii of 0.10 nm and 0.1107 nm in its seven and nine-fold coordinated sites respectively [35, 36]. When comparing the atomic radii of these elements to that of Dy^{3+} which are 0.1052 nm and 0.1167 nm in its six and eight-fold coordinated sites [34], it can be seen that they are quite similar in size, and as such Dy^{3+} ions can easily replace any of the two ions without causing any significant effect on the main structure [37]. The XRD patterns match with the standard monoclinic structures of La_2SiO_5 and Gd_2SiO_5 referenced in JCDPS file no: 40-0234 and 74-1795 respectively. The crystallographic planes indicated with the symbol "*" are from La_2SiO_5, while those indicated with "♦"are from Gd_2SiO_5. The average crystallite size (L) and the lattice train (ε) were calculated using the Williamson-Hall equation [38, 39] given by eqn. 8.1.

$$\beta_{hkl} Cos\theta = 4\varepsilon\ Sin\theta\ + \frac{K\,\lambda}{L} \tag{8.1}$$

where β_{hkl} is the peak width at half maximum of the diffraction peaks, θ is the Bragg angle, λ is the X-ray wavelength in nanometer (nm) and K is a constant usually taken as 0.9 or 0.89. The estimated crystallite sizes and the lattice strains are shown in table 8.1.

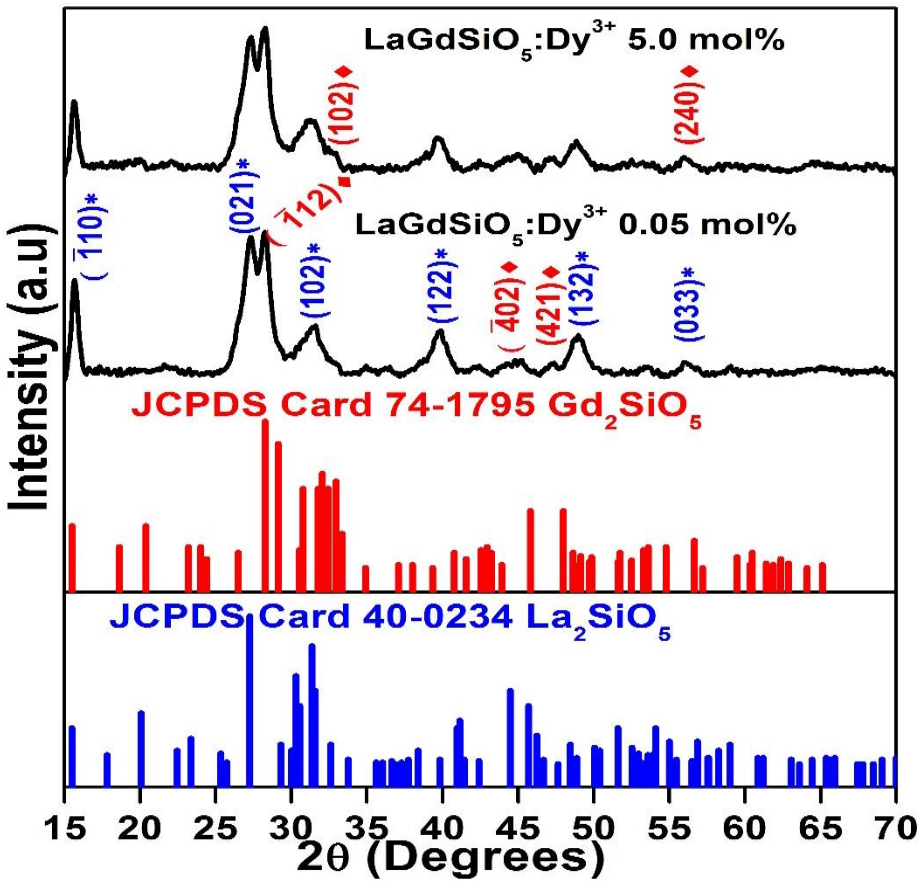

Fig. 8.1: XRD patterns of $LaGdSiO_5:Dy^{3+}$ x mol % (x = 0.05 and 5.0) and the standards of La_2SiO_5 and Gd_2SiO_5.

Table 8.1: The crystallite sizes and lattice strain of $LaGdSiO_5:Dy^{3+}$ nanophosphors

$LaGdSiO_5:Dy^{3+}$ x mol%	Crystallite size (*L*) (nm)	Strain (ε) ($\times 10^{-2}$)
x = 0.05	15	2.05
x = 0.75	16	1.95
x = 1.5	14	2.43
x = 3.0	12	1.64
x = 5.0	16	2.41

The stretching mode frequencies of our nanophosphors were determined using Fourier transformed infrared (FTIR) spectroscopy. The FTIR result obtained from $LaGdSiO_5:Dy^{3+}$ 1.0 mol % is shown in Fig. 8.2. The absorption peak observed around 3605 cm^{-1} have been assigned to the stretching mode of the OH groups, whereas the peak around 665, 880 and 1100 cm^{-1} are the characteristics of Si-O-Si group [40, 41]. The peak observed around 455 cm^{-1} is associated with La-OH and Gd-OH bending modes in $La(OH)_3$ and $Gd(OH)_3$ [40, 42-

45]. The bands at 1380, 1500 and 1655 cm^{-1} are assigned to the bending mode of water, whereas those at 3120 and 3430 cm^{-1} are assigned to the stretching mode of water [40, 46, 47].

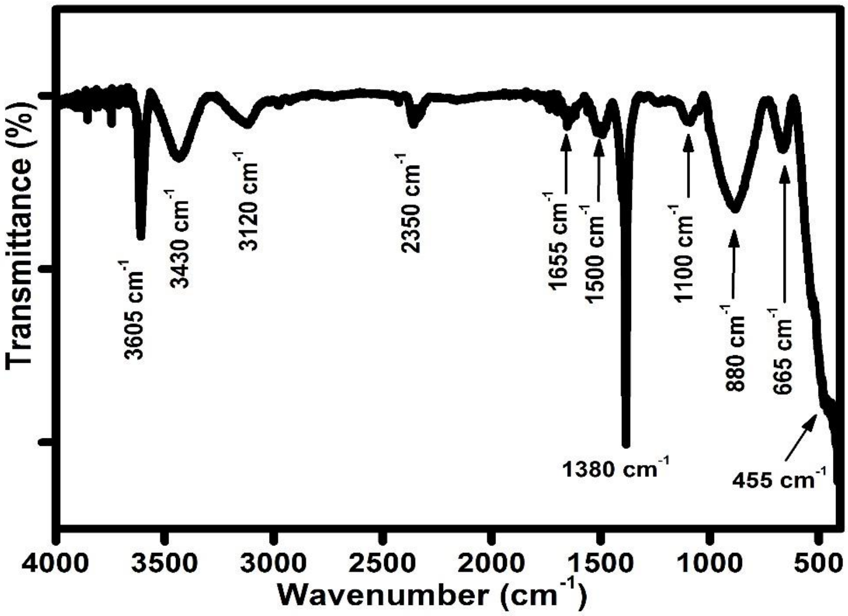

Fig. 8.2: FTIR spectrum of $LaGdSiO_5:Dy^{3+}$ 1.0 mol % nanophosphor.

UV-Vis reflectance measurement was performed on $LaGdSiO_5:Dy^{3+}$ x mol % for different values of x (x = 0.05, 0.75, 1.5, 3.0 and 5.0) and the resulting spectra are shown in Fig. 8.3. The absorption peaks observed at 275 and 313 nm are respectively assigned to the $^8S_{7/2} \rightarrow ^6I_J$ and $^6P_J \rightarrow ^8S_{7/2}$ f-f transitions of Gd^{3+} [48] while the ones at 351 and 386 nm are assigned to the $^6H_{15/2} \rightarrow ^6P_{7/2}$ and $^6I_{15/2} \rightarrow ^4I_{13/2}$ f-f transition of Dy^{3+} [49]. The absorption observed around 270 nm is probably due to the interband transition. The band gaps of $LaGdSiO_5:Dy^{3+}$ x mol % (x = 0.05, 0.75, 1.5, 3.0 and 5.0) was determined using Tauc plot [50]. Tauc plot uses the relation between the absorption coefficient and the band gap of a material given in eqn. 8.2 to estimate the band gap of the material.

$$(\alpha h v)^{1/n} = A\left(hv - E_g\right) \tag{8.2}$$

In eqn. 8.2, α is the absorption coefficient, h is Planck's constant, v is the frequency of vibration, E_g is the band gap, n stand for the nature of the sample transition and A is a constant. Fig. 8.4 shows the calculated $(hv) - [hvF(R_\infty)]^{1/2}$ curve of the nanophosphors. The estimated band gaps are shown in table 8.2. The observed variation in the band gap can be as a result of three possible factors; lattice strain, crystallite size or carrier concentration

[51, 52]. But since the crystallite sizes are approximately the same, the observed variations in the band gaps can be attributed to lattice strain and carrier concentration.

Table 8.2: The estimated band gap of $LaGdSiO_5:Dy^{3+}$ x mol% (x = 0.05, 0.75, 1.5, 3.0 and 5.0)

$LaGdSiO_5:Dy^{3+}$ x mol%	Band gap (eV)
x = 0.05	4.72
x = 0.75	4.64
x = 1.5	4.36
x = 3.0	4.65
x = 5.0	4.59

Fig. 8.5 shows the excitation spectra of $LaGdSiO_5:Dy^{3+}$ x mol% (x = 0.05, 0.1, 0.25, 0.75, 1, 1.5, 2, 3 and 5 mol %) nanophosphors recorded when monitoring the emission at the wavelength of 575 nm. The excitation peaks at 425 nm ($^6H_{15/2}\rightarrow{}^4G_{11/2}$), 454 nm ($^6H_{15/2}\rightarrow{}^4I_{15/2}$) and 475 nm ($^6H_{15/2}\rightarrow{}^4F_{9/2}$) are ascribed to the f→f transition of Dy^{3+} [53].

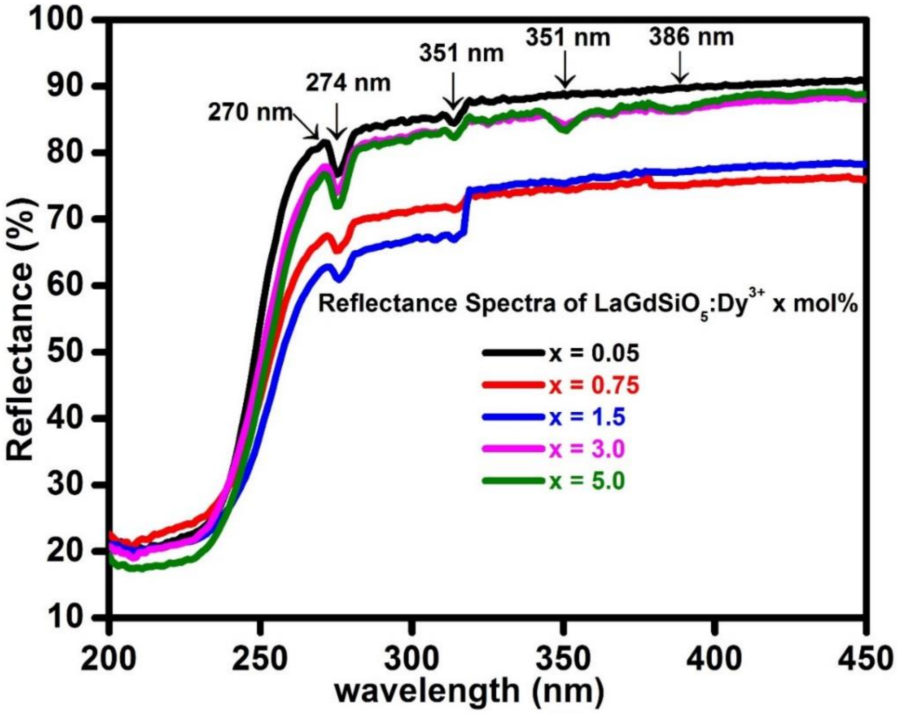

Fig. 8.3: UV-Vis reflectance spectra of $LaGdSiO_5:Dy^{3+}$ x mol% (x = 0.25, 0.75, 1.0, 3.0 and 5.0).

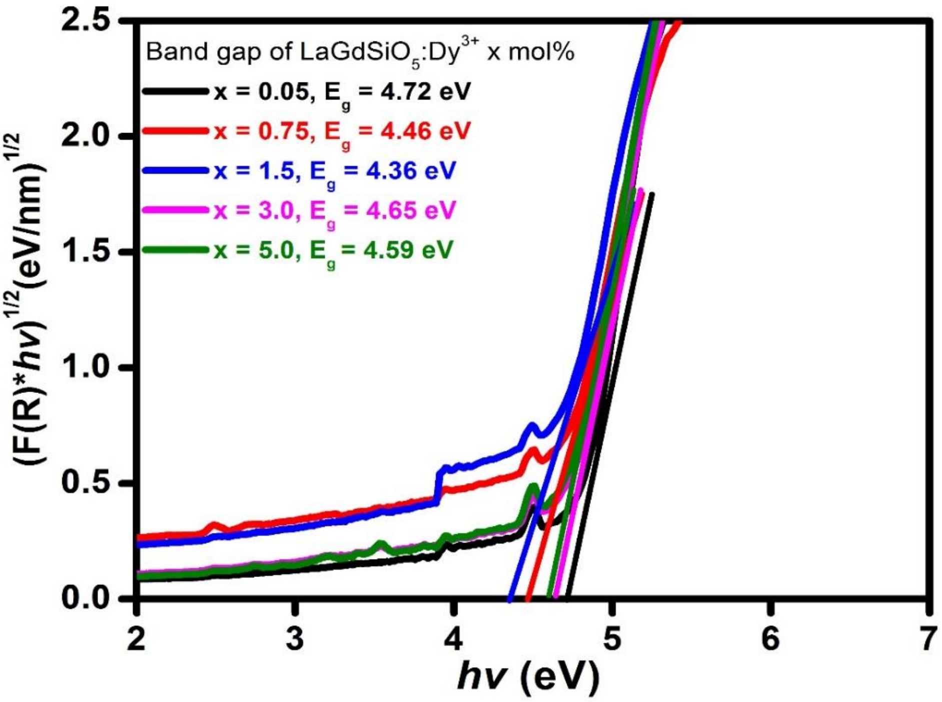

Fig. 8.4: Band gap of LaGdSiO$_5$:Dy^{3+} x mol % (x = 0.05, 0.75, 1.5, 3.0 and 5.0).

The PL emission spectra were measured from each of the three electronic transitions observed in the excitation spectra (425, 454 and 475 nm). In each case, part of the excitation wavelength was absorbed and re-emitted. This is analogous to the InGaN-based YAG:Ce system, where InGaN LED is used to excite YAG:Ce and a portion of the blue light from InGaN LED is absorbed and re-emitted [32]. Fig. 8.6 shows the emission spectra under 425 nm excitation. The emission spectra exhibit an emission peak at 425 nm that is assigned to radiative recombination from $^4F_{9/2}\rightarrow{}^6H_{15/2}$ f→f electronic transition of Dy^{3+} ions after undergoing a non-radiative transition from $^4G_{11/2}\rightarrow{}^4F_{9/2}$ level (see fig. 8.8). Other emission lines observed at 485 nm, 575 nm, 668 nm and 756 nm are respectively from $^4F_{9/2}\rightarrow{}^6H_{15/2}$, $^4F_{9/2}\rightarrow{}^6H_{13/2}$, $^4F_{9/2}\rightarrow{}^6H_{11/2}$ and $^4F_{9/2}\rightarrow{}^6H_{9/2}$ f→f electronic transitions from Dy^{3+} ions. Under 454 nm excitation, the emission peak which is due to radiative recombination from $^4F_{9/2}\rightarrow{}^6H_{15/2}$ f→f electronic transition from Dy^{3+} ions was also observed at 454 nm (the spectra not shown) after a non-radiative transition from $^4I_{15/2}\rightarrow{}^4F_{9/2}$ level (see fig. 8.8). Also observed at 485, 575, 668 and 756 nm are respectively $^4F_{9/2}\rightarrow{}^6H_{15/2}$, $^4F_{9/2}\rightarrow{}^6H_{13/2}$, $^4F_{9/2}\rightarrow{}^6H_{11/2}$ and $^4F_{9/2}\rightarrow{}^6H_{9/2}$ f→f electronic transitions also from Dy^{3+} ions [54]. When the emission was monitored under 475 nm excitation wavelength (Fig. 8.7), the radiative recombination emission peak from 475 nm ($^4F_{9/2}\rightarrow{}^6H_{15/2}$ f→f transition from Dy^{3+} ions) was found to be dominant while the 485 nm ($^4F_{9/2}\rightarrow{}^6H_{15/2}$) peak form a shoulder on it. Other emission peaks observed at 575 nm ($^4F_{9/2}\rightarrow{}^6H_{13/2}$), 668 nm ($^4F_{9/2}\rightarrow{}^6H_{11/2}$), and 756 nm ($^4F_{9/2}\rightarrow{}^6H_{9/2}$) are also from f→f transition of Dy^{3+}.

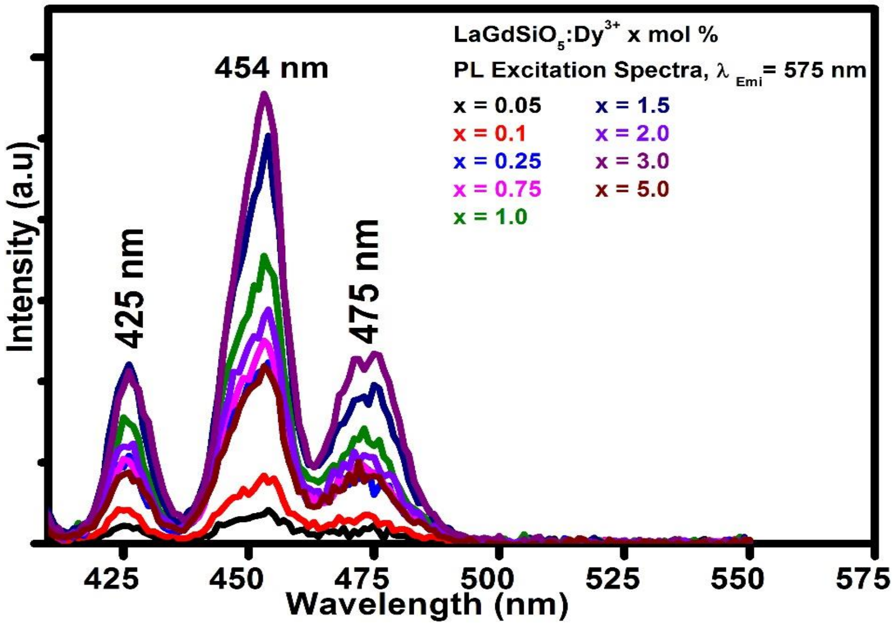

Fig. 8.5: PL excitation spectra of $LaGdSiO_5$:Dy^{3+} x mol % (x = 0.05, 0.1, 0.25, 0.75, 1.0, 1.5, 2.0, 3.0 and 5.0) monitored under 575 nm emission wavelength.

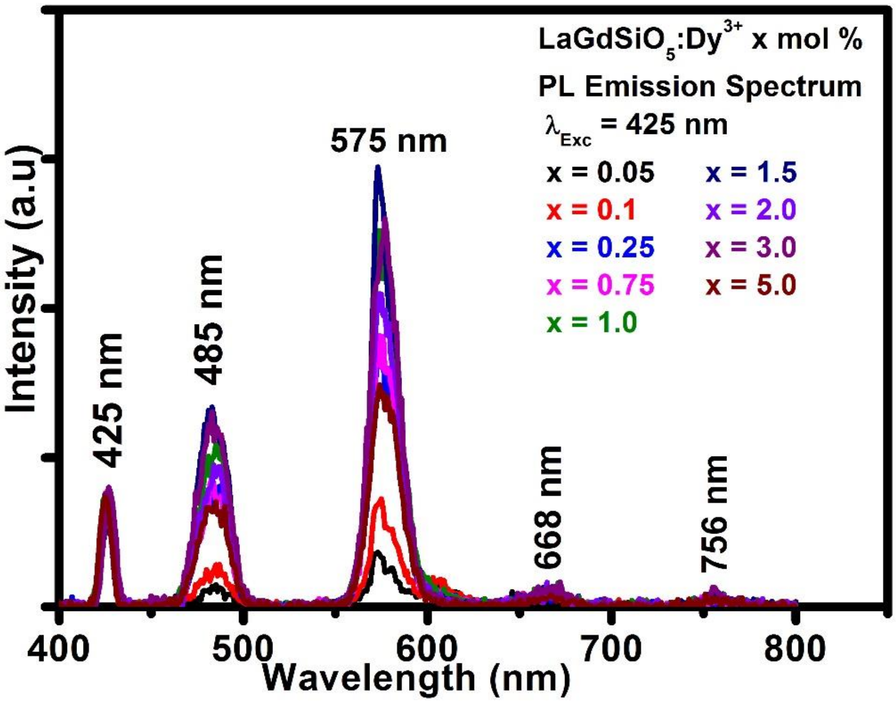

Fig. 8.6: PL emission spectra of $LaGdSiO_5$:Dy^{3+} x mol % (x = 0.05, 0.1, 0.25, 0.75, 1.0, 1.5, 2.0, 3.0 and 5.0) monitored under 425 nm excitation wavelength.

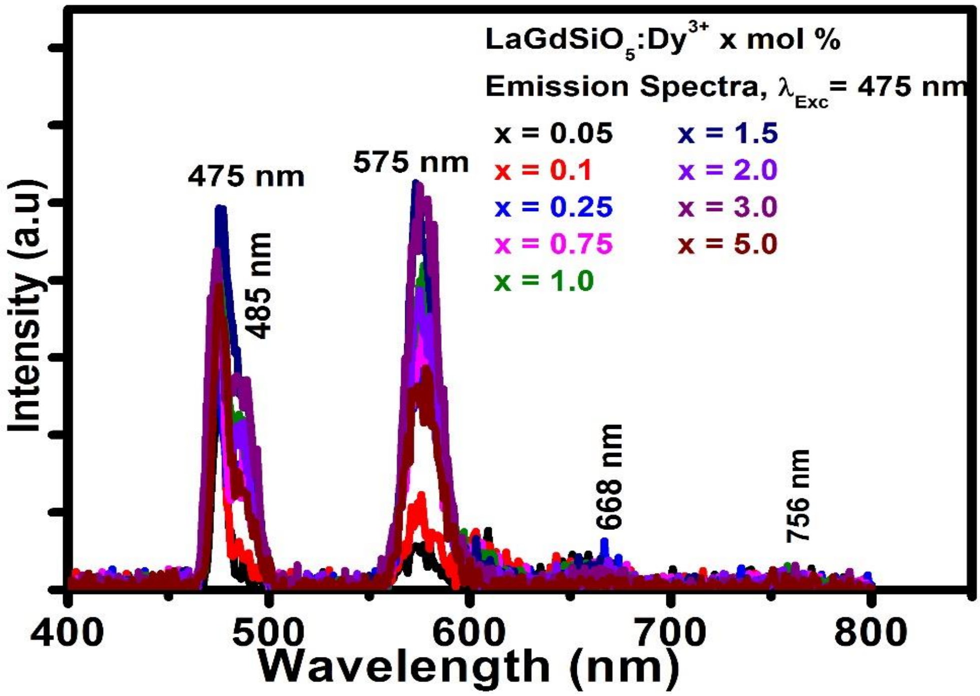

Fig. 8.7: PL emission spectra of LaGdSiO$_5$:Dy^{3+} x mol % (x = 0.05, 0.1, 0.25, 0.75, 1.0, 1.5, 2.0, 3.0 and 5.0) monitored under 475 nm excitation wavelength.

From Fig. 8.6 and 8.7, it is evident that the intensity ratios of the emission peaks at 425 and 475 nm respectively are not the same when compared to the corresponding peaks at 485 nm and 575 nm. Under certain assumptions, the two emission lines (425 nm and 475 nm) can have similar emission intensity ratios when compared to the emission intensities of their respective 485 and 575 nm peaks. These assumptions include that: (i) the luminescence intensity usually measured as the time average luminescence intensity is proportional to the number of the excited activator ions in a finite volume in the crystals arranged in the first layer on the fixed screen area, if the size of the electron beam on the phosphor screen is kept constant for all measurement. (ii) The time average luminescence intensities of a phosphor is proportional to the number of quanta emitted from the excited activator ions in unit time, if we assume that each excited activator ion in the crystal emits and returns to the ground state [55]. (iii) The mode of excitation of the activator ions in each case are the same [56].

By and large, the three emission lines meet the first and the third assumptions since the phosphor screen and the size of electron beam incident on it is constant for all measurements and they are all excited in the same mode. However, the second assumption is not the same for the emission lines. This can be understood by studying the energy diagram of Dy^{3+} shown in Fig. 8.8. In the 425 and 454 nm transition lines, non-radiative transitions occurred from

${}^4G_{11/2}$ and ${}^4I_{15/2}$ respectively to ${}^4F_{6/2}$ energy level before the final radiative transition from ${}^4F_{6/2}$ to ${}^6H_{15/2}$. Hence 425 and 454 nm transition lines fail to meet the second assumption since they lost some photons to the non-radiative transition process and this led to the decrease in their luminescence intensity. On the other hand, 475 nm transitions underwent only radiative transition from ${}^4F_{9/2}$ to ${}^6H_{15/2}$ and as a result of that, it has luminescence emission intensity higher than 485 nm comparable to 575 nm emission line.

Fig. 8.9 shows the CIE (International Commission on Illumination) colour space of the nanophosphors for x = 0.05 and 3.0 mol% when monitored at 454 nm and 475 nm excitation respectively. The CIE coordinates of (0.336, 0.313) and (0.359, 0.361) were obtained for x = 0.05 and 3.0 mol% which are close to the standard D65 daylight (white light) with colour coordinates (0.3129, 0.3292) [57]. The colour coordinate for the rest of the samples and their excitation wavelengths are shown in table 8.3.

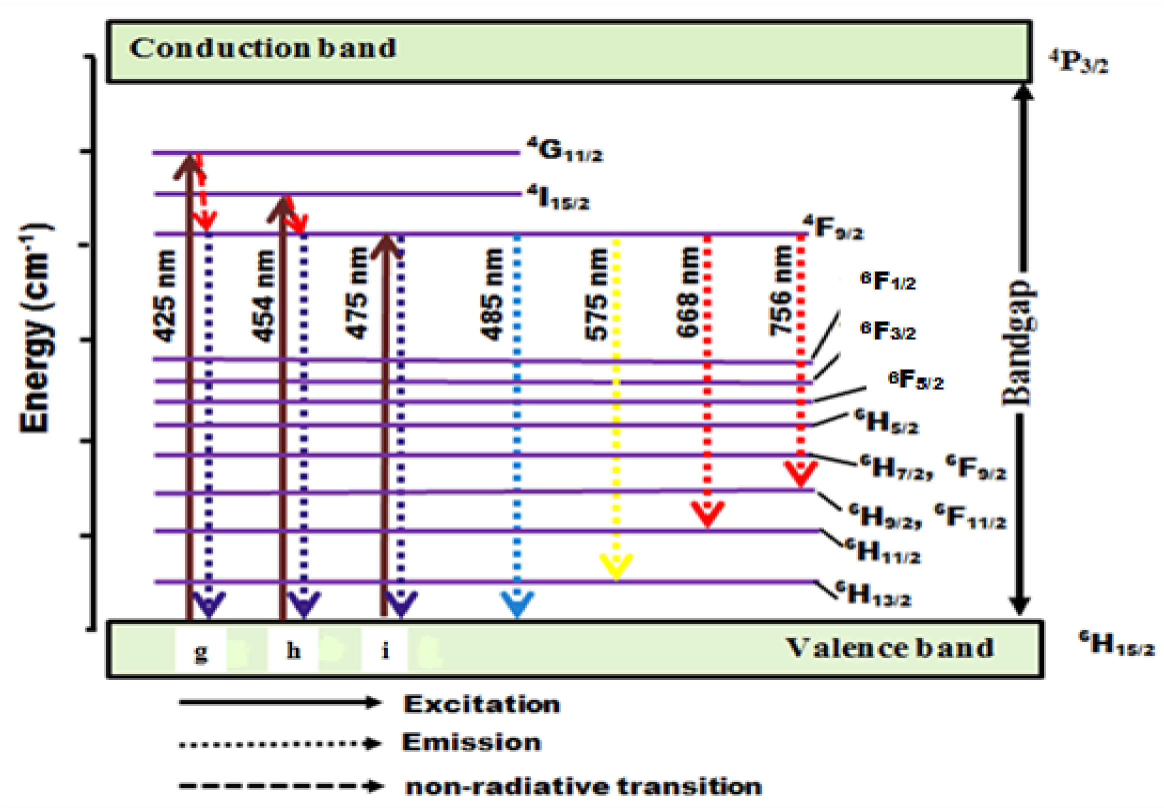

Fig. 8.8: Energy levels of Dy^{3+} showing the excitation, emission and non-radiative transitions.

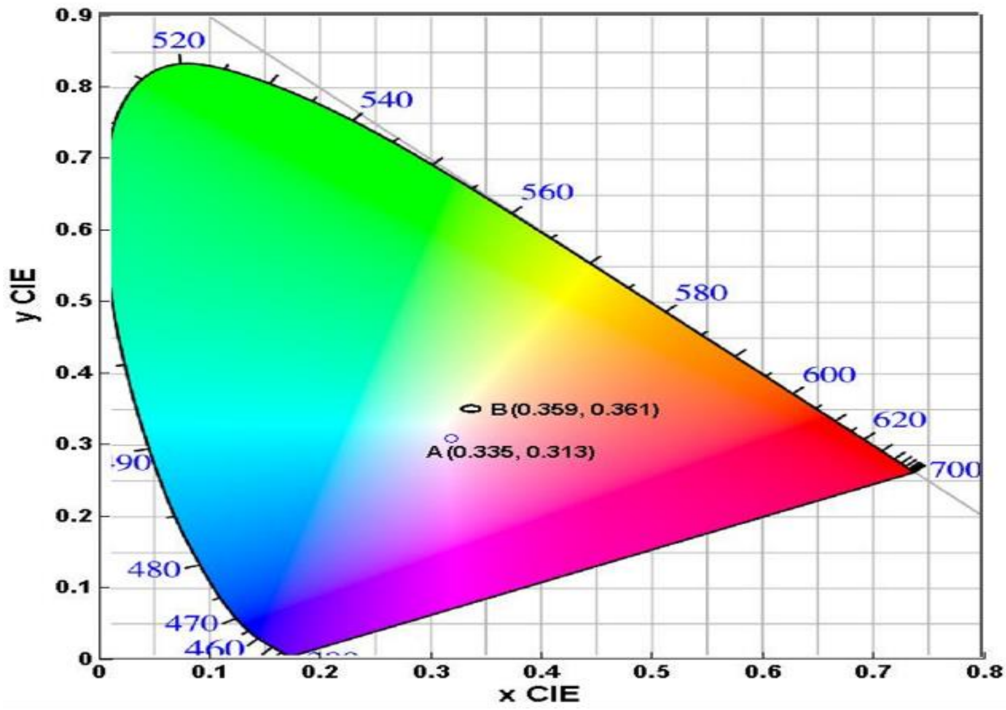

Fig. 8.9: CIE coordinates diagram of $LaGdSiO_5:Dy^{3+}$ x mol % for x = 0.05 (A) and x = 3.0 (B).

Table 8.3: CIE colour coordinate for $LaGdSiO_5:Dy^{3+}$ x mol% (x = 0.05, 0.1, 0.25, 0.75, 1.0, 1.5, 2.0, 3.0 and 5.0 mol %)

Dy^{3+} Concentrations (mol %)	$\lambda_{Exc}(nm)$		
	425	454	475
	CIE colour coordinates		
0.05	(0.387, 0.294)	(0.335, 0.313)	(0.413, 0.303)
0.1	(0.389, 0.343)	(0.362, 0.361)	(0.373, 0.323)
0.25	(0.391, 0.387)	(0.399, 0.409)	(0.369, 0.354)
0.75	(0.388, 0.382)	(0.390, 0.401)	(0.382, 0.358)
1.0	(0.394, 0.394)	(0.393, 0.410)	(0.395, 0.392)
1.5	(0.385, 0.400)	(0.370, 0.396)	(0.368, 0.380)
2.0	(0.394, 0.397)	(0.395, 0.406)	(0.371, 0.377)
3.0	(0.377, 0.855)	(0.393, 0.412)	(0.359, 0.361)
5.0	(0.372, 0.373)	(0.363, 0.393)	(0.367, 0.379)

8.4. Conclusion

Under various blue wavelength excitations, lanthanum gadolinium oxyorthosilicate ($LaGdSiO_5$) doped with different molar concentrations of dysprosium (Dy^{3+}) can produced white light. For each excitation, emission line corresponding to the excitation line was observed. The CIE colour spaces of (0.336, 0.313) and (0.359, 0.359, 0.361) were obtained for molar concentration of Dy^{3+} of 0.05 and 3.0 when monitoring the emission at the excitation wavelength of 454 nm and 475 nm respectively. These suggest that our material have potential application in blue light excited white LED. The crystallite sizes and the lattice strains calculated from the X-ray diffraction peaks using Williamson-Hall equation ranges from 12 nm to 16 nm and 1.6×10^{-2} to 2.43×10^{-2} respectively. The band gap initially decreased with increasing Dy^{3+} molar concentration, but at higher concentration of Dy^{3+}, it increased.

8.5. References

[1] K.J. McClellan and D. Cooke. Crystalline Rare-earth Activated Oxyorthosilicate phosphor. U.S. Patent. Sr. No. 6,689,293 B2 (2004).

[2] D.W. Cooke, E.A. McKigney, R.E. Muenchausen and B.L. Bennett., Nanocomposite scintillators, detector, and method. U.S. Patent. Sr. No. 60/752,981 (2005).

[3] V.G. Bondar, B.V. Grinyov, K.A. Katrunov, L.N. Lisetski, L.L. Nagornaya, V.D. Ryzhikov, V.G. Spasov, N. Starzhinskiy and G. Tamulaitis. Nucl. Istru. Meth. Phys.Res. A., 537 (2005) 215-218.

[4] X. Qin, Y. Ju, S. Bernhard and N. Yao. Mat. Res. Bul. 42 (2007) 1440-1449.

[5] K. Takagi and T. Fukazawa, Appl. Phys. Lett., 42 (1983) 43–45.

[6] H. Ishibashi, K. Shimizu and K. Susa, IEEE Trans. Nucl. Sci., 36 (1989) 170–172.

[7] T.E. Peters. J. Electrochem. Soc. 116 (1969) 985-989.

[8] J. Wang, S. Tian, G. Li, F. Liao, X. Jing.. J. Electrochem. Soc. 148 (6) (2001) H61-H66.

[9] R.Y. Lee, F.L. Zhang, J. Penczek, B.K. Wagner, P.N. Yocom, C.J. Summers. J. Vac. Sci. Technol. B, 16 (1998) 855.

[10] C.M Michail, A. Toutountzis, I.G. Valais, I. Seferis, M. Georgousis, G. Fountos, I.S. Kandarakis , G.S. Panayiotakis. e-JST., 2 (2010) 25-32.

[11] T. Kamae, Y. Fukazawa, N. Isobe, M. Kokubun, A.Kubota, S. Osone, T. Takahashi, N. Tsuchida, H. Ishibashi. Nucl. Instr. Meth. Phys. Res. A,, 490 (2002) 456-464.

[12] V. Avdeichikov, B. Jakobsson, V. A. Nikitin, V. Nomokonov, A. Wegner. Nucl. Instr. Meth. Phys. Res. A., 484 (2002) 251-258.

[13] W. Mangesha, T.D. Taulbee, J.D. Valentine, B.D. Rooney. Nucl. Instr. Meth. Phys. Res. A., 486 (2002) 448-452.

[14] L. Zheng, L. Su and J. Xu. Growth and Characterization of Ytterbium Doped Silicate Crystals for Ultra-Fast Laser Applications, Modern Aspects of Bulk Crystal and Thin Film Preparation, Dr. N. Kolesnikov (Ed.) (2012) pp. 26.

[15] D. Meiss, W. Wischert and S. Kemmler-Sack. Phys. Status Solidi., A133 (1992) 575–584.

[16] M. Yin, C. Duan, W. Zhang, L. Lou, S. Xia and J.C. Krupa, ,J. Appl. Phys., 86 (1999) 3751–3757.

[17] W.M. Yen, S. Shionoya and H. Yamamoto. Phosphor hand book, 2nd edition. CRC Press, Florida, (2007) Section 5.92.

[18] C.F. Guo, L. Luan, Y. Xu, F. Gao and L.F. Liang. J. Electrochem. Soc., 155 (2008) 310.

[19] V. Sivakumar and U.V. Varadaraju. J. Electrochem. Soc., 156 (2009) 179.

[20] X. Zhang and M. Gong. R. Soc. Chem., (2014) DOI: 10.1039/c3dt52328d.

[21] S. Shaat, H. Swart and O. Ntwaeaborwa. Opt. Mat. Exp., 2(7) (2012) 962.

[22] C. Lorbeer and A. Mudring. J. Phys. Chem., C, 17 (2013) 12229-12238.

[23] N. Guo, Y. jia, W. Lv, Q. Zhao, M. Jiao, B. Shao and H. You. Dalton Trans., 42 (2013) 5649.

[24] C. H. Huang, W.R. Liu, T.S. Chan and Y.T. Lai. Dalton Trans., 43 (2014) 7917.

[25] C. Ronda (ed.), Luminescence: from theory to applications, WILEY-Verlag GmbH & Co. KGaA, Weinheim, (2008) pp. 20.

[26] K.G. Sharma and N.R. Singh, New J. Chem., 37 (2013) 2784.

[27] M.N. Luwang, R.S. Ningthoujam, S.K. Srivastava and R.K. Vats., J. Mater. Chem., 21(2011) 5326.

[28] C.R. Kesavulu and C.K. Jayasankar., Mat. Chem. & Phy. 130 (2011)1078-1085.

[29] C. Cao, H.K. Yang, B.K. Moon, B.C. Choi and J.H. Jeong., J. Electrochem. Soci. 158 (2011) J6-J9.

[30] P. Bahu, K. J. Jang, E. S. Kim, L. Shi and H. J. Sed., J. Korean Phy. Soc. 54 (2009) 1488-1491.

[31] L.P. Du, K. Bharat, X.Y. Guan, and J.S. Yu., J. App. Phys. 117 (2015) 083112.

[32] W.Z. Jun, L.P. Lai, Y.Z. Ping, G.Q. Lin, and L. Xu., Chin. Phys. B 19 (2010) 017801

[33] S.N. Ogugua, S.K.K. Shaat, H.C. Swart and O.M. Ntwaeaborwa. J. Phy. & Chem. of Solids, 83 (2015) 109–116.

[34] R.D. Shannon. Acta Crystallogr., 32 (1976) 751–767.

[35] J. Felsche. The crystal chemistry of the rare-earth silicates, Structure and Bonding, Springer-Verlag, New York (1973) pp.99-197.

[36] A.A. Bosak, C. Dubourdieu, J.P. Sénateur, O. Yu. Gorbenko and A.R. Kaul. Crystal Engineering, 5 (2002) 355-364.

[37] R.D. Shannon, C.T. Prewitt, Acta Crystallogr., B 25 (1969) 925.

[38] G.K. Williamson and W.H. Hall. X-ray line broadening from filed aluminium and wolfram. Acta Metallurgica, (1953) 1.

[39] V.D. Mote, Y. Purushotham and B.N. Dole. J. Theoretical and Applied Phys., 6 (2012) 6.

[40] S. Bernal, F. J. Botana, R. Garcia and J. M. Rodriguez-Izquerdo. React. Solids, 4 (1985) 537.

[41] G.X. Liu, G.Y. Hong, and D.X. Sun. J. Colloid Interface Sci., 278 (2004) 133.

[42] Y. Wang et al. ISRN Nanotechnology, (2011) doi:10.5402/2011/715183, pp 5.

[43] R. Krsmanovic et al. Acta Physica Polonnica. 112 (2007) 975-980.

[44] M.P. Rosynek and D.T. Magnuson. J. Catal. 46 (1977) 402.

[45] C. Louis, R. Bazzi, M.A. Flores, W. Zheng, K. Lebbou, O. Tillement, B. Mercier, C. Dujardin, and P. Perriat. J. Solid State Chem., 173 (2003) 335.

[46] S. Bernal, J. A. Diaz, R. Garcia and J. M. Rodriguez-Izquerdo, J. Mater. Sci. 20 (1985) 537.

[47] S. Bernal, F. J. Botana, R. Garcia and J.M. Rodriguez-Izquerdo. Thermochim. Acta 66 (1983) 139.

[48] Y. Li, Y. Chang, Y. Chang, Y. Lin and C Laing. J. Phys. Chem. C, 111 (2007) 10682-10688.

[49] X. Liu, W. Xiang, F. Chen, Z. Hu and W. Zhang, Mater. Res. Bull. 48 (2013) 281.

[50] J. Tauc. The optical properties of solids (North-Holland, Amsterdam, 1970) Young, PA.J. Phys. C: Solid State Phys. 4 (1971) 93.

[51] U.N. Maiti, P.K. Ghosh, S. Nandi and K.K. Chatopadhyay, Physica B, 387 (2007) 103.

[52] A. Lila, S. Husain, W. Khan, and S. Alim. Asian J. of Chem. 23 (2011) 5605-5607.

[53] X. Liu, W. Xiang, F. Chen, Z. Hu and W. Zhang. Mater. Res. Bull., 48 (2013) 281.

[54] R. Lisiecki, G. Dominiak-Dzik, P. Solarz, W. Ryba-Romanowski, M. Berkowski, and M. Glowacki. Appl Phys B 98 (2010) 337-346.

[55] L. Ozawa. J. ELectrochem. Soc. 1 (1981) 128.

[56] L. Ozawa and H. N. Hersh, Phys. Rev. Lett., 36 (1976) 683.

[57] Hunterlab, available online hunterlab.com, accessed June, 2014.

CHAPTER NINE

Summary, conclusion, future work and research presentations and publications

9.1. Summary

This section gives summary and conclusion of this thesis.

Chapter five titled "Structure, Optical Properties and Elemental Analyses of mixed rare earth oxyorthosilicate (R_2SiO_5, R = La, Gd and Y) doped Dy^{3+} nanophosphors" discussed the synthesis and characterization of rare earth oxyorthosilicates doped with dysprosium (Dy^{3+}). Dysprosium (Dy^{3+}) doped lanthanum gadolinium oxyorthosilicate ($LaGdSiO_5$), lanthanum yttrium oxyorthosilicate ($LaYSiO_5$) and gadolinium yttrium oxyorthosilicate ($GdYSiO_5$) phosphors (in powder form) were synthesized by urea-assisted combustion method. The X-ray diffractometer analysis confirmed that the $LaGdSiO_5$, $LaYSiO_5$ and $GdYSiO_5$) crystalized in monoclinic phases. The chemical composition of the phosphors was analyzed by measuring the atomic and molecular ionic species using the time of flight secondary ion mass spectroscopy (ToF SIMS). In addition, ToF SIMS imaging technique was used to determine the distribution of the Dy^{3+} dopant ions on the surface on the phosphors. The average crystallite sizes and lattice strains of the phosphor were increased by Dy^{3+} doping. The field emission scanning electron microscope images showed that the powders were made up of an agglomeration of particles with no regular shape. The photoluminescence data showed narrow line emission peaks at the wavelengths of 485 nm (minor emission) and 573 nm (major emission) associated with the f→f transitions of Dy^{3+}. The photoluminescence (PL) measurements showed that the emission peak of $LaGdSiO_5:Dy^{3+}$ was ~ 2× more intense than $GdYSiO_5:Dy^{3+}$ and ~ 3× more intense than $LaYSiO_5:Dy^{3+}$ when excited using monochromatic lamp with a wavelength of 241 nm. However, when the powders were excited using a 325 nm He-Cd laser, the highest PL emission intensity was observed from $GdYSiO_5:Dy^{3+}$.

Chapter six was titled "Structure, scanning electron microscopy, and spectroscopy of $La_{2-x}Gd_xSiO_5:Dy^{3+}$ nanophosphors". Lanthanum gadolinium oxyorthosilicate or $La_{2-x}Gd_xSiO_5$ (x = 0, 0.5, 1.0, 1.5 and 2.0) nanophosphors doped with dysprosium (Dy^{3+}) were prepared by urea- and ammonium nitrate-assisted solution combustion method. The X-ray diffraction (XRD) patterns confirmed that the phosphors crystallized in pure monoclinic phases of

La_2SiO_5 and Gd_2SiO_5 or the admixtures of the two phases depending on the ratio of La:Gd in the host lattice. The estimated crystallite sizes were found to vary from 10 to 21 nm. The field emission scanning electron microscopy (FE-SEM) images showed that the particles were agglomerated together and they had no definite sizes. The chemical composition analyses and the electronic state were analyzed using the energy-dispersive X-ray spectroscopy (EDS) and X-ray photoelectron spectroscopy (XPS) respectively. The Fourier transform infrared spectroscopy (FTIR) data supplemented both the XRD and EDS data by confirming that the stretching mode frequencies all related to La_2SiO_5 and Gd_2SiO_5, except a few absorption peaks ascribed to atmospheric moisture and hydrocarbons. The X-ray photoelectron spectroscopy data suggested that there were a few plasmonic satellite peaks on the surface. The band gaps measured from the ultraviolet visible spectroscopy (UV-Vis) data were shown to vary with the molar ratio of La to Gd. The phosphorescence spectra showed the two characteristic emission of Dy^{3+} at 485 nm (blue) and 573 nm (yellow) while the fluorescence spectra showed an additional broad blue emission with maximum around 415 nm. Reduction in the impurity level led to decrease in the 415 nm emission and enhanced the yellow emission. The CIE chromaticity coordinates calculated from the fluorescence emission showed colours which were tuned from blue to white and yellow when the molar ratio of La to Gd in the $La_{2-x}Gd_xSiO_5:Dy^{3+}$ lattices were varied.

Chapter seven was titled "The influence of Dy^{3+} ions concentration and post-annealing on the properties of $LaGdSiO_5:xDy^{3+}$ (x = mol %) nanophosphors". A novel $LaGdSiO_5:Dy^{3+}$ x mol% (x = 0.025, 0.1, 0.25, 0.75, 1.0, 1.5, 2.0, 3.0 and 5.0) nanophosphors were prepared by urea- and ammonium nitrate-assisted combustions. A change of phase was observed in the X-ray diffractions pattern from the low to high temperature phase in the samples annealed at 1000 °C for 1hr. The crystallite size varies from 12 to 16 nm. The photoluminescence (PL) studies were studied in both phosphorescence and in fluorescence mode using a PL system equipped with xenon lamp as the excitation source and a PL using 325 nm He-Cd gas laser as the excitation source. The phosphorescence excitation spectra showed two peaks at 227 and 241 nm which was ascribed to f→d allowed transition of Dy^{3+}. The PL intensities of 241 nm excitation decreased drastically after annealing while the 227 nm peaks increased. The phosphorescence emission spectra showed two prominent peaks from Dy^{3+} at 485 nm and 573 nm. The fluorescence emission spectra showed a similar emission lines as the phosphorescence emission spectra except for an additional broad blue emission with maximum around 415 nm ascribed to self-trapped excitons (STE) in SiO_2. The CIE calculated from the fluorescence spectra showed coordinates which varies from blue to yellow of with change in Dy^{3+} molar concentration with coordinates of (0.343, 0.358) and (0.342, 0.357) which are close to white light generated for Dy^{3+} concentrations of 1.5 and 3.0 mol% respectively.

Chapter eight was titled "Blue Light excited $LaGdSiO_5$ doped x molar % Dy^{3+} white light-emitting nanophosphors for solid state lighting applications". The PL emission spectra of lanthanum gadolinium oxyorthosilicate ($LaGdSiO_5$) doped with different molar concentrations of dysprosium (Dy^{3+}) nanophosphors were monitored using 425, 454 and 475 nm excitation wavelength. For each excitation wavelength, part of the excitation energy were absorbed and converted to emission. The crystallite size and the lattice strain calculated from the X-ray diffraction peaks using Williamson-Hall equation varies between 12 nm to 16 nm and 1.6×10^{-2} nm to 2.43×10^{-2} nm respectively. CIE colour space of (0.336, 0.313) and (0.359, 0.359, 0.361) were obtained for Dy^{3+} molar concentration of 0.05 and 3.0 when the emission was monitored using 454 nm and 475 nm respectively. The band gap measured from the reflectance curve using Tauc plot initially decreased with increasing Dy^{3+} concentration, but at high Dy^{3+} concentration, it decreases.

9.2. Conclusion

It can be concluded that: (i) single and mixed rare earth oxyorthosilicate (R_2SiO_5, R = La, Gd or Y) doped with different concentration of Dy^{3+} nanophosphors were successfully prepared by urea and ammonium nitrate-assisted solution combustion method with the crystallite size ranging from 8 nm to 21 nm. (ii) When excited in phosphorescence mode using monochromatic xenon lamp with a wavelength of 241 nm, $LaGdSiO^5:Dy^{3+}$ can yield emission ~ 3× more intense than those of $LaYSiO_5:Dy^{3+}$ and $GdYSiO_5:Dy^{3+}$. (iii) When excited in fluorescence mode using a 325 nm He-Cd laser, $GdYSiO_5:Dy^{3+}$ can yield highest PL emission intensity. (iv) By varying the molar ratio of La and Gd in $La_{2-x}Gd_xSiO_5:Dy^{3+}$ (x = 0, 0.5, 1, 1.5 and 2) matrices or varying the molar concentration of Dy^{3+} in $LaGdSiO_5:Dy^{3+}$ matrices, the colour of the emitted light can be varied from blue, through white to yellow when excited using a 325 nm He-Cd laser. (v) When excited at 454 nm and 475 nm using monochromatic xenon lamp as the excitation source, $LaGdSiO_5:Dy^{3+}$ x mol% (x = 0.05, 0.1, 0.25, 0.75, 1, 1.5, 2, 3 and 5) can yield white light.

Mixed rare earth oxyorthosilicates doped with Dy^{3+} has shown their ability to emit multicolour and white light when excited with UV-vis light and white light when excited with blue light. These made them novel phosphors for application in UV-pumped multicolour and white light emitting diodes and blue light-pumped white light emitting diodes. The ability of a phosphor to be stable in chemical composition and crystal structure including the valence of the doped rare earth ions when exposed to either chemical attach or UV or blue irradiation is known as its chemical stability. Also thermal quenching refers to the measure of the thermal stability of a phosphor. Phosphors used in LEDs are expected to have high chemical stability, small thermal quenching and short lifetime

9.3. Future work

Although phosphors are usually commercially available in powder form, for practical purposes, they are in thin film forms. It is well known that in thin film form, phosphors has more advantages than powders, as a results our future work will focus on preparing thin films using these materials and performing additional characterizing such as investigation of the thermal and the chemical stability and determining of the lifetime among others things.

9.4. Research presentations and publications

The work contained in this thesis has been presented in the following conferences:

(i) **S.N. Ogugua**, S.K.K Shaat, Swart, H.C., O.M. Ntwaeaborwa 2014. Blue light excited LaGdSiO$_5$:Dy^{3+} x mol% white light emitting nanophosphors synthesized via combustion method. The 5th international conference on nanoscience & nanotechnology, Vaal University of Technology, Vanderbijlpark, South Africa, 30 March - 02 April 2014.

(ii) **S.N. Ogugua**, S.K.K. Shaat, H.C. Swart, O.M. Ntwaeaborwa. 2015. Synthesis and characterization of a novel rare-earth oxyorthosilicates (R$_2$SiO$_5$) (R = La, Gd, Y) doped Dy^{3+} nanophosphors. The 6th South African conference on photonic materials, Mabula game lodge, South Africa, 4-8 May, 2015.

(iii) **O.M. Ntwaeaborwa**, S.N. Ogugua, S.K.K. Shaat, H.C. Swart. Synthesis and characterization of multicolour and white light emitting R$_2$SiO$_5$:Dy^{3+} (R = La, Gd, Y) phosphors. Proceeding Advanced Materials World Congress, Stockholm, Sweden, 23-26 August, 2015.

List of publications include:

(i) **S.N. Ogugua**, S.K.K. Shaat, H.C. Swart, O.M. Ntwaeaborwa. Optical properties and chemical composition analyses of mixed rare earth oxyorthosilicate (R$_2$SiO$_5$, R = La, Gd and Y) doped Dy^{3+} phosphors prepared by urea-assisted solution combustion method. J. Phys. & Chem. Solids 83 (2015) 109-116.

(ii) **Simon N. Ogugua**, Samy K.K. Shaat, Hendrik C. Swart and Odireleng M. Ntwaeaborwa. Structure, scanning electron microscopy, and spectroscopy of La$_{2-x}$Gd$_x$SiO$_5$:Dy^{3+} nanophosphors. Under review.

(iii) **Simon N. Ogugua**, Samy K.K. Shaat, Hendrik C. Swart and Odireleng M. Ntwaeaborwa. White light emitting LaGdSiO$_5$:Dy^{3+} nanophosphors for solid state lighting applications. Under review.

(iv) **Simon N. Ogugua**, Samy K.K. Shaat, Hendrik C. Swart and Odireleng M. Ntwaeaborwa. The Influence of Dy^{3+} ions Concentration and Annealing on the Properties of LaGdSiO$_5$:Dy^{3+} Nanophosphors. Under review.